The Topochemical Reduction of Ru-containing Double Perovskite Oxides

---

Zhilin Liang

St. Catherine's College



A thesis submitted to the Board of the Faculty of Physical Sciences in partial fulfilment of the requirements for the degree of Doctor of Philosophy

The Topochemical Reduction of Ru-containing Double Perovskite Oxides

This work focuses on the topochemical reduction of some ruthenium-containing double perovskite phases using various reducing agents (Zr, LiH, CaH_2) to form novel metastable reduced phases and anion-substituted phases.

The progress of the reduction of $LaSrNiRuO_6$ with CaH_2 to yield $LaSrNiRuO_4$ is related to the synthesis conditions of the parent oxide $LaSrNiRuO_6$ phase, where quenched samples of $LaSrNiRuO_6$ react much faster than the slow-cooled samples. Detailed structural and microstructural characterisation of quenched and slow-cooled samples of $LaSrNiRuO_6$ show that both samples are structurally indistinguishable, with differences in reactivity arising from their microstructures: quenched samples of $LaSrNiRuO_6$ have small/strained crystalline domains while slow-cooled samples have large/less strained crystalline domains. The difference in the reactivity is attributed to the microstructure of $LaSrNiRuO_6$, where small crystalline domains have greater plasticity and lower the activation energy of the reduction reaction. In addition, it is likely that enhanced microstructural strain in the quenched sample act to destabilise the starting material, which further lowers the activation energy of this reduction reaction. These observations have demonstrated that the microstructure of a starting material plays an important role in topochemical reactions.

Similarly, the reactivity of the analogous Ru-containing double perovskite phase $LaSrCoRuO_6$ can be enhanced through rapid cooling. The quenched $LaSrCoRuO_6$ is then reduced with various reducing agents and several novel metastable reduced phases are successfully synthesised.

Reduction of $LaSrCoRuO_6$ with a Zr getter yields a novel oxygen deficient phase $LaSrCoRuO_5$. $LaSrCoRuO_5$ adopts a complex anion-vacancy ordered structure which can be described in the space group $P112_1$. The structure of $LaSrCoRuO_5$ consists of corner sharing CoO_6 octahedra, RuO_5 square-based pyramidal units and CoO_4 square-planar units. BVS calculations indicate the Co^{2+} centres in this compound disproportionate into a 1:1 ratio of Co^{+} and Co^{3+} centres, with Co^{+} centres residing at the square-planar sites and Co^{3+} centres locating at the octahedral sites. The magnetisation data collected from the sample show a ferromagnetic state at 5 K while neutron powder diffraction data collected from the sample at 5 K show no evidence of long-range magnetic ordering,

The more metastable $LaSrCoRuO_4$ phase can be prepared via the reduction of $LaSrCoRuO_6$ with LiH under flowing argon. This compound adopts an infinite layer structure, containing corner sharing CoO_4 and RuO_4 square-planar units. Magnetisation data collected from $LaSrCoRuO_4$ show that this sample is ferromagnetic up to room temperature.

The disproportionation of Co^{2+} centres observed in $LaSrCoRuO_5$ is highly unusual. Therefore, doping of $LaSrCoRuO_5$ was investigated by varying the ratio of La and Sr at the A-site. When the system is slightly hole/electron doped, the resulting doped reduced phases are isostructural with the undoped $LaSrCoRuO_5$ phase. However, when the system becomes heavily hole doped, a different anion-vacancy ordered structure is observed. This observation suggests that the

oxidation states of the transition metals are coupled with the complicated anion-ordered structure adopted $LaSrCoRuO_5$.

Finally, reduction of $LaSrCoRuO_6$ with CaH_2 and LiH in sealed ampoules yields novel oxyhydride phases with a range of oxide/hydride contents. Short-ranged anion ordering is observed in one of the oxyhydride phases. The partial anion ordering can be explained via the different preferences of the *cis* and *trans* MO_4H_2 arrangements.

Declaration

The work described in this thesis was carried out at the Inorganic Chemistry Laboratory at the University of Oxford between October 2019 and May 2023 under the supervision of Professor Michael A. Hayward. All the work presented in this thesis is my own except where I have either acknowledged help from a named person of given reference to a published source. None of the work has been submitted by the author for any degree at any other university.

Zhilin Liang
May 2023

To my family

Acknowledgements

First of all, I would like to thank my supervisor Professor Michael Hayward for giving me the opportunity to join this group. I am extremely grateful for your invaluable guidance and support throughout the whole degree. Your expertise and dedication into scientific research have inspired me to achieve further in the field of science.

I would also like to thank Prof Joke Hadermann and her student Dr Maria Batuk for collecting the electron diffraction data, Dr Pascal Manuel and Dr Fabio Orlandi for their assistance in collecting neutron diffraction data and the instrument scientists at Diamond I11 beamline for their assistance in collecting synchrotron X-ray diffraction data. I would also like to thank Dr Simon Cassidy for the XRD and SQUID training and Dr Robert Jacobs for TGA and TGA-MS training.

Also, I would like to thank the MAH and the SJC group members. I will miss those trips to spoons, the shots and the chicken wings. Covid was tough, but I am glad that I got through it with you guys. Big thanks to everyone that helped me with my thesis, now I guess everyone in the group knows very well about what I have been doing for the past three years.

Finally, I would like to thank my family, for their limitless support. And thank you Jon, for always believing in me.

Table of Contents

The Topochemical Reduction of Ru-containing Double Perovskite Oxides ……..I

Declaration……..……..……..……..……..……V

Acknowledgements ……..……...……..……..……..……IX

Chapter 1 Introduction.....1

1.1 Complex Transition Metal Oxides.....1

1.2 Perovskite Structure and Tolerance Factor.....2

1.2.1 Double Perovskites.....4

1.3 Traditional Solid-State Synthesis and Low Temperature Topochemical Reduction of Complex Metal Oxides.....6

1.3.1 Binary Metal Hydrides.....7

1.3.1.1 Calcium Hydride.....8

1.3.1.2 Lithium Hydride.....10

1.3.1.3 Sodium Hydride.....11

1.3.2 Finely Divided Electropositive Metals.....12

1.4 Electronic Properties of Solids.....13

1.4.1 Spin States of Transition Metal Cations.....13

1.4.2 Basic Band Theory and the Hubbard Model.....14

1.5 Magnetic Properties of Solids.....18

1.5.1 Correlated Magnetic Behaviour and Magnetic Ordering.....18

1.5.2 Exchange Interactions and Goodenough-Kanamori Rules.....19

1.6 The Motivation of this Work.....21

Chapter 2 Experimental Methods and Techniques.....23

2.1 Synthesis of Thermodynamically Stable Materials: Citrate Gel Method.....23

2.2 Binary Metal Hydride Reductions.....24

2.2.1 Reaction with CaH_2/LiH in Sealed Glass Ampoules.....24

2.2.2 Reaction with CaH_2/ LiH in a Flowing Tube System.....25

2.2.3 Washing Reaction Mixtures.....26

2.2.4 Zirconium Getter Reductions.....26

2.3 Handling Air-sensitive Compounds.....28

2.3.1 Argon-filled Glove box.....28

2.3.2 Air-sensitive X-ray Sample Holder.....28

2.4 Powder Diffraction.....29

2.4.1 X-ray Powder Diffraction.....31

2.4.1.1 Panalytical Empyrean and Panalytical X'Pert Diffractometers.....31

2.4.1.2 Bruker AXS D8 Advance Pro Diffractometer 32
2.4.1.3 Synchrotron X-ray Powder Diffraction 33
2.4.2 Neutron Powder Diffraction 34
2.4.2.1 WISH 35
2.5 Rietveld Refinement 36
2.5.1 Sample Contribution to Diffraction Peak Broadening 37
2.5.1.1 Crystalline Domain Size Broadening 38
2.5.1.2 Microstructural Strain Broadening 38
2.6 Pawley Refinement 39
2.7 Thermogravimetric Analysis (TGA) and Mass Spectrometer (MS) 39
2.8 SQUID Magnetometry 40
2.8.1 Ferromagnetic subtraction ('Ferrosubtraction') Measurements 42
2.9 Magnetism 43
2.9.1 Curie Weiss Law 43
2.10 Electron Diffraction (ED) 45
2.11 Bond Valence Sum (BVS) 45
2.12 Iodometric Titration 46
Chapter 3 Microstructural Characterisation of $LaSrNiRuO_6$ 47
3.1 Introduction 47
3.2 Experimental 48
3.2.1 Synthesis of $LaSrNiRuO_6$ 48
3.2.2 Preparation of Quenched and Slow-cooled Samples of $LaSrNiRuO_6$ 48
3.3 Results 49
3.3.1 Structural Characterisation of the Quenched and Slow-cooled Samples of $LaSrNiRuO_6$ 49
3.3.2 Comparison of the SXRD Diffraction Peak Profiles of Quenched and Slow-cooled Samples of $LaSrNiRuO_6$ 52
3.3.3 Quenching Experiments for $LaSrNiRuO_6$ 54
3.3.4 Investigating the Phase Transition of Quenched and Slow-cooled Samples of $LaSrNiRuO_6$ 56
3.3.5 $LaSrNiRuO_6$ Samples Annealing at the Reduction Temperature 60
3.3.6 Particle Size Analysis of Quenched and Slow-cooled samples of $LaSrNiRuO_6$ 61
3.4 Discussion 62
3.4.1 The Difference in the Microstructures of the Quenched and Slow-cooled Samples of $LaSrNiRuO_6$ 62
3.4.2 Structural Phase Transition of $LaSrNiRuO_6$ 65
3.5 Conclusion 66

Chapter 4 Microstructure-Dependent Reactivity of $LaSrNiRuO_6$ in a Topochemical Reduction 67
4.1 Introduction 67
4.2 Experimental 69
4.2.1 Synthesis of Quenched and Slow-cooled Samples of $LaSrNiRuO_6$ 69
4.2.2 Topochemical Reduction of $LaSrNiRuO_6$ with CaH_2 69
4.3 Results 70
4.3.1 Reduction of Quenched and Slow-cooled Samples of $LaSrNiRuO_6$ with CaH_2 70
4.3.2 Preparation of $LaSrNiRuO_6$ Samples with Different Combinations of Particle Size and Microstructure 72
4.3.3 Microstructural Characterisation of Quenched-slow-cooled and Slow-cooled-quenched samples of $LaSrNiRuO_6$ 75
4.3.4 Reduction of Quenched-slow-cooled and Slow-cooled-quenched Samples of $LaSrNiRuO_6$ with CaH_2 79
4.4 Discussion 81
4.5 Conclusion 85
Chapter 5 Topochemical Reduction of $LaSrCoRuO_6$ 87
5.1 Introduction 87
5.2 Experimental 88
5.2.1 Synthesis of $LaSrCoRuO_6$ 88
5.2.2 Initial Investigation of Reactivity of $LaSrCoRuO_6$ with Zr 88
5.2.3 Initial Investigation of Reactivity of $LaSrCoRuO_6$ with LiH under Flowing Argon 89
5.3 Results 89
5.3.1 Initial Investigation of Reactivity of $LaSrCoRuO_6$ with Zr 89
5.3.2 Initial Investigation of Reactivity of $LaSrCoRuO_6$ with LiH under Flowing Argon 92
5.4 Discussion 94
5.4.1 Reduction with Zr getters 94
5.4.2 Reduction with LiH 97
5.4.3 Structural Rearrangement During the Reduction of $LaSrCoRuO_6$ 99
5.5 Conclusion 101
Chapter 6 Synthesis and Characterisation of $LaSrCoRuO_5$ 103
6.1 Introduction 103
6.2 Experimental 103
6.3 Results 103
6.3.1 Thermogravimetric Analysis 103
6.3.2 Structural Characterisation of $LaSrCoRuO_5$ 104
6.3.2.1 Synchrotron X-ray Diffraction Characterisation $LaSrCoRuO_5$ 104

6.3.2.2 Electron Diffraction Characterisation of $LaSrCoRuO_5$ 106
6.3.2.3 Room Temperature Neutron Powder Diffraction Data of $LaSrCoRuO_5$ 107
6.3.3 Magnetic Characterisation of $LaSrCoRuO_5$ 120
6.3.3.1 SQUID Magnetometry 120
6.3.3.2 Low Temperature Neutron Powder Diffraction Data 123
6.4. Discussion 128
6.4.1 Crystallographic Structure of $LaSrCoRuO_5$ 128
6.4.2 Room Temperature Structural Data 130
6.4.3 Disproportionation in $LaSrCoRuO_5$ 130
6.4.4 Low Temperature Magnetisation Data 132
6.5 Conclusion 134
Chapter 7 Synthesis and Characterisation of $LaSrCoRuO_4$ 137
7.1 Introduction 137
7.2 Experimental 137
7.3 Results 138
7.3.1 Thermogravimetric Analysis of $LaSrCoRuO_{6-x}$ 138
7.3.2 Structural Characterisation of $LaSrCoRuO_4$ 140
7.3.2.1 Synchrotron X-ray Powder Diffraction 140
7.3.2.2 Neutron Powder Diffraction Data Collected from $LaSrCoRuO_4$ at Room Temperature 142
7.3.3 Magnetic Characterisation of $LaSrCoRuO_4$ 148
7.3.3.1 SQUID Magnetometry 148
7.3.3.2 Low Temperature Neutron Powder Diffraction Data 150
7.4 Discussion 157
7.4.1 Electronic Structure of $LaSrCoRuO_4$ 157
7.4.2 Magnetic Behaviour of $LaSrCoRuO_4$ 159
7.5 Conclusion 160
Chapter 8 A-site Substitution of a Reduced Oxide Phase Derived from $LaSrCoRuO_6$ 163
8.1 Introduction 163
8.2 Experimental 163
8.2.1 Synthesis of $La_xSr_{2-x}CoRuO_6$ 163
8.2.2 Synthesis of $La_xSr_{2-x}CoRuO_5$ 164
8.3 Results 165
8.3.1 Characterisation of $La_xSr_{2-x}CoRuO_6$ ($0.6 \leq x \leq 1.4$) 165
8.3.2. Thermogravimetric Analysis of $La_xSr_{2-x}CoRuO_{6-\delta}$ ($0.6 \leq x \leq 1.4$) 171
8.3.3 Structural Characterisation of $La_xSr_{2-x}CoRuO_5$ ($0.6 \leq x \leq 1.4$) 174
8.3.4 Magnetic Characterisation of $La_xSr_{2-x}CoRuO_5$ ($0.7 \leq x \leq 1.4$) 179

8.4 Discussion 188
8.4.1 Doping Limits of $La_xSr_{2-x}CoRuO_6$ and $La_xSr_{2-x}CoRuO_5$ ($0.6 \leq x \leq 1.4$) 188
8.4.2 Magnetic Behaviours of the Reduced Oxide Phases 189
8.5 Conclusion 190
Chapter 9 Synthesis and Characterisation of $LaSrCoRuO_{6-x}H_y$ 193
9.1 Introduction 193
9.2 Experimental 193
9.2.1 Reduction of $LaSrCoRuO_6$ with CaH_2 193
9.2.2 Reduction of $LaSrCoRuO_6$ with LiH 193
9.3 Results 194
9.3.1 Chemical Analysis of 'Sample A (CaH_2)' 194
9.3.1.1 Thermogravimetric Analysis of 'Sample A (CaH_2)' 194
9.3.1.2 Iodometric Titration of 'Sample A (CaH_2)' 196
9.3.1.3 Structural Characterisation of 'Sample A (CaH_2)' 196
9.3.1.4 SQUID Magnetometry of 'Sample A (CaH_2)' 198
9.3.2 Thermogravimetric Analysis of 'Sample B (LiH)' 199
9.3.3 Structural Characterisation of 'Sample B (LiH)' 202
9.3.3.1 Neutron Powder Diffraction Data Collected from 'Sample B (LiH)' at Room Temperature 202
9.3.3.2 Electron Diffraction Characterisation of 'Sample B (LiH)' 210
9.3.4 Magnetic Characterisation 212
9.3.4.1 SQUID Magnetometry of 'Sample B (LiH)' 212
9.3.4.2 Low Temperature Neutron Powder Diffraction Data of 'Sample B (LiH)' 214
9.4 Discussion 219
9.4.1 Compositions of $LaSrCoRuO_{6-x}H_y$ 219
9.4.2 Anion Order in Oxyhydride Phases 220
9.5 Conclusion 222
Chapter 10 Conclusion 223
Appendix 1 Index of Figures 229
Appendix 2 Additional Data for Chapter 3-9 238
Appendix 2.1 Synchrotron X-ray diffraction data (SXRD) from $LaSrNiRuO_6$ Quenched at Different Temperatures 238
Appendix 2.2 SEM Particle size Analysis of Quenched and Slow-cooled samples of $LaSrNiRuO_6$ 241
Appendix 2.3 X-ray diffraction data (XRD) from Quenched and Slow-cooled Samples of $LaSrNiRuO_6$ 244
Appendix 2.4 Synchrotron X-ray Diffraction Data (SXRD) from $La_xSr_{2-x}CoRuO_6$ ($0.6 \leq x \leq 1.4$) 246

Appendix 2.5 Thermogravimetric Analysis (TGA) Data from $La_xSr_{2-x}CoRuO_{6-\delta}$ ($0.6 \leq x \leq 1.4$) 251
Appendix 2.6 Synchrotron X-ray Diffraction data (SXRD) from $La_xSr_{2-x}CoRuO_5$ ($0.7 \leq x \leq 1.4$) 258
Appendix 2.7 Magnetisation Data from $La_xSr_{2-x}CoRuO_5$ ($0.7 \leq x \leq 1.3$) 261
Appendix 2.8 TGA-MS of $LaSrCoRuO_6$.....269
Appendix 3 Bibliography 270

Chapter 1 Introduction

1.1 Complex Transition Metal Oxides

Complex transition metal oxides are a well-researched class of compound across a wide range of disciplines due to their diverse chemical and physical properties. In a solid-state oxide, transition metal centres are arranged in regular arrays that are connected by oxide anions acting as bridging ligands. In addition, in a complex transition metal oxide, transition metal centres can adopt variable oxidation states depending on the neighbouring chemical environment, which leads to the presence of partially filled *d*-orbitals in the system. The electrons in the partially filled *d*-orbitals on the transition-metal centres can interact with those on the neighbouring transition-metal cations via electronic couplings, such as direct exchange couplings, or superexchange couplings via ligand oxide 2*p* orbitals etc. These electronic couplings give rise to collective properties of materials, for example, magnetoresistance,[1–3] high-temperature superconductivity,[4] collective magnetism[5] and multiferroicity.[6–8] These properties lead to the application of complex transition metal oxides in areas such as data storage and superconductors.[9,10]

The collective properties of complex transition-metal oxides are typically sensitive to the local electronic configuration of the transition-metal cations (e.g. oxidation states, coordination geometries etc.). Thus, it is possible, in principle, to design materials with novel electronic and magnetic properties via modification of the structural and compositional chemistry of complex transition metal oxides.

1.2 Perovskite Structure and Tolerance Factor

One of the most common structures adopted by complex transition metal oxides is the perovskite structure. The perovskite structure has a general formula of ABO_3, where the A-site is occupied by large cations from the *s*- or *f*- block, while the B site is occupied by smaller transition metal cations. The perovskite structure can be described as an array of corner-sharing BO_6 octahedra arranged throughout three directions, leaving 12-coordinate cavities to be occupied by the large A cations.[11] An ideal perovskite network adopts a cubic unit cell described in the *Pm*-3*m* space group. A classic example of an ideal perovskite is $SrTiO_3$ (Fig 1.1).[12] In this structure, all the Ti-O-Ti angles are 180°, where the overlap between the transition metal *d*-orbitals and the oxide 2*p* orbitals is maximised. In an ideal cubic perovskite, the *A*-*O* bond distance is equal to $a/\sqrt{2}$ and the *B*-*O* bond distance is equal to $a/2$ (where *a* is the lattice parameter of an ideal cubic perovskite unit cell) (Fig 1.1). This gives the relationship of $<A\text{-}O> = \sqrt{2} <B\text{-}O>$. Therefore, the Goldschmidt tolerance factor (*t*) is defined as follows:[13]

$$t = \frac{< A - O >}{\sqrt{2} < B - O >} = \frac{r_A + r_O}{\sqrt{2}(r_B + r_O)}$$

<*A*-*O*> and <*B*-*O*> correspond to the average bond lengths between the A/B-site cations and the oxide ions while r_A and r_B and r_O are the radii of A-site cation, B-site cation and oxide anion, respectively.

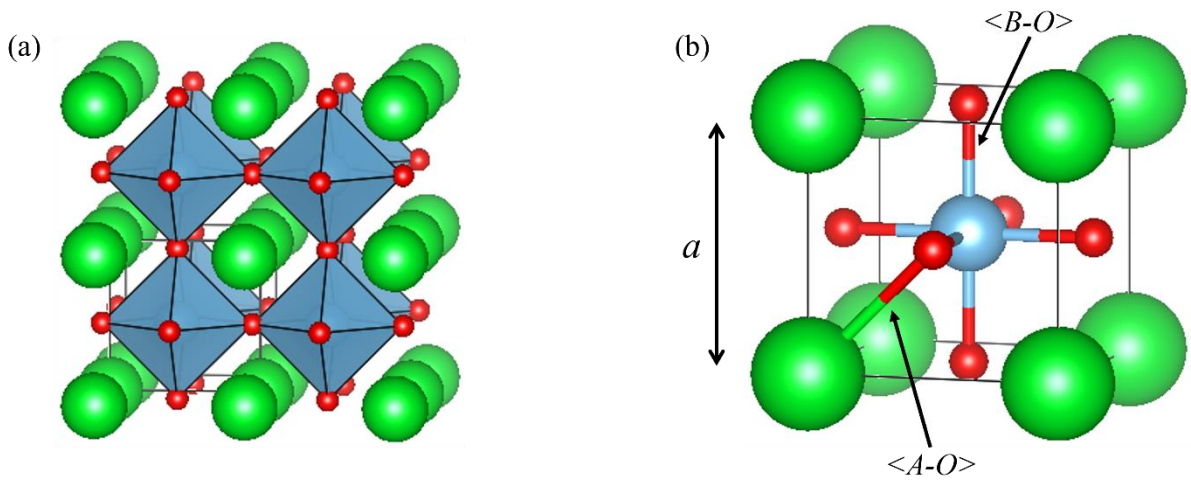


Figure 1.1. (a) A cubic *Pm*-3*m* unit cell of $SrTiO_3$; (b) <*A*-*O*> and <*B*-*O*> bond lengths in a ABO_3 perovskite structure.

When the size of the A-site cavities created by the BO_6 octahedra perfectly matches the size of the cation located at the A-site (<*A*-*O*> = √2<*B*-*O*>), the tolerance factor, *t*, is equal to 1. This is the case for the ideal perovskite structure mentioned above ($SrTiO_3$), where the perovskite structural framework is undistorted. The perovskite structural framework can also distort to accommodate a range of <*A*-*O*>:<*B*-*O*> ratios ($t \neq 1$). The cooperative twisting and tilting of the BO_6 octahedra enable a large variation of A- and B-site cation combinations to be accommodated in a perovskite structure, which allows the access to a large variation of thermodynamically stable perovskite oxide phases.

When the cation located at the A-site is smaller than the 12-coordinate cavities created by the BO_6 octahedra, the <*A*-*O*> bond length is smaller than √2<*B*-*O*>, and the tolerance factor *t* is smaller than 1. In this scenario, cooperative tilting and twisting of the BO_6 octahedra is needed to accommodate the smaller A-site cation to form a three-dimensional framework. For example, replacing Sr^{2+} with a smaller Ca^{2+} cation leads to the cooperative twisting of the TiO_6 octahedra in $CaTiO_3$, where the Ti-O-Ti bond angles deviate from 180°.[14] The distortions of the TiO_6 octahedra result in a lowering of the symmetry of the $CaTiO_3$ unit cell to an

orthorhombic symmetry. In some cases, the tilting of the BO_6 octahedra can lower the symmetry of the unit cell further to rhombohedral or monoclinic.[14–16]

On the other hand, when the cation located at the A-site is larger than the 12-coordinate cavities created by the BO_6 octahedra, the <*A*-*O*> bond length is larger than $\sqrt{2}$<*B*-*O*> and *t* is bigger than 1. In this scenario, the BO_6 octahedra change their connectivity from corner- to face-sharing. This class of perovskite normally adopts a hexagonal or trigonal symmetry.[17]

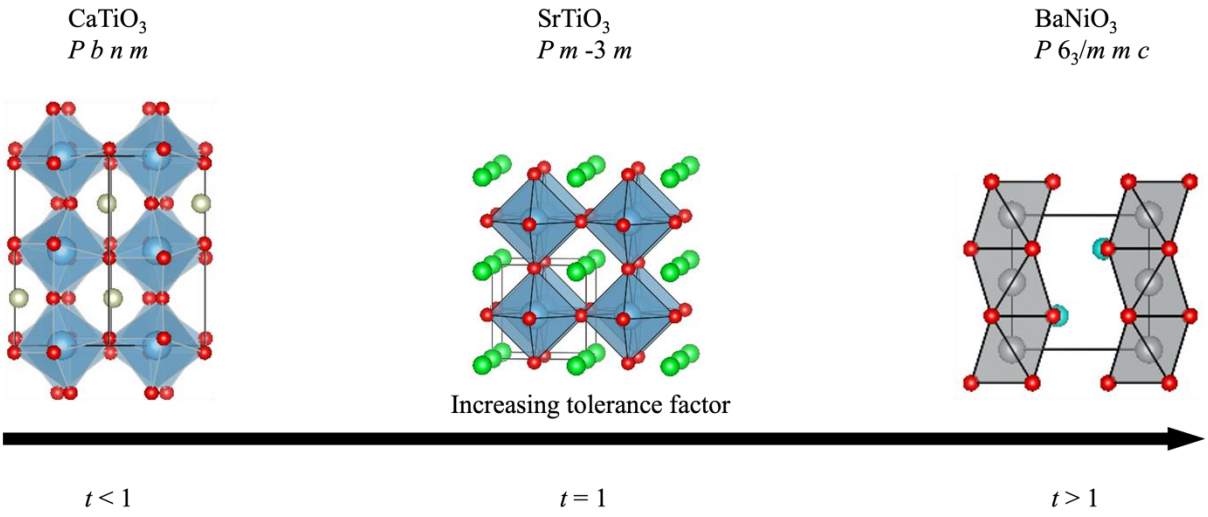


Figure 1.2. The ABO_3 structures with different tolerance factors: $CaTiO_3$ (space group: *Pbmn*) (*t* < 1);[14] $SrTiO_3$ (space group: *Pm*-3*m*) (*t* = 1);[12] $BaNiO_3$ (space group: *P*6$_3$/*mmc*) (*t* > 1).[18]

1.2.1 Double Perovskites

The perovskite structure can be modified by chemical substitution of B-site cations. When the B-site are occupied by B and B' cations at a 1:1 ratio, a chemical composition of $A_2BB'O_6$ will result, where the B-site cations can be arranged in either an ordered or a disordered manner. The B-site cation ordering is favoured if the sizes and the oxidation states of the B and B' cations differ significantly. In general, when the oxidation state difference between the B and B' cations is greater than two, an ordered arrangement of the B-site cations will be observed.

The different types of cation ordering are summarised in Fig 1.3. The cation ordering at the B-site gives rise to a structure type which is known as the double perovskite structure.[19]

The ordering of the B-site cations plays a crucial role in determining the physical and chemical properties of materials. For example, Sr_2FeRuO_6 contains Fe^{3+} and Ru^{5+} centres at the B-site, and the Fe and Ru cations are arranged in a disordered manner. Neutron powder diffraction data collected from Sr_2FeRuO_6 at 5 K do not show extra magnetic scattering, indicating that this compound does not have long-range magnetic order at low temperature.[20] On the contrary, $LaSrNiRuO_6$ contains Ni^{2+} and Ru^{5+} centres at the B-site, with the Ni and the Ru centres arranged in a rocksalt ordered manner. A magnetic transition from a paramagnetic to an antiferromagnetic state is observed below 93 K. NPD data collected from $LaSrNiRuO_6$ at low temperature show extra Bragg reflections that are not present in the room temperature data set, indicating this compound has a long-range magnetic order at low temperature.[16]

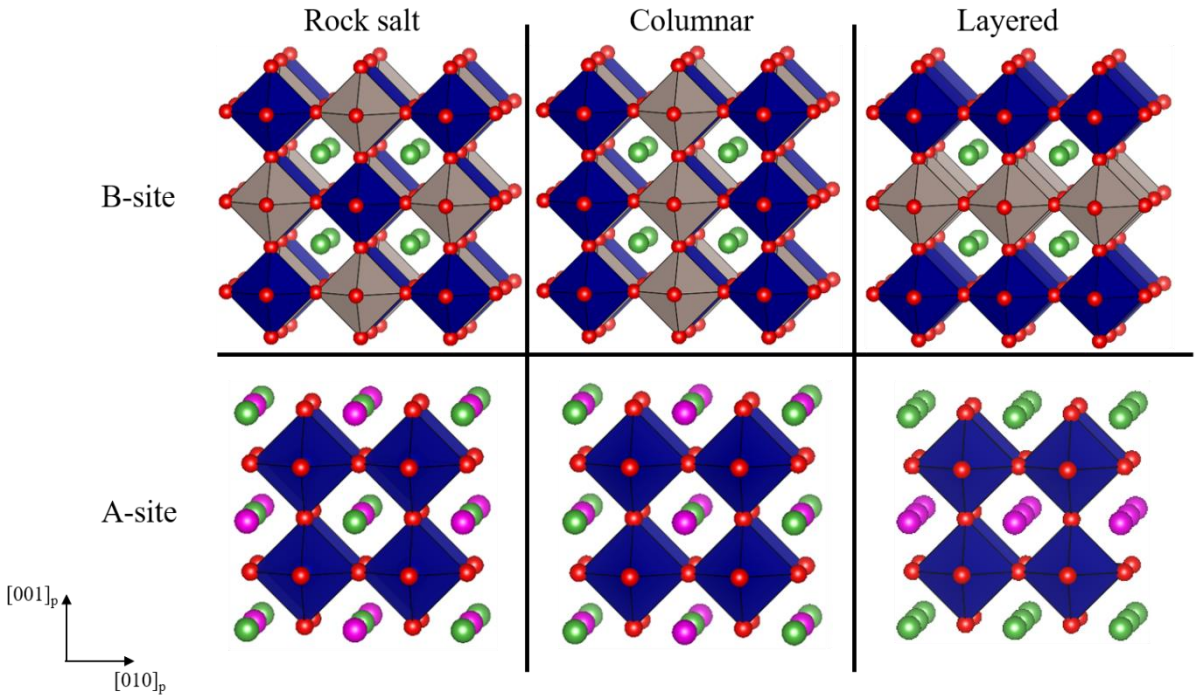


Figure 1.3. Table of ordering schemes in double perovskite.[19]

1.3 Traditional Solid-State Synthesis and Low Temperature Topochemical Reduction of Complex Metal Oxides

Traditional solid-state synthesis methods have been widely used to prepare a range of solid-state compounds. However, these methods require high synthesis temperatures to overcome the large energetic barriers of solid-state ion diffusion. As a result, only thermodynamically stable compounds can be synthesised via these high-temperature solid-state synthesis methods, which limits the scope of solid-state chemistry. In order to explore and prepare novel metastable solid-state compounds, synthesis routes that can prepare phases in a kinetically stable state are needed.

A series of low temperature techniques using kinetic control have been developed to synthesise metastable solid-state compounds that cannot be attained using conventional high-temperature methods.[21,22] These low-temperature synthetic methods utilise the difference in the ion mobilities in a crystalline solid to modify the framework of lighter ions (e.g. oxide anions) while maintaining the structural lattice of heavier ions (e.g. metal cations).[23] These methods allow access to kinetically stable phases which cannot be prepared using high-temperature solid-state synthesis methods. One example of these low temperature synthetic methods is the topochemical reduction via anion deintercalation/exchange, which can be performed using reducing agents such as binary metal hydrides and finely divided electropositive metals.[24–29] The choice of the reducing agents is dependent on the chemical compositions of the target reduced phases, desired reaction temperature range and the nature of the complex oxides to be reduced.[22]

Since the physical properties of complex transition metal oxides are dependent on the local electronic configuration of the transition-metal cations (e.g. oxidation states, coordination geometries etc.), topochemical reduction via anion-sublattice modification (e.g. introducing vacancies/exchanging oxide for hetero anions) allows the fine tuning of the physical properties

of extended solid oxides. For example, the complex transition metal oxide $BaTiO_3$ is an insulator. Reacting $BaTiO_3$ with CaH_2 yields an oxyhydride phase $BaTiO_{2.4}H_{0.6}$ which exhibits high electronic conductivity.[29,30] In summary, low temperature topochemical reduction is a powerful method to synthesise novel metastable materials with diverse electronic and magnetic properties.[31]

1.3.1 Binary Metal Hydrides

Reductive anion deintercalation/exchange using binary metal hydrides has enabled a wide range of metastable compounds to be synthesised at relatively low reaction temperatures. The chemical equations of the topochemical reduction of perovskite oxides with binary metal hydrides via anion de-intercalation are listed below:[32]

$$ABO_3 + CaH_2 \longrightarrow ABO_{3-x} + x\,CaO + xH_2 \qquad [1]$$

$$ABO_3 + LiH \longrightarrow ABO_{3-x} + x\,Li_2O + xH_2 \qquad [2]$$

$$ABO_3 + NaH \longrightarrow ABO_{3-x} + x\,NaOH \qquad [3]$$

The upper limit for the reaction temperature using different binary metal hydrides in silica ampoules, and the decomposition temperatures of the binary metal hydrides are listed in Table 1.1. In general, the upper limit for the reaction temperature of a binary metal hydride is determined by the decomposition temperature of the hydride reagent. However, for CaH_2, the upper limit for the reaction temperature is much lower than its decomposition temperature. This is because the silica ampoules that are used to contain the reduction mixtures are only stable up to 630 °C, above this temperature the silica ampoule will start to react with the binary metal hydride (CaH_2) and form unwanted side products. Above 630 °C, the silica ampoule will

also lose its structural integrity. As a result, the upper limit for the reaction temperature using CaH_2 is 630 °C when silica ampoules are used to contain the reduction mixture.

Binary Metal Hydride	Decomposition temperature/°C[33]	Upper limit reaction temperature (reacting in silica ampoules)/°C
CaH_2	885	630
LiH	550	550
NaH	210	210

Table 1.1. The decomposition temperature of the binary metal hydrides and the upper limit for the reaction temperature using binary metal hydrides in sealed silica ampoules.

Previous work has demonstrated that binary metal hydrides can be used to prepare transition metal cations with unusually low oxidation states in extended solid state oxides, such as Co^+, Ni^+, Ru^{2+} and Ir^{2+}.[24,34–36] Examples of topochemical reduction using binary metal hydrides will be discussed below.

1.3.1.1 Calcium Hydride

Calcium hydride is a powerful reducing agent which can be used up to 630 °C when the reaction mixtures are contained in silica ampoules. For example, $LaSrNiRuO_4$ can be yielded by heating $LaSrNiRuO_6$ with CaH_2 in a venting apparatus under flowing argon.[37] The venting apparatus experimental set-up prevents the accumulation of H_2 gas formed as a by-product inside the reaction vessel by purging the system with a constant flow of argon. In this reaction, the oxide anions are de-intercalated from the parent structure ($LaSrNiRuO_6$), leaving both Ni^+/Ru^{2+} centres in square-planar coordination. The side product of the reaction is CaO, which can be removed by weak acids such as 0.1 M NH_4Cl in methanol.

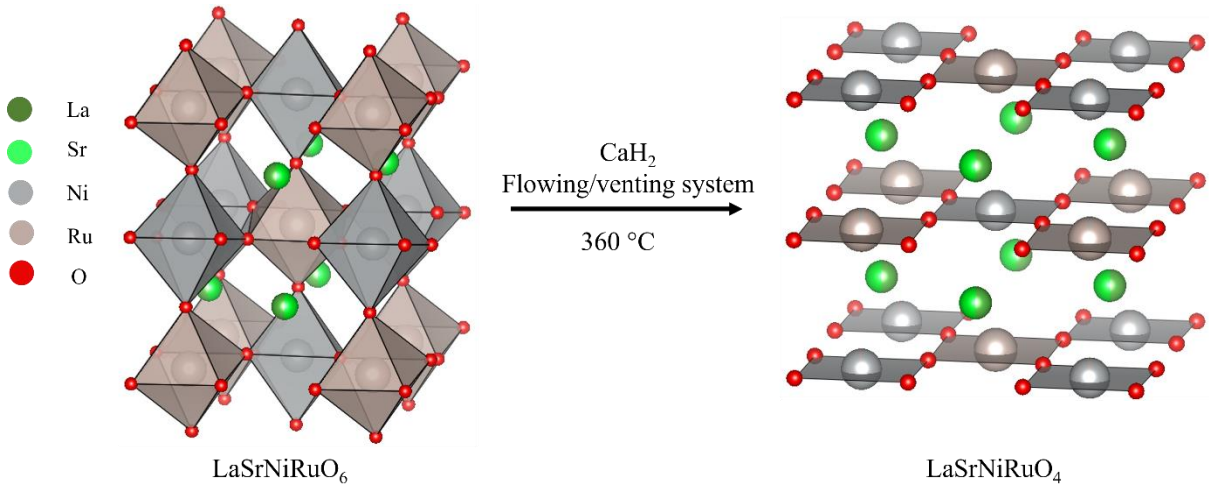


Figure 1.4. Topochemical reduction of $LaSrNiRuO_6$ with CaH_2 at 360 °C under flowing argon to form $LaSrNiRuO_4$.[37]

Reductions with CaH_2 can also yield oxyhydride phases. For example, the reduction of $LaSr_3NiRuO_8$ with CaH_2 in a sealed silica ampoule leads to the incorporation of hydride into the structure and yields an oxyhydride phase $LaSr_3NiRuO_4H_4$ (Fig 1.5).[38] $LaSr_3NiRuO_4H_4$ adopts an anion ordered structure with hydride anions residing at the equatorial sites of the octahedra and the oxide anions residing at the apical sites of the octahedra.

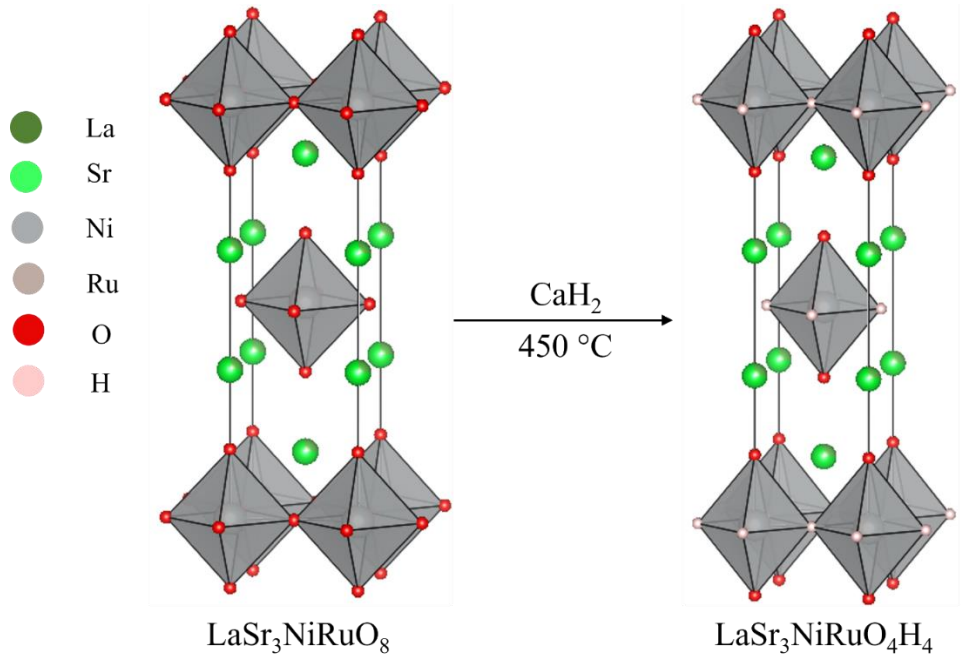


Figure 1.5. Topochemical reduction of $LaSr_3NiRuO_8$ with CaH_2 at 450 °C in a sealed ampoule to form $LaSr_3NiRuO_4H_4$.[38]

1.3.1.2 Lithium Hydride

Lithium hydride can also be used as a reducing agent at low reaction temperatures (T < 550 °C). For example, the reduction of the hexagonal perovskite $Ba_{0.5}Sr_{0.5}MnO_{3-x}$ with LiH in a sealed ampoule at 350 °C yields an oxygen deficient phase $Ba_{0.5}Sr_{0.5}MnO_{2.03}$. During the reduction process, oxide anions were de-intercalated from the structure in a disordered manner, forming 'tetrahedral' MnO_4 coordination sites.[39] The side product of the reaction is Li_2O, which can be easily removed by a weak acid such as methanol. Topochemical reduction of $Ba_{0.5}Sr_{0.5}MnO_{3-x}$ with LiH has demonstrated that LiH can also be a powerful reducing agent at low temperature.

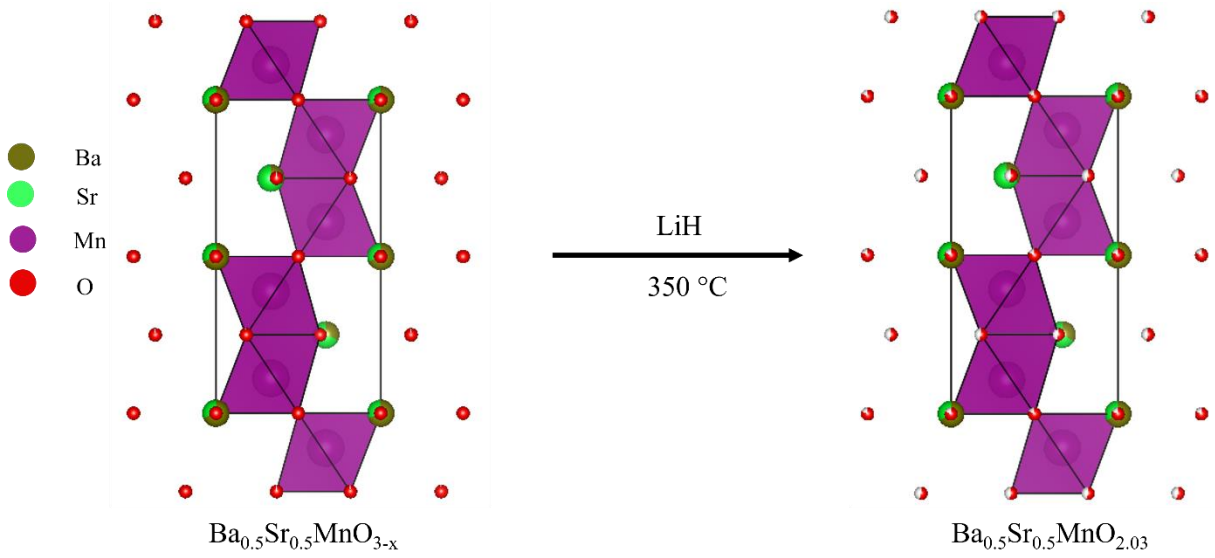


Figure 1.6. Topochemical reduction of $Ba_{0.5}Sr_{0.5}MnO_{3-x}$ with LiH in a sealed ampoule to form $Ba_{0.5}Sr_{0.5}MnO_{2.03}$.[39]

1.3.1.3 Sodium Hydride

Sodium hydride is a powerful solid-state reducing agent in a low reaction temperature range (T < 210 °C). For example, the reduction of $LaNiO_3$ with NaH at 190 °C yields $LaNiO_2$ which adopts an infinite layer structure.[24] The side-product of this reaction is NaOH which can be easily removed by washing in a weak acid like methanol.

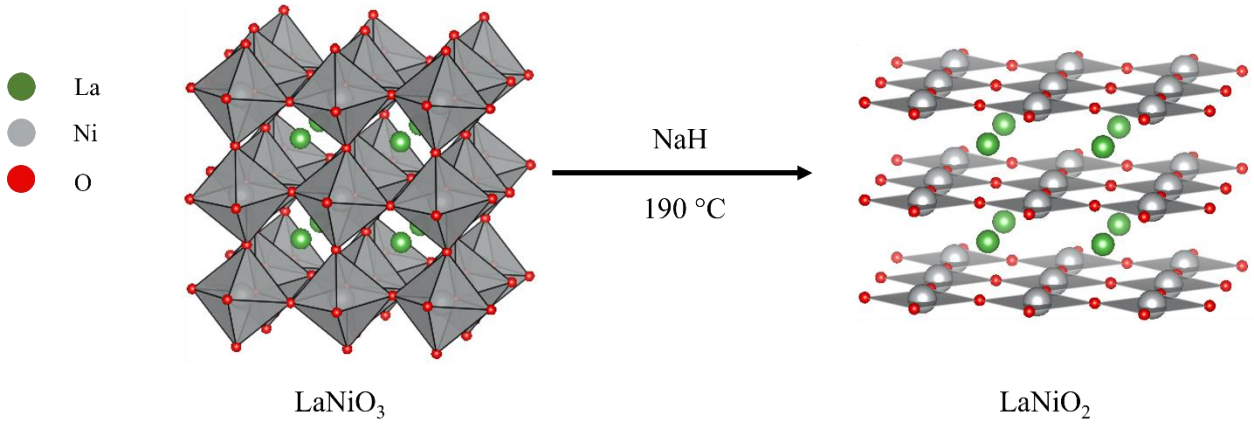


Figure 1.7. Topochemical reduction of $LaNiO_3$ with NaH to yield $LaNiO_2$, this oxygen deficient phase adopts an infinite layer structure.[24]

1.3.2 Finely Divided Electropositive Metals

Finely divided electropositive metals (e.g. Ti, Zr, Al) can be used as an alternative way to reduce complex metal oxides. For example, heating $LaCoO_3$ to 400 °C in the presence of zirconium (as an oxygen getter) yields an oxygen deficient phase $LaCoO_{2.5}$. The reaction equation is shown as follows:[40]

$$LaCoO_3 \longleftrightarrow LaCoO_{3-x} + x\ O_2 + Zr \longleftrightarrow ZrO_2 + LaCoO_{2.5}$$

The reduced phase, $LaCoO_{2.5}$, adopts a brownmillerite structure, which is one of the most common forms of the anion deficient perovskite structure. This structure consists of sheets of CoO_6 octahedra and sheets of CoO_4 tetrahedra stacked in alternating layers.

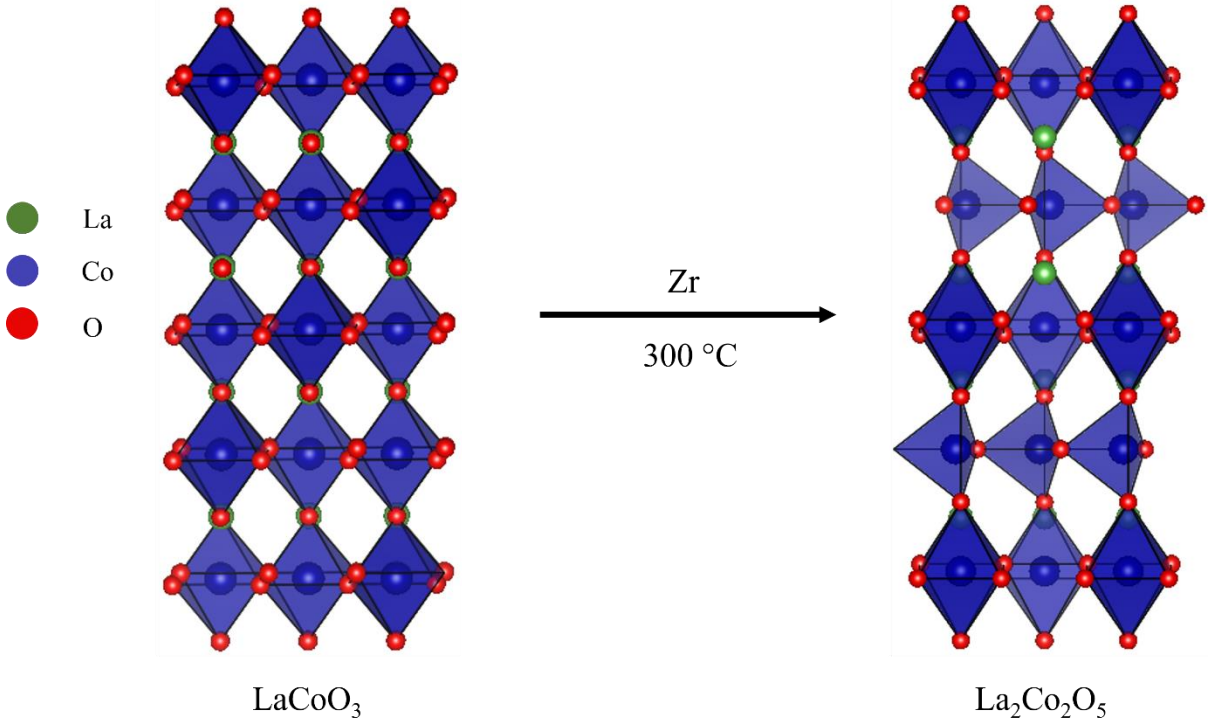


Figure 1.8. Topochemical reduction of $LaCoO_3$ with Zr as an oxygen getter to form $La_2Co_2O_5$.[40]

1.4 Electronic Properties of Solids

1.4.1 Spin States of Transition Metal Cations

In an octahedral transition metal complex, the transition metal cations can adopt either high spin (HS) or low spin (LS) configurations. The elucidation of these configurations can be comprehended via crystal field theory and ligand field theory. There are two factors that determine the spin states of the transition-metal cations in a complex, namely the ligand field splitting energy (Δ) and the paring energy (*P*) (energy penalty for pairing up electrons in the same orbital).

In general, in an octahedral transition metal complex, when the ligand field splitting energy (Δ) is smaller than the pairing energy (*P*), a high spin configuration is preferred (Fig 1.9 left); Alternatively, if Δ > *P*, a low spin configuration is more favourable (Fig 1.9 right).[41]

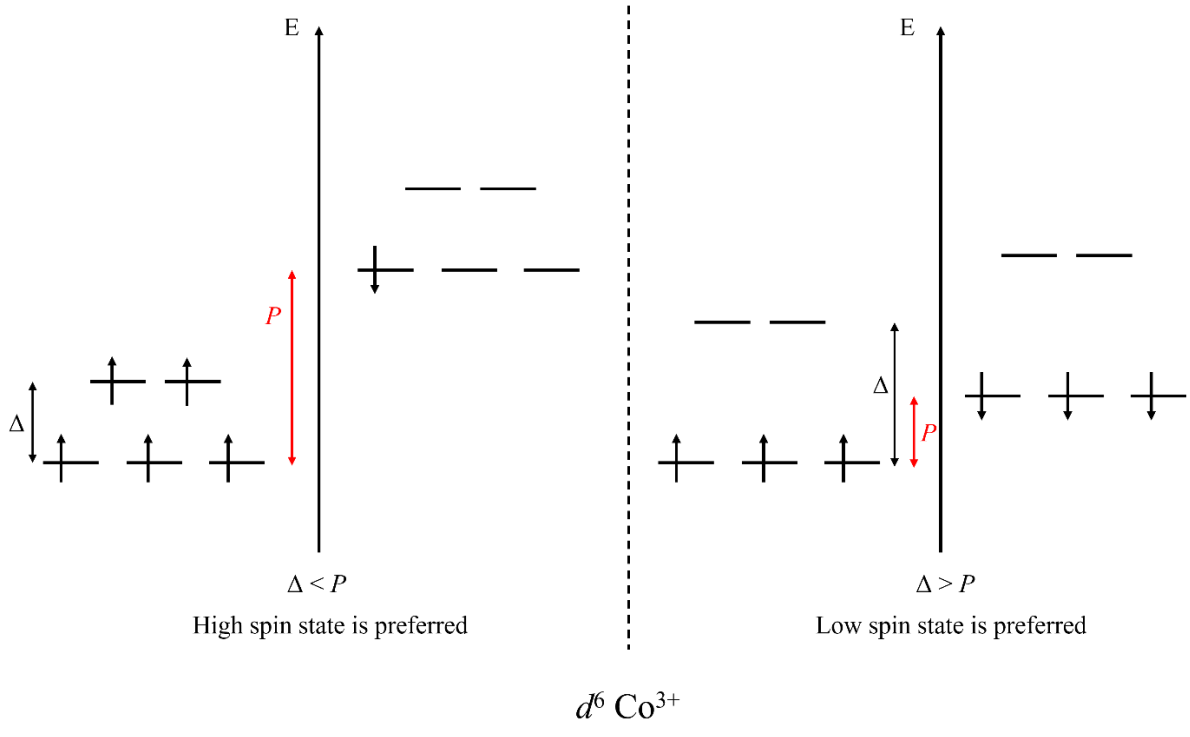


Figure 1.9. An example of d^6 Co^{3+} centres in an octahedral environment in high spin configuration (left) and low spin configuration (right). Schematic representations of filling of the *d*-orbitals with paring energy (*P*) shown explicitly.

There are some general guidelines to consider when anticipating the spin state of a transition metal cation in a complex. First of all, 4*d*/5*d* orbitals are more radially extended than 3*d* orbitals. Consequently, 4*d*/5*d* orbitals can overlap better with the ligand orbitals, resulting in a large Δ. In addition, the larger size of the 4*d*/5*d* orbitals lowers the electron-electron repulsions, resulting in a smaller value of *P*. As a result, 4*d*/5*d* transition metal cations almost always adopt low spin configurations. Secondly, the value of Δ is also dependent on the type of ligands. For example, the Fe^{3+} centres in $[Fe(CN)_6]^{3-}$ adopt a low spin configuration while the Fe^{3+} centres in $[Fe(H_2O)_6]^{3+}$ adopt a high spin configuration.[41,42]

The spin states of transition metal cations play an important role in determining the physical properties of transition metal compounds. Considering Co^{3+} centres as an example: d^6 Co^{3+} centres can adopt either low spin or high spin configurations in an octahedral ligand field. Low spin d^6 Co^{3+} centres are diamagnetic (S = 0) while high spin d^6 Co^{3+} centres are paramagnetic (S = 2).[41]

1.4.2 Basic Band Theory and the Hubbard Model

In an extended array of atoms, the atomic orbitals (AOs) in an atom interact with one another to form crystal orbitals. As the number of atoms increases, the crystal orbitals formed become closer in energy. In an infinite periodic solid, the number of crystal orbitals in the solid will be large enough so that the energy differences between the crystal orbitals formed are negligible. As a result, these energy levels can be considered as a continuous distribution of states, which can be regarded as a continuous energy band (Fig 1.10).[41]

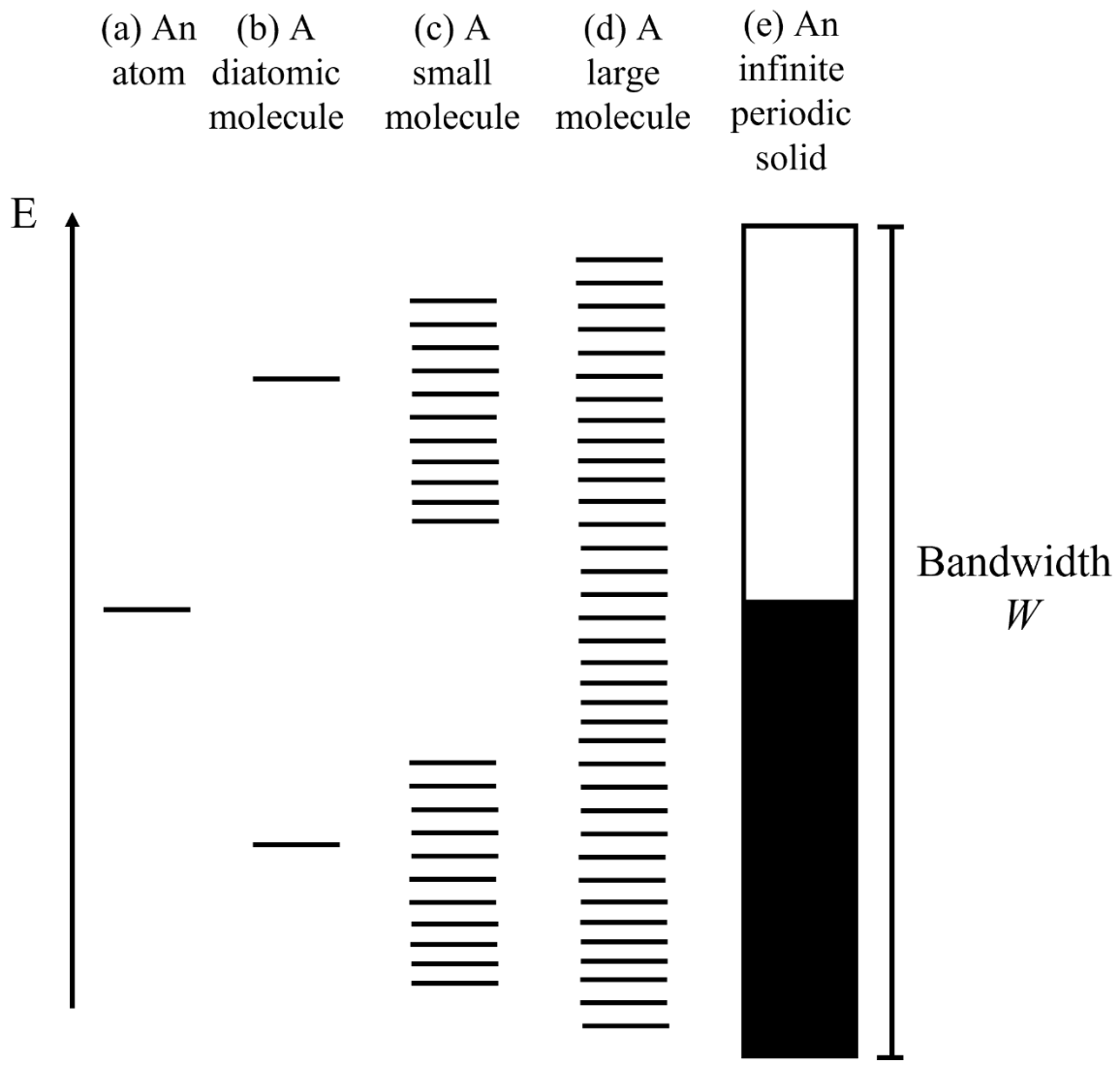


Figure 1.10. A schematic representation of the orbital energies of (a) an atom, (b) a diatomic molecule, (c) a small molecule, (d) a large molecule and (e) an infinite periodic solid.

The energy between the top and bottom of a band is the bandwidth *W*. The bandwidth of an electronic band is primarily determined by the degree of overlap between the AOs. If the interatomic distance in a solid is small (the degree of the overlap between the AOs is high), a wide band will result.

The filling of the band depends on the occupancy of the AOs. At 0 K, the energy level that separates the occupied state from the empty state is known as the Fermi energy (E_f). If E_f is located at a partially filled band, metallic conductivity will occur. However, the prediction that a partially filled band will lead to metallicity is not always true. For example, NiO and CoO

are both antiferromagnetic insulators, despite having partially filled *d*-bands.[43,44] This inconsistency is due to the omittance of electron repulsions in the simple band theory. Electron repulsions are particularly important for solids with poor AO overlap (narrow band, small *W*).[45] The Hubbard model was introduced to account for electron electron repulsions in solids. In the Hubbard model, only the repulsion effects of electrons on the same atomic site were considered, the electronic repulsions between atoms were ignored. Consider a 1D chain of equally spaced, weakly interacting atoms, each atom with one singly occupied 1*s* orbital (Fig 1.11(a)). When the electrons are allowed to move (just like in a metallic conductor), the electrons will hop from one orbital to the neighbouring one. As a result, an atom with a doubly occupied 1*s* orbital will be created and an energy penalty must be paid (Fig 1.11(b)). This energy penalty, *U*, is equal to the on-site electron repulsion between the two electrons. For atoms in a gas phase, the value of *U* is equal to the difference between the ionisation energy and the electron affinity of an atom ($U = I - A$). However, in solids, the polarisation effects reduce the magnitude of *U* significantly. This on-site electron repulsion (*U*) favours electron localisation.[41,45]

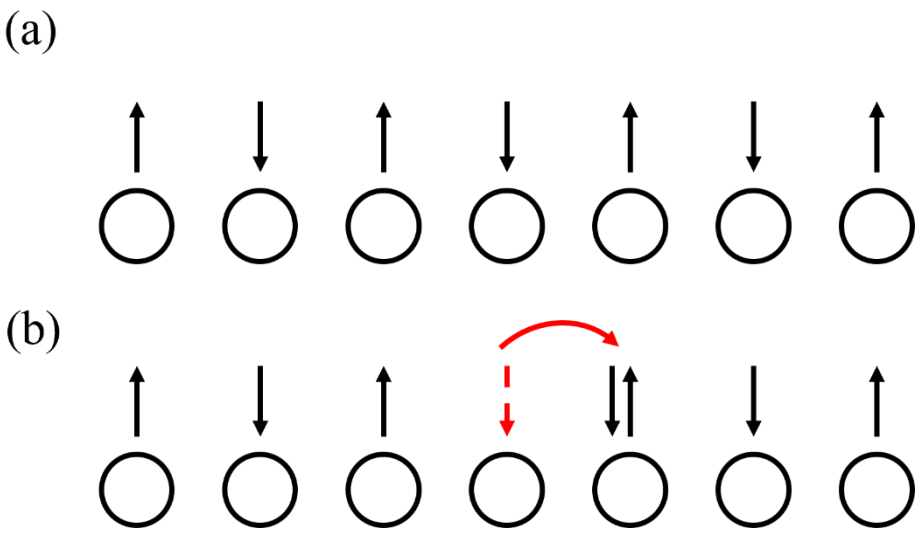


Figure 1.11. (a) A 1D chain of equally spaced atoms with partially filled 1*s* orbitals. The electrons are localised in each orbital; (b) Electron hopping introduces on-site electron repulsion due to the doubly occupied orbital.

While the on-site electron repulsion (*U*) favours electron localisation, there is also a kinetic energy gain (*t*) that results from electron delocalisation. The competition between the kinetic term *t* and the on-site electron repulsion *U*, where the former favours electron delocalisation and the latter favours electron localisation, determines whether a system is metallic or insulating. For example, if the overlap between the orbitals is small (widely spaced orbitals), the energy cost from the on-site electron repulsion *U* will outweigh the kinetic energy gain (*t*), which leads to an insulating behaviour.[41]

As shown in Fig 1.12, the introduction of on-site electron repulsion (*U*) splits a single band into two sub-bands, which will be referred to as the lower Hubbard band and the upper Hubbard band. The lower Hubbard band is the energy of singly occupied levels and the upper Hubbard band represents the energy of an electron that moves to a site that is already partially occupied. The sub-bands are separated by the Mott-Hubbard gap of magnitude *U*. When *W* is small (left-hand side of Fig 1.12), the on-site electron repulsion prevails, which leads to an insulating behaviour. Compounds such as NiO and CoO which are insulating due to the on-site electron repulsion are called Mott-Hubbard insulators. When the interatomic interactions increase, the sub-bands become broader and eventually overlap when the bandwidth *W* is approximately equal to the electron repulsion *U*. Upon reaching this point, there is no energy gap and the system becomes metallic (right-hand side of Fig 1.12).[45]

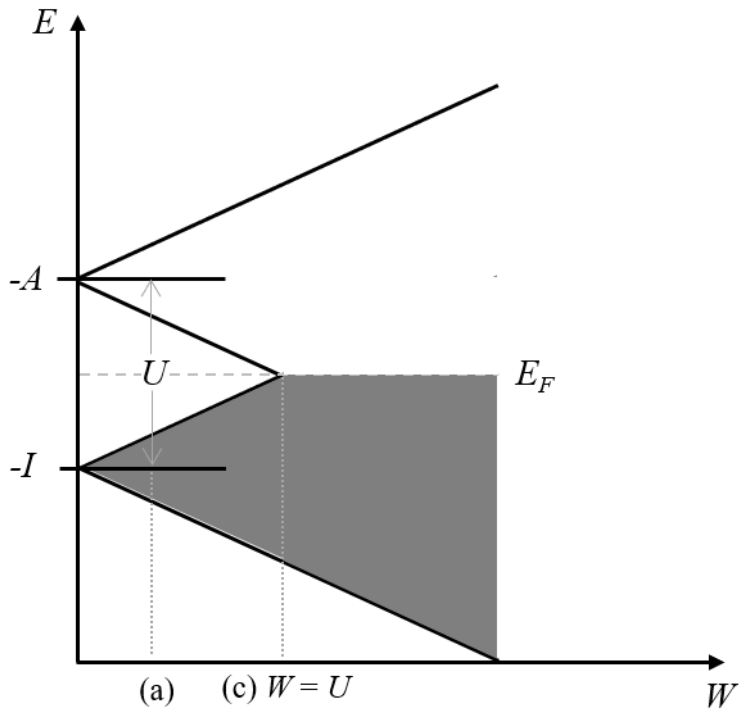


Figure 1.12. Schematic representation of Hubbard sub-bands as a function of band width *W*. *–I* represents the ionisation energy and *–A* represents electron affinity.[45]

1.5 Magnetic Properties of Solids

1.5.1 Correlated Magnetic Behaviour and Magnetic Ordering

For systems that have magnetic interaction between electron spins, the observation of correlated magnetic behaviour is possible. There are different types of correlated magnetic behaviours, such as ferromagnetism, antiferromagnetism, canted antiferromagnetism, ferrimagnetism etc.

In a ferromagnetic material, the magnetic spins are aligned parallel to each other and hence a net magnetic moment will result. In contrast, antiferromagnets are made up of localised magnetic spins aligning anti-parallel to each other, hence the net magnetic moment of an antiferromagnet will be zero. However, in some antiferromagnetic materials, a small non-zero net magnetic moment can exist. This non-zero net magnetic moment observed in the

antiferromagnetic material arises from the canted arrangement of the magnetic spins. In this type of materials, the localised magnetic spins are still aligned in the opposite direction, but the spins are slightly canted and the angle between the spins is not 180°. As a result, the system has a non-zero net magnetic moment. This type of magnetic ordering is called canted antiferromagentism. In a ferrimagnetic material, the system has anti-aligned localised magnetic spins while these magnetic spins have different magnitudes of magnetic moment, which results in a net magnetic moment.[9,41]

1.5.2 Exchange Interactions and Goodenough-Kanamori Rules

In insulating transition metal oxides, there are several types of exchange interactions between the transition metal centres. The simplest type of magnetic coupling is direct exchange, which is a virtual 'hopping' of electrons between the neighbouring metal centres. The direction of the collective electron spins resulted from direct exchange can be either aligned or anti-aligned, depending on the filling of the transition metal *d*-orbitals. However, this type of exchange coupling is rare, this is due to the transition metal centres are too far apart in most of the transition metal oxides to have any significant direct orbital overlap.[41]

Compared with direct exchange interactions, superexchange interactions are much more common. In superexchange interactions, oxide ligands act as a bridge to mediate the magnetic coupling of the spins. The strength of this interaction depends on the degree of orbital overlap, such as bond angles and bond distances between the M-O-M bonds, and also the energy match between the metal *d*-orbitals and the oxygen 2*p* orbitals.

The Goodenough-Kanamori rules are semi-empirical rules that can be used to understand and predict the sign of the magnetic coupling between metal centres.[46,47] For example, a 180° M-O-M superexchange interaction between two half-filled *d*-orbitals leads to a strong antiferromagnetic interaction (Fig 1.13 (top)); On the other hand, a 90° M-O-M superexchange

interaction between two half-filled *d*-orbitals results in a weak ferromagnetic coupling (Fig 1.13 (bottom)).[41]

The 180° M-O-M superexchange interactions are more common in the complex transition metal oxides presented in this thesis. The Goodenough-Kanamori rules state that the 180° M-O-M superexchange interaction between a half-filled orbital and a filled orbital favours a ferromagnetic coupling. The 180° M-O-M superexchange interaction between a half-filled orbital and an empty orbital also favours a ferromagnetic coupling.[41]

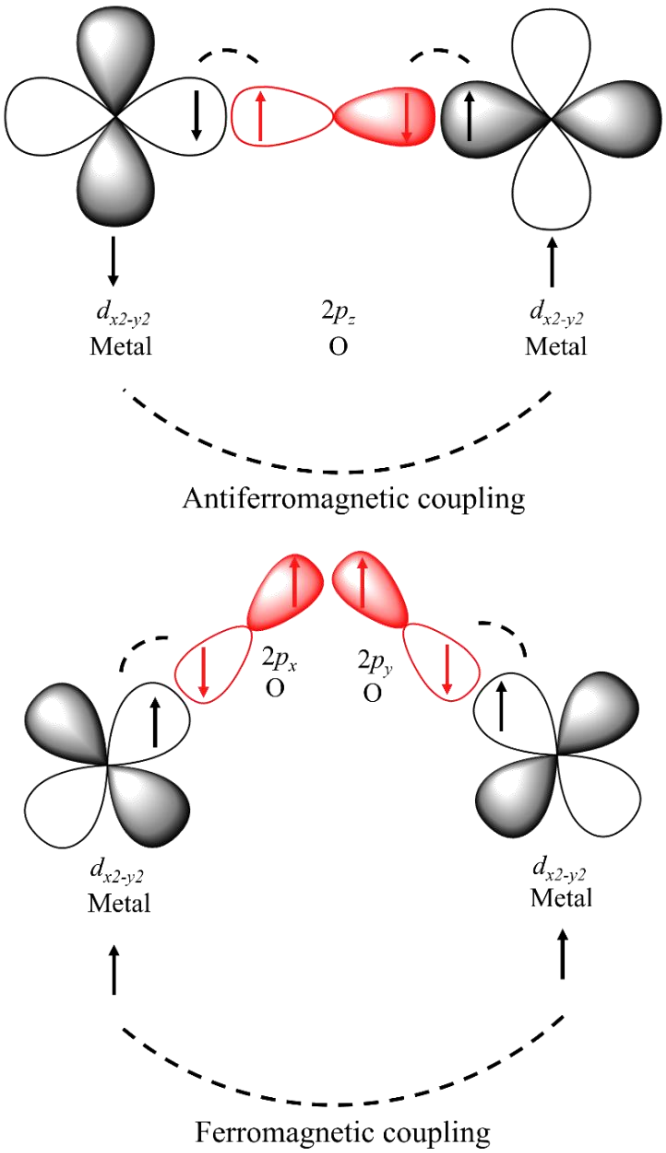


Figure 1.13. A schematic representation of superexchange interactions of M-O-M in 180° (top) and in 90°(bottom).

1.6 The Motivation of this Work

The aim of this work is to prepare novel topochemical reduced phases with unusual electronic and magnetic properties.

Previous works have shown that most of the reported topochemically reduced phases containing only 3*d* transition metals have antiferromagnetic ground states and are semiconducting at ambient pressure. These behaviours can be attributed to the poor overlap between the relatively small 3*d* orbitals and the ligand orbitals: Firstly, the weak ligand field splitting which arises from the poor orbital overlap favours high spin configurations (Section 1.4.1). In general, the high spin configurations adopted by the 3*d* transition metal cations result in the partial occupation of e_g orbitals (when the electron counts of the transition metal centres are between d^4 and d^9), which leads to strong antiferromagnetic superexchange couplings (Section 1.5.2); Secondly, the electronic bands derived from the 3*d* orbitals are generally narrow, which favours electron localisation (Section 1.4.2).[48]

Therefore, in order to synthesise metastable compounds with diverse and interesting electronic and magnetic properties, the topochemical reduction of mixed 3*d*/4*d* double perovskite phases was investigated in this work. 4*d* transition metals were chosen due to their orbital features: Firstly, the better overlap between the radially extended 4*d* orbitals and the ligand orbitals results in a large ligand field stabilisation energy, which favours low- or intermediate- spin configurations of the 4*d* transition metal cations. As a result, it is less likely for a mixed 3*d*/4*d* system to adopt an antiferromagnetic ground state. Secondly, the large 4*d* orbitals would be expected to broaden the metal-based *d*-band (large *W*). In addition, the radially extended nature of 4*d*-orbitals reduces the on-site electron repulsion (*U*). These two effects favour itinerant electron behaviour. As a result, the incorporation of 4*d* metals into the system is likely to expand the range of physical properties observed.

Mixed 3*d*/4*d* complex metal oxides were chosen in this work because previous work has demonstrated that the topochemical reduction of 4*d* transition metal oxide perovskites tends to decompose. For example, the reduction of $SrRuO_3$ yielded elemental ruthenium and SrO. This observation is attributed to the positive redox potential of the Ru^{2+} cations (Ru^{2+}/Ru $E°$ = +0.455 V).[26] Incorporating 3*d* transition metal cations into the structure can pillar the extended oxide framework, which allows the reduction of 4*d* transition metal centres to take place.[26] Therefore, building on these studies, the topochemical reduction of the B-site cation ordered double perovskite $LaSrNiRuO_6$ and $LaSrCoRuO_6$ was investigated, and the resulting reduced oxide phases and oxyhydride phases were characterised in detail and will be presented in this thesis.

Chapter 2 Experimental Methods and Techniques

2.1 Synthesis of Thermodynamically Stable Materials: Citrate Gel Method

Most of the thermodynamically stable complex metal oxide phases discussed in this thesis were synthesised via a citrate gel method.[49] In a typical citrate gel synthesis, a suitable stoichiometric ratio of precursors such as metal oxides, metal carbonates and elemental metals were weighed and ground in an agate mortar and pestle. The resulting powder was then dissolved in a minimum quantity of 6 M nitric acid and deionised water at a 1:1 ratio. An excess amount of citric acid (a chelating agent) was added into the reaction mixture and metal-citrate chelate complexes were formed. Then, a suitable amount of ethylene glycol was added into the reaction mixture and the resulting mixture was heated to 200 °C to drive the esterification process. This process was followed by the release of NO_x gas and water vapour. This process led to a formation of a homogenous polymer framework coordinated with the metal cations. Once a highly viscous gel was formed, the temperature was turned up to 400 °C to combust most of the organic precursors, until a coarse black powder was obtained. The resulting powder was subsequently transferred into an agate mortar and pestle and ground thoroughly into a fine powder. The powder was then transferred into a crucible and heated to 900 °C in air for 12 hours to fully decompose the organic residues. The powder was then pressed into a 13 mm diameter pellet and further heated to the desired reaction temperature (> 1000 °C). After each cycle of heating, the sample was re-ground thoroughly and re-pelleted. This process was repeated until the reaction was deemed complete and a pure sample had been acquired. Reaction progression was monitored by X-ray powder diffraction.

2.2 Binary Metal Hydride Reductions

Binary metal hydrides (CaH_2, LiH) have been widely used to reduce a large range of complex transition metal oxides to form novel kinetically stable compounds at a relatively low temperature range (T < 630°C).[25,39] The topochemical reductions of perovskite phases (ABO_3) with CaH_2 and LiH to form kinetically stable reduced phases can be described as the following reaction scheme:[50]

$$ABO_3 + CaH_2 \rightarrow ABO_{3-x} + x\ H_2 + x\ CaO$$

$$ABO_3 + 2x\ LiH \rightarrow ABO_{3-x} + H_2 + x\ Li_2O$$

H_2 gas is formed as a by-product during the reduction with CaH_2 and LiH. Therefore, both CaH_2 and LiH can be used to yield oxyhydride phases.

2.2.1 Reaction with CaH_2/LiH in Sealed Glass Ampoules

Sealed glass ampoules are used for reactions with CaH_2 and LiH when the target reduced products are oxyhydride phases. The H_2 gas formed as a by-product during the reaction with CaH_2/LiH is trapped inside the sealed glass ampoule, which promotes the formation of an oxyhydride phase. Since both CaH_2 and LiH produce H_2 gas upon heating, the size of the sealed ampoule used for reactions with CaH_2 and LiH needs to be carefully considered. The size of the glass ampoule is chosen based on the calculation of the maximum partial pressure of H_2 that can be generated during the reaction with CaH_2 and LiH.

The reaction mixture of the parent oxide phase and the chosen metal hydride (CaH_2 or LiH) were ground thoroughly in an argon-filled glove box. The resulting mixture was then loaded into a glass ampoule and sealed under vacuum. The sealed ampoule was heated to the desired reaction temperature at 1 °C min^{-1} to avoid overshooting. The reaction mixture was held at the

desired reaction temperature for a suitable period of time before being cooled to room temperature. The glass ampoule was then opened inside the glove box. Fresh binary metal hydride was added into the reaction mixture in between each cycle. The reaction mixture was re-ground. The reaction progression was monitored by X-ray powder diffraction.

2.2.2 Reaction with CaH_2/ LiH in a Flowing Tube System

The flowing tube system is used when the target reduced products are oxygen deficient phases.[37] The flowing tube system allows argon gas to flow through the experimental set up to purge the H_2 gas formed during the reduction with CaH_2 and LiH. The reaction mixture of the parent oxide phase and the chosen metal hydride (CaH_2 or LiH) was ground in an argon-filled glove box. The reaction mixture was then transferred into an open glass thimble and placed inside a silica tube as shown in Fig 2.1. The silica tube was then closed with both end caps with T-junction taps. The silica tube was placed into a flowing tube furnace and connected to a constant argon flow. The system was first purged with argon for ~30 min, it was then heated to the desired reaction temperature at 1 °C min^{-1} to avoid overshooting the relatively low desired reaction temperature. The reaction mixture was held at the desired reaction temperature for a suitable period of time before being cooled to room temperature. After the heating cycle, the reaction vessel was evacuated and pumped into the glove box. The reaction mixture was re-ground, and fresh binary metal hydride was added between each heating cycle. This process was repeated until the reaction was deemed complete. The reaction progress was monitored by laboratory X-ray powder diffraction.

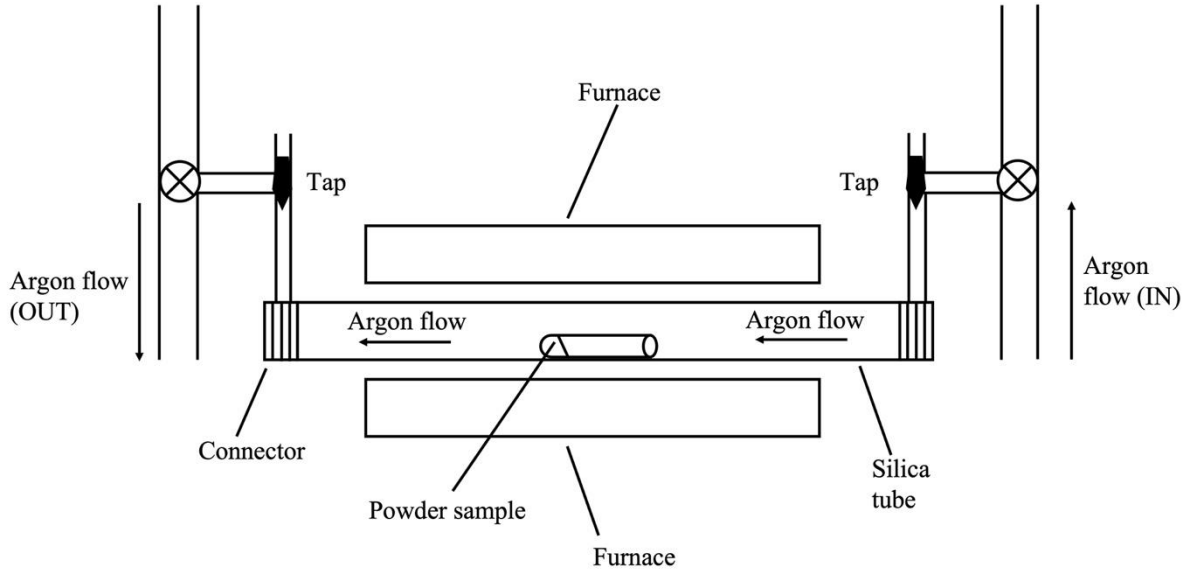


Figure 2.1. Schematic representation of a flowing tube system with flowing argon. Arrows indicate the direction of the argon flow during the reaction.

2.2.3 Washing Reaction Mixtures

After the completion of a topochemical reaction with binary metal hydrides, a purification process is needed to get rid of the unreacted binary metal hydrides (CaH_2/LiH) and their by-products (CaO/Li_2O) so that a pure reduced phase can be obtained. This was done by washing the reaction mixture under a nitrogen atmosphere, using standard Schlenk techniques, with clean methanol (for the LiH/Li_2O) or with 0.1 M NH_4Cl in methanol (for CaH_2/CaO). The sample was then dried under vacuum after the washing process. The removal of the unreacted binary metal hydride and its by-product was confirmed by laboratory X-ray powder diffraction.

2.2.4 Zirconium Getter Reductions

Apart from the binary metal hydrides, zirconium getters can also be used as an alternative method to reduce complex transition metal oxides. The reaction mechanism with zirconium as an oxygen getter is proposed below:[22]

$$ABO_3 \rightarrow ABO_{3-x} + \tfrac{1}{2}\, x\, O_2$$

$$Zr + \frac{1}{2} x\, O_2 \rightarrow ZrO_x$$

As shown in Fig 2.2, dented silica ampoules with a small indent ~ 1 cm from the base of the silica ampoule are used for Zr getter reactions. Inside an argon-filled glove box, 2 mole equivalents of Zr powder (compared to the starting material to be reduced) were weighed and transferred to the bottom of the silica ampoule via a glass funnel. The starting material to be reduced was placed in a small silica 'thimble' and was then loaded into the dented silica ampoule so that the two powders were not in physical contact but share an atmosphere. The whole apparatus was then connected to a closed Young's tap to avoid oxygen exposure. The reaction vessel was taken out from the glove box, evacuated and sealed under vacuum. The sealed silica ampoule was placed in a low temperature furnace and heated to the desired reaction temperature at 1 °C min^{-1} to avoid overshooting the desired reaction temperature. After being held at the desired reaction temperature for a suitable period of time, the ampoule was cooled to room temperature and opened inside the glovebox. The reduced sample was reground and fresh 2 mole equivalents of Zr powder was added at the bottom of a new dented silica ampoule. This process was repeated until the reaction was deemed complete and a pure reduced product had been acquired. The reaction progression was monitored by laboratory X-ray powder diffraction.

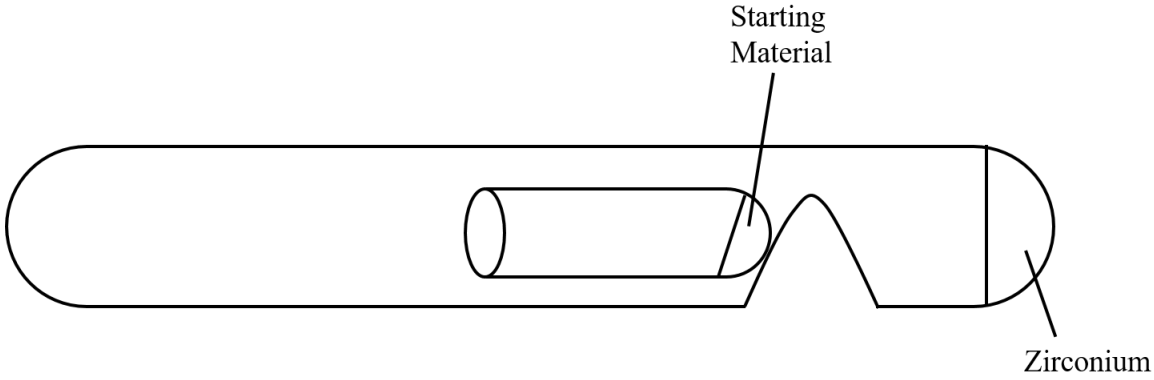


Figure 2.2. Schematic representation of a zirconium getter set up.

2.3 Handling Air-sensitive Compounds

All the oxygen deficient/oxyhydride phases discussed in this thesis are air-sensitive, meaning that these phases will slowly react with O_2 in air and they will be re-oxidised back to their parent oxides. In addition, the reducing agents (binary metal hydrides/zirconium powder) discussed above also react readily with O_2 and moisture in air to form their respective oxides and hydroxides. Therefore, both the topochemically reduced products and the reducing agents need to be handled air-sensitively and avoid any contact with air during the reaction set up and the analysis process.

2.3.1 Argon-filled Glove box

All the reaction mixtures for the topochemical reactions were handled in an argon-filled glove box. The oxygen and the water partial pressures within the glove box are lower than 30 ppm and 10 ppm respectively. The internal atmosphere of the glove box is constantly circulating by a column made of copper catalyst in order to keep the partial pressure of oxygen and moisture inside the glove box low. The glove box is regenerated by heating under 5% H_2/N_2 gas flow when the catalyst is exhausted and the O_2 level starts to rise slowly.

2.3.2 Air-sensitive X-ray Sample Holder

X-ray powder diffraction data of these air-sensitive samples were collected using air-sensitive X-ray sample holders shown in Fig 2.3. In an argon-filled glove box, a small amount of air-sensitive sample was sprinkled onto a glass slide coated with a thin layer of Dow-Corning high vacuum grease. The glass slide was then placed into an air-tight sample holder, with the powder side facing up. The air-sensitive sample holder was sealed by screwing the brass cap/X-ray lid and compressing the O-ring between the lid to form an airtight environment.

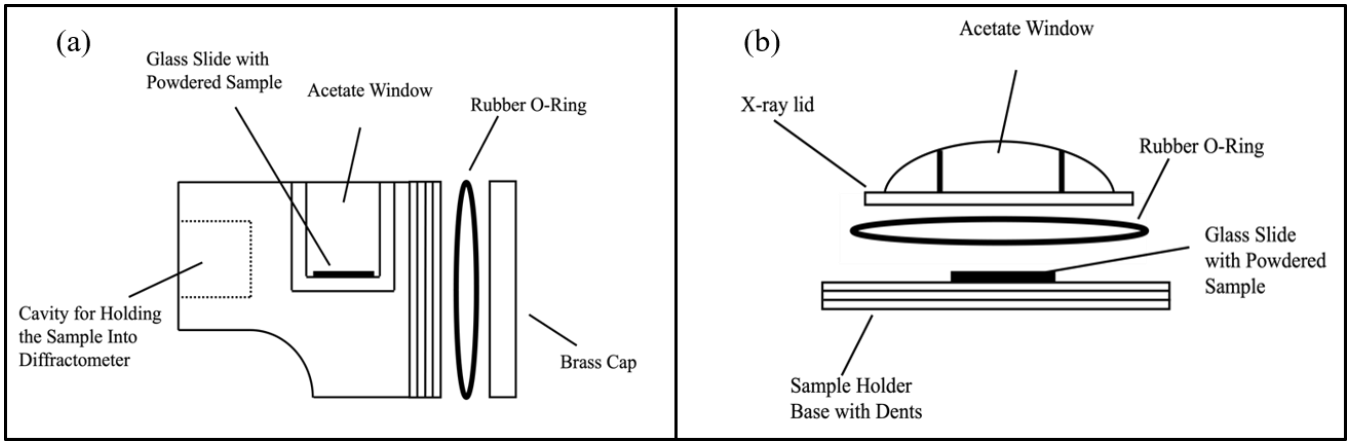


Figure 2.3. (a) Air-sensitive X-ray sample holder for Panalytical Empyrean and Panalytical X'Pert diffractometers; (b) Air-sensitive X-ray sample holder for Bruker AXS D8 Advance Pro diffractometers.

2.4 Powder Diffraction

Powder diffraction technique is one of the most common and important techniques used in solid state chemistry. It is widely used for structural characterisation of crystalline materials. Both X-ray powder diffraction and neutron powder diffraction techniques were utilised for structural characterisation of the phases presented in this thesis.

Diffraction takes place when a wave is irradiated through an aperture of comparable size to its wavelength. In a crystalline solid, the periodic arrangement of atoms or molecules can act as a diffraction grating if the wavelength of the radiation (λ) is of the same order as the lattice spacing (d). Since the d-spacing between the lattice planes are comparable to the wavelengths of X-ray and neutron radiations, diffractions will occur if a beam of X-rays or neutrons are irradiated towards a crystalline solid. The regular array of lattice diffracts the incident beam and produces a regular array of scattered waves. In most directions, those scattered waves will interfere destructively and give rise to zero intensity; However, under certain geometrical conditions, those scattered waves will interfere constructively and give rise to Bragg peaks. The geometrical condition to be satisfied is known as Bragg's Law:[51]

$$n\lambda = 2d_{hkl}\sin(\theta)$$

Where *d* is the interplanar distance, θ is the angle between the beam and the lattice plane, *n* is an integer and λ is the wavelength of the incident beam. Bragg's Law shows that the positions of the Bragg peaks are determined by d_{hkl} in a diffraction pattern, which is related to the unit cell dimensions.

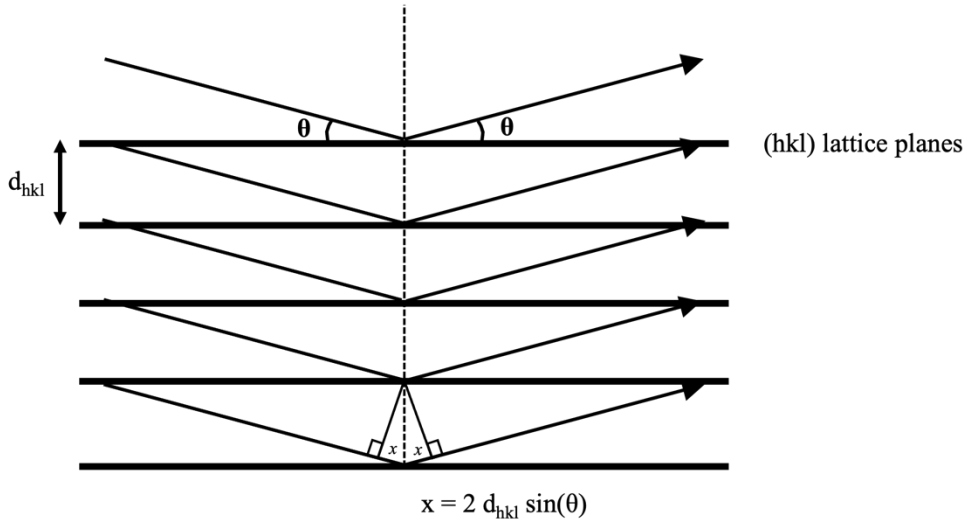


Figure 2.4. Bragg's law reflection. Bragg's construction for diffraction of monochromatic beams by a set of parallel lattice beam.

The intensity of a reflection (I_{hkl}) is given by:

$$I_{hkl} \propto LmA\,|F_{hkl}|^2$$

Where *L* is the sample-independent Lorentzian polarisation factor, *m* is the multiplicity of the *{hkl}* planes, *A* is the absorption factor and F_{hkl} is the structure factor. The structure factor F_{hkl} describes the arrangement and the identity of atoms:

$$\boldsymbol{F_{hkl} = \sum_n f_n(\theta) \cdot \exp\left[2\pi i(hx_n + ky_n + lz_n)\right] \cdot \exp\left(\frac{-8\pi^2 U_{iso_n} \sin^2\theta_{hkl}}{\lambda^2}\right)}$$

Where f_n is the scattering power of each atom n, x_n, y_n, z_n, are the fractional coordinates of atom n in the unit cell, the U_{ison} is the isotropic displacement parameter. The second exponential term describes the effect of U_{ison} on the intensity of the Bragg peaks, which falls off as a function of the scattering angle (θ).

2.4.1 X-ray Powder Diffraction

In this thesis, X-ray powder diffraction technique was used to determine the crystal structure and monitor the reaction progression. X-ray radiation interacts with electron density within the crystal structure. Therefore, the scattering factor of an atom (f_j) is proportional to its atomic number (Z). This makes X-ray diffraction technique insensitive towards light elements (e.g. O, H), especially when heavy atoms are present in the structure.[52] As a result, structural characterisation using only X-ray powder diffraction is insufficient, as the subject matter in this thesis is concerned with the modified anion framework in the presented phases.

2.4.1.1 Panalytical Empyrean and Panalytical X'Pert Diffractometers

Panalytical Empyrean and Panalytical X'Pert were both used as a characterisation technique to monitor the reaction progression and characterisation of the crystal structures. Both diffractometers adopt Bragg-Brentano focussing geometry and use Cu $K\alpha_1$ radiation to irradiate the sample. A Ge (111) monochromator is installed so that only Cu $K\alpha_1$ radiation is used to irradiate the sample. The beam optics can be adjusted by fitting different sizes of beam masks, anti-scattered slits and soller slits.

The Empyrean and Panalytical X'Pert diffractometers yield data with high resolution, hence they are suitable for Rietveld refinement for detailed structural characterisation.

For both diffractometers, samples were prepared as follows:

- Air-sensitive sample preparation was described in Section 2.3.2.

- For non-air sensitive samples, a silicon wafer that was cleaved along the [110] systematic absence plane was used, so that it does not produce any diffraction peak in the diffraction data. A small amount of Dow-Corning high vacuum grease was applied onto the appropriate position of the glass slide. A small amount of powdered sample was then sprinkled onto the silicon wafer. The silicon wafer was then assembled into the flat stage sample holder of the diffractometer.

2.4.1.2 Bruker AXS D8 Advance Pro Diffractometer

Bruker D8 diffractometer was frequently used to monitor the reaction progression when a large amount of sample could not be yielded. In contrast to Empryean and X'pert, Bruker D8 diffractometer uses an energy dispersive detector which discriminates Cu Kβ wavelengths and fluorescence from samples (if applied). Therefore, both Cu $K\alpha_1$ and Cu $K\alpha_2$ are used to irradiate the sample as they are too close in energy to be distinguished by the detector. The intensity produced from Bruker D8 diffractometer is thus much higher than that from Empryean and X'pert diffractometers. Soller slits and beam mask are fixed in the diffractometer, but the divergence slit can be programmed. Antiscatter object can be adjusted or removed by using a knife at 2 mm above the sample for non-air sensitive samples. For air sensitive samples, the antiscatter object is a wooden hat placed on top of the air sensitive sample holder.

For Bruker D8 Advance Pro diffractometer, samples were prepared as follows:

- Air-sensitive sample preparation was described in Section 2.3.2.
- For non-air sensitive samples, a small amount of powdered sample was sprinkled on a round-shaped glass slide coated with a thin layer of Dow-Corning high vacuum grease and was then placed on the sample holder. The sample was measured with spinning so that the impact of uneven sample distribution and preferred orientation is reduced.

2.4.1.3 Synchrotron X-ray Powder Diffraction

In a synchrotron, electrons are accelerated in an orbit (the direction of the travelling of electrons is curved by a magnetic field) at a speed close to the speed of light. As a result, a continuum of electromagnetic radiation tangential to the orbit will be emitted, with the X-ray part of the radiations used for diffraction. Synchrotron X-rays produced in a synchrotron light source have very high intensity and low beam divergence. As a result, high resolution and high signal-to-noise-ratio X-ray powder diffraction data can be collected using synchrotron radiation.[53]

The synchrotron X-ray powder diffraction data presented in this thesis were collected using the I11 beamline at the Diamond Light Source Facility in Didcot, Oxfordshire. The I11 beamline is a high-resolution powder diffraction beamline that can produce X-rays ranging from 5 to 30 keV and is dedicated to high-resolution powder diffraction. A double-crystal-monochromator (DCM) comprising two liquid nitrogen cooled Si (111) is used to select the energy of the incident beam. A wide-angle position sensitive detector (PSD) is used for data collection, which allows high-resolution, wide-angle range powder diffraction data to be collected. Variable temperature synchrotron X-ray measurements can also be conducted at the I11 beamline. A hot air blower is used for measurements at high temperature (300 K to 1273 K).[54]

Samples were loaded and sealed in borosilicate/silicate capillaries of different diameters (0.3 mm to 0.5 mm), the capillaries were then mounted onto the brass holders with magnetic bases. Afterwards, these sample holders were placed onto a magnetic stage pre-aligned to the centre of the diffractometer. Synchrotron X-ray diffraction data collected were analysed by Rietveld refinement using the TOPAS suite.[55]

2.4.2 Neutron Powder Diffraction

Neutron powder diffraction technique is often used alongside with X-ray powder diffraction for structural characterisation. The principal difference between X-ray and neutron powder diffraction techniques is that the X-ray radiation interacts with the electron cloud of atoms while neutron radiation interacts with the atomic nucleus. As a result, neutron scattering lengths of atoms do not follow a linear relationship with the electron density. Thus, it is possible to accurately determine the positions and the occupancies of light elements using neutron powder diffraction. For example, oxide and hydride anions have very different neutron scattering lengths (O: 5.80 fm, H: -3.74 fm), which are comparable to that of Co (2.49 fm). Therefore, in a crystal structure containing oxide, hydride and cobalt, neutron powder diffraction can help accurately determine the position and the occupancy of lighter anions.[56] However, it is worth noting that hydrogen has a large incoherent scattering cross section and gives rise to a large incoherent scattering. As a result, in an oxyhydride phase, the incoherent scattering from the hydride anions adds to the background of the neutron diffraction data.

Since neutron radiation interacts with the atomic nucleus of an atom, neutron scattering form factor is angle independent, unlike the X-ray form factor which decreases with increasing scattering angle. The high intensity of the diffraction peaks observed in the high angle region of the neutron powder diffraction data allows more structural information to be gathered, which helps improve the accuracy and the precision of the refinement.

In addition, neutrons are half spin particles, thus, they can be scattered by periodic arrays of ordered magnetic moments (unpaired electrons). Therefore, neutron powder diffraction allows the characterisation of the magnetic structure of a material.

The magnetic structure factor (F_{mag}^{hkl}) for an unpolarised neutron source can be described as follows:[57]

$$F_{mag}^{hkl} = \sum_{j} q_j p_j e^{2\pi i h x_j}$$

Where q_j is the magnetic interaction vector, p_j is the magnetic form factor, h is the magnetic scattering vector and x_j is the position vector of magnetic atoms in the unit cell.

The observed intensity of the magnetic reflection ($I_{hkl,mag}$) is proportional to the square of the projection of the magnetic structure factor onto the scattering vector:[57]

$$I_{hkl,mag} = \left|F_{mag}^{hkl}\right|^2 cos^2\alpha$$

Where α is the angle between the magnetic scattering structure and the relevant lattice plane.

Since the interaction between neutrons and atomic nuclei is relatively weak, large-scale samples (> 1 g) are needed for neutron powder diffraction. Samples were loaded into vanadium cans for neutron powder diffraction measurements. Vanadium has a very low neutron scattering length (-0.38 fm), as a result, the Bragg scattering from the vanadium has negligible contribution to the neutron diffraction data.[56]

In this thesis, the neutron powder diffraction data were collected from WISH instrument at ISIS neutron facility, Rutherford Appleton Laboratory in Oxfordshire, UK.[58,59]

2.4.2.1 WISH

At ISIS, neutrons are generated by spallation sources using protons. High energy pulsed protons are accelerated in the main ring in a synchrotron and directed onto a heavy metal target made of tungsten. The collision of the proton beam into the nuclei of the metal target produces pulses of neutrons. The neutrons produced via this process have very high thermal energy, they are then slowed down by using a methane moderator, so that the neutrons beams have suitable wavelengths for time-of-flight diffraction experiments.[60]

Time-of-flight measurement employs energy dispersive neutrons with detectors at various fixed angles. The diffraction data are hence measured with the time taken to travel from the moderator to the detector via the sample. The d-spacing can be calculated by relating the de Broglie equation and the Bragg's law:

$$\lambda = \frac{h}{mv} = \frac{ht}{mL} = 2dsin\theta$$

where *h* is Planck's constant, *v* is the velocity of neutron, *m* is the neutron mass, *t* is the time taken to travel distance *L* from the moderator to the detector via the sample.

The WISH instrument is designed for magnetic studies on both single crystals and powdered samples. It provides high resolution data over d-spacing ranging from 0.7-1.7 Å. The ^{3}He detectors cover scattering angle from 10° to 170°.[59]

2.5 Rietveld Refinement

In this thesis, Rietveld refinement was used to analyse X-ray and neutron powder diffraction data. Extracting structural information from powder diffraction is inherently difficult due to the peak overlap resulting from the similar values of d-spacing but different *hkl* value. Since all the overlapping peaks contribute to the observed peak intensity, the exact structural factor magnitude cannot be extracted from the reflection intensities. The Rietveld method can overcome this barrier by calculating the diffraction data from a proposed structural model (which is close to the 'real' structure) and comparing the simulated data with the experimental diffraction data. The crystallographic parameters of the proposed structural model are refined until the calculated diffraction data are consistent with the experimental diffraction data.[61]

The aim of Rietveld refinement is to minimise the difference between the calculated and experimental diffraction data using a least squares algorithm:

$$S = \sum_i w_i \, (y_{io} - y_{ic})^2$$

Where w_i is the weighting factor, y_{io} is the observed intensity at point i in the collected data, and y_{ic} is the calculated intensity at point i. Diffraction and structural parameters are then refined against the experimental data to minimise S, using the least squares optimisation techniques.

The statistical fit of the model to the data is assessed using three parameters: the goodness of fit, χ^2; the profile factor, R_p; and the weighted profile factor, wR_p. These parameters are defined as follows:

$$\chi^2 = \frac{\sum w_i (y_{io} - y_{ic})^2}{n_{obs} - n_{var} + n_{constraint}} = \frac{S}{n_{obs} - n_{var} + n_{constraint}}$$

$$R_p = 100\% \times \frac{\sum |y_{io} - y_{ic}|}{\sum y_{io}}$$

$$wR_p = 100\% \times \sqrt{\left(\frac{\sum w_i (y_{io} - y_{ic})^2}{\sum w_i y_{io}^2}\right)} = \sqrt{\frac{S}{\sum w_i y_{io}^2}}$$

Where n_{obs} is the number of observations in all histograms, n_{var} is the number of variables, $n_{constraint}$ is the number of constraints used in the least square refinement. The structural refinements presented in this thesis were conducted using Topas V7.13 suite of programmes.[62]

2.5.1 Sample Contribution to Diffraction Peak Broadening

The peak profile of a diffraction peak of a sample is described by a convolution of Instrumental Resolution Function (IRF) and the sample contribution (MS from Microstructure).[55]

$$Peak\ profile\ \phi(X) = (IRF \circ MS)(X)$$

There are two principal features of a powdered sample that contribute to the diffraction peak broadening: crystalline domain size and microstructural strain. The diffraction peak broadening contributions from these two features have different angle (θ) dependences. Therefore, the contributions from crystalline domain size broadening and microstructural strain broadening can be separated and quantified if data sets with a sufficient 2θ range is measured.[55]

2.5.1.1 Crystalline Domain Size Broadening

The crystalline domain size contribution to the peak profile broadening is described by a pseudo-Voigt function in TOPAS. The crystalline domain size broadening command in the TOPAS refinement software allows the average crystalline domain size *D* to be refined and acquired. The crystalline domain size broadening contribution to the full width half maximum of a peak at 2θ ($fwhm_{2\theta}$) can be calculated using the following relationship:

$$fwhm_{2\theta} = \frac{\lambda}{D\cos(\theta_0)}$$

Where λ is the wavelength of the incident X-ray. The unit of *D* is angstrom (Å), the unit of wavelength is nanometre (nm) and the unit of $fwhm_{2\theta}$ is radians. This equation assumes that the crystalline domain size broadening is *hkl* independent (isotropic crystalline domain size broadening).[55]

2.5.1.2 Microstructural Strain Broadening

The microstructural strain contribution from the sample can be fitted with a pseudo-Voigt function. Lattice strain broadening can be described using the following relationship:

$$fwhm_{2\theta} = 2fwhm_{\varepsilon}tan\theta$$

Where $fwhm_{2\theta}$ is the strain broadening contribution to the *fwhm* of a peak at 2θ (in radians), $fwhm_{\varepsilon}$ is the lattice strain parameter (in radians) which can be obtained from the refinment.[55]

2.6 Pawley Refinement

In this thesis, Pawley refinement was used for structure-independent powder diffraction data fitting. Pawley refinement provides information about the dimensions of a unit cell, peak profile and background of the diffraction data. Knowing this information can help one focus on the structural aspects of the model during the initial phases of Rietveld refinement. Unlike Rietveld refinement method, where the intensity of a diffraction peak is determined by the structure factor (F_{hkl}) (which is related to the crystal structural parameters), the diffraction peak intensities in Pawley refinement method are treated as refinable parameters. The pre-determined lattice parameters can then be directly transferred to Rietveld refinement. This method utilises the least-squares algorithm, similar to the Rietveld refinement method.[63]

2.7 Thermogravimetric Analysis (TGA) and Mass Spectrometer (MS)

In this thesis, thermogravimetric analysis was used to estimate the oxygen stoichiometries of the topochemical reduced phases presented. The measurements were performed using a Mettler Toledo TGA/DSC 1 STARe system. A small amount of sample (20 – 50 mg) was accurately weighed and placed in a small crucible. The small crucible was then loaded into the instrument, the sample was heated under a steady flow of either 5%/95% H_2/N_2 (reductive TGA) or O_2 (oxidative TGA) at 10 °C min^{-1} to the target temperature (set at 800 °C for all TGA measurements conducted in this work). The sample was held at the target temperature for a sufficient period of time to ensure a complete reaction before cooling to room temperature. Both the weight change and the heat flow were recorded as a function of time. After the experiment, X-ray diffraction data from the reduced/oxidised sample were collected and

analysed to confirm a complete reaction had taken place. A reductive TGA (heating sample in 5%/95% H_2/N_2 environment) usually decomposes the sample completely into binary oxides and elemental metals, while an oxidative TGA (heating sample in O_2 environment) leads to a re-oxidation of the reduced phase back into its parent oxide phases. In both cases, by taking the mass of the sample before and after the experiment, together with the composition of the sample after the experiment, the oxygen stoichiometry of the reduced oxide phase can be calculated.

It is worth noting that the TGA measurements only provide information about the oxygen content, they cannot distinguish if a reduced phase is an oxyhydride phase or an oxygen-deficient phase. Therefore, a mass spectrometer (MS) is then connected to a TGA instrument. The sample was heated to the target temperature (set at 800 °C) under an oxygen environment, the water release behaviour of oxyhydride phases upon heating can then be monitored by the mass spectrometer. This TGA-MS set up can distinguish whether a reduced phase is an oxyhydride phase or an oxygen-deficient phase. The TGA-MS measurements were conducted using a Perkin Elmer TGA instrument and a Hiden Analytical Mass Spectrometer. Samples preparation using this TGA-MS set up is the same as the TGA set-up described previously.

2.8 SQUID Magnetometry

The magnetic properties of samples presented in this work were measured using a Quantum Design MPMS-3 Superconducting Quantum Interference Device (SQUID). A SQUID magnetometer is highly sensitive to a small change in a magnetic field by making use of the Josephson Effect. The SQUID magnetometer has a closed superconducting loop intersected by two thin strips of insulating material, forming two Josephson Junctions. The application of a small current across the junction enables the Cooper pair electrons tunnel through the insulating barriers in the absence of a magnetic field. This superconducting state ‘breaks’ when the applied current exceeds the critical current and a small voltage across the device will be

established. The presence of an external magnetic field affects the critical current of the Josephson Junctions. As a result, the change of the voltage across the junction can then be monitored by the SQUID magnetometer, which is proportional to the magnetic moment of the sample.[64]

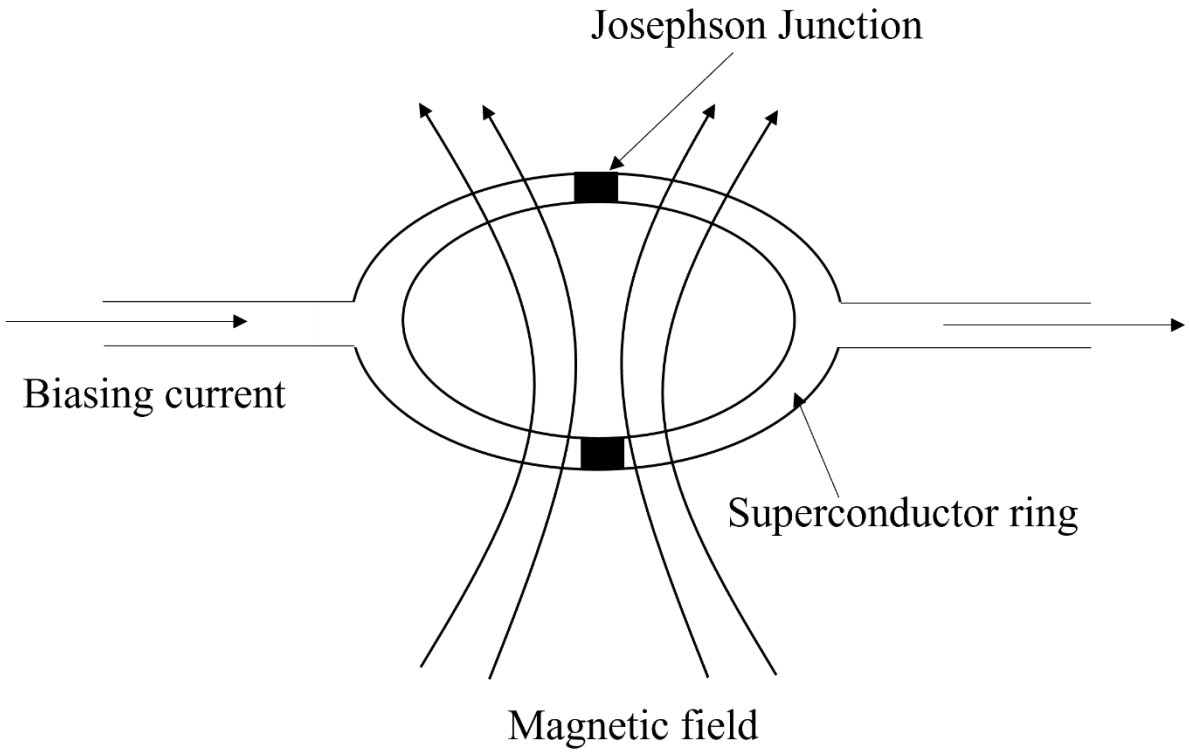


Figure 2.5. Schematic representation of the principle component in a SQUID magnetometer.[64]

For the measurement in this work, samples of approximately 10 - 20 mg were weighed and placed into a gelatine capsule. The gelatine capsule containing the sample to be measured were then placed inside a drinking straw, with three empty capsules on both sides of the sample gelatine capsule. The outermost capsules were covered in a layer of diamagnetic Kapton sticky tape to prevent the sample from moving in the application of magnetic fields. Air-sensitive samples were prepared in the glovebox and kept under inert atmosphere until loading into the chamber of SQUID. The straw was pierced with a needle for multiple times, to prevent air from going into the chamber of SQUID.

Magnetisation data was collected using 'ferromagnetic subtraction' measurements. Measurements as a function of applied field were conducted over the field range of -5 T ≤ H ≤ 5 T at a constant temperature (e.g. 5 K, 300 K).

2.8.1 Ferromagnetic subtraction ('Ferrosubtraction') Measurements

The magnetic properties of some topochemical reduced compounds are masked by traces of ferromagnetic impurities (e.g. Co or Ni) presented in the samples (< 2 mol%). Therefore, ferromagnetic subtraction technique is utilised to measure the magnetic properties of those phases. Since the magnetisation of the ferromagnetic impurities (e.g. Co or Ni) saturate at a relatively low field, in this technique, large magnetic fields (3 T – 5 T) are used to saturate the magnetisation of the ferromagnetic impurities. The sample is cooled under a magnetic field of 100 Oe, the magnetisation of the sample is measured between 3 T ≤ H ≤ 5 T from 5 K to 300 K at a 5 K increment. At each temperature point, the resulted magnetisation can be plotted as a function of the applied field, with the gradient of the plot gives the paramagnetic susceptibility, and the intercept gives the saturated magnetic moment. Combined whole range of temperatures, a field-cooled plot can be made. Figure 2.6 shows the graphic representation of the principles of ferromagnetic subtraction measurements.

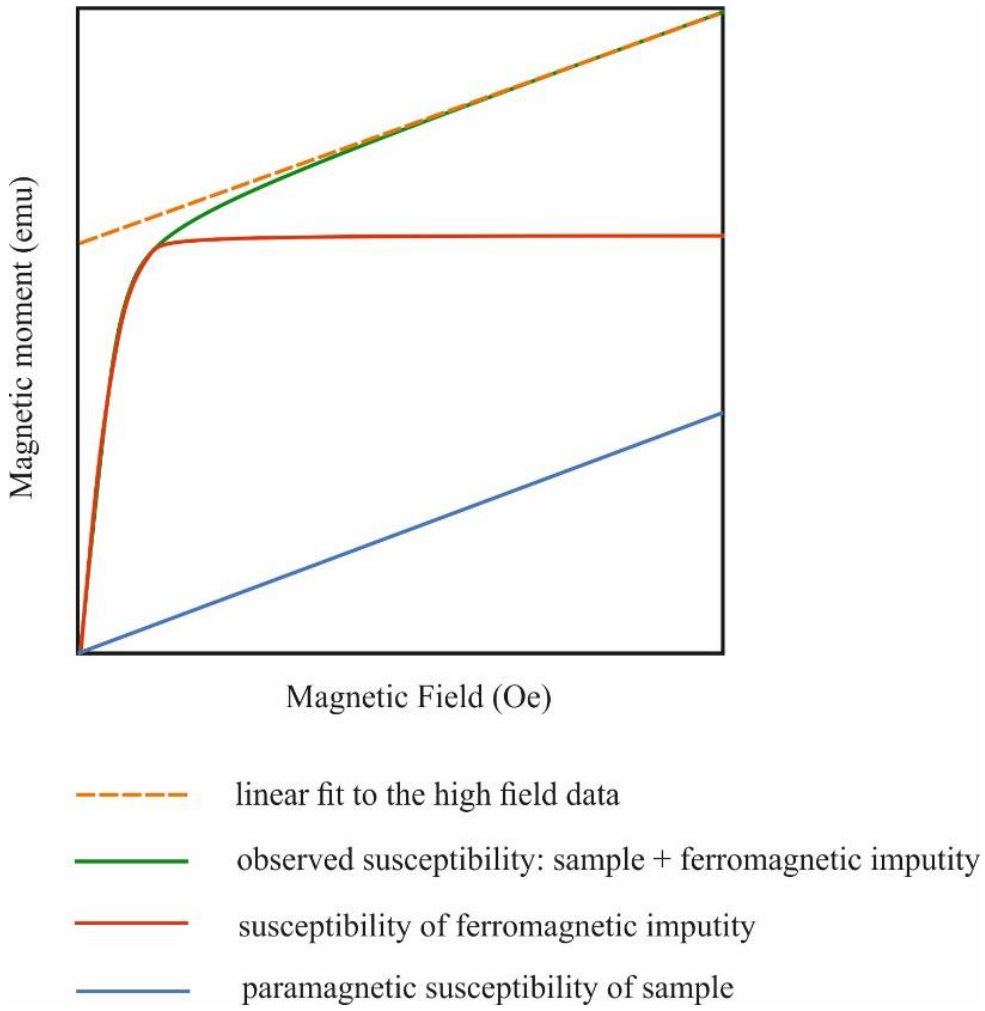


Figure 2.6. Graphic representation of the principles of 'ferrosubtraction' measurements.

2.9 Magnetism

2.9.1 Curie Weiss Law

The paramagnetic susceptibility of a material indicates the responsiveness of the material in an applied magnetic field. The paramagnetic susceptibility is a ratio between the magnetization of the sample (***M***) and the applied magnetic field (***H***), both are vectors.[9]

$$\chi_m = \frac{\boldsymbol{M}}{\boldsymbol{H}}$$

The relationship between the paramagnetic susceptibility and temperature can be described via the Curie Law:

$$\chi_m = \frac{C}{T}$$

Where χ_m is the molar paramagnetic susceptibility, C is the Curie constant and T is the temperature in K. The Curie Law assumes that the electrons (individual magnetic moments) do not interact with each other. In reality, this is only true for magnetic dilute systems. Systems with correlated magnetic behaviour like ferromagnet and antiferromagnet cannot be correctly described using the Curie Law. In this case, an extra parameter is added to the Curie law to better describe the relationship between the paramagnetic susceptibility and temperature:

$$\chi_m = \frac{C}{T - \theta} + K$$

Where θ is the Weiss constant, which measures the strength of the interaction between the spins in the sample; K is the 'temperature independent contribution', the rest of the parameters are the same as defined from the Curie Law. The Curie constant (C) is related with the effective magnetic moment of the sample through:[9]

$$C = \frac{N_A {\mu_B}^2 g^2 S(S+1)}{3k_B} \approx \frac{1}{8}\mu_{eff}^2$$

Where N_A is the Avogadro's number, μ_B is the Bohr magneton, g is the Landé factor, S is the total spin quantum number, k_B is the Boltzmann's constant and μ_{eff} is the effective magnetic moment. It is worth noting that this equation assumes that the effective magnetic moment is temperature independent, which is mostly true for the transition metal cations in complex oxides.

2.10 Electron Diffraction (ED)

In this thesis, some of the topochemical reduced phases were analysed by electron diffraction (ED) to help resolve their crystal structures. Electron diffraction experiment is usually performed in a transmission electron microscopy (TEM), where a beam of electrons is transmitted through a specimen and the resulted electron diffraction data are measured. The electron diffraction data presented in this thesis were performed by Dr Maria Batuk and Prof. Joke Hadermann at the University of Antwerp. ED data were acquired at a FEI Titan 80-300 "cubed" microscope operated at 300 kV. The specimens for the TEM study were prepared by grinding the material in ethanol and depositing a few drops of the suspension onto a copper TEM grid covered by a continuous carbon layer. Samples were analysed by using both tomography single-tilt holder (non-air sensitive) and vacuum transfer holder (air-sensitive) to transfer the grids to the microscope.

2.11 Bond Valence Sum (BVS)

The bond valence sum is a useful concept that is used to estimate the valence of an ion in a crystal structure. The valence of an ion, V_i, is the sum of the individual bond valences within the coordination sphere of the ion. This approximation can be expressed as:[65]

$$V_i = \sum_j v_{ij}$$

where v_{ij} is the valence of a bond between atoms i and j, and v_{ij} is given by:

$$v_{ij} = e^{(R_{ij} - d_{ij})/b}$$

where b is an empirical constant (taken to be 0.37), R_{ij} is the bond valence parameter, and d_{ij} is the measured bond length between ion *i* and *j*. The bond valence parameters reported by Brese and O'Keeffe were used for bond valence sum calculation in this thesis.[66] Bond valence sums

were used to evaluate the likelihood of charge-disproportionation of the transition metal centres in different geometries in a structure.

2.12 Iodometric Titration

The hydride content in some $LaSrCo^{a+}Ru^{b+}O_{6-x}H_y$ oxyhydride phases presented in this thesis was determined via titration with I_2.[67] The major redox reactions of the iodometric titration are stated as follows:

$$Co^{a+} + {}^{(2-a)}/_{2}\ I_2 \rightarrow Co^{2+} + (2-a)\ I^-$$

$$Ru^{b+} + {}^{(2-b)}/_{2}\ I_2 \rightarrow Ru^{2+} + (2-b)\ I^-$$

Approximately 30 mg of sample was dissolved in 10 ml of 2 M HCl solution. Then, 10 ml of 0.00166 M KIO_3 solutions was added into the mixture, followed by an excess of KI (~0.07 g). This process liberated I_2, which then reacted with the reduced Co^{a+} and Ru^{b+} centres. The unreacted I_2 was titrated with $Na_2S_2O_4$ solution of known concentration, determined by the standardisation process with KIO_3, using starch as an indicator. 1 ml of freshly prepared starch solution (~0.005 gcm^{-3}) was added just before the endpoint of the titration. A constant argon flow was maintained to avoid oxidation of the samples by air throughout the whole titration process. The total oxidation states of the transition metal centres can be determined via the titration process. Combining the values of the oxidation states of the transition centres obtained from the iodometric titration and the oxygen content obtained from the TGA experiment, the hydride content in an oxyhdyride phase can then be calculated.

Chapter 3 Microstructural Characterisation of $LaSrNiRuO_6$

3.1 Introduction

The topochemical reduction of the B-site cation ordered double perovskite $LaSrNiRuO_6$ with CaH_2 at 360 °C yields $LaSrNiRuO_4$, which adopts an infinite layer structure (Fig 3.1(a)).[37] During the reduction process, an unusual behaviour was observed: The reactivity of the starting material ($LaSrNiRuO_6$) appeared to be coupled with the final cooling step of its synthesis. Samples of $LaSrNiRuO_6$ that had been rapidly cooled (quenched) from the synthesis temperature (1200 °C) were reduced to $LaSrNiRuO_4$ much faster than samples of $LaSrNiRuO_6$ that were cooled slowly (slow-cooled) from the synthesis temperature (1200 °C). (Fig 3.1.(b))

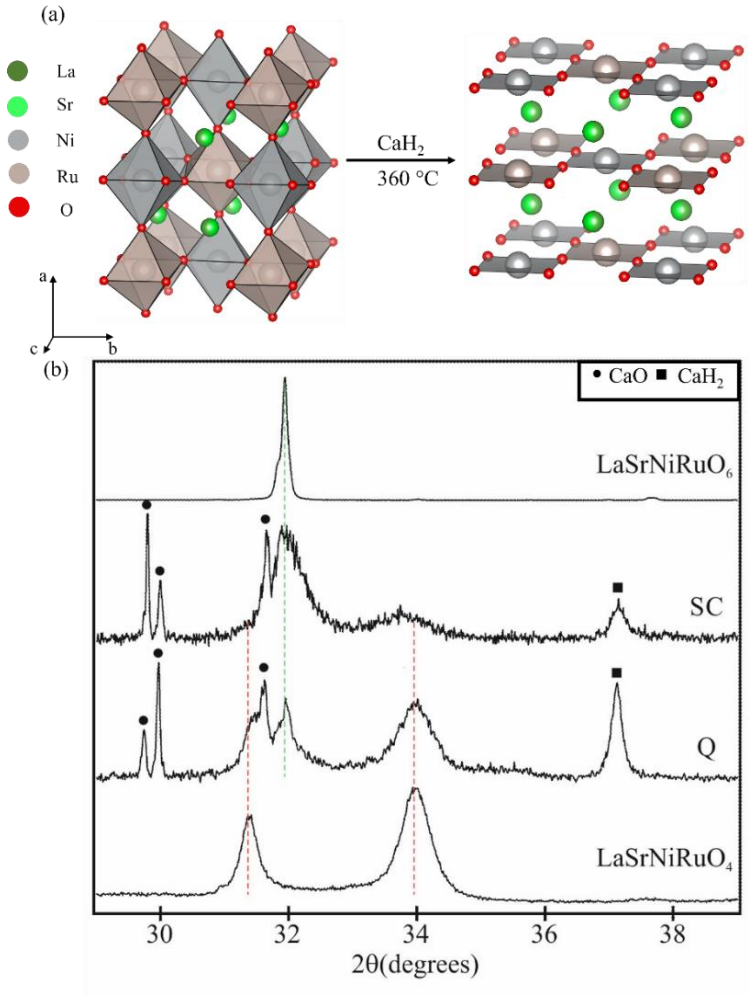


Figure 3.1. X-ray powder diffraction data collected from the first cycle of reduction of quenched and slow-cooled samples of $LaSrNiRuO_6$ with CaH_2 (Q: Quenched, SC: Slow-cooled).

In order to determine the reason for the difference in reactivity with CaH_2 of the quenched and slow-cooled samples of $LaSrNiRuO_6$, the crystal structures and the microstructures of the quenched and slow-cooled samples of $LaSrNiRuO_6$ have been examined.

Results from this chapter are published as: Z. Liang, M. Amano Patino, M. Hendrickx, J. Hadermann and M. A. Hayward. Microstructural activation of a topochemical reduction reaction. *ACS Organic & Inorganic Au*, **2** (2022) 75.

3.2 Experimental

3.2.1 Synthesis of $LaSrNiRuO_6$

A powdered sample of $LaSrNiRuO_6$ was prepared via a citrate gel method. A suitable stoichiometric ratio of La_2O_3 (dried at 900 °C), $SrCO_3$, Ni and RuO_2 (from RuO_2 hydrate, dried at 800 °C) was weighed, ground thoroughly and dissolved in a minimum quantity of water and 6 M nitric acid at a 1:1 ratio. Then, 3 mole equivalents of citric acid monohydrate and 2 ml of ethylene glycol were added to the mixture. The solution was heated to 200 °C with constant stirring. The solution was kept at 200 °C, it then became viscous and set into a gel, which then pyrolyzed. The resulting powder was ground, transferred into an alumina crucible and heated in air to 900 °C at 5 °C min^{-1}. The powder was kept at 900 °C for 12 hours. The powder was then reground, pressed into 13 mm pellets, and heated to 1200 °C in air at 1 °C min^{-1} for two cycles of 48 hours. After the final heating period, the pellets were ground thoroughly and characterised by X-ray powder diffraction.

3.2.2 Preparation of Quenched and Slow-cooled Samples of $LaSrNiRuO_6$

A quenched sample of $LaSrNiRuO_6$ was prepared by heating a pellet of $LaSrNiRuO_6$ to 1200 °C and holding it at this temperature for 12 hours. The pellet was cooled to 450 °C at 5 °C min^{-1}. The pellet was then quenched by quickly transferring it to a pre-cooled crucible embedded in dry ice. (As will be discussed in Section 3.3.3, quenching from 450 °C was found

to be the most effective temperature to yield sample with broadest diffraction peaks. Quenching directly from the synthesis temperature 1200 °C was also investigated but found not as effective.) The pellet was ground into a fine powder and characterised by X-ray powder diffraction.

A slow-cooled sample of $LaSrNiRuO_6$ was prepared by heating a pellet of $LaSrNiRuO_6$ to 1200 °C and holding at this temperature for 12 hours, before being cooled to room temperature at 2 °C min^{-1}. The pellet was then ground thoroughly and characterised by X-ray powder diffraction.

3.3 Results

3.3.1 Structural Characterisation of the Quenched and Slow-cooled Samples of $LaSrNiRuO_6$

Synchrotron X-ray powder diffraction (SXRD) data were collected from the quenched and slow-cooled samples of $LaSrNiRuO_6$ using the I11 instrument at the Diamond Light Source Ltd (Section 2.4.1.3). A structural model based on the previously reported structure of $LaSrNiRuO_6$ (space group $P2_1/n$)[16] was refined against the SXRD data collected from the quenched and slow-cooled samples of $LaSrNiRuO_6$. The refinements against the SXRD data collected from the quenched and slow-cooled samples of $LaSrNiRuO_6$ achieved good statistical fits. The observed, calculated and difference plots from the structural refinements of both quenched and slow-cooled samples of $LaSrNiRuO_6$ are shown in Fig 3.2. The results from the structural refinements (Table 3.1) of the quenched and slow-cooled samples of $LaSrNiRuO_6$ show that both samples are indistinguishable.

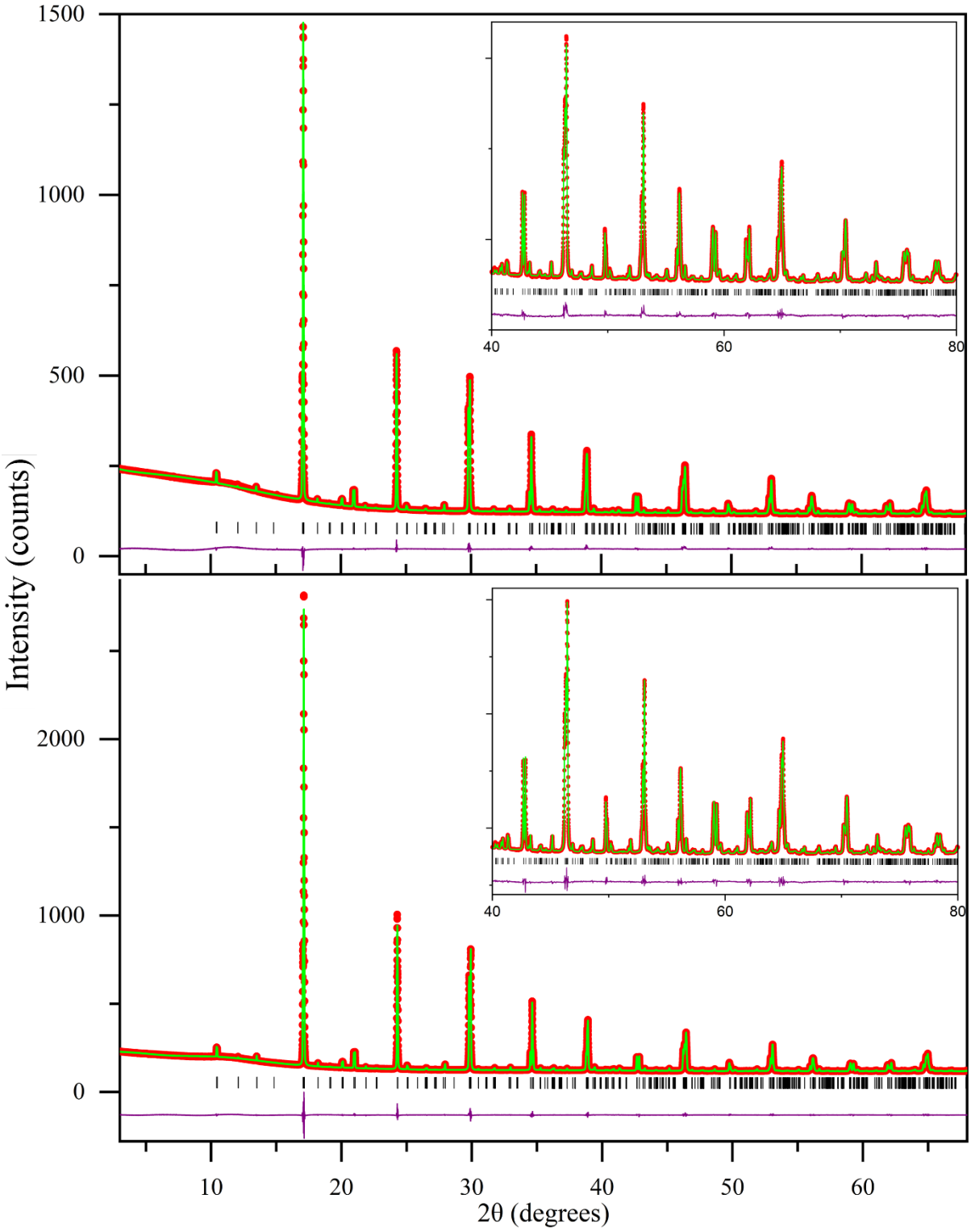


Figure 3.2. Observed, calculated, and difference plots from the structural refinements of quenched (top) and slow-cooled (bottom) samples of $LaSrNiRuO_6$ against SXRD data collected at room temperature. Insets show an expanded view of the high angle region.

Quenched $LaSrNiRuO_6$, space group $P2_1/n$ (#14)						
Atom	Wyckoff	*x*	*y*	*z*	Fraction	B_{iso} equiv. ($Å^2$)
Sr(1)/La(1)	4*e*	0.0038(2)	0.0187(1)	0.2494(1)	$^1/_2/^1/_2$	0.010(8)
Ni(1)/Ru(2)	2*c*	$^1/_2$	0	$^1/_2$	0.966(3)/0.034(3)	0.010(9)
Ru(1)/Ni(2)	2*d*	$^1/_2$	0	0	0.966(3)/0.034(3)	0.010(9)
O(1)	4*e*	0.282(1)	0.278(1)	0.023(1)	1	0.186(40)
O(2)	4*e*	0.225(1)	0.781(1)	0.045(1)	1	0.186(40)
O(3)	4*e*	0.942(1)	0.495(1)	0.254(1)	1	0.186(40)
a = 5.57509(2) Å, *b* = 5.54010(2) Å, *c* = 7.84755(3) Å *β* = 89.991(4)° *wRp = 3.35%; Rp = 2.43%*						
Slow-cooled $LaSrNiRuO_6$, space group $P2_1/n$ (#14)						
Atom	Wyckoff	*x*	*y*	*z*	Fraction	B_{iso} equiv. ($Å^2$)
Sr(1)/La(1)	4*e*	0.0033(2)	0.0206(1)	0.2496(1)	$^1/_2/^1/_2$	0.010(4)
Ni(1)/Ru(2)	2*c*	$^1/_2$	0	$^1/_2$	0.976(2)/0.024(8)	0.010(5)
Ru(1)/Ni(2)	2*d*	$^1/_2$	0	0	0.976(2)/0.024(8)	0.010(5)
O(1)	4*e*	0.285(1)	0.273(1)	0.028(1)	1	0.182(25)
O(2)	4*e*	0.230(1)	0.774(1)	0.041(1)	1	0.182(25)
O(3)	4*e*	0.942(1)	0.495(1)	0.253(1)	1	0.182(25)
a = 5.57519(1) Å, *b* = 5.54088(1) Å, *c* = 7.84754(2) Å *β* = 89.9777(6)° *wRp = 2.5%; Rp = 1.84%*						

Table 3.1. Parameters from the structural refinements of quenched and slow-cooled samples of $LaSrNiRuO_6$.

3.3.2 Comparison of the SXRD Diffraction Peak Profiles of Quenched and Slow-cooled Samples of $LaSrNiRuO_6$

Although the refined crystal structures of the quenched and slow-cooled samples of $LaSrNiRuO_6$ are indistinguishable, a direct comparison of the SXRD data collected from these two samples reveals a difference in the diffraction peak profiles (Fig 3.3). The diffraction peaks from the quenched sample are notably broader than the diffraction peaks from the slow-cooled sample.

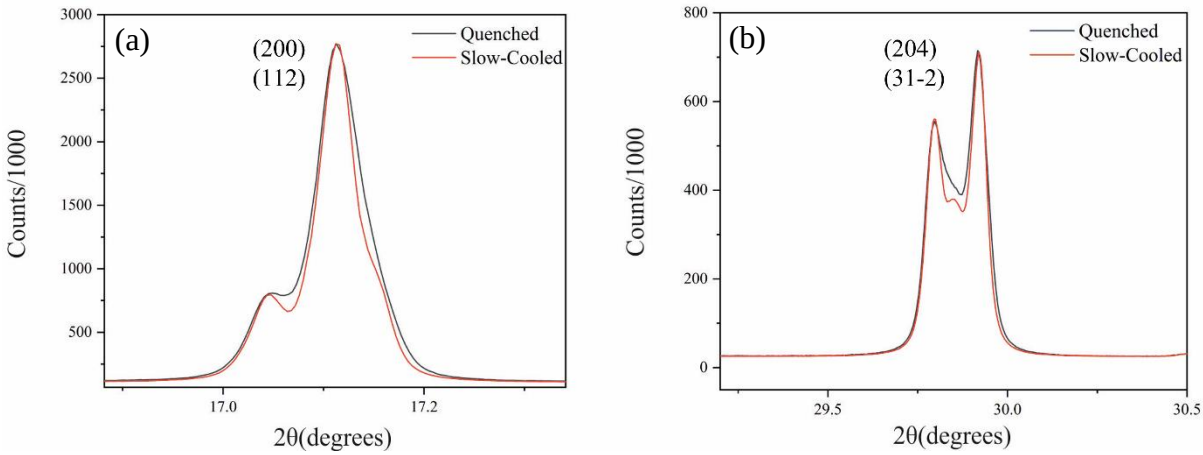


Figure 3.3. Diffraction peaks from selected angles of SXRD data collected from quenched and slow-cooled samples of $LaSrNiRuO_6$ at (a) $2\theta \approx 17.1°$ and (b) $2\theta \approx 29.8°$.

As detailed in Section 2.5.1, both the X-ray diffractometer and the sample contribute to the broadening of diffraction peaks. The instrumental peak broadening contribution from the I11 diffractometer (Section 2.4.1.3) is minimal.[54] Therefore, it is clear that the difference in the broadening of the SXRD diffraction peaks originates from a microstructural difference between the quenched and slow-cooled samples of $LaSrNiRuO_6$. The sample contribution to the broadening of diffraction peaks is primarily the result of its crystalline domain size and/or microstructural strain. As the broadening contribution from the crystalline domain size and microstructural strain have different 2θ dependences, a plot of peak full-width-half-maximum (*fwhm*) against 2θ of the SXRD diffraction peaks enables the contributions from these

parameters to be separated. The SXRD diffraction profiles can be fitted using a pseudo-Voigt function, which allows the *fwhm* of diffraction peaks to be extracted from the SXRD data collected from both quenched and slow-cooled samples of $LaSrNiRuO_6$.

Fig 3.4 shows a plot of peak *fwhm* as a function of 2θ for the SXRD diffraction peaks collected from both quenched and slow-cooled samples of $LaSrNiRuO_6$. As mentioned in Section 2.5.1, the crystalline domain contribution to the broadening of diffraction peaks follows a 1/cos(θ) dependence, while the strain broadening follows a tan(θ) dependence. Thus, these values can be extracted from the plot of peak *fwhm* as a function of 2θ. The extracted values of the average crystalline domain size and microstructural strain from these data show that the quenched sample of $LaSrNiRuO_6$ has smaller crystalline domains with a higher microstructural strain than the slow-cooled sample (Table 3.2).

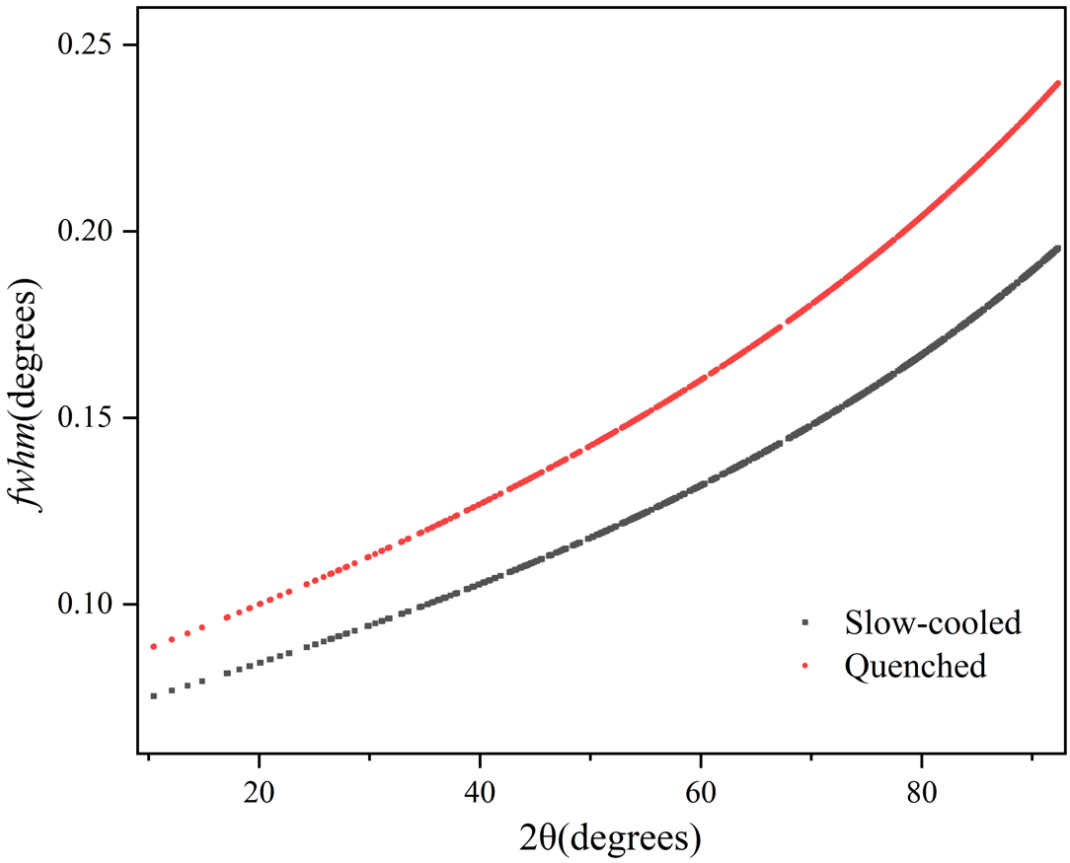


Figure 3.4. A plot of peak *fwhm* against 2θ of SXRD diffraction peaks collected from quenched and slow-cooled samples of $LaSrNiRuO_6$.

	Crystalline domain size (nm)	Strain (°)
Quenched $LaSrNiRuO_6$	113.1(8)	0.0720(6)
Slow-cooled $LaSrNiRuO_6$	133.7(7)	0.0608(4)

Table 3.2. Microstructural parameters extracted from SXRD collected from quenched and slow-cooled samples of $LaSrNiRuO_6$.

3.3.3 Quenching Experiments for $LaSrNiRuO_6$

The formation of small crystalline domains with a high lattice strain that results from the rapid cooling of $LaSrNiRuO_6$ from high temperature seems to be related to a structural phase transition of this compound which occurs at ~ 400 °C. During this structural phase transition, the arrangement of the cooperatively tilted NiO_6/RuO_6 octahedra changes from an $a^-a^-a^-$ tilt in Glazer notation (space group $R\bar{3}$) to an $a^-a^-c^+$ tilt (space group $P2_1/n$) upon cooling.[68] To further probe the connection between the microstructure of $LaSrNiRuO_6$ and this structural phase transition, a series of 'quenching' experiments were conducted. A range of 'quenching' temperatures (350 °C to 600 °C) was selected around the structural phase transition temperature of $LaSrNiRuO_6$. Pellets of $LaSrNiRuO_6$ were heated to 1200 °C (synthesis temperature) and cooled to different 'quenching' temperatures at 5 °C min^{-1}. The samples were kept at the quenching temperatures for 2 hours, they were then quickly quenched into a pre-cooled alumina crucible nested in dry ice. SXRD data were collected from samples of $LaSrNiRuO_6$ with different quenching temperatures. Refinements of a model based on the previously reported $LaSrNiRuO_6$ structure (space group $P2_1/n$)[16] against these diffraction data converged rapidly.

The results from the structural refinement of the $LaSrNiRuO_6$ samples with different quenching temperatures show that all samples are not readily distinguishable. A plot of the observed, calculated and difference plots from the refinement of the $LaSrNiRuO_6$ sample quenched from

425 °C is shown as a representative. The rest of the observed, calculated and difference plots from the structural refinements of $LaSrNiRuO_6$ quenched from different temperatures can be found in Appendix 2.1.

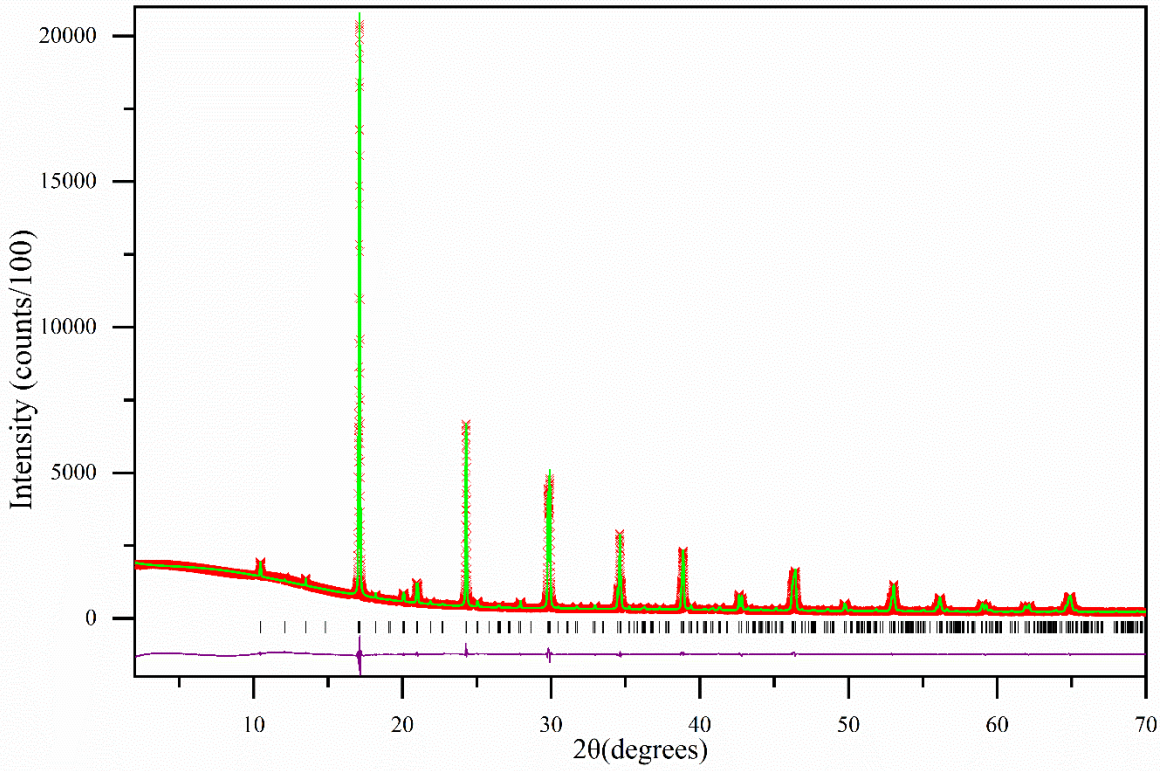


Figure 3.5. The observed, calculated and difference plots from the structural refinement of the $LaSrNiRuO_6$ sample quenched from 425 °C against SXRD data collected at room temperature.

A plot of peak *fwhm* against 2θ of SXRD diffraction peaks collected from samples of $LaSrNiRuO_6$ with different quenching temperatures is shown in Fig 3.6. These data indicate that quenching from 450 °C yields samples with the broadest diffraction peaks. The peak *fwhm* from the SXRD diffraction peaks are biggest when samples of $LaSrNiRuO_6$ are quenched from slightly above the structural phase transition temperature (400 °C), and smaller when the quenching temperature is either much higher, or lower than the phase transition temperature (400 °C). This suggests that the changes in the microstructure of $LaSrNiRuO_6$ correlate to the

quenching temperature, which is attributed to the structural phase transition occurring at ~ 400 °C. This will be further discussed in Section 3.4.1.

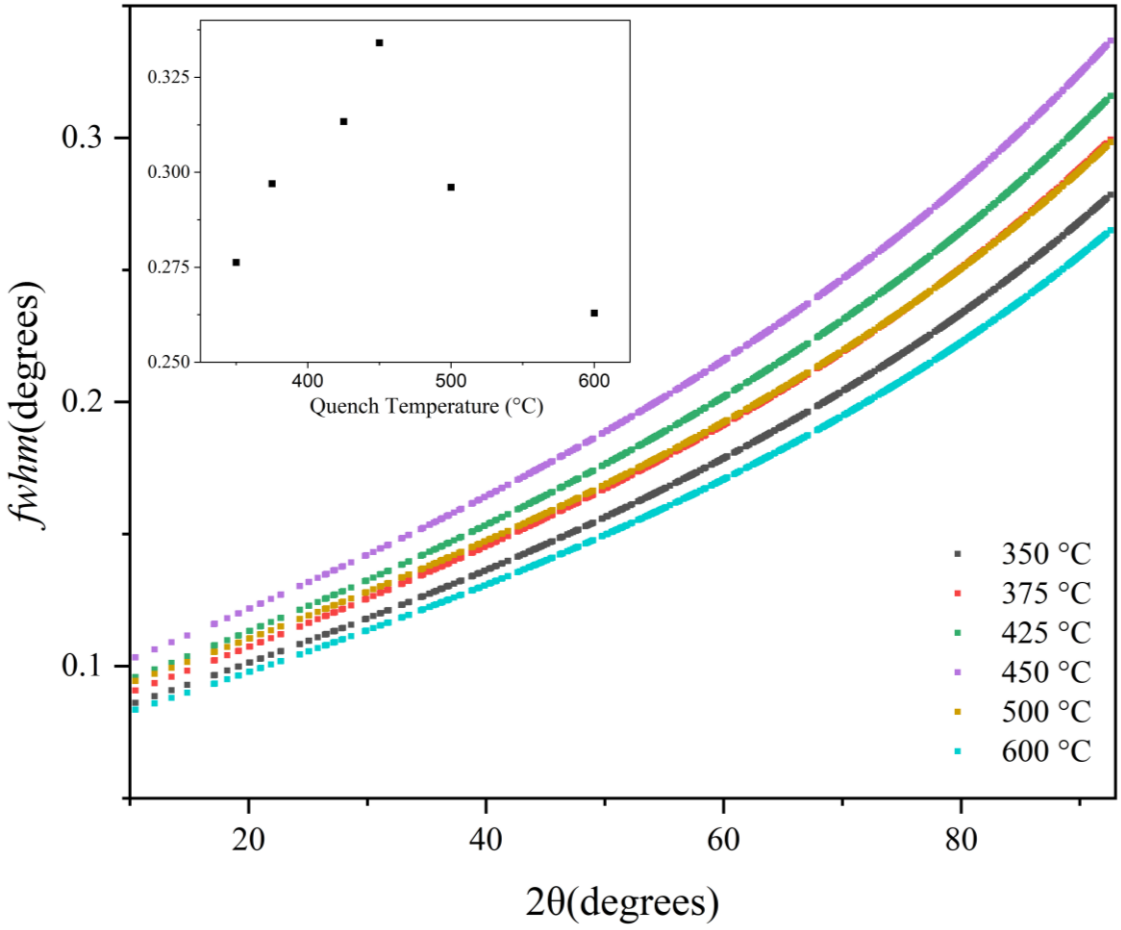


Figure 3.6. A plot of peak *fwhm* of SXRD diffraction peaks against 2θ collected from different quenched samples of $LaSrNiRuO_6$. Inset shows the peak *fwhm* of the diffraction peak at 2θ = 92° as a function of quenching temperature.

3.3.4 Investigating the Phase Transition of Quenched and Slow-cooled Samples of $LaSrNiRuO_6$

Variable temperature synchrotron X-ray diffraction measurements were performed to gain a deeper insight into the effects of quenching and slow-cooling on the structural phase transition of $LaSrNiRuO_6$. SXRD data were collected from both slow-cooled and quenched samples as a function of temperature, as they were heated from 100 °C to 950 °C at 12 °C min^{-1} and then

cooled back to 100 °C at the same rate. Refinement of a model based on the reported high temperature structure of $LaSrNiRuO_6$ (space group *R*-3)[68] against SXRD data collected at 950 °C confirmed a complete structural transformation from the $P2_1/n$ phase to the *R*-3 phase. The observed, calculated and difference plots from the structural refinement of $LaSrNiRuO_6$ (space group *R*-3) against SXRD data collected at 950 °C are shown in Fig 3.7. Full details of the structural parameters obtained from the refinement are given in Table 3.3.

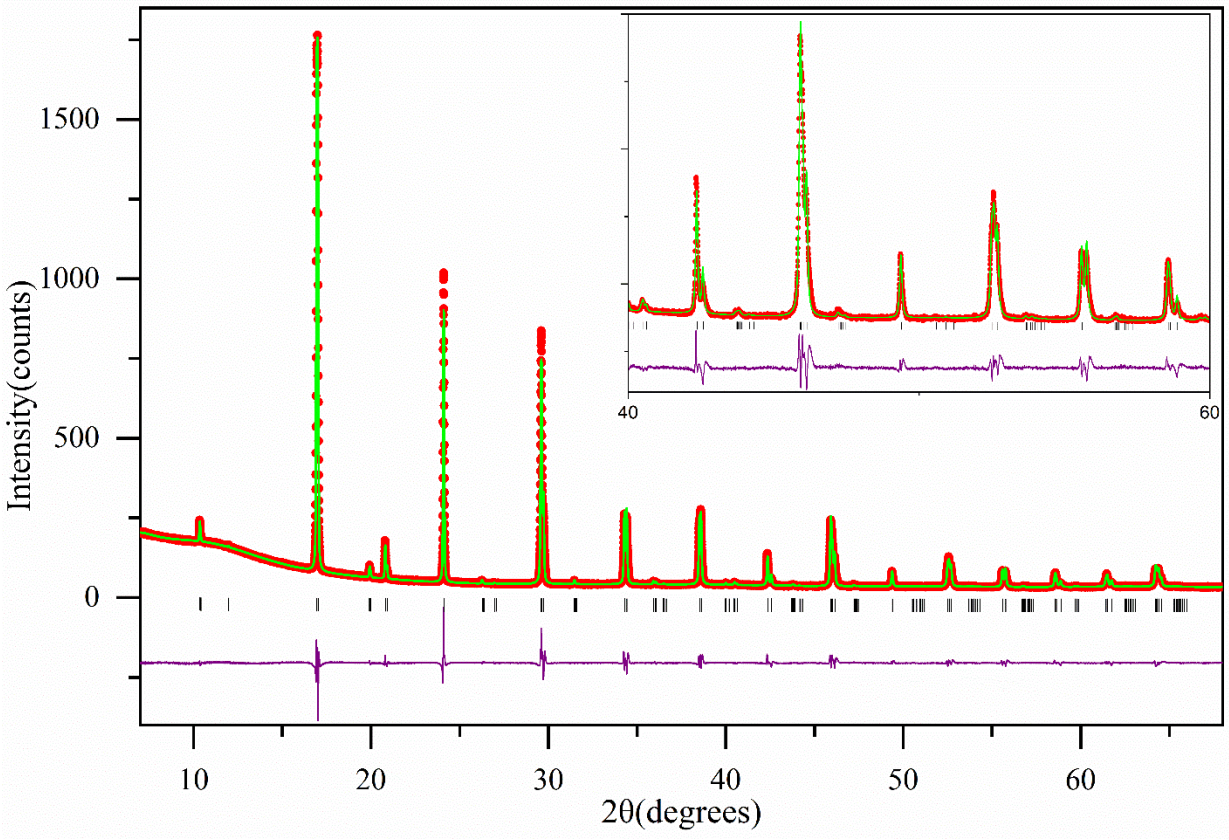


Figure 3.7. Observed, calculated, and difference plots from the refinement of $LaSrNiRuO_6$ with *R*-3 symmetry model against SXRD data collected at 950 °C. Insets show an expanded view of the high angle region.

High temperature phase of quenched $LaSrNiRuO_6$, space group *R*-3 (#148)						
Atom	Wyckoff	*x*	*y*	*z*	Fraction	B_{iso} equiv. (Å^2)
Sr(1)/La(1)	2*c*	0.2487(1)	0.2487(1)	0.2487(1)	$^1/_2/^1/_2$	0.947(20)
Ni(1)/Ru(1)	1*b*	$^1/_2$	$^1/_2$	$^1/_2$	0.920(5)/0.080(5)	0.264(21)
Ru(2)/Ni(2)	1*a*	0	0	0	0.920(5)/0.080(5)	0.264(21)
O(1)	6*f*	0.2904(8)	0.2012(8)	0.7930(10)	1	0.896(55)
a = 5.58788(3) Å, $\alpha = \beta = \gamma$ = 60.2368(3)° *wRp=4.44%; Rp=2.54%*						

Table 3.3. Parameters from the structural refinement of the *R*-3 symmetry model of $LaSrNiRuO_6$ against SXRD data collected at 930 °C.

A direct comparison of the SXRD data collected from the quenched and slow-cooled samples of $LaSrNiRuO_6$ at 100 °C before and after the heating cycle displayed similar peak *fwhm* (Fig 3.8), indicating that the heating cycle did not significantly alter the microstructure of either sample.

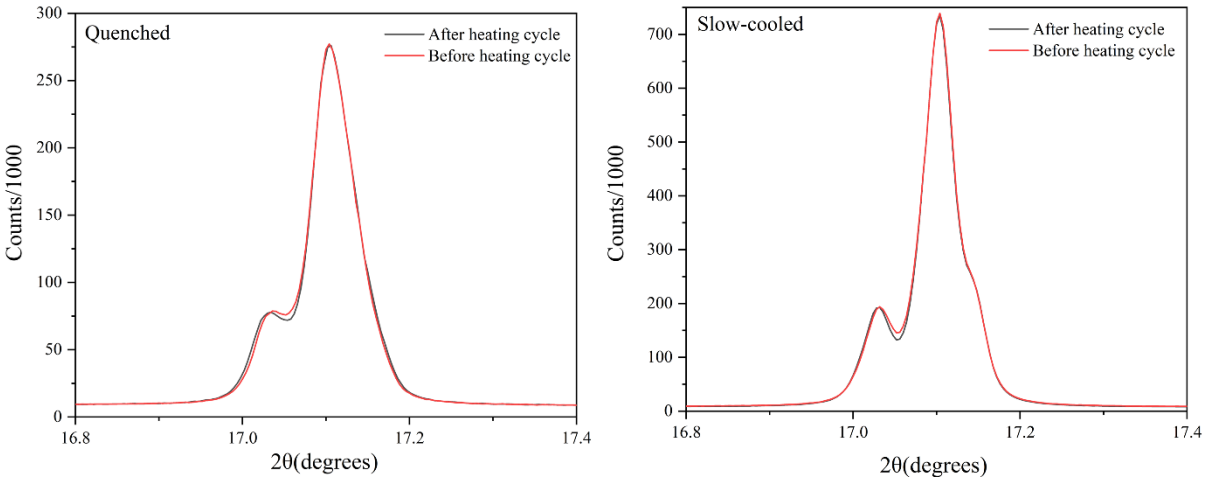


Figure 3.8. Direct peak shape comparison of the quenched and slow-cooled samples of $LaSrNiRuO_6$ before and after the heating cycle at selected angle 2θ ≈ 17.1°.

Both temperature dependent SXRD data sets collected from the quenched and slow-cooled samples of $LaSrNiRuO_6$ were fitted by a 2-phase structural model of $LaSrNiRuO_6$ consisting of phases described in the space group $P2_1/n$ and $R\bar{3}$. The weight fraction of each phase in the sample at a given temperature can then be obtained. The data in Figure 3.9 show the phase transition of both quenched and slow-cooled samples of $LaSrNiRuO_6$ span across a large temperature range in contrast to the sharp structural phase transition temperature reported previously.[68] The broad two-phase region suggests the structural transition from $P2_1/n$ to $R\bar{3}$ is kinetically slow, which will be discussed in Section 3.4.2.

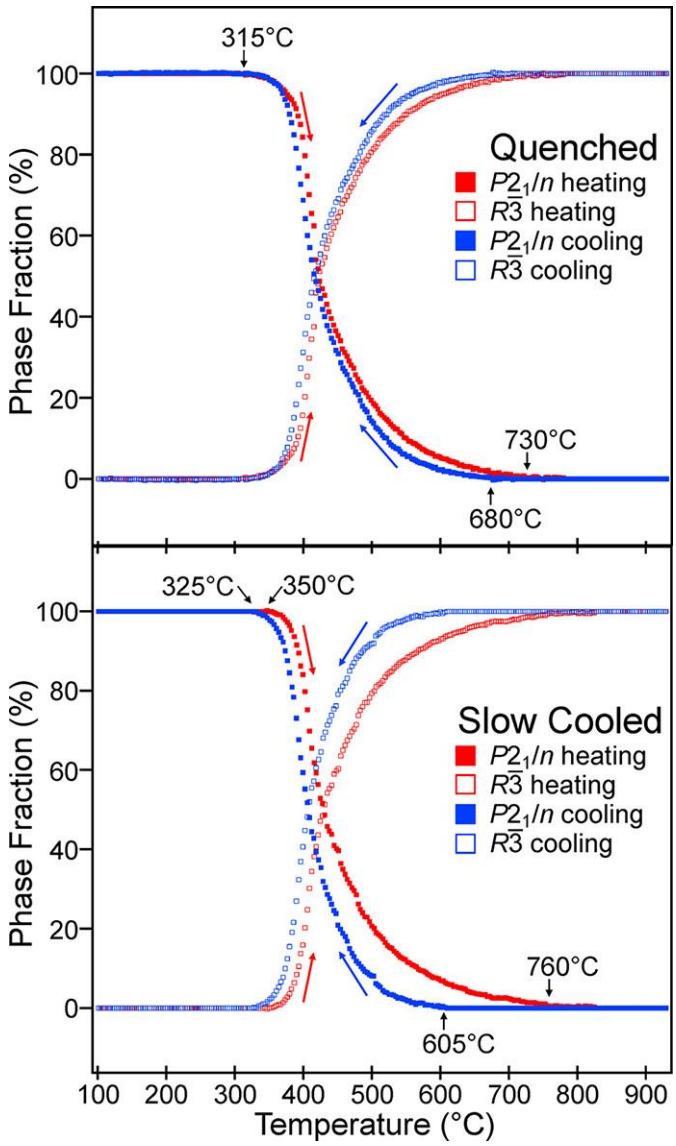


Figure 3.9. Plot of phase fraction against temperature for quenched and slow-cooled samples of $LaSrNiRuO_6$ extracted from the refinement against the SXRD data sets.

3.3.5 $LaSrNiRuO_6$ Samples Annealing at the Reduction Temperature

In order to investigate whether the microstructure of $LaSrNiRuO_6$ is modified during the reduction process with CaH_2, both quenched and slow-cooled samples of $LaSrNiRuO_6$ were annealed at 360 °C (reduction temperature) for 48 hours. Fig 3.10 shows a slight sharpening of the SXRD diffraction peaks from the annealed-quenched sample of $LaSrNiRuO_6$, while the SXRD diffraction peaks from the slow-cooled sample do not change.

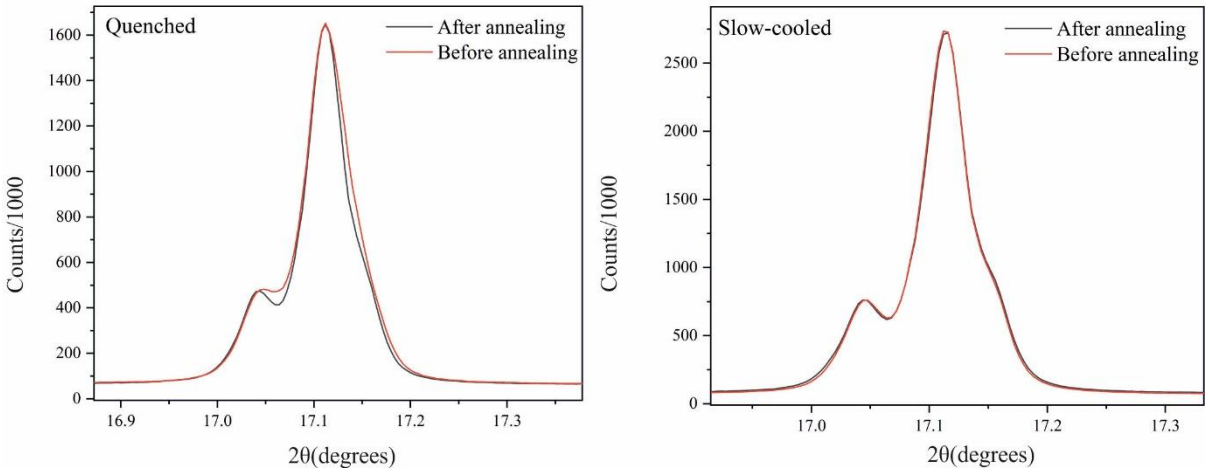


Figure 3.10. SXRD diffraction peaks collected from (a) quenched sample before and after annealing at 360 °C and (b) slow-cooled sample before and after annealing at 360 °C.

Refinement of a model based on the reported structure of $LaSrNiRuO_6$ (space group $P2_1/n$) against the SXRD data collected from the quenched sample of $LaSrNiRuO_6$ after annealing achieved a good statistical fit. It was found that annealed quenched sample of $LaSrNiRuO_6$ had a smaller microstructural strain while the average crystalline domain size remained almost unchanged (Table 3.4). It is hence reasonable to conclude that the sharpening of the diffraction peaks from the annealed quenched sample of $LaSrNiRuO_6$ is due to a relief in the lattice strain with no observable change in the average crystalline domain size.

	Average crystalline domain size (nm)	Strain (°)
Quenched $LaSrNiRuO_6$	113.1(8)	0.0720(6)
Annealed quenched $LaSrNiRuO_6$	119.1(5)	0.0539(4)

Table 3.4. Microstructural parameters extracted from SXRD data collected from quenched sample of $LaSrNiRuO_6$ before and after annealing at 360 °C.

3.3.6 Particle Size Analysis of Quenched and Slow-cooled samples of $LaSrNiRuO_6$

During the process of preparing slow-cooled and quenched samples of $LaSrNiRuO_6$, the size of the particles becomes correlated to the size of the crystalline domains. Throughout the grinding process, a pellet tends to break along the interface of the crystalline domains. As the quenched sample has a smaller average crystalline domain size, the quenched pellet is expected to be ground into a powder with a smaller average particle size. Therefore, to further examine the microstructure of the quenched and slow-cooled samples of $LaSrNiRuO_6$, SEM images were collected from these samples. This analysis shows that the quenched sample of $LaSrNiRuO_6$ has a smaller average particle size 184(3) nm than that of the slow-cooled sample 214(5) (Appendix 2.2). These values are ~50% larger than the average crystalline domain size extracted from the SXRD data (Section 3.3.2), indicating that a particle of $LaSrNiRuO_6$ contains multiple crystalline domains. Moreover, the particle size distribution has shown that the slow-cooled sample of $LaSrNiRuO_6$ has a significant fraction of particles that have diameters greater than 400 nm (~13%), while only < 4% of the particles in the quenched sample have particles with diameters of over 400 nm. The SEM images collected from the quenched and slow-cooled samples of $LaSrNiRuO_6$ clearly show that the quenched sample contains smaller particles than the slow-cooled sample. This is consistent with observation where the

quenched sample of $LaSrNiRuO_6$ has smaller crystalline domains than those from the slow-cooled sample.

3.4 Discussion

3.4.1 The Difference in the Microstructures of the Quenched and Slow-cooled Samples of $LaSrNiRuO_6$

Table 3.1 shows that the crystal structures of the quenched and slow-cooled samples of $LaSrNiRuO_6$ are effectively identical. However, samples of $LaSrNiRuO_6$ that are cooled rapidly exhibit broader diffraction peaks than the slow-cooled samples, which is a result of smaller and more strained crystalline domains. This observation can be explained by the occurrence of a structural phase transition of $LaSrNiRuO_6$ at ~ 400 °C, which involves the conversion from the rhombohedral crystal system (space group *R*-3) to the monoclinic crystal system (space group $P2_1/n$) upon cooling from high temperature. The two structures are shown in Fig 3.11.

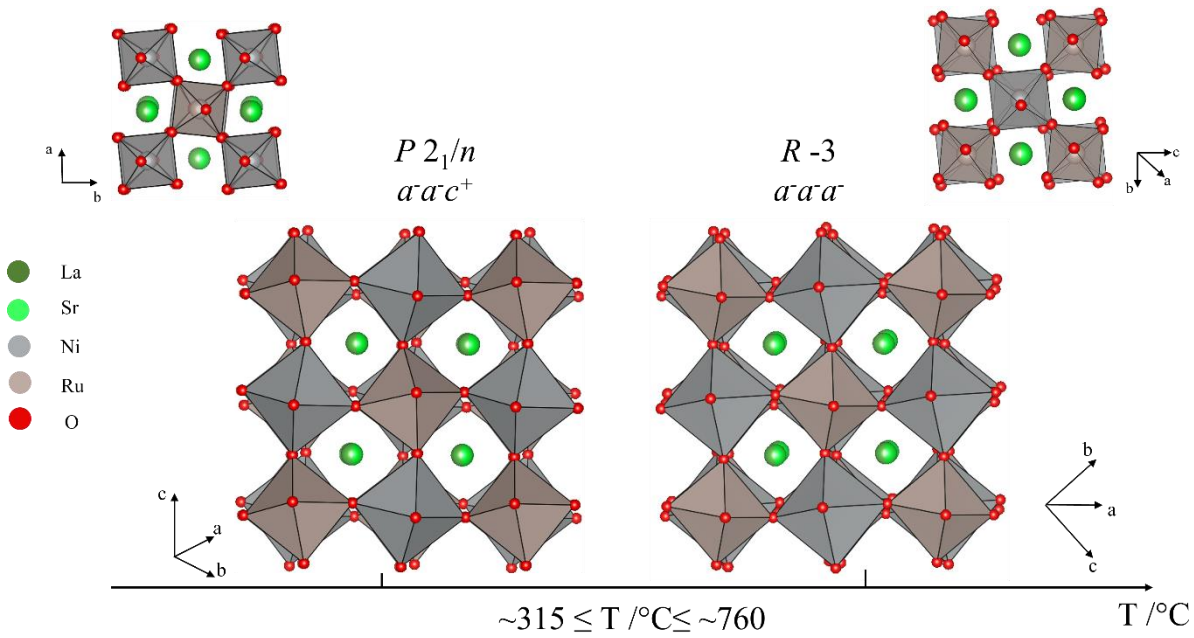


Figure 3.11. The low temperature structure ($P2_1/n$) and the high temperature structure (R-3) of $LaSrNiRuO_6$ viewed along different Cartesian axes.

On cooling from high temperature to room temperature, the arrangement of the cooperatively tilted NiO_6 and RuO_6 octahedra changes from an $a^-a^-a^-$ tilting pattern (space group R-3) to an $a^-a^-c^+$ tilting pattern (space group $P2_1/n$).[69] Thus, during the cooling process, one of the a^- out-of-phase tilts becomes a c^+ in-phase tilt, which can take place along any of the three Cartesian axes: x, y and z. This gives the system three degrees of freedom. Furthermore, the c^+ in-phase tilt can rotate either 'clockwise' or 'anticlockwise'. Combining these two possibilities gives rise to six possible permutations of the relative orientations of the unit cell axes for the newly formed domains of $LaSrNiRuO_6$ (space group $P2_1/n$) in relation to those of the high temperature rhombohedral cell. Therefore, when a sample of $LaSrNiRuO_6$ is cooled from the synthesis temperature (1200 °C), the structural symmetry of the $LaSrNiRuO_6$ framework is lowered. Domains of the monoclinic phase are formed, each with different cell axes orientations. This leads to the formation of small crystalline domains, which then grow to reduce the interfacial surface area between them, and thus lower the free energy of the system. As schematised in Fig 3.12, two steps take place during the cooling process: (1) a structural

phase transition from *R*-3 to $P2_1/n$ which requires a change of the tilting of the octahedra and (2) crystalline domain growth to lower the free energy of the system.

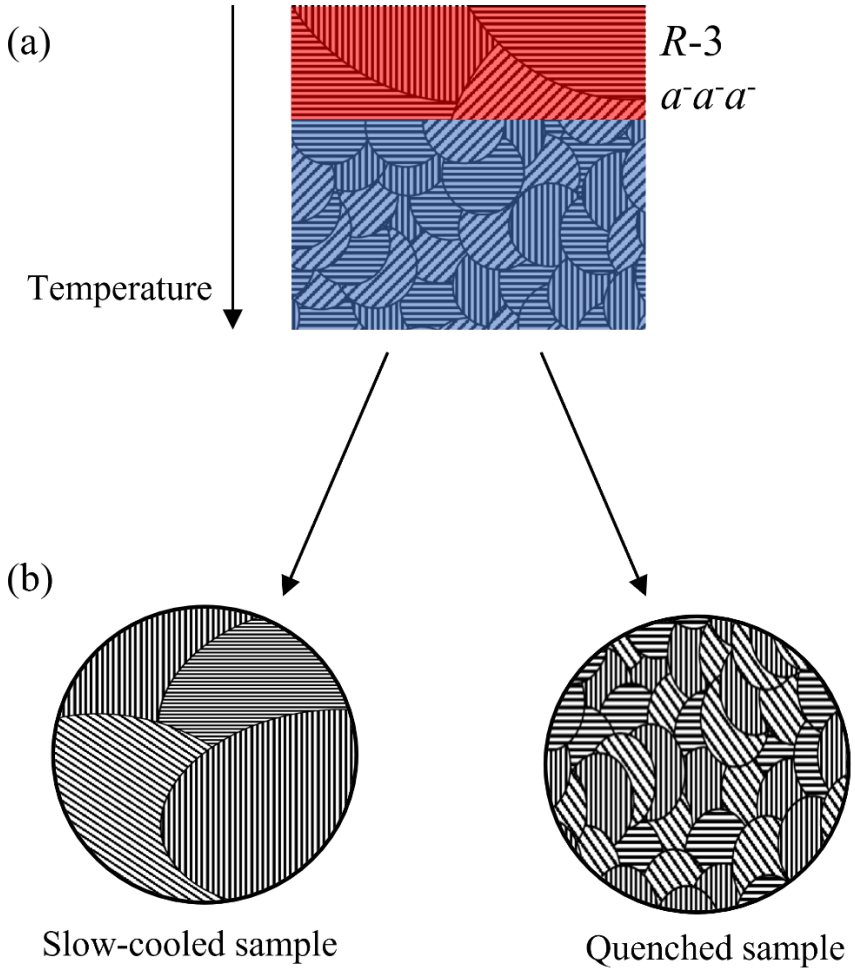


Figure 3.12. Schematic representation of (a) domains evolution during the cooling process of $LaSrNiRuO_6$ below the phase transition temperature and (b) crystalline domains in slow-cooled and quenched $LaSrNiRuO_6$.

However, domain growth requires a reorientation, which has a large activation energy. As a result of this, the rate of domain growth strongly correlates to temperature, becoming essentially zero below a 'freezing temperature'. Therefore, there exists a 'domain growth temperature window', which lies below the structural phase transition temperature and above the domain freezing temperature. Samples which are rapidly cooled from temperatures just above the structural phase transition temperature (quenched samples) do not spend much time

in the domain growth temperature window. Consequently, samples quenched from a temperature just above the phase transition temperature experience little domain growth and therefore have small average crystalline domain sizes. In contrast, samples slowly cooled from the synthesis temperature spend a long time in the domain growth temperature window, which promote a substantial domain growth. Therefore, a slow-cooled sample of $LaSrNiRuO_6$ has a larger average crystalline domain size than a quenched sample.

Moreover, the lattice mismatch at the interface between the high temperature phase of $LaSrNiRuO_6$ (space group *R*-3) and low temperature phase (space group $P2_1/n$) causes a strain within the crystalline domains. Compared to an undistorted perovskite structure with *Pm*-3*m* symmetry, the [111] direction is stretched for the high temperature structure of $LaSrNiRuO_6$ (space group *R*-3), while the [1-10] and [110] directions of the low temperature structure of $LaSrNiRuO_6$ (space group $P2_1/n$) are elongated. The change of the lattice parameters during the structural phase transition affects the aspect ratio for the crystalline domains. The aspect ratio change of a domain will influence that of the neighbouring domains, which causes strain. Therefore, the change of the aspect ratio is hindered vastly when a large number of small domains are present. Consequently, small crystalline domains are under considerable strain.

3.4.2 Structural Phase Transition of $LaSrNiRuO_6$

The *R*-3 to $P2_1/n$ structural phase transition of $LaSrNiRuO_6$ is kinetically slow as it spans a large temperature range (Fig 3.9). A close inspection of the phase transition plots of the quenched and slow-cooled samples of $LaSrNiRuO_6$ shows some differences in the broad two-phase region: The phase transition of the quenched sample of $LaSrNiRuO_6$ begins at 315 °C, while the phase transition of the slow-cooled sample begins at 350 °C. Moreover, the structural transition of the quenched sample of $LaSrNiRuO_6$ finishes earlier than the slow-cooled sample, as indicated in Fig 3.9. The lowering of the onset temperature for the quenched sample of $LaSrNiRuO_6$ suggests that the quenched sample has a lower activation energy barrier associate

with the structural phase transition. This can be accounted for by the higher microstructural strain and/or smaller average domain size of the quenched sample of $LaSrNiRuO_6$.

The broad two-phase region and the large thermal hysteresis in the phase diagram of $LaSrNiRuO_6$ suggest there is a large energy barrier which must be overcome to change the cooperative tilting of the NiO_6/RuO_6 octahedra upon cooling. The effect of the formation of small and strained domains is enhanced due to this kinetically slow phase transition.

3.5 Conclusion

Synchrotron X-ray diffraction was used to study how the microstructure of $LaSrNiRuO_6$ varies with different post-synthesis cooling methods. The quenched and slow-cooled samples of $LaSrNiRuO_6$ have been proven to be chemically identical within experimental error, with the only difference arising in their microstructures.

The difference in the microstructures of the quenched and slow-cooled samples of $LaSrNiRuO_6$ is a consequence of the kinetically slow structural phase transition of the material from the *R*-3 rhombohedral crystal structure to the $P2_1/n$ monoclinic crystal structure upon cooling from the synthesis temperature. The change in the tilting of the NiO_6/RuO_6 octahedra encourages the formation of small crystalline domains upon cooling. The structural phase transition of $LaSrNiRuO_6$ is kinetically slow, and the quenched sample of $LaSrNiRuO_6$ has a smaller energy barrier associated with the structural phase transition compared with the slow-cooled sample. This is attributed to the formation of small crystalline domains/enhanced microstructural strain for the quenched sample of $LaSrNiRuO_6$.

The difference in the microstructures of $LaSrNiRuO_6$ that emerged from different post synthesis cooling methods appeared to affect the reactivity of $LaSrNiRuO_6$ with CaH_2.[70] This will be discussed in Chapter 4.

Chapter 4 Microstructure-Dependent Reactivity of $LaSrNiRuO_6$ in a Topochemical Reduction

4.1 Introduction

Quenched and slow-cooled samples of $LaSrNiRuO_6$, which exhibit different microstructures and different average particle sizes (Chapter 3), were reduced with CaH_2 at 360 °C to yield an infinite layer compound $LaSrNiRuO_4$. During the reduction process, the quenched sample of $LaSrNiRuO_6$ appeared to react much faster than the slow-cooled sample. This observation is consistent with previous work.[37,71] However, this raises a question as to whether the reaction rate difference is related to the microstructure of the sample or just the particle size of the $LaSrNiRuO_6$ starting material.

The 'microstructure' of a material refers to the features of a solid sample that are not explicitly defined by the crystal structure. Typically, this means the defects in a material or the 'texture' of a material (i.e. the size of a single crystalline domain in a material or the degree of microstructural strain). In the following discussion, a specific distinction is made between the 'particle size' of a sample (i.e. how big the powder grains are) and the crystalline domain size of a sample (i.e. the length scale over which the material is a single crystal), as illustrated in Fig 4.1. In general, samples consisting of small particles react much faster than those with large particles, this is because small particles have a larger net surface area and the larger net surface area enables a larger surface contact between reactants ($LaSrNiRuO_6$ and CaH_2). Therefore, the faster reaction rate observed in the reduction of quenched samples of $LaSrNiRuO_6$ could be merely due to the particle size (surface area) effect, rather than the influence of the sample microstructure.

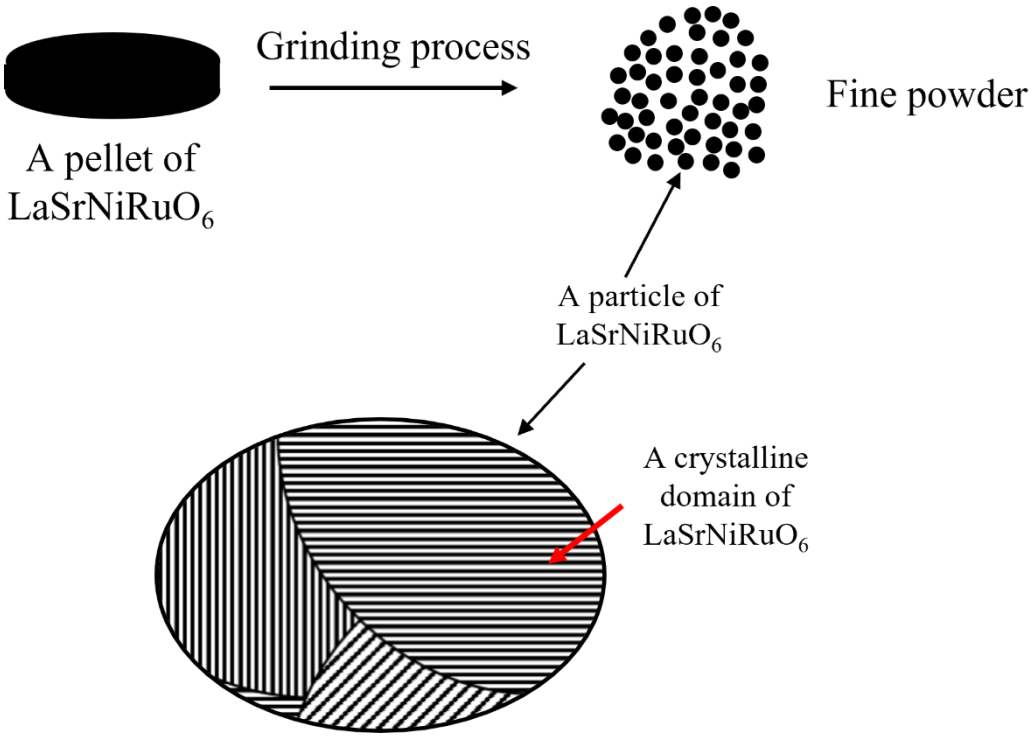


Figure 4.1. Schematic illustration of particle and crystalline domain of $LaSrNiRuO_6$.

In order to find out whether the reactivity of $LaSrNiRuO_6$ is microstructure-dependent or particle size-dependent (surface area), samples of $LaSrNiRuO_6$ with different combinations of microstructure and particle size were prepared so that the effect of the microstructure and particle size on the reactivity of $LaSrNiRuO_6$ with CaH_2 can be separated.

Results from this chapter are published as: Z. Liang, M. Amano Patino, M. Hendrickx, J. Hadermann and M. A. Hayward. Microstructural activation of a topochemical reduction reaction. *ACS Organic & Inorganic Au*, **2** (2022) 75.

4.2 Experimental

4.2.1 Synthesis of Quenched and Slow-cooled Samples of $LaSrNiRuO_6$

A 2 g powdered sample of $LaSrNiRuO_6$ was synthesised as described in Section 3.2.1. X-ray powder diffraction was used to monitor the progress of the reaction. Once the reaction was deemed complete, the powdered sample of $LaSrNiRuO_6$ was then separated into two parts:

Quenched sample of $LaSrNiRuO_6$: 1 g of the powdered sample of $LaSrNiRuO_6$ was pressed into a 13 mm pellet. The pellet was then heated to 1200 °C and kept at this temperature for 12 hours before being cooled to 450 °C at 5 °C min^{-1}. The pellet was held at 450 °C for 2 hours before being rapidly quenched by placing it into a pre-cooled crucible nested in dry ice. The sample was ground thoroughly into a powder and characterised by X-ray powder diffraction.

Slow-cooled sample of $LaSrNiRuO_6$: 1 g of the powdered sample of $LaSrNiRuO_6$ was pressed into a 13 mm pellet. The pellet was then heated to 1200 °C and kept at this temperature for 12 hours before being cooled to room temperature at 2 °C min^{-1}. The pellet was ground thoroughly into a powder and characterised by X-ray powder diffraction.

4.2.2 Topochemical Reduction of $LaSrNiRuO_6$ with CaH_2

Portions of the samples of $LaSrNiRuO_6$ prepared using different post-synthesis cooling methods obtained from Section 4.2.1 were ground with 4 mole equivalents of CaH_2.[37] The reaction mixtures were heated to 360 °C at 1 °C min^{-1} for 4 cycles of 48 hours in a flowing tube furnace with a constant flow of argon (Section 2.2.2). Intermediate grinding was performed between the reaction cycles. The reaction progression was monitored by X-ray powder diffraction. The reaction equation is outlined as follows:

$$LaSrNiRuO_6 + 2\ CaH_2 \xrightarrow[360\ ^\circ C]{\text{Argon flow}} LaSrNiRuO_4 + 2\ CaO + 2\ H_2$$

After the reaction, the resulting mixtures were washed under nitrogen with 5 × 25 ml of 0.1 M solution of NH_4Cl in methanol in order to remove the CaO formed as a by-product and any unreacted CaH_2. This was followed by washing with 5 × 25 ml of clean methanol to dissolve any NH_4Cl residue. The sample was then dried under vacuum.

4.3 Results

4.3.1 Reduction of Quenched and Slow-cooled Samples of $LaSrNiRuO_6$ with CaH_2

X-ray powder diffraction (XRD) data collected from the products of the reaction between CaH_2 and the quenched and slow-cooled samples of $LaSrNiRuO_6$, after a heating period of 48 hours at 360 °C, showed that the products of both reactions were mixtures of pseudocubic $LaSrNiRuO_{6-x}$, pseudotetragonal $LaSrNiRuO_{4+x}$, CaO and unreacted CaH_2 (Fig 4.2). The estimated fraction of the reduced product ($LaSrNiRuO_4$) was calculated from the relative area of the overlapping (020)/(200) and (112)/(-112) sets of reflections of $LaSrNiRuO_4$ with respect to the (020)/(200)/(112)/(11-2) sets of reflections of the $LaSrNiRuO_6$ starting material. The area of the reflections was fitted using the STOE WinXPOW suite of programs. Fig 4.3 shows the estimated fraction of the reduced product ($LaSrNiRuO_4$) plotted as a function of heating cycle (each heating cycle is 48 hours) for the quenched and slow-cooled samples. It is clear that the quenched sample of $LaSrNiRuO_6$ reacted much faster than the slow-cooled sample: After two heating periods of 48 hours at 360 °C, the quenched $LaSrNiRuO_6$ had been almost entirely converted into $LaSrNiRuO_4$, whilst the slow-cooled sample of $LaSrNiRuO_6$ was only partially reduced (50% conversion). This demonstrates that the quenched sample of $LaSrNiRuO_6$ is more reactive than the slow-cooled sample, consistent with previous work.[71]

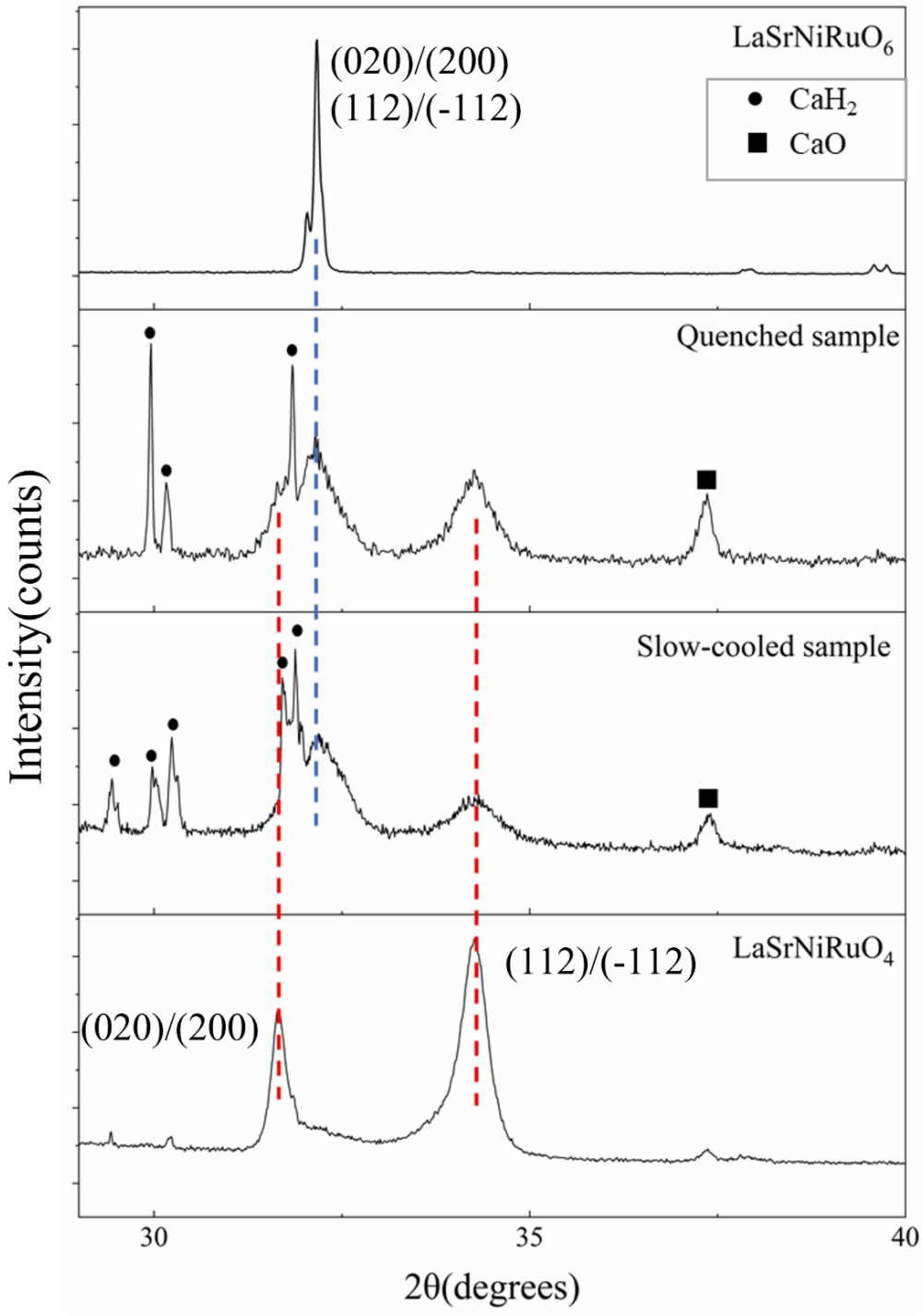


Figure 4.2. X-ray powder diffraction data collected from the products of reaction between CaH_2 and the quenched and slow-cooled samples of $LaSrNiRuO_6$ after 48 hours of heating at 360 °C under flowing argon. Analogous data collected from $LaSrNiRuO_6$ and $LaSrNiRuO_4$ are shown as a comparison.

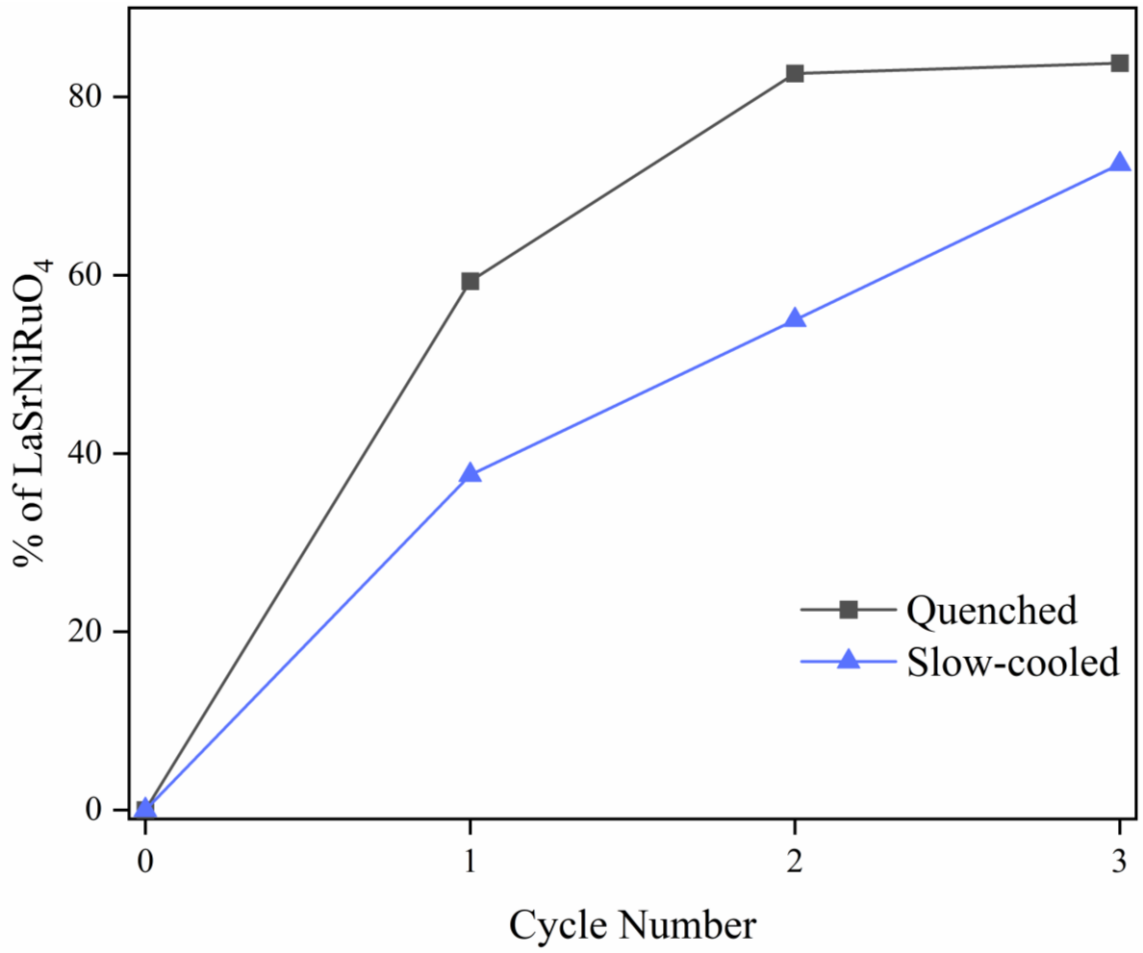


Figure 4.3. Estimated fraction of the reduced phase $LaSrNiRuO_4$ from the reduction of quenched and slow-cooled samples of $LaSrNiRuO_6$ with CaH_2 calculated from the relative area of the main reflections of each phase as a function of heating cycle.

4.3.2 Preparation of $LaSrNiRuO_6$ Samples with Different Combinations of Particle Size and Microstructure

There are two factors that could contribute to the differing rate of reaction between CaH_2 and quenched and slow-cooled samples of $LaSrNiRuO_6$, namely, the particle size and the microstructure of $LaSrNiRuO_6$. Considering the particle size contribution to the reaction rate first, small particles have a net large surface area, the net large surface area increases the surface contact between the reactant ($LaSrNiRuO_6$) and the reducing agent (CaH_2). As a result of this, samples with small particles would be expected to react faster. As discussed in Section 3.3.6,

the quenched sample of $LaSrNiRuO_6$ contains smaller particles than the slow-cooled sample. This could potentially explain the faster rate of reduction observed for the quenched sample of $LaSrNiRuO_6$ than the slow-cooled sample (Section 4.3.1).

The second factor that may contribute to the reaction rate difference is the microstructure of $LaSrNiRuO_6$. As discussed in Chapter 3, a quenched sample of $LaSrNiRuO_6$ contains smaller and more strained crystalline domains than the slow-cooled sample. The microstructural difference between these two samples may also be responsible for the difference in the reactivity of the quenched and slow-cooled samples of $LaSrNiRuO_6$ towards the reduction with CaH_2.

Since quenched samples of $LaSrNiRuO_6$ contain small particles with small/strained crystalline domains and slow-cooled samples of $LaSrNiRuO_6$ contain big particles with larger/less strained crystalline domains, in order to distinguish between the particle size and the microstructure effects on the reactivity of $LaSrNiRuO_6$, samples of $LaSrNiRuO_6$ with small particles but large/less strained crystalline domains, and samples of $LaSrNiRuO_6$ with large particles but small/strained crystalline domains are needed. The particle size of a sample is defined after the first grinding of a pellet, while the microstructure of $LaSrNiRuO_6$ can be re-defined by heating the sample of $LaSrNiRuO_6$ to its synthesis temperature (1200 °C) and controlling the cooling procedure. By using this method, samples of $LaSrNiRuO_6$ with different combinations of particle size and microstructure were prepared, namely, quenched-slow-cooled and slow-cooled-quenched samples.

A quenched-slow-cooled sample was prepared by heating a powdered quenched sample of $LaSrNiRuO_6$, which contains small particles, to 1200 °C and keeping it at this temperature for 12 hours. This sample was then cooled slowly using the method discussed in Section 4.2.1. The slow-cooling process led to the formation of large and less strained crystalline domains

within the small powder grains. No further grinding was performed after the slow-cooling treatment, ensuring the average particle size of this sample remain unchanged. Therefore, the particles in the quenched-slow-cooled sample of $LaSrNiRuO_6$ are small and contain large and less strained crystalline domains.

Similarly, a slow-cooled-quenched sample was prepared by rapidly quenching a powdered slow-cooled sample of $LaSrNiRuO_6$ (which contains large particles). No further grinding was performed after the rapid cooling process, ensuring the average particle size remain unchanged. This process yields a $LaSrNiRuO_6$ sample with a large average particle size, but the particles of this sample contain small, highly strained crystalline domains.

A summary of the particle size and microstructure of quenched, slow-cooled, slow-cooled-quenched and quenched-slow-cooled samples of $LaSrNiRuO_6$ is shown in Fig 4.4. The quenched-slow-cooled and slow-cooled-quenched samples of $LaSrNiRuO_6$ were then reduced with CaH_2 at 360 °C. The reduction of the quenched-slow-cooled and slow-cooled-quenched samples of $LaSrNiRuO_6$ will be discussed in Section 4.3.4.

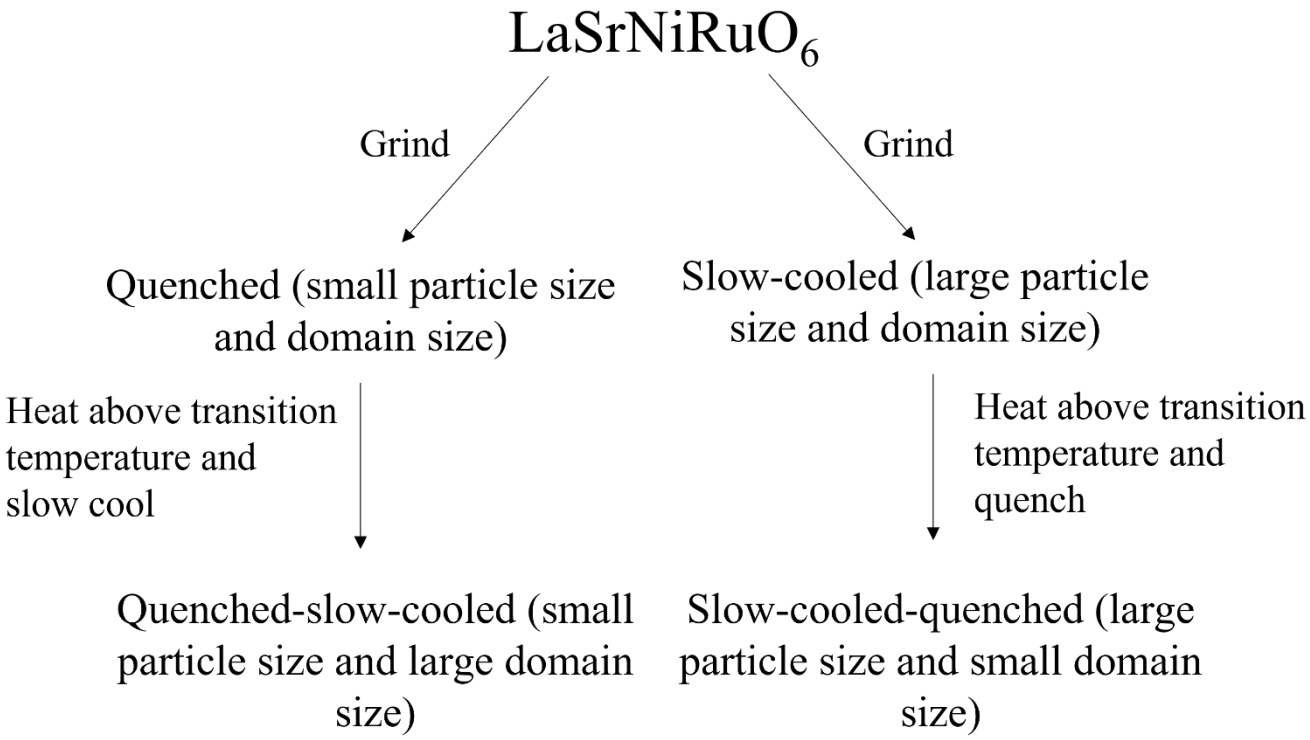


Figure 4.4. A summary of the particle size and microstructure of quenched, slow-cooled, slow-cooled-quenched and quenched-slow-cooled samples of $LaSrNiRuO_6$.

4.3.3 Microstructural Characterisation of Quenched-slow-cooled and Slow-cooled-quenched samples of $LaSrNiRuO_6$

Laboratory X-ray powder diffraction (XRD) data were collected from the slow-cooled-quenched and quenched-slow-cooled samples of $LaSrNiRuO_6$ to identify the microstructures of these compounds. The observed, calculated and difference plots from the structural refinements of the quenched-slow-cooled and the slow-cooled-quenched samples of $LaSrNiRuO_6$ are shown in Fig 4.5.

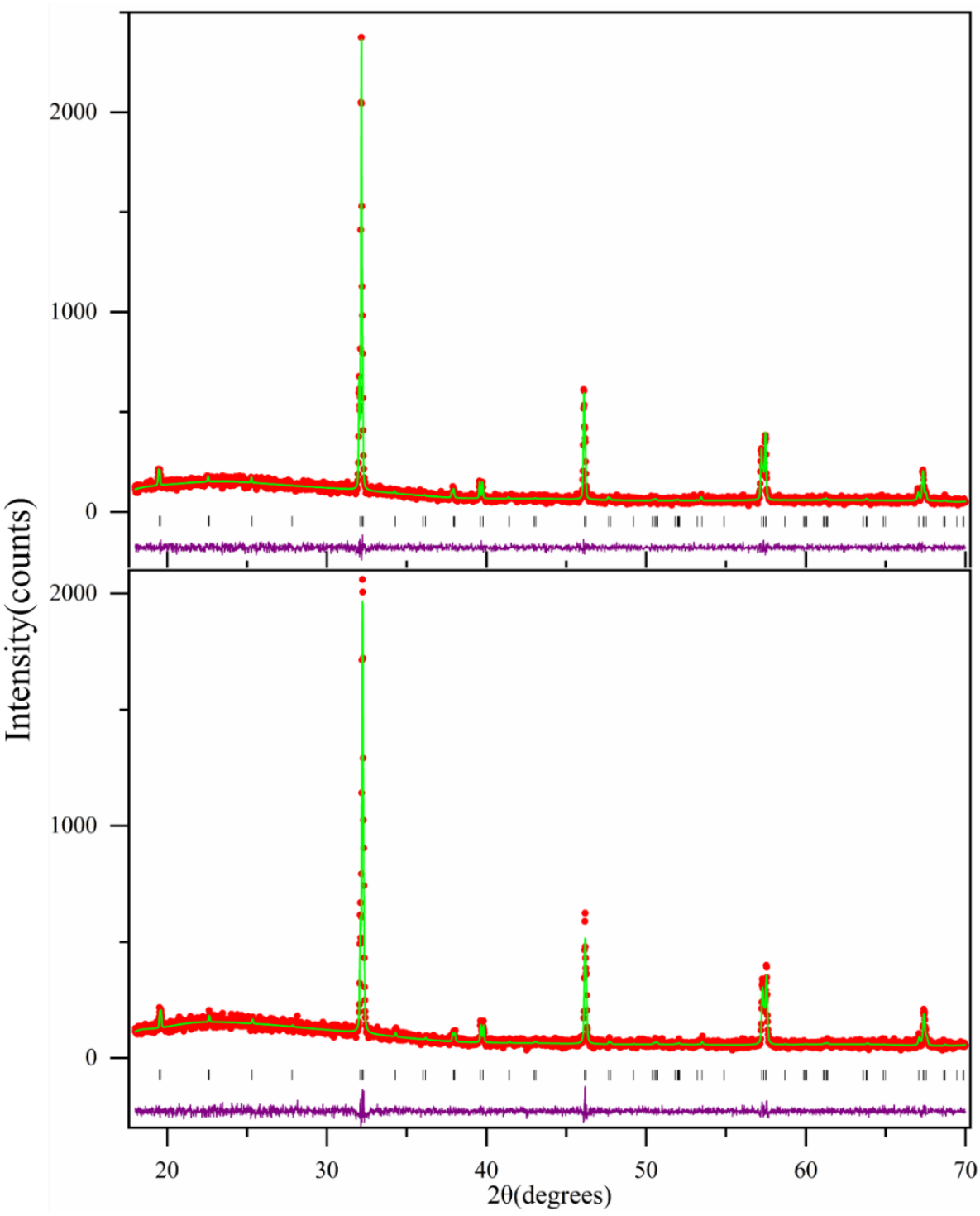


Figure 4.5. Observed, calculated and difference plots from structural refinements of quenched-slow-cooled (top) and slow-cooled-quenched (bottom) samples of $LaSrNiRuO_6$ against XRD data collected at room temperature.

Fig 4.6. shows a plot of peak full-width-half-maximum (*fwhm*) against 2θ of the XRD data collected from the quenched-slow-cooled and slow-cooled-quenched samples of $LaSrNiRuO_6$. The peak *fwhm* extracted from the laboratory XRD data collected from the quenched and slow-cooled samples of $LaSrNiRuO_6$ were also plotted as a function of 2θ as a comparison. The quenched sample and the slow-cooled-quenched sample of $LaSrNiRuO_6$ exhibit broader diffraction peaks than the slow-cooled and quenched-slow-cooled samples throughout the whole 2θ range (Fig 4.6). The extracted average crystalline domain size and the microstructural strain from the laboratory XRD data collected from the quenched, slow-cooled, slow-cooled-quenched and quenched-slow-cooled samples of $LaSrNiRuO_6$ showed that the quenched and slow-cooled-quenched samples of $LaSrNiRuO_6$ have much smaller and more strained crystalline domains compared with those of the slow-cooled and quenched-slow-cooled samples (Table 4.1). These results are in agreement with the proposed microstructures of the samples described in Section 4.3.2.

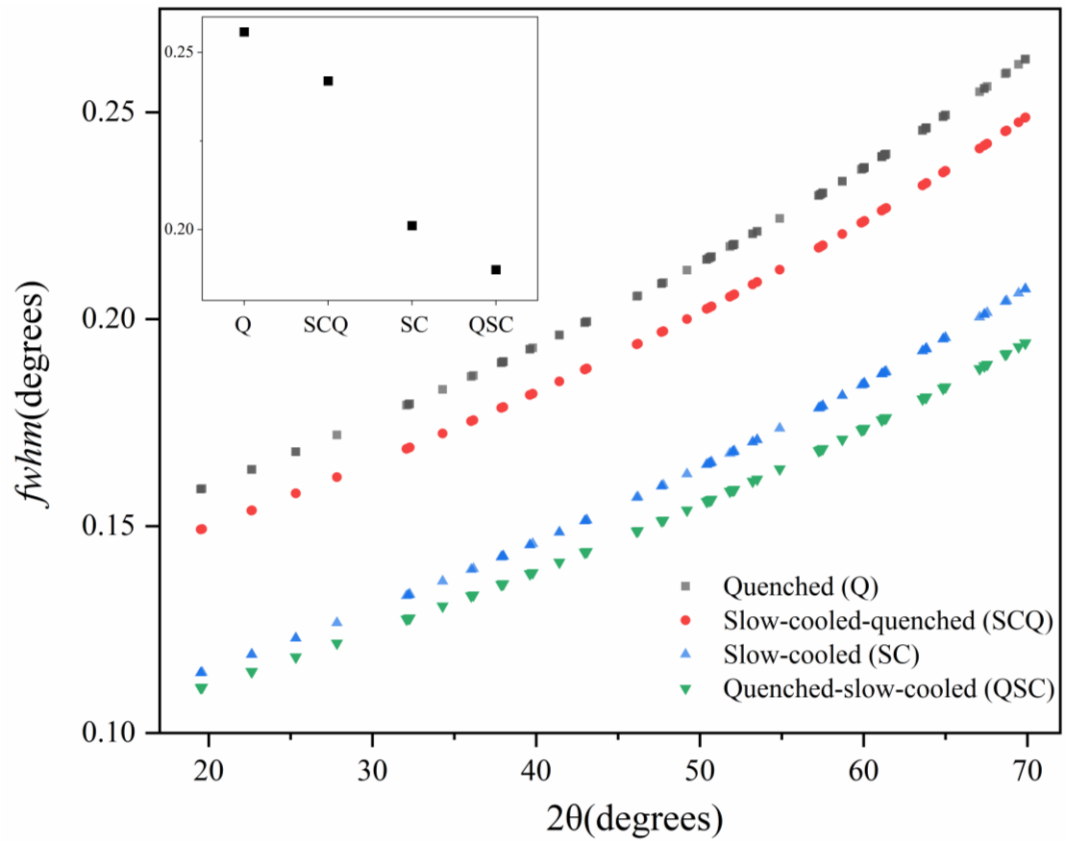


Figure 4.6. Plot of peak *fwhm* against 2θ of XRD data collected from the quenched, slow-cooled, quenched-slow-cooled and slow-cooled-quenched samples of $LaSrNiRuO_6$. Inset shows the peak *fwhm* of XRD diffraction peak at 2θ = 50.4° from four samples.

	Average crystalline domain size (nm)	Microstructural Strain (°)
Quenched	133(13)	0.072(8)
Slow-cooled	199(32)	0.071(9)
Quenched-slow-cooled	197(18)	0.067(5)
Slow-cooled-quenched	143(28)	0.070(2)

Table 4.1. Microstructural parameters extracted from XRD data collected from quenched, slow-cooled, quenched-slow-cooled and slow-cooled-quenched samples of $LaSrNiRuO_6$.

Finally, it is worth noting that the XRD data from the quenched, slow-cooled, slow-cooled-quenched and quenched-slow-cooled samples of $LaSrNiRuO_6$ were collected using the laboratory Panalytical Empyrean diffractometer (Section 2.4.1.1). Therefore, there could be a considerable instrumental contribution to the diffraction peak broadening. The instrumental contribution to the diffraction peak broadening adds to the diffraction peak *fwhm*, making the extracted values of the crystalline domain size and the microstructural strain from the XRD data potentially inaccurate. Therefore, the microstructural parameters extracted from the quenched, slow-cooled, quenched-slow-cooled and slow-cooled-quenched samples of $LaSrNiRuO_6$ were only used as a comparison between these samples.

4.3.4 Reduction of Quenched-slow-cooled and Slow-cooled-quenched Samples of $LaSrNiRuO_6$ with CaH_2

XRD data collected from the products of reaction between CaH_2 and the quenched-slow-cooled and slow-cooled-quenched samples of $LaSrNiRuO_6$, after a heating period of 48 hours at 360 °C, showed that the products of both reactions were mixtures of $LaSrNiRuO_{6-x}$, $LaSrNiRuO_{4+x}$, CaO and unreacted CaH_2 (Fig 4.7). The estimated fractions of the reduced phase ($LaSrNiRuO_4$) for the slow-cooled-quenched and quenched-slow-cooled samples of $LaSrNiRuO_6$ were fitted using the same method discussed Section 4.3.1. The estimated fraction of the reduced phase ($LaSrNiRuO_4$) for the slow-cooled-quenched and quenched-slow-cooled samples of $LaSrNiRuO_6$ is plotted as a function of heating cycles (each heating cycle is 48 hours) and is shown in Fig 4.8. The estimated fraction of the reduced phase ($LaSrNiRuO_4$) for the quenched and slow-cooled samples of $LaSrNiRuO_6$ as a function of heating cycle is also shown as a comparison (Fig 4.8). The reduction reaction with CaH_2 proceeds much faster for the slow-cooled-quenched sample (large particles, small and strained crystalline domains) than the quenched-slow-cooled sample (small particles, large and less strained crystalline domains)

of $LaSrNiRuO_6$, indicating that the particle size of samples does not have a dominant effect on the rate of the reaction. In addition, samples of $LaSrNiRuO_6$ with similar microstructures (e.g. slow-cooled-quenched and quenched samples) exhibit similar reactivity with CaH_2 (Fig 4.8). This observation indicates that the reactivity of $LaSrNiRuO_6$ is dependent on its microstructure.

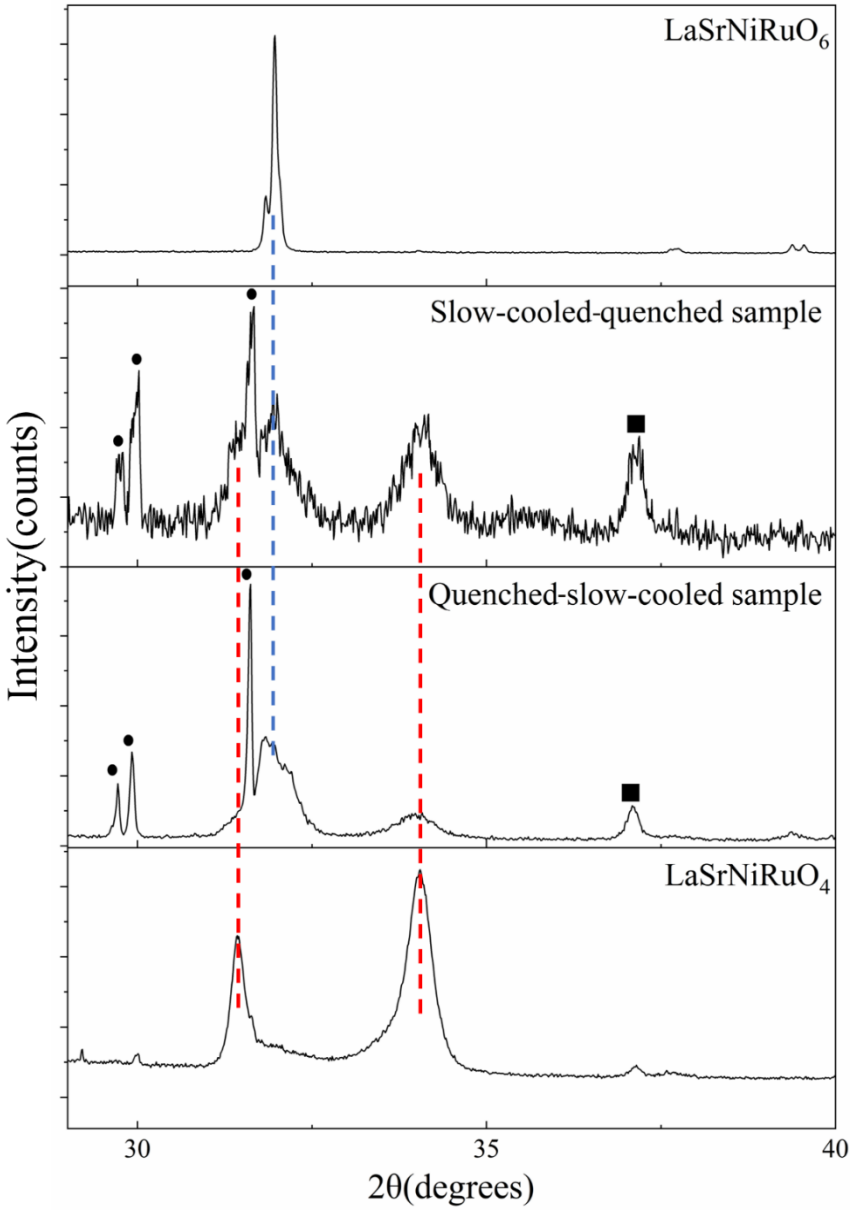


Figure 4.7. XRD data collected from the products of reaction between CaH_2 and slow-cooled-quenched and quenched-slow-cooled samples of $LaSrNiRuO_6$ after 48 hours of heating at 360 °C under flowing argon. Analogous data collected from $LaSrNiRuO_6$ and $LaSrNiRuO_4$ are shown in comparison.

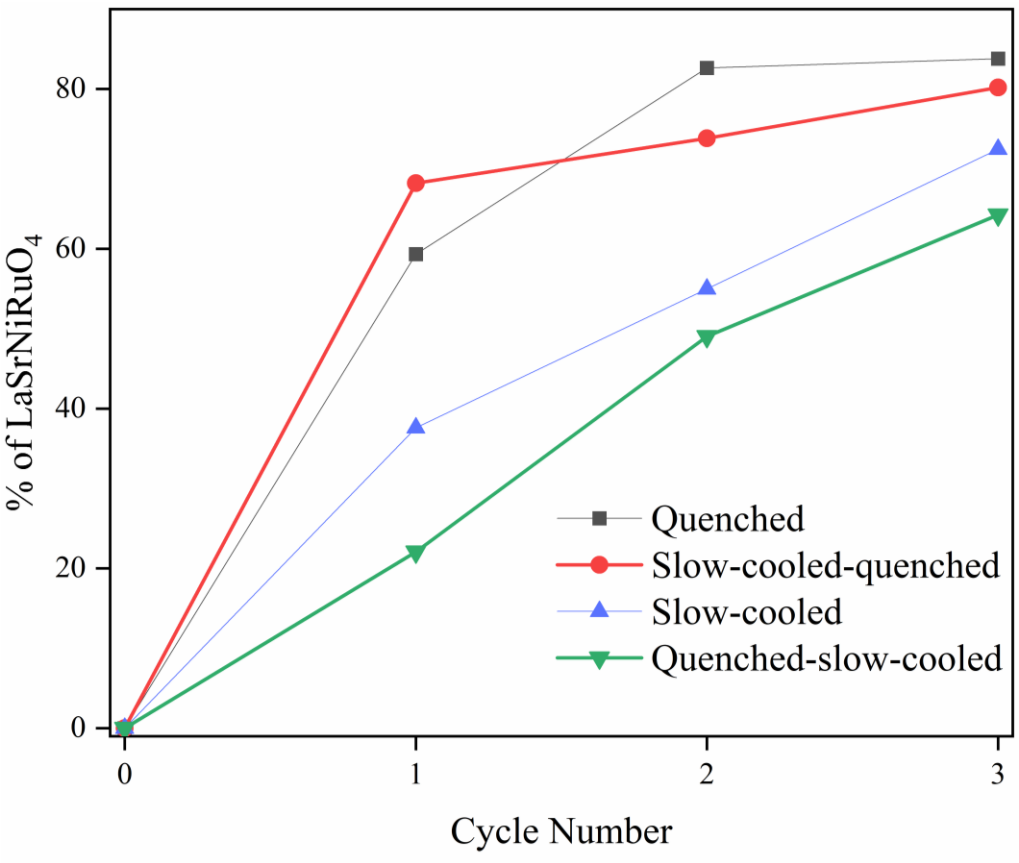


Figure 4.8. Estimated fractions of the reduced phase $LaSrNiRuO_4$ from reduction of quenched-slow-cooled and slow-cooled-quenched samples of $LaSrNiRuO_6$ with CaH_2 calculated from the relative area of the main reflections of each phase.

4.4 Discussion

XRD data collected during the reduction of $LaSrNiRuO_6$ with CaH_2 showed a direct conversion from the pseudo-cubic $LaSrNiRuO_{6-x}$ phase to the pseudo-tetragonal $LaSrNiRuO_{4+x}$ phase, with no evidence of an intermediate phase forming. This indicates that $LaSrNiRuO_6$ and $LaSrNiRuO_4$ are close to being 'line phases', where $LaSrNiRuO_6$ is converted directly into $LaSrNiRuO_4$, without forming an appreciable concentration of compounds with intermediate oxygen stoichiometries. Therefore, as the oxide anions are deintercalated from a domain of $LaSrNiRuO_6$, a layer of $LaSrNiRuO_4$ will form at the domain surface. The formation of $LaSrNiRuO_4$ is separated by a sharp interface from the unreduced $LaSrNiRuO_6$ in the rest of

the crystalline domain (Fig 4.9). The topochemical reduction of $LaSrNiRuO_6$ to $LaSrNiRuO_4$ causes a dramatic lattice parameter change: There is a large contraction along the *c*-axis (~11.9%) and an expansion on the *ab* plane (expansion ~3.3%), this results in a decrease in the cell volume of ~9.1%. As a result, there is a large lattice mismatch between $LaSrNiRuO_6$ and $LaSrNiRuO_4$, which will strain the reaction interface between the unreduced $LaSrNiRuO_6$ and the reduced $LaSrNiRuO_4$ phase. As a domain of $LaSrNiRuO_6$ is reduced to $LaSrNiRuO_4$, the large, energetically unfavourable lattice strain which builds up across the reaction interface opposes the reduction of $LaSrNiRuO_6$ and thus appears to add to the activation energy of the reduction reaction. It is this lattice strain built-up at the reaction interface ($LaSrNiRuO_6$ to $LaSrNiRuO_4$) that leads to the microstructure-dependent reactivity of $LaSrNiRuO_6$.

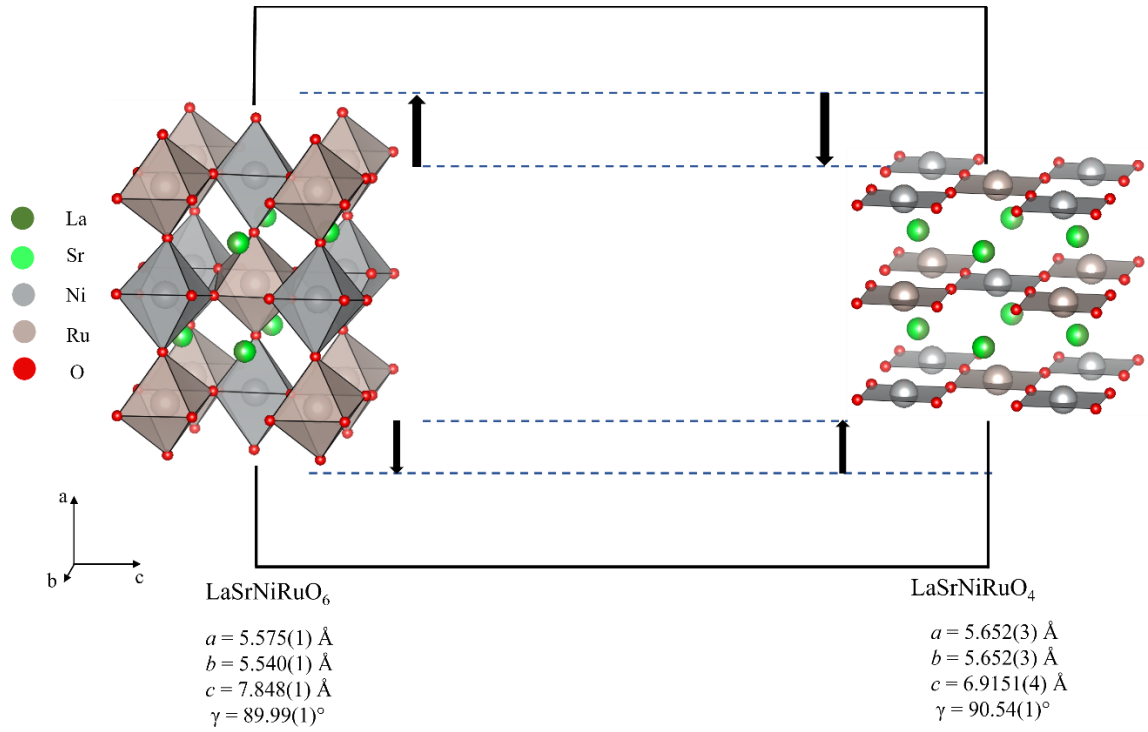


Figure 4.9. Schematic diagram of the interface between $LaSrNiRuO_6$ and $LaSrNiRuO_4$ during the topochemical reduction. Arrows indicate the strain arising from the parameter mismatch at the interface.

Smaller crystalline domains of $LaSrNiRuO_6$ are more flexible than larger crystalline domains due to their enhanced plasticity. Therefore, small crystalline domains can accommodate the reaction-interfacial strain ($LaSrNiRuO_6$ to $LaSrNiRuO_4$) better. As a result, samples of $LaSrNiRuO_6$ with small crystalline domains will have a lower activation energy for the reduction reaction than samples with large crystalline domains (Fig 4.10(a)). Moreover, domains of $LaSrNiRuO_6$ with high microstructural strain are less stable than those with less strain. The destabilisation of $LaSrNiRuO_6$ via microstructural strain pushes up the energy level of the starting material ($LaSrNiRuO_6$), which helps further reduce the activation energy barrier of the reduction reaction (Fig 4.10(b)).

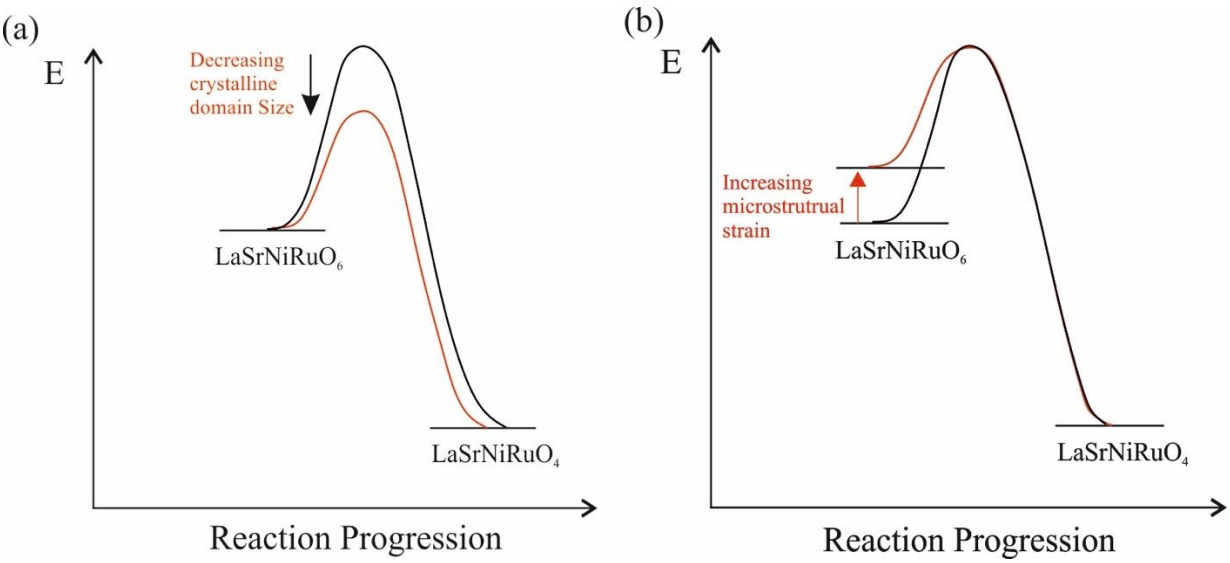


Figure 4.10. A schematic diagram showing the influence of microstructural effects on the activation energy of reduction of $LaSrNiRuO_6$ with CaH_2.

Since the activation energy of the $LaSrNiRuO_6$-to-$LaSrNiRuO_4$ reaction is strongly affected by the microstructure (crystalline domain size and microstructural strain), the activation energy of the reduction of $LaSrNiRuO_6$ with CaH_2 can be separated into two factors. The first factor is the 'intrinsic' activation energy, which is the activation energy associated with the chemical transformation from $LaSrNiRuO_6$ to $LaSrNiRuO_4$; The second factor is a microstructural contribution from the starting material ($LaSrNiRuO_6$), which lowers the activation energy by

the processes described above (Fig 4.10). Any powdered sample of $LaSrNiRuO_6$ contains a population of powder grains with a range of crystalline domain sizes and microstructural strains which lower the activation energy of the reduction with CaH_2 by different amounts. The activation energy of the reaction between CaH_2 and the quenched and slow-cooled samples of $LaSrNiRuO_6$ thereby spans a range of values. The range of the activation energies is dependent on the distribution of crystalline domain sizes and microstructural strains of domains within the samples ($LaSrNiRuO_6$). Fig 4.11 shows a schematic representation of a range of reduction activation energies for a quenched and a slow-cooled sample of $LaSrNiRuO_6$. The quenched sample of $LaSrNiRuO_6$ has a smaller average reduction activation energy due to its smaller average crystalline domain size and higher microstructural strain. Thus, the reaction between CaH_2 and the quenched sample of $LaSrNiRuO_6$ proceeds much faster.

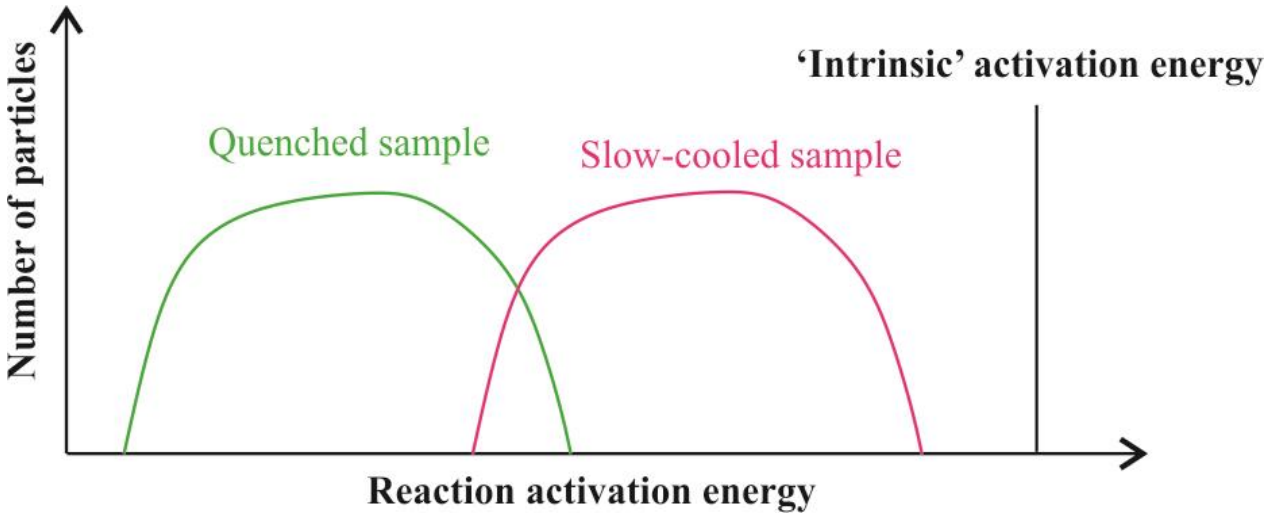


Figure 4.11. A schematic diagram showing how the influence of microstructural effects on the activation energy of the reduction of $LaSrNiRuO_6$ with CaH_2 can lead to the observed differences in the reactivity of quenched and slow-cooled samples of $LaSrNiRuO_6$.

Similar observations have been reported before: For example, the reduction of a sample of $BaTiO_3$ with a large average particle size leads to the formation of $BaTiO_{3-x}H_y$ with a distribution of hydride content, while a sample of $BaTiO_3$ with small average particle size can

be reduced homogeneously.[72] In addition, a large strain build-up during the intercalation-deintercalation process affects the rate of conversion in olivine-based Li-ion secondary battery cathodes.[73] These studies support the idea that the microstructure and particle size of a sample play an important role in affecting the reactivity of a starting material in a topochemical reaction.

4.5 Conclusion

Different reaction rates were observed for the reduction of the quenched and slow-cooled samples of $LaSrNiRuO_6$ with CaH_2. The difference in the reactivity is attributed to the differing microstructure of the samples, rather than the particle size difference. The microstructure-dependent reactivity is attributed to a strain built up at the reaction interface as a result of a direct conversion from $LaSrNiRuO_6$ to $LaSrNiRuO_4$. Samples of $LaSrNiRuO_6$ with smaller crystalline domains can better accommodate strain at the reaction interface ($LaSrNiRuO_6$-$LaSrNiRuO_4$) due to their enhanced plasticity, which reduce the activation energy barrier for the reduction reaction. In addition to this, the microstructural strain in $LaSrNiRuO_6$ also acts to destabilise the starting material, and further reduce the activation energy barrier.

The reactivity of $LaSrNiRuO_6$ correlates to its microstructure, where samples of $LaSrNiRuO_6$ are more reactive when small and strained crystalline domains are yielded. In addition to the 'quenching' method, the ball-milling method is also potentially a good technique to 'activate' a starting material by yielding samples with small and strained crystalline domains. More solid-state compounds could potentially be activated using this method, which enables a wider range of solid phases to be explored.

Chapter 5 Topochemical Reduction of $LaSrCoRuO_6$

5.1 Introduction

As discussed in Chapter 1, in order to widen the scope of solid-state chemistry, topochemical reduction via anion deintercalation/exchange has been used to prepare a wide range of novel compounds that are kinetically but not thermodynamically stable.[25,26,28,29,74] This type of compound contains transition metal centres in unusual oxidation states and coordination geometries, which could potentially exhibit interesting magnetic and physical properties. Building on previous work, the topochemical reduction of the B-site cation ordered double perovskite $LaSrCoRuO_6$ was explored.

Previous attempts to reduce $LaSrCoRuO_6$ with various reducing agents were unsuccessful, no novel reduced phase was obtained.[75] It is likely that the unsuccessful reductions of $LaSrCoRuO_6$ are related to its microstructure: As discussed in Chapter 3 and Chapter 4, rapidly quenching the double perovskite oxide $LaSrNiRuO_6$ through a phase transition (*R*-3 to $P2_1/n$) which occurs at ~ 400 °C significantly enhanced the reactivity of this material towards the reduction with CaH_2.[70] Fortunately, $LaSrCoRuO_6$ undergoes an analogous structural phase transition from the rhombohedral crystal system (space group *R*-3) to the monoclinic crystal system (space group $P2_1/n$) at ~ 450 °C. Therefore, rapidly quenching samples of $LaSrCoRuO_6$ through this phase transition also enhances its reactivity. This process enables the preparation of two novel oxygen deficient phases derived from $LaSrCoRuO_6$ via reactions with Zr and LiH. In this chapter, the reduction pathways of $LaSrCoRuO_6$ with LiH and Zr powder as reducing agents will be discussed. The differences between these two reducing agents will also be highlighted.

5.2 Experimental

5.2.1 Synthesis of $LaSrCoRuO_6$

Powdered samples of $LaSrCoRuO_6$ were prepared via a citrate gel method. A suitable stoichiometric ratio of dried La_2O_3, $SrCO_3$, Co, RuO_2 (from hydrated RuO_2, dried at 800 °C) was measured, ground thoroughly and dissolved in a minimum quantity of water and 6 M nitric acid at a 1:1 ratio. Then, 3 mole equivalents of citric acid monohydrate and 2 ml of ethylene glycol were added to the reaction mixture. The solution was heated to 200 °C and kept at this temperature with constant stirring. The solution became viscous and set into a gel, which then pyrolyzed. The resulting powder was ground into a fine powder, transferred into an alumina crucible and heated to 900 °C at 5 °C min^{-1} in air. The powder was kept at 900 °C for 12 hours. The powder was then reground, pressed into 13 mm pellets, and heated to 1200 °C in air at 1 °C min^{-1} for two cycles of 48 hours. During the final cycle, the pellets were cooled to 450 °C at 5 °C min^{-1} and were subsequently quenched by quickly transferring them into a pre-cooled crucible nested in dry ice. The sample was ground thoroughly and characterised by X-ray powder diffraction.

5.2.2 Initial Investigation of Reactivity of $LaSrCoRuO_6$ with Zr

A series of small-scale test reactions was performed in which 200 mg of $LaSrCoRuO_6$ was placed in a glass ‘thimble’ and sealed in an evacuated silica ampoule along with 2 mole equivalents of Zr powder (Section 2.2.4). The reaction mixtures were heated to temperatures ranging from 400 °C to 530 °C at 1 °C min^{-1}. X-ray powder diffraction was used to monitor the reaction progression.

5.2.3 Initial Investigation of Reactivity of $LaSrCoRuO_6$ with LiH under Flowing Argon

A series of small-scale test reactions was performed by grinding 200 mg of $LaSrCoRuO_6$ with 8 mole equivalents of LiH in an argon-filled glove box. The resulting mixture was heated between 330 °C ≤ T ≤ 380 °C under a constant flow of argon using a flowing tube furnace set-up (Section 2.2.2). X-ray powder diffraction was used to monitor the reaction progression. Once the reactions were deemed complete, the reaction mixtures were washed with methanol under nitrogen to remove the by-product Li_2O and unreacted LiH. The samples were then dried under vacuum.

5.3 Results

5.3.1 Initial Investigation of Reactivity of $LaSrCoRuO_6$ with Zr

The changes observed in the X-ray powder diffraction (XRD) data collected during the reduction of $LaSrCoRuO_6$ with Zr at different reaction temperatures are summarised in Table 5.1. The symmetry of the main phase observed in XRD data was lowered from pseudocubic to pseudotetragonal once the deintercalation of oxide anions started. Two distinct oxygen deficient phases, assigned as $LaSrCoRuO_5$ and $LaSrCoRuO_4$, were observed during the reduction of $LaSrCoRuO_6$ with Zr before the non-topochemical decomposition took place at 530 °C.

Temperature(°C)	Chemical composition	Lattice parameter(Å)	Observation
Starting material	$LaSrCoRuO_6$	a = 5.5847 b = 5.5592 c = 7.8674	Sharp (200)/(020) and (112)/(11-2) sets of diffraction peaks, crystalline sample

400	$LaSrCoRuO_6$	a = 5.58 b = 5.56 c = 7.87	Visible broadening of all peaks, slight splitting of (200)/(020) and (112)/(11-2) sets of reflections
450	$LaSrCoRuO_5$	a = 5.38 b = 5.39 c = 8.13	Complete splitting of (200)/(020) and (112)/(1-12) sets of reflections
470	$LaSrCoRuO_5$, $LaSrCoRuO_4$	N/A	Complete splitting of (200)/(020) and (112)/(1-12) sets of reflections accompanied by the formation of a secondary reduced phase. Partial decomposition was also observed.
530	La_2O_3, SrO, Co, Ru	N/A	Decomposition

Table 5.1. Results from initial investigation from topochemical reduction of $LaSrCoRuO_6$ with Zr.

The first distinct reduced phase observed at 450 °C is assigned as $LaSrCoRuO_5$, which can be indexed using a body centred monoclinic unit cell with a slight contraction of the *a* and *b* lattice parameters and an elongation of the *c* lattice parameter compared to its parent $LaSrCoRuO_6$ phase. The two sets of reflections (112)/(11-2) and (200)/(020) of the starting material ($LaSrCoRuO_6$) at ~32° clearly split into two distinct peaks upon reduction with Zr at 450 °C (Fig 5.1). The phase composition was determined by an oxidative thermogravimetric analysis

(TGA), which showed a mass gain of one oxygen per formula unit (described in detail in Chapter 6). XRD data collected from the product after the TGA experiment confirmed a complete re-oxidation of the reduced phase ($LaSrCoRuO_5$) back to the starting material $LaSrCoRuO_6$.

The reaction temperature was then raised to 470 °C to investigate whether a further reduction of $LaSrCoRuO_6$ with Zr would occur. Close inspection of the XRD data collected after a heating cycle of 48 hours at 470 °C showed the initial formation of a second topochemically reduced phase. The (112) reflection of the second phase appeared at a higher angle, corresponding to a large contraction of the *c* lattice parameter. This observation suggests that the oxide anions are removed along the *c* direction. The position of the (200) reflection was shifted to a lower angle, indicating an elongation of both *a* and *b* lattice parameters. The second topochemical reduced phase can be indexed using a tetragonal cell with lattice parameters: $a = 5.66$ Å, $c = 6.88$ Å. The indexed lattice parameters of the second reduced phase are similar to those of $LaSrNiRuO_4$, which adopts an infinite-layer structure.[37] Therefore, it is likely that the second topochemical reduced phase is $LaSrCoRuO_{4+x}$, where all oxide anions are de-intercalated along the [001] direction. However, the formation of $LaSrCoRuO_{4+x}$ was accompanied by the appearance of La_2O_3 (Fig 5.1). Continuing the heating cycles in an attempt to form a single $LaSrCoRuO_4$ phase led to non-topochemical decomposition. Therefore, $LaSrCoRuO_5$ appears to be the most reduced phase which can be prepared when reducing $LaSrCoRuO_6$ with Zr powder. This attempt has demonstrated that $LaSrCoRuO_4$ cannot be attained at high reaction temperature, indicating that it is more metastable compared with $LaSrCoRuO_5$.

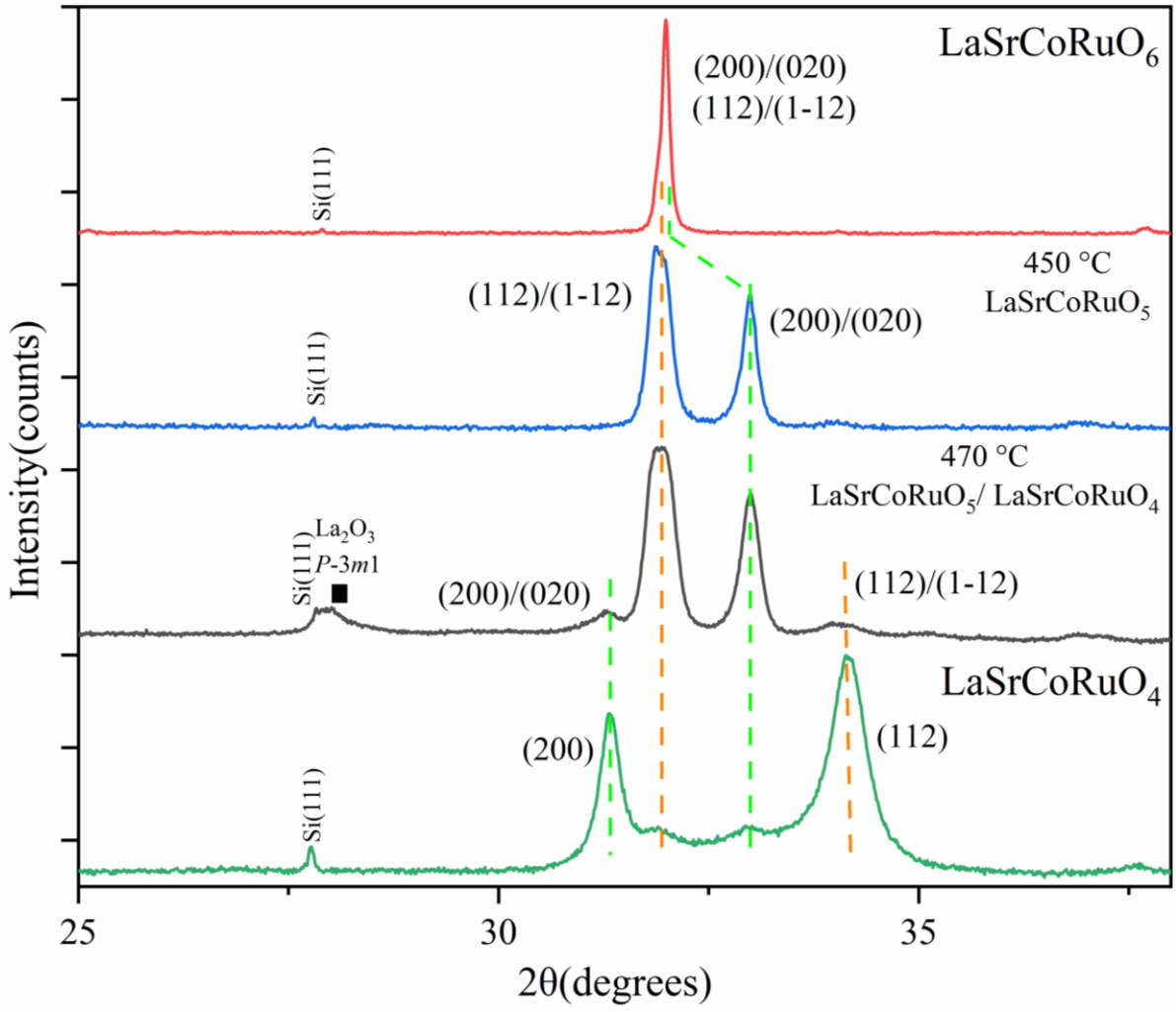


Figure 5.1. Topochemical reduction profile of $LaSrCoRuO_6$ with Zr at different temperatures to form two compositions of $LaSrCoRuO_{6-x}$. The lower part of the diagram shows X-ray diffraction data from $LaSrCoRuO_4$ synthesised via reduction with LiH.

5.3.2 Initial Investigation of Reactivity of $LaSrCoRuO_6$ with LiH under Flowing Argon

As LiH is a more powerful reducing agent than Zr powder, the reduction of $LaSrCoRuO_6$ was then trialled with LiH in an attempt to extract a pure phase of $LaSrCoRuO_4$. As discussed in Chapter 2, the accumulation of H_2 gas formed as a by-product during the reaction with LiH in a sealed reaction vessel may lead to the formation of oxyhydride phases. Therefore, a flowing tube experimental set-up, as described in Section 2.2.2, was used with a constant flow of argon.

The constant argon flow purges the build-up of H_2 gas formed by LiH in the system. This experimental set-up maintains a low partial pressure of H_2 gas within the reaction vessel, so that the formation of an oxygen deficient phase is preferred. A mixture of two distinct phases, namely $LaSrCoRuO_5$ and $LaSrCoRuO_4$, was observed between the reaction temperatures 335 °C to 380 °C. The $LaSrCoRuO_6$ starting material can be reduced with LiH to form $LaSrCoRuO_5$ at a much lower reaction temperature range (335 °C to 360 °C) compared with the reduction with Zr (450 °C). The reaction temperature was then raised to 375 °C, where a majority of $LaSrCoRuO_5$ was converted to $LaSrCoRuO_4$. After three heating periods of 48 hours at 375 °C, $LaSrCoRuO_4$ had become the majority reduced phase. This observation suggests the reduction of $LaSrCoRuO_6$ to $LaSrCoRuO_4$ proceeds through the intermediate phase $LaSrCoRuO_5$.

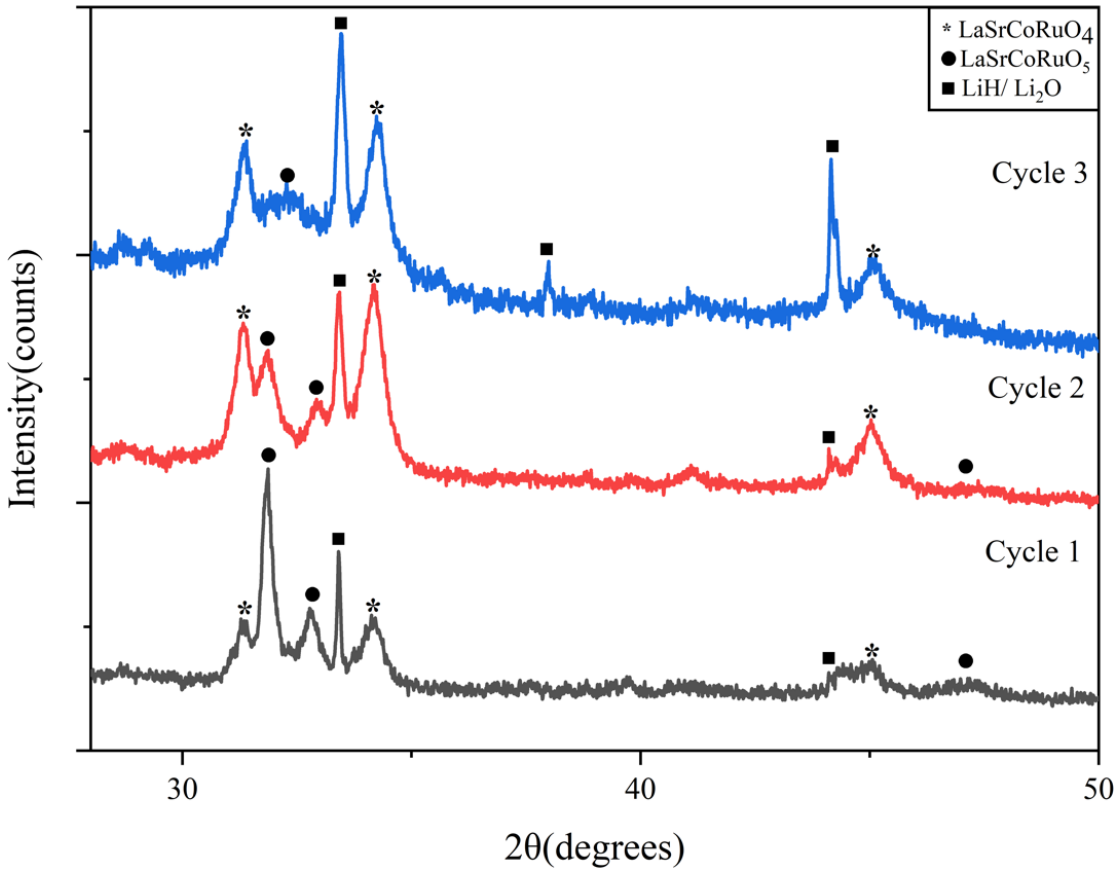


Figure 5.2. Topochemical reduction progression of $LaSrCoRuO_6$ with LiH to form two compositions of $LaSrCoRuO_{6-x}$.

However, the reduction of $LaSrCoRuO_6$ with LiH to extract a single phase of $LaSrCoRuO_4$ was challenging, as it was always accompanied by a secondary phase, $LaSrCoRuO_5$. Since the flowing tube experimental set-up is not completely sealed, it is not as airtight as presumed. It is hence likely that the formation of the secondary phase $LaSrCoRuO_5$ is due to the presence of air (oxygen) within the reaction vessel. Therefore, after three periods of 48 hours heating at 375 °C, the reaction mixture was transferred into a borosilicate ampoule without adding extra LiH, and the ampoule was sealed under vacuum. The sealed borosilicate ampoule was heated to 375 °C at 1 °C min^{-1} and was held at this temperature for 24 hours. The sealed borosilicate ampoule ensured a low oxygen partial pressure within the experimental set-up. However, this process led to the formation of a potential oxyhydride phase. These attempts have shown that $LaSrCoRuO_4$ is very metastable, making it very difficult to prepare a pure phase of $LaSrCoRuO_4$.

5.4 Discussion

As discussed in Section 5.3, the topochemical reduction of $LaSrCoRuO_6$ with Zr and LiH leads to different outcomes. Reduction with Zr yields $LaSrCoRuO_5$, while the more reduced phase, $LaSrCoRuO_4$, can only be prepared with LiH. This observation highlights the differences between Zr powder and LiH as reducing agents, which will be further discussed below.

5.4.1 Reduction with Zr getters

Reduction of a substrate with a Zr getter, as detailed in Section 2.2.4, relies on the oxygen release from the substrate, according to the reaction:

$$ABO_3 \longleftrightarrow ABO_{3-x} + {}^{x}/_{2}\, O_2$$

The equilibrium of the oxygen release process is a competition between the lattice enthalpy of the substrate (ΔH) and the entropy gain of the system (ΔS), according to the Gibbs free energy

equation $\Delta G = \Delta H - T\Delta S$. The oxygen release process is thermodynamically favourable if $\Delta G < 0$.

Since the entropy of a system is proportional to temperature, high temperatures favour the oxygen release process and hence push the formation of an oxygen-deficient perovskite phase (equilibrium shift to the right-hand side). Above a certain temperature, the entropy gain of the system (ΔS) will outweigh the unfavourable endothermic lattice enthalpy (ΔH). As a result, the oxygen release process will become thermodynamically favourable ($-\Delta G$).

The O_2 gas released by the substrate in the system can then react with a Zr getter to push the equilibrium further to the product side (oxygen deficient perovskite side), according to the reaction equations:

$$ABO_3 \longleftrightarrow ABO_{3-x} + {}^{x}/_{2}\, O_2 \qquad (1)$$

$$Zr + O_2 \longleftrightarrow ZrO_2 \qquad (2)$$

The ZrO_2 by-product formed will establish an equilibrium shown in eqn (2). The partial pressure of the oxygen released from ZrO_2 at equilibrium is labelled as Zr $P(O_2)$, which is shown in Fig 5.3. At a low temperature ($< T_1$), the amount of oxygen released from the substrate is small (< Zr $P(O_2)$) and the equilibrium of eqn (2) will lie on the left-hand side. As a result of this, the presence of Zr does not lower the oxygen partial pressure in the sealed reaction vessel, and hence there is not a strong driving force for the reduction of ABO_3 to take place at a low temperature ($< T_1$).

Above a certain temperature (T_1), the oxygen partial pressure released from the substrate in the system is high enough (> Zr $P(O_2)$) for the equilibrium of eqn (2) to shift to the right (favour the formation of ZrO_2). This process will lower the oxygen partial pressure within the sealed reaction system, which further pushes the equilibrium of eqn (1) to the right-hand side and hence leads to the formation of oxygen-deficient perovskite.

The high reaction temperatures required for the oxygen release process from the substrate preclude the formation of the most metastable phases. In addition, the high reaction temperatures may lead to the decomposition of the substrate before any topochemical reactions take place. Therefore, reductions with Zr getters form reduced phases that are not too metastable.[22]

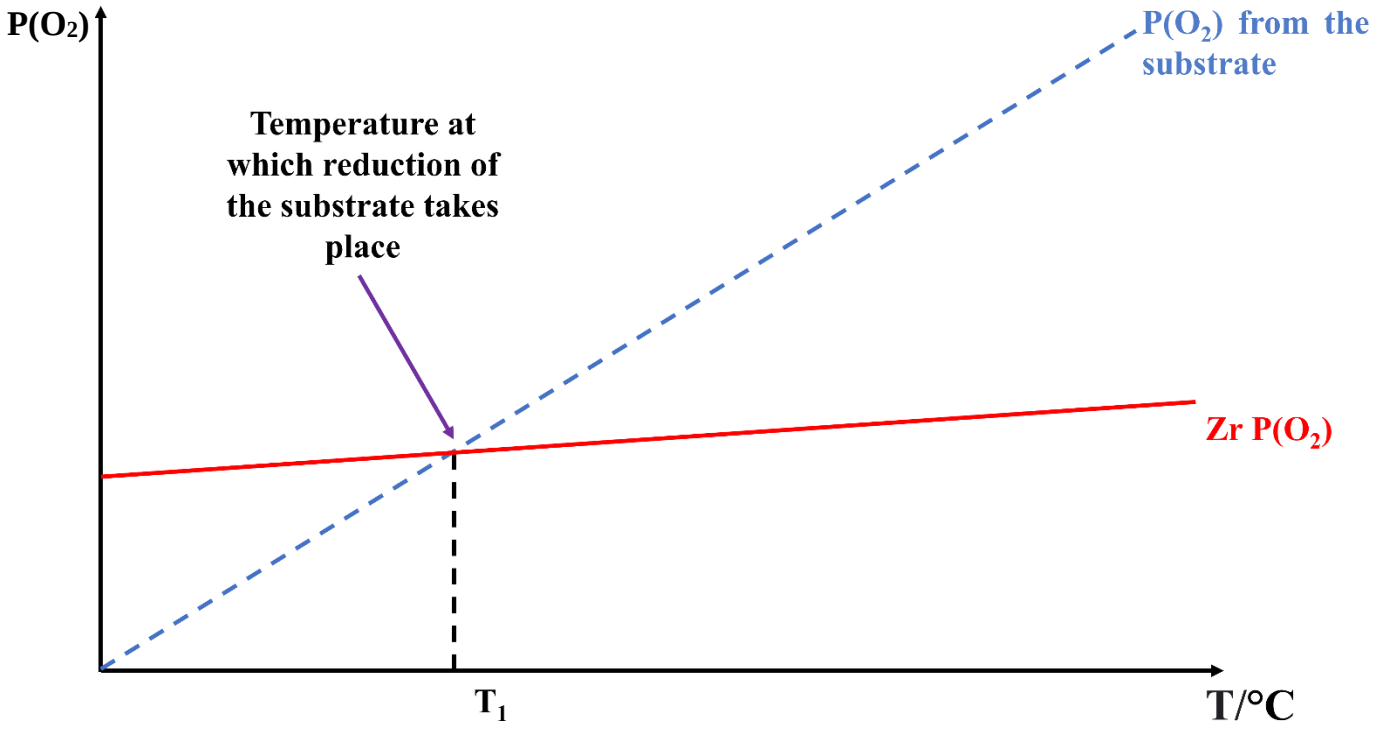


Figure 5.3. Reduction of a substrate using a Zr getter as a reducing agent.

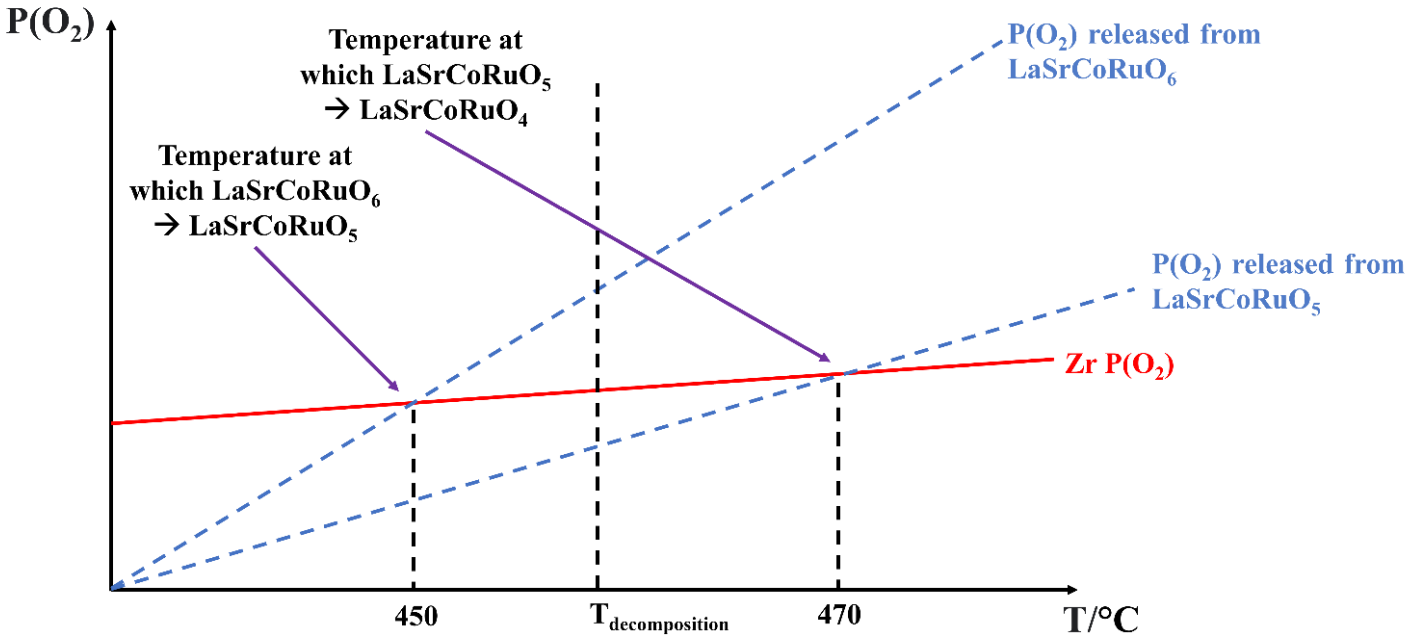
Now considering the reduction of $LaSrCoRuO_6$ with a Zr getter, there is a sequence of reactions:

$$LaSrCoRuO_6 + {}^1/_2\,Zr \longleftrightarrow LaSrCoRuO_5 + {}^1/_2\,ZrO_2$$

$$LaSrCoRuO_5 + {}^1/_2\,Zr \longleftrightarrow LaSrCoRuO_4 + {}^1/_2\,ZrO_2$$

The oxygen release from $LaSrCoRuO_6$ to form $LaSrCoRuO_5$ takes place at a relatively lower temperature than the corresponding oxygen release from $LaSrCoRuO_5$ to form $LaSrCoRuO_4$,

as the defects in the latter phase are more 'enthalpically expensive'. The extent of the reduction reaction of $LaSrCoRuO_6$ is therefore determined by thermodynamics. A graphic representation



of the reduction of $LaSrCoRuO_6$ is shown in Fig 5.4.

Figure 5.4. Reduction profile of $LaSrCoRuO_6$ with a Zr getter.

Unfortunately, $LaSrCoRuO_5$ undergoes non-topochemical decomposition before the topochemical reduction to form $LaSrCoRuO_4$ takes place. Therefore, the reduction of $LaSrCoRuO_6$ with Zr getters cannot yield the metastable phase $LaSrCoRuO_4$.

5.4.2 Reduction with LiH

LiH is a more efficient reducing agent and can be used at a low temperature range. This is because reduction reactions with LiH proceed via a solid-state process, which is primarily driven by the formation of the thermodynamically stable by-product Li_2O as shown in the following equation:

$$LaSrCoRuO_6 + 2x\ LiH \longrightarrow LaSrCoRuO_{6-x} + x\ Li_2O + x\ H_2$$

As a result, the free energy of the system is lowered upon reacting with LiH at all temperatures. However, the exact reaction that occurs depends on the relative activation energy barriers of the different reduction reactions, thus reactions with LiH are under kinetic control.

The reduction profile of $LaSrCoRuO_6$ with LiH is shown in Fig 5.5. As reactions with LiH take place at relatively low temperatures (335 °C to 375 °C), the activation energy barrier of the topochemical reduction of $LaSrCoRuO_6$ and $LaSrCoRuO_5$ is small (Ea_1, Ea_2). On the contrary, no sign of decomposition was observed at those reaction temperatures, indicating that these low reaction temperatures cannot overcome the activation energy barrier of the non-topochemical decomposition (Ea_3). This observation suggests that the activation energy of the non-topochemical decomposition (Ea_3) is large. The large Ea_3 and the small Ea_2 successfully trap the highly metastable $LaSrCoRuO_4$ phase. In addition, the activation energy of the topochemical reduction of $LaSrCoRuO_6$ to $LaSrCoRuO_5$ and the activation energy of the topochemical reduction of $LaSrCoRuO_5$ to $LaSrCoRuO_4$ are likely to be similar, as the formation of $LaSrCoRuO_4$ is always accompanied by the formation of $LaSrCoRuO_5$ (Fig 5.5).

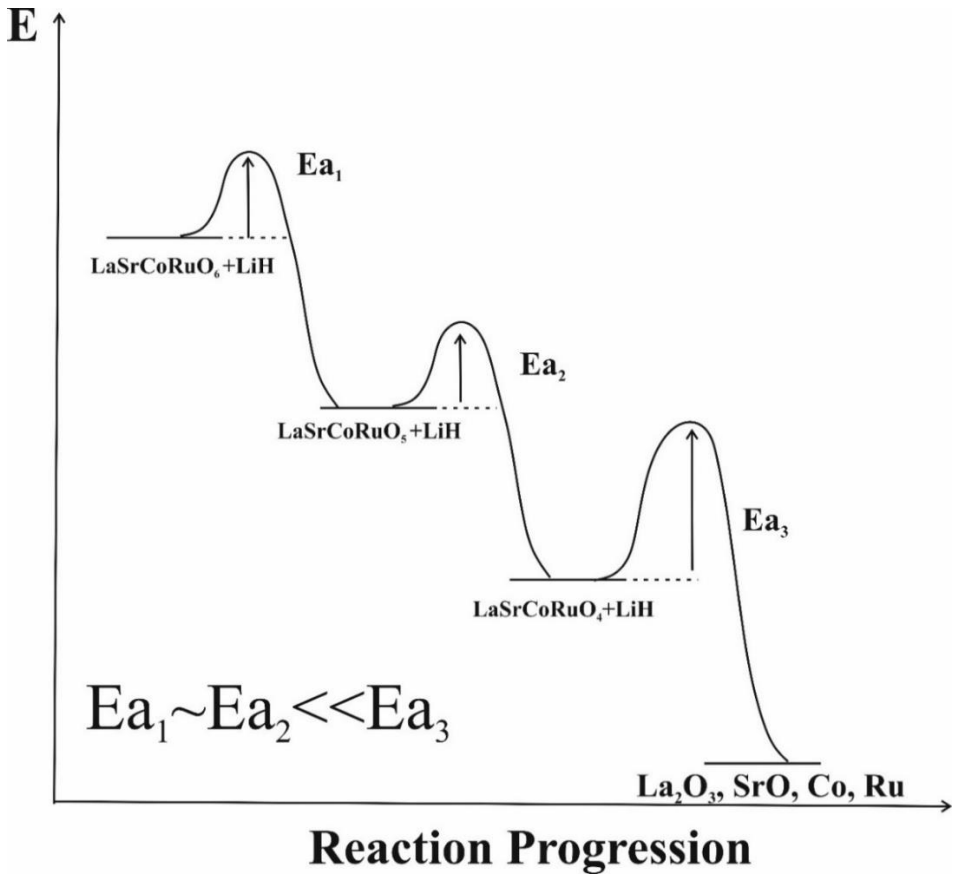


Figure 5.5. Proposed reaction pathway for the topochemical reduction of $LaSrCoRuO_6$ using LiH as a reducing agent.

In conclusion, the successful isolation of $LaSrCoRuO_4$ with LiH highlights an important difference between Zr getters and LiH as reducing agents. Reductions with Zr getters are based on thermodynamic control, hence a higher reaction temperature is needed to increase the entropy of a system. Instead, reductions with LiH are based on kinetic control, therefore, reductions with LiH can take place at low temperatures and yield the most metastable compounds.

5.4.3 Structural Rearrangement During the Reduction of $LaSrCoRuO_6$

As demonstrated in Section 5.3.2, the reduction of $LaSrCoRuO_6$ with LiH at 375 °C to form $LaSrCoRuO_4$ takes place via the formation of $LaSrCoRuO_5$. $LaSrCoRuO_5$ adopts an anion-vacancy ordered structure resembling that of $LaNi_{0.9}Co_{0.1}O_{2.5}$, where the transition metal

centres are in three different geometries, namely square-planar, square-based pyramidal and octahedral coordination.[76] The more reduced phase, $LaSrCoRuO_4$, adopts an infinite layer structure resembling that of $LaNiO_2$.[24] It is worth noting that the reduction from $LaSrCoRuO_5$ to $LaSrCoRuO_4$ is not a simple topotactic reduction, instead, a rearrangement of the oxide anions is required (Fig 5.6(a)). A similar anion reorganisation was observed in the reduction of $SrFeO_3$ with CaH_2 to form $SrFeO_2$, which adopts an infinite layer structure. The reduction of $SrFeO_3$ to form $SrFeO_2$ takes place via $SrFeO_{2.5}$, which adopts a brownmillerite structure (Fig 5.6(b)).[25,77]

The reduction of $LaSrCoRuO_6$ has demonstrated that the oxide anions are highly mobile even at low temperatures, while the metal framework remains intact. This observation highlights the essence of topochemical reduction via anion deintercalation, where a significant difference in

the mobility between the anion and cation sublattices is needed for a topochemical reaction to take place.

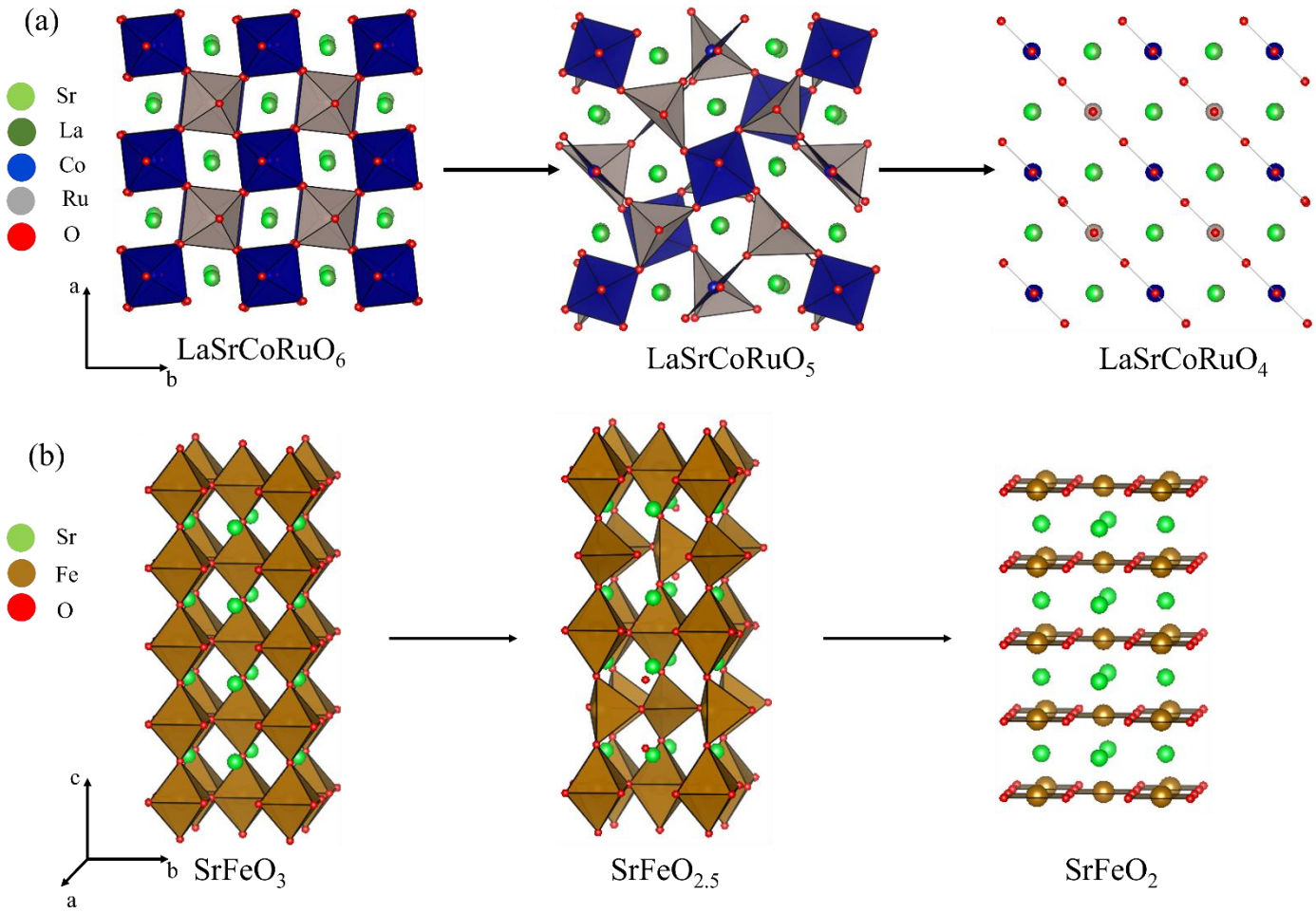


Figure 5.6. Structural transformation of (a) reduction of $LaSrCoRuO_6$ to $LaSrCoRuO_4$ via the intermediate phase $LaSrCoRuO_5$ and (b) reduction of $SrFeO_3$ to form $SrFeO_2$ via the intermediate phase $SrFeO_{2.5}$.

5.5 Conclusion

The topochemical reduction of $LaSrCoRuO_6$ with Zr and LiH yields $LaSrCoRuO_5$ and $LaSrCoRuO_4$, where $LaSrCoRuO_4$ can only be extracted using LiH. The reduction between $LaSrCoRuO_6$ and $LaSrCoRuO_4$ proceeds via the anion-vacancy ordered intermediate phase

$LaSrCoRuO_5$. The oxide anions in $LaSrCoRuO_5$ need to be re-arranged upon further reduction, indicating that the anion framework is highly mobile even at low temperature.

The reduction of $LaSrCoRuO_6$ has demonstrated that the choice of the reducing agent is important, with different reducing agents favouring the formation of different metastable phases. Full details of the structural and magnetic characterisation of $LaSrCoRuO_5$ and $LaSrCoRuO_4$ will be discussed in Chapter 6 and 7.

Chapter 6 Synthesis and Characterisation of $LaSrCoRuO_5$

6.1 Introduction

The topochemical reduction of the B-site cation ordered double perovskite $LaSrCoRuO_6$ with Zr powder at 450 °C yields an oxygen deficient phase $LaSrCoRuO_5$, according to the reaction:

$$LaSrCoRuO_6 + {}^1/_2\ Zr \rightarrow LaSrCoRuO_5 + {}^1/_2\ ZrO_2$$

A detailed structural and magnetic characterisation of this oxygen deficient phase $LaSrCoRuO_5$ will be described in this chapter.

6.2 Experimental

A 2 g sample of $LaSrCoRuO_6$ was prepared using a citrate gel method as described in Section 5.2.1. Once the reaction was deemed complete, the sample of $LaSrCoRuO_6$ was quenched to enhance its reactivity. A sample of $LaSrCoRuO_5$ suitable for analysis by neutron powder diffraction was prepared by heating 1.5 g of quenched $LaSrCoRuO_6$ with 2 mole equivalents of Zr powder in an evacuated silica ampoule (Section 2.2.4). The reaction apparatus was heated to 450 °C at 1 °C min^{-1} for 1 cycle of 48 hours. X-ray powder diffraction was used to monitor the reaction progression.

6.3 Results

6.3.1 Thermogravimetric Analysis

The composition of the reduced $LaSrCoRuO_{6-x}$ phase was determined by performing an oxidative thermogravimetric analysis (TGA) experiment. A small quantity of the reduced $LaSrCoRuO_{6-x}$ sample was heated to 800 °C under a constant flow of O_2. The sample was kept at 800 °C for 6 hours before being cooled to room temperature. During the reaction, a mass gain of 3.29% was recorded. X-ray powder diffraction data collected from the re-oxidised

product after the TGA experiment confirmed a complete re-oxidation to its parent oxide $LaSrCoRuO_6$. The mass increase of 3.29% is consistent with a composition of $LaSrCoRuO_{5.01}$ (Fig 6.1). Henceforth, this reduced phase will be referred to as $LaSrCoRuO_5$.

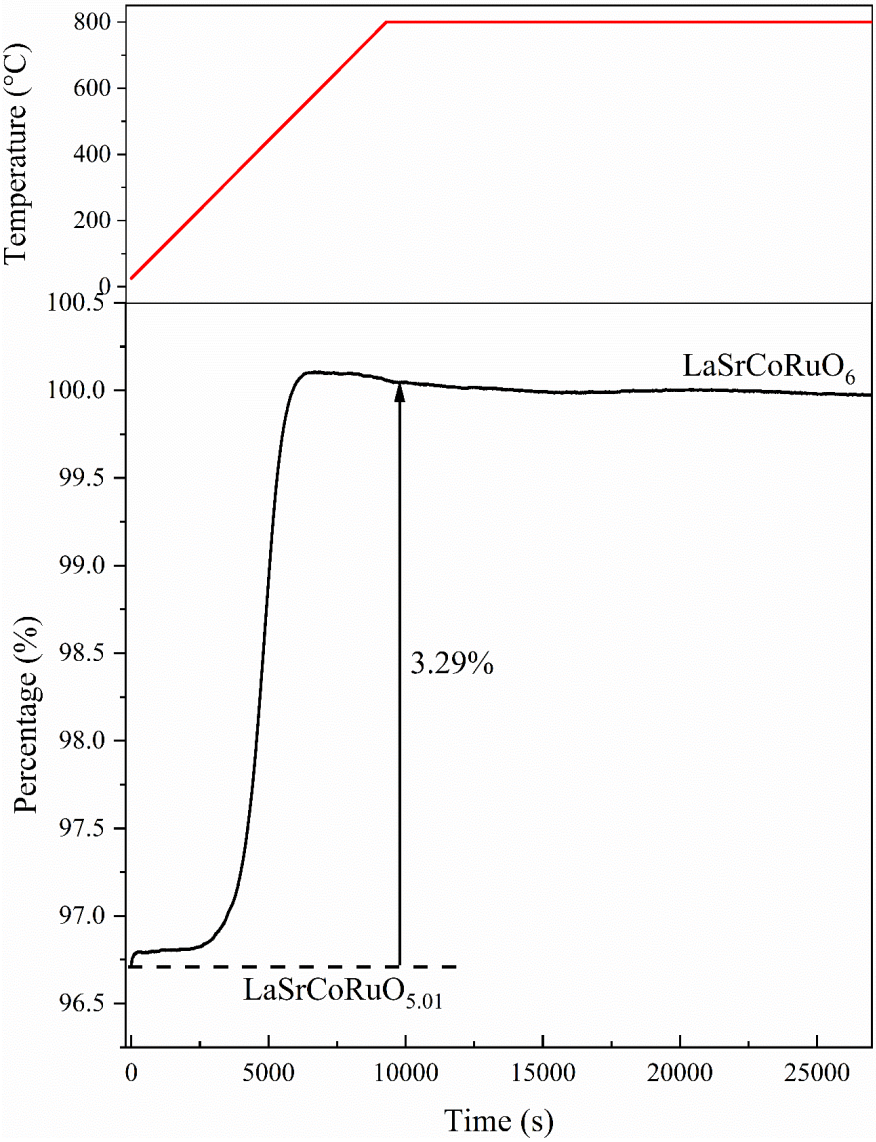


Figure 6.1. Oxidative thermogravimetric analysis of $LaSrCoRuO_{6-x}$, plot shows temperature and mass as a function of time.

6.3.2 Structural Characterisation of $LaSrCoRuO_5$

6.3.2.1 Synchrotron X-ray Diffraction Characterisation $LaSrCoRuO_5$

Synchrotron X-ray diffraction (SXRD) data collected from a large-scale neutron sample of $LaSrCoRuO_5$ can be indexed using a body centred monoclinic unit cell with a $\sqrt{2} \times \sqrt{2} \times 2$ cell

expansion of the aristotype *Pm*-3*m* perovskite unit cell (a = 5.38 Å, b = 5.39 Å, c = 8.13 Å, γ = 90.52°). A Pawley refinement against the SXRD data was performed using a monoclinic unit cell with lattice parameters described above. The refinement converged rapidly and gave a good statistical fit (*wRp* = 6.37%; *Rp* = 3.70%). However, close inspection of the refinement plot revealed some weak additional reflections that cannot be indexed by this unit cell (Fig 6.2). These observations suggest that a larger unit cell is needed to describe the structure of $LaSrCoRuO_5$.

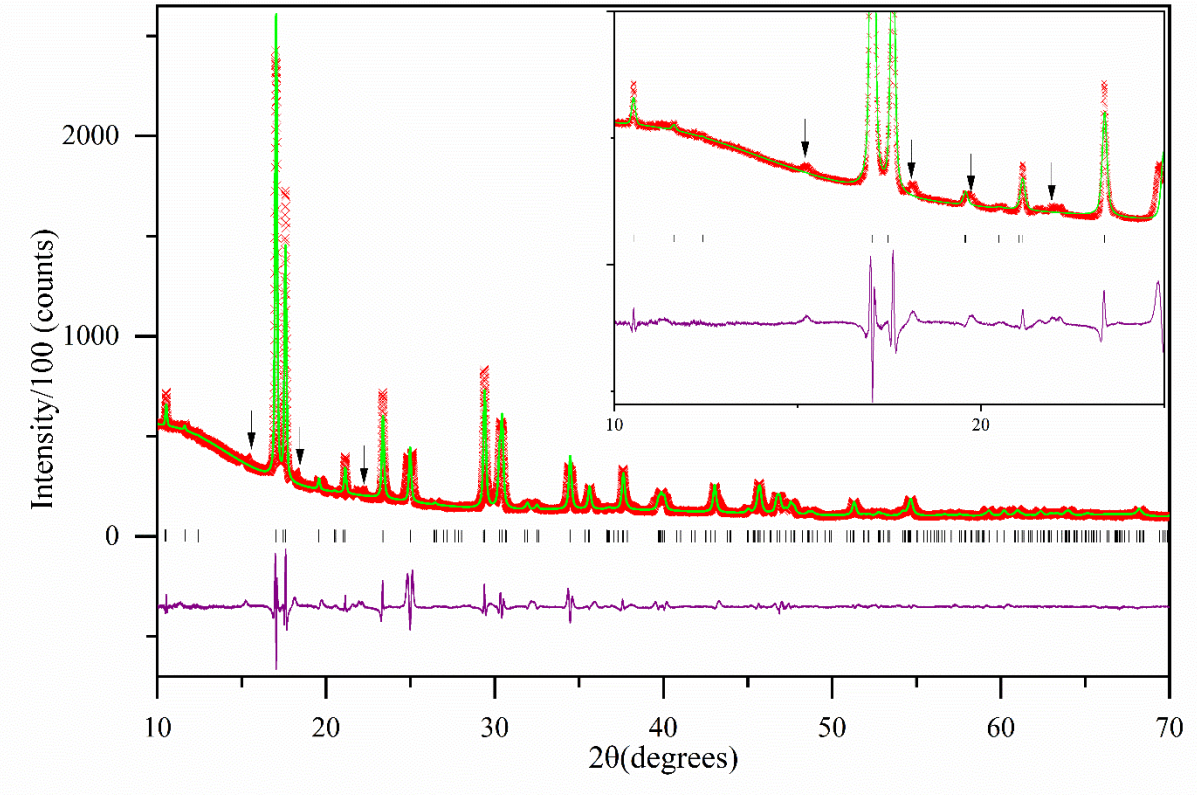


Figure 6.2. Observed, calculated and difference plots of the Pawley refinement of $LaSrCoRuO_5$ against SXRD data using a body centred unit cell with a $\sqrt{2} \times \sqrt{2} \times 2$ geometric cell expansion of the aristotype perovskite unit cell; Inset shows additional diffraction peaks that cannot be indexed using this cell.

6.3.2.2 Electron Diffraction Characterisation of $LaSrCoRuO_5$

Electron diffraction (ED) data presented in this thesis were collected by Dr Maria Batuk and Prof. Joke Hadermann at the University of Antwerp. A sample of $LaSrCoRuO_5$ was analysed by electron diffraction using an FEI Titan 80-300 'cubed' microscope operated at 300 kV. The ED data collected from a large-scale neutron sample of $LaSrCoRuO_5$ are shown in Fig 6.3. The orange cell indicates the basic perovskite unit cell with a $\sqrt{2} \times \sqrt{2} \times 2$ geometric cell expansion. The presence of the bright reflection in the [001] zone axis (Fig 6.3(a)) justifies the necessity to use a $2 \times 2 \times 1$ cell expansion compared to the $LaSrCoRuO_6$ parent phase ($2\sqrt{2} \times 2\sqrt{2} \times 2$ compared to a simple undistorted perovskite unit cell ABO_3). The reflection conditions obtained from the ED patterns are as follows: *00l*: *l=2n*. These reflection conditions are consistent with a primitive unit cell with a possible 2_1 screw axes along the *c* direction.

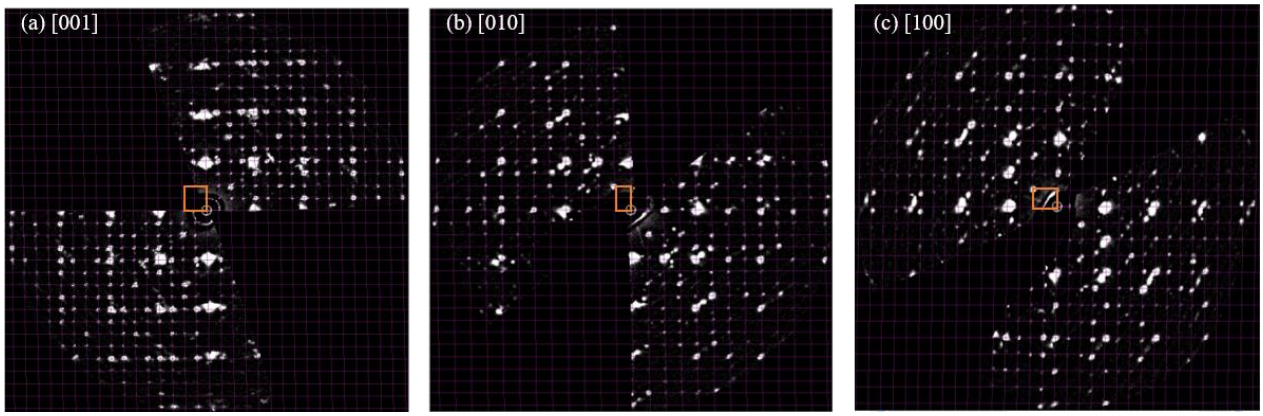


Figure 6.3. Electron diffraction data collected from $LaSrCoRuO_5$ sample. Orange unit cell indicates the basic cell with $\sqrt{2}a_p$ x $\sqrt{2}a_p$ x $2a_p$.

A Pawley refinement was conducted using a large monoclinic unit cell described in space group $P112_1$ with a $2\sqrt{2} \times 2\sqrt{2} \times 2$ cell expansion. Those weak diffraction peaks that could not be indexed before are now accounted for, as shown in Fig 6.4.

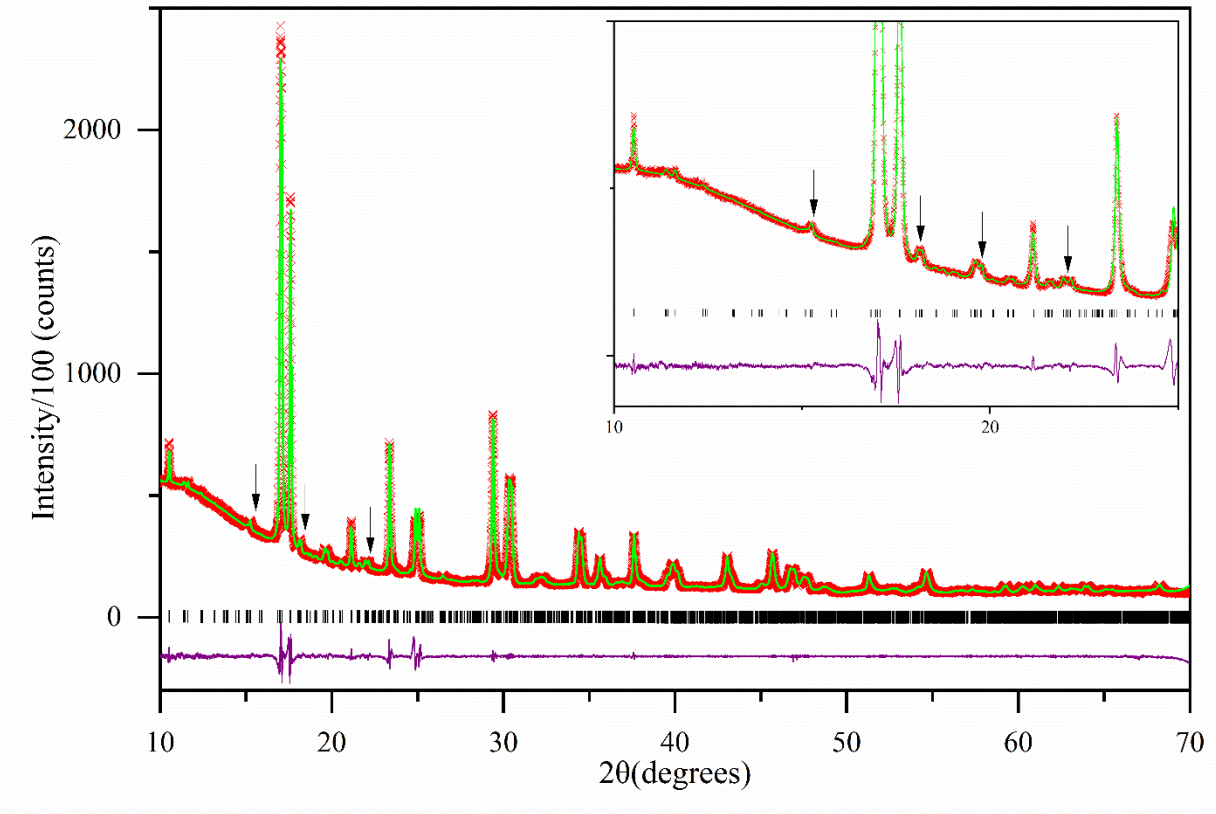


Figure 6.4. Observed, calculated and difference plots of the Pawley refinement of $LaSrCoRuO_5$ against SXRD data using a monoclinic unit cell described in space group $P112_1$ with a $2\sqrt{2} \times 2\sqrt{2} \times 2$ geometric cell expansion of the aristotype perovskite unit cell.

6.3.2.3 Room Temperature Neutron Powder Diffraction Data of $LaSrCoRuO_5$

Room temperature neutron powder diffraction (NPD) data were collected from a large-scale sample of $LaSrCoRuO_5$ using the WISH instrument at ISIS (Section 2.4.2.1). The NPD data can be indexed using a $2\sqrt{2} \times 2\sqrt{2} \times 2$ geometric expansion of the aristotype perovskite unit cell (a = 10.80 Å, b = 10.82 Å, c = 8.14 Å). In order to find the correct symmetry describing the unit cell of $LaSrCoRuO_5$, a series of Pawley refinements were performed against the SXRD data collected from the large-scale sample of $LaSrCoRuO_5$ using tetragonal, orthorhombic and monoclinic unit cells with a $2\sqrt{2} \times 2\sqrt{2} \times 2$ cell expansion. The Pawley refinement with a monoclinic unit cell gave the best statistical fit, indicating that the structure $LaSrCoRuO_5$ is best described using a monoclinic unit cell (Fig 6.5).

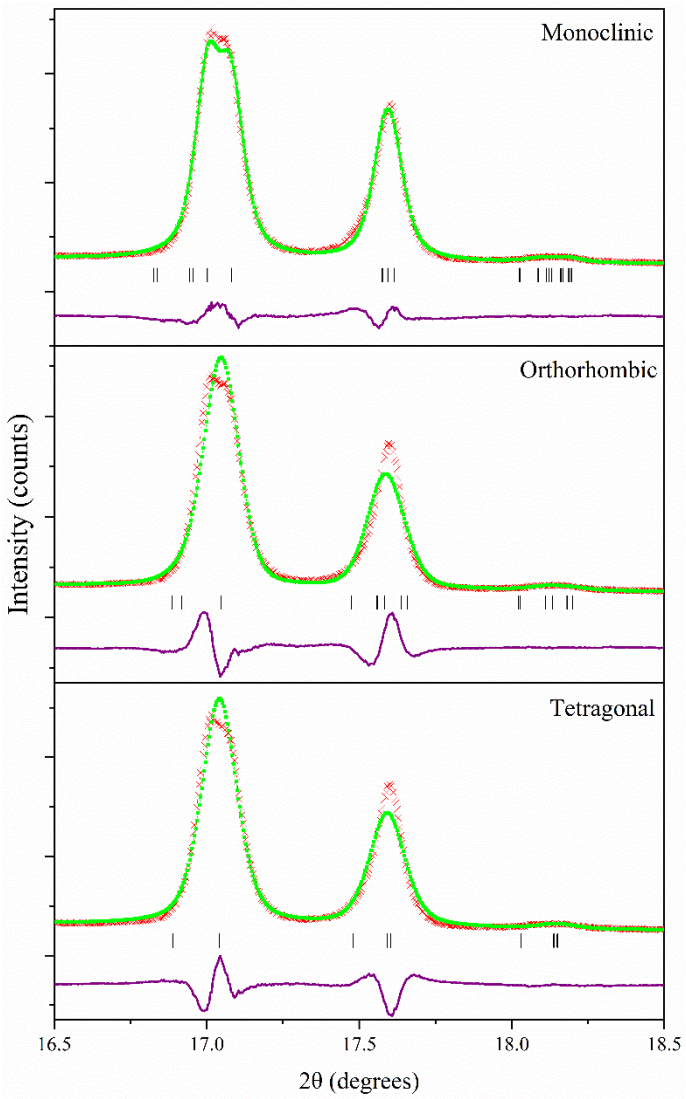


Figure 6.5. Observed, calculated and difference plots from the Pawley refinements of $LaSrCoRuO_5$ using unit cells with different symmetries.

For any description of the anion-vacancy ordering of $LaSrCoRuO_5$ to be correct, there are two factors that must be considered. First, the elongation of the *c* lattice parameter on reduction implies that the oxygen vacancies are in the sheets of the corner linked BO_2 planes rather in the La/SrO planes. Locating the anion vacancies in the BO_2 planes is consistent with the doubling of the *a* and *b* lattice parameters. Second, the anion-vacancy ordering in $LaSrCoRuO_5$ must be compatible with the electronic configurations of the Co^{2+} and Ru^{3+} cations, where the tetrahedral coordination is strongly disfavoured by the Ru^{3+} cations ($(e_g)^4(t_{2g})^1$).

After a series of investigations, two models based on the anion-vacancy ordered structure of $LaNi_{0.9}Co_{0.1}O_{2.5}$ with rocksalt ordering of Co and Ru cations at the B-site were constructed (Fig 6.6).[76] The difference between these models arises from the geometries that the transition metal cations can adopt. In model 1, both Co and Ru cations are in three different geometries, namely octahedral, square-based pyramidal and square-planar BO_x units; In model 2, Ru cations only adopt the square-based pyramidal coordination, while the Co cations are in both the octahedral and square-planar coordination but not the square-based pyramidal coordination. The NPD data were simulated for both models and compared with the experimental NPD data. Simulated NPD data for model 2 give a much better match to the experimental NPD data, model 2 was then refined against the NPD data (Fig 6.7).

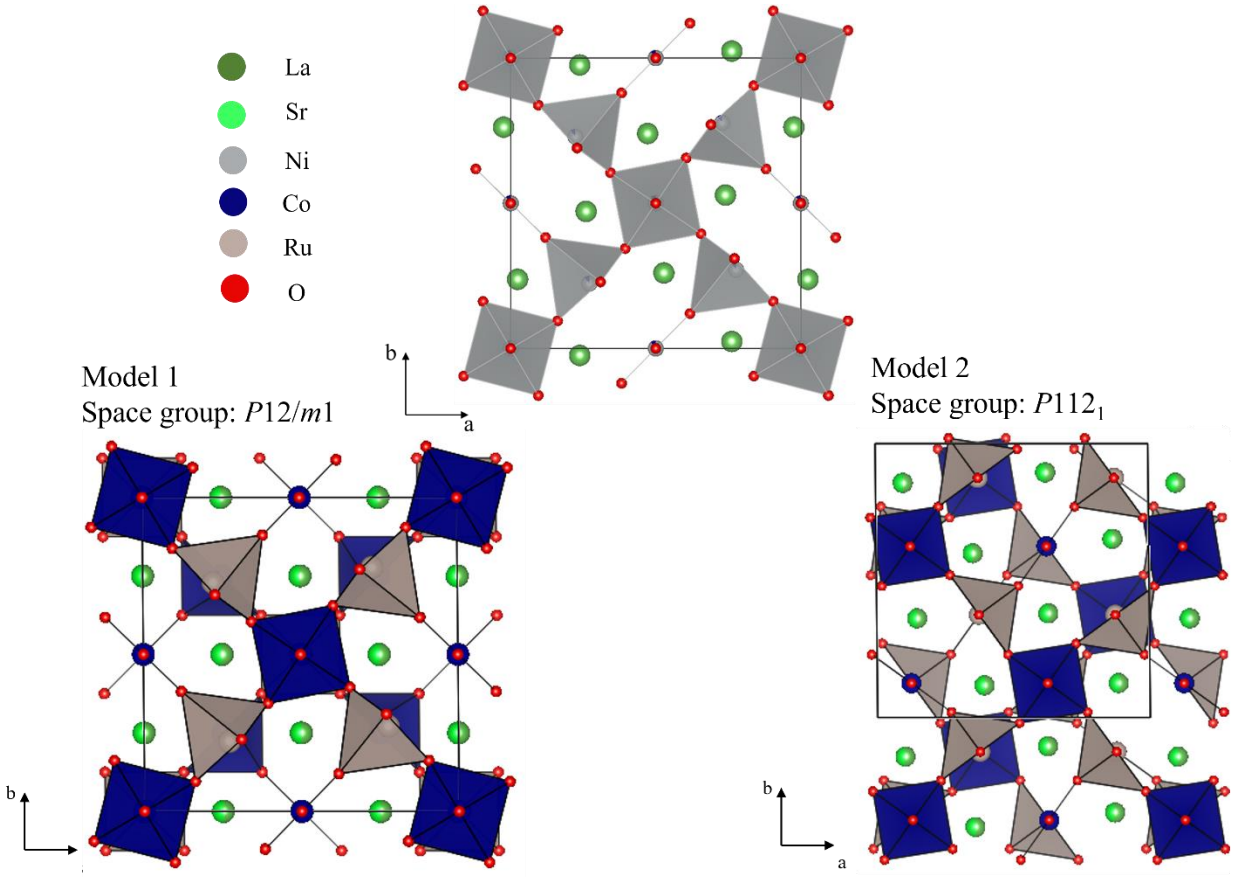


Figure 6.6. Structure of $LaNi_{0.9}Co_{0.1}O_{2.5}$ (top),[76] and two structural models of $LaSrCoRuO_5$ constructed based on the anion-vacancy ordering of $LaNi_{0.9}Co_{0.1}O_{2.5}$ (bottom).

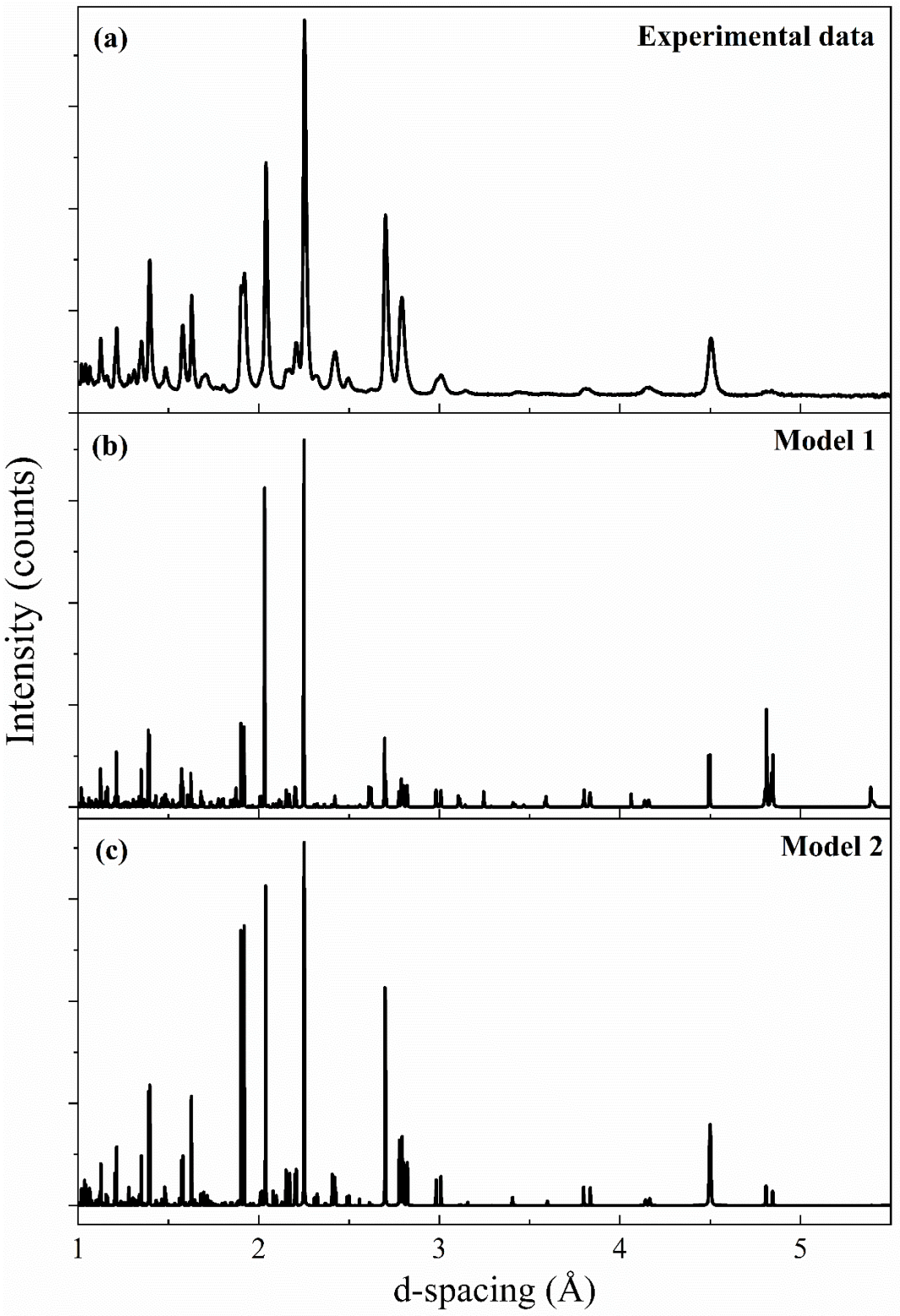


Figure 6.7. A direct comparison of (a) experimental NPD data collected from $LaSrCoRuO_5$ at room temperature and simulated NPD data for (b) model 1 and (c) model 2.

It is worth noting that in model 2, the interplay between the cation ordering and this particular anion ordering requires a shift of ($^1/_4$, $^1/_4$, 0) between layers which can only be described in the

space group $P112_1$. This model (model 2) was refined against the NPD data collected from a large-scale sample of $LaSrCoRuO_5$, initial refinement converged rapidly.

Due to the low symmetry and large dimensions of the $LaSrCoRuO_5$ unit cell, there are a large number of variables to be considered during the refinement. In order to decrease the degrees of freedom during the refinement, some constraints were added to the model. The displacements of the oxide ions were constrained in a way that the magnitudes of the tilting distortions of the BO_x polyhedra were the same for all transition metal cations. The refinement of the more symmetric $P112_1$ model against the NPD data achieved a good statistical fit. The following tilting scheme gave the best statistical fit: clockwise tilt of the $Co(4)O_6$ octahedra, anticlockwise tilt for the $Co(2)O_6$ octahedra, anticlockwise tilt for the $Co(3)O_4$ square-planar unit and clockwise tilt for the $Co(1)O_4$ square-planar unit. The tilting scheme is shown in Fig 6.8.

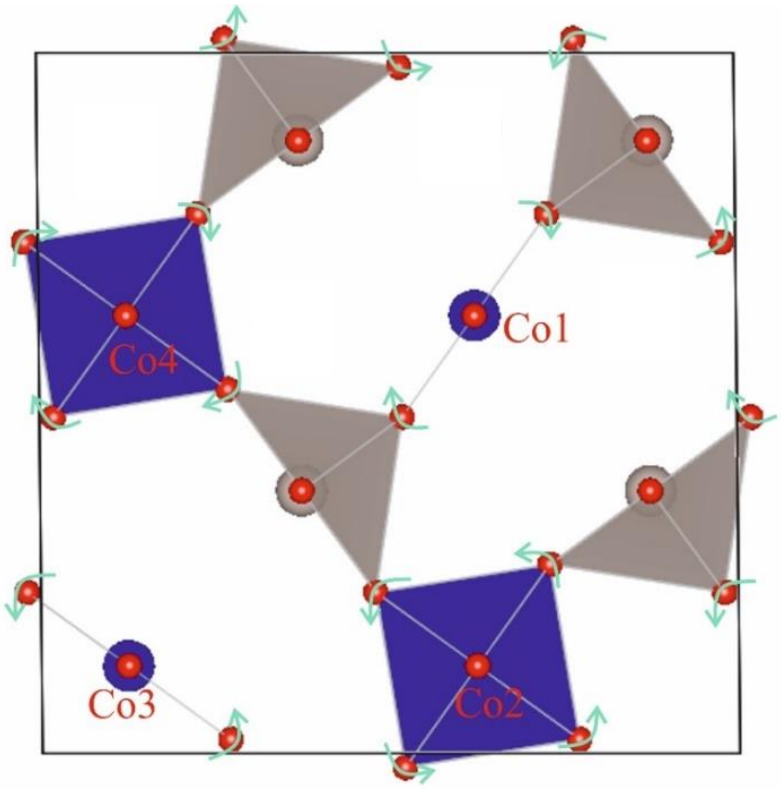


Figure 6.8. Schematic representation of the tilting system within the structure. La/Sr atoms were omitted for clarity.

The refinement of the $P112_1$ model of $LaSrCoRuO_5$ with constraints of the positions of the oxide ions following the tilting scheme in Fig 6.8 against NPD data converged rapidly and gave a reasonable statistical fit (wRp = 6.69%; Rp = 5.97%). However, close inspection of the refined model of $LaSrCoRuO_5$ revealed that the resulting structure was very irregular, with chemically equivalent cations (cations in the same geometry) in very different local bonding environments, as evident from the average M-O bond lengths (Table 6.1).

Cations	Average bond lengths/Å	Coordination
Co(1)	2.187(7)	Square-planar
Co(2)	2.028(1)	Octahedral
Co(3)	2.087(3)	Square-planar
Co(4)	2.013(1)	Octahedral
Ru(1)	1.8946(7)	Square pyramidal
Ru(2)	1.9922(10)	Square pyramidal
Ru(3)	1.9881(7)	Square pyramidal
Ru(4)	1.9844(10)	Square pyramidal

Table 6.1. Average M-O bond lengths extracted from the structural refinement of $LaSrCoRuO_5$.

To address these problems, additional symmetry constraints were added to the model to ensure the M - O bond lengths for the chemically equivalent cations are similar. It was observed that the transition metal cations of similar chemical environments were related by a mirror plane along the [110] direction. The positions of the transition metal cations were therefore constrained such that their positions were consistent with this symmetry (Fig 6.9(a)). Similarly, the oxide ions in similar chemical environments within the *ab* plane were observed to be related by mirror planes along [110] and [1-10] directions (Fig 6.9(b)), they were then constrained

such that their positions were consistent with these symmetries. In addition, the apical oxide ions were constrained through a mirror plane perpendicular to the [001] direction, as indicated in Fig 6.9(b). The refinements of this more symmetric $P112_1$ model of $LaSrCoRuO_5$ converged rapidly and achieved an even better statistical fit (*wRp* = 5.97%; *Rp* = 5.14%). The refined structural model (Fig 6.10) obtained from the refinements of $LaSrCoRuO_5$ against NPD data was then refined against the SXRD data collected from the same sample of $LaSrCoRuO_5$. The additional symmetry constraints described above were still imposed during the SXRD refinement. The refinement against the SXRD data converged rapidly and gave a good statistical fit (*wRp* = 2.60%; *Rp* = 1.82%).

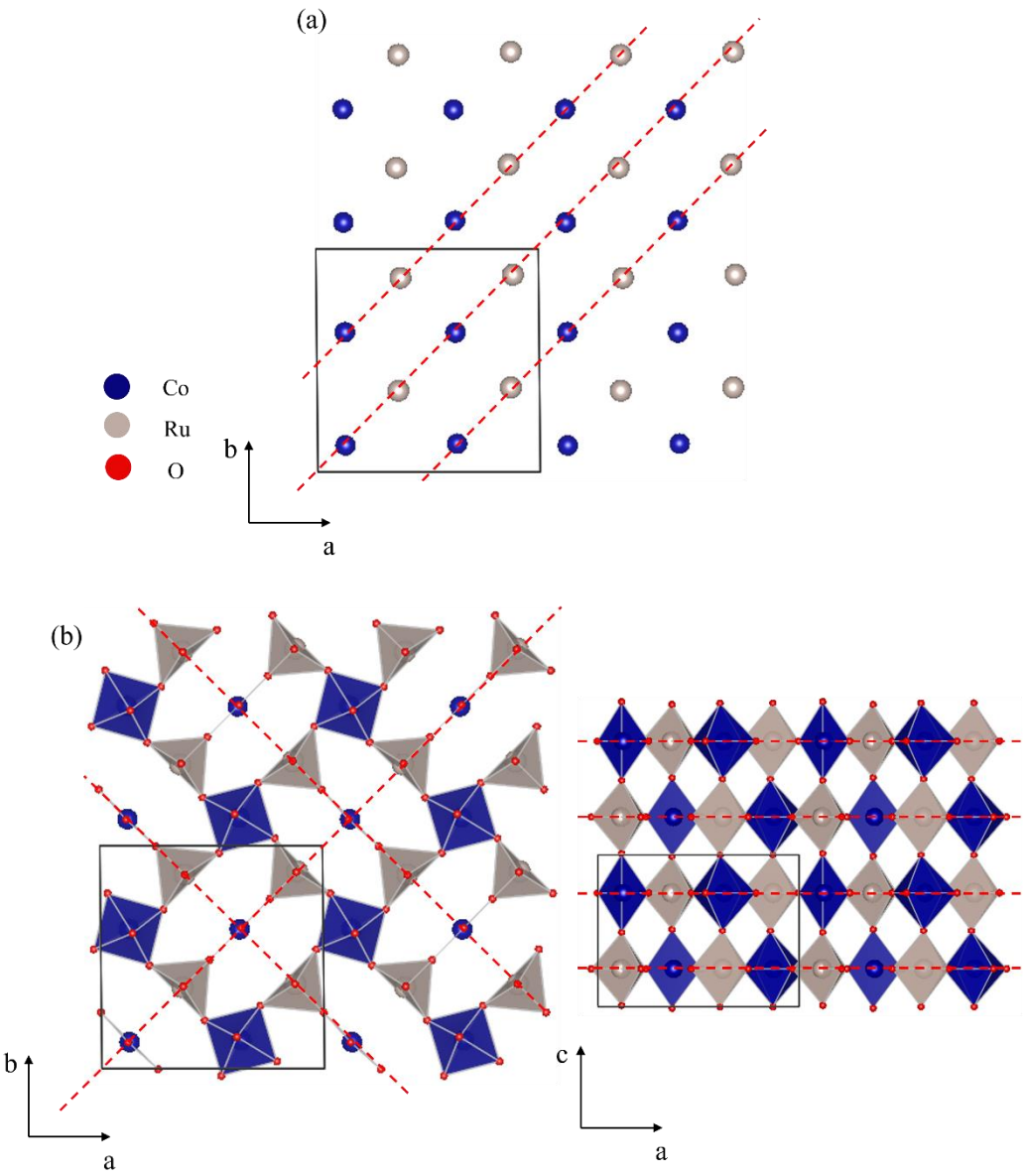


Figure 6.9. Schematic representation of the mirror planes constraint within the structure. La/Sr atoms were omitted for clarity.

The observed, calculated and difference plots from the structural refinement of the large-scale sample of $LaSrCoRuO_5$ against the SXRD data and NPD data are shown in Fig 6.11 and Fig 6.12; full structural parameters from the refinement of the large-scale sample of $LaSrCoRuO_5$ against the NPD data are shown in Table 6.2 with selected bond lengths shown in Table 6.3.

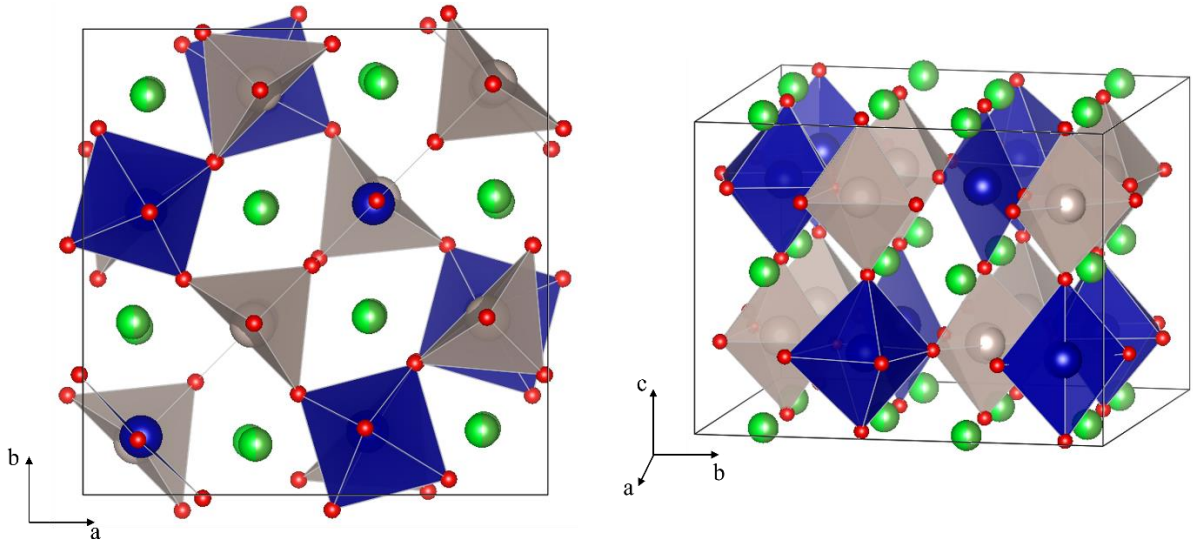


Figure 6.10. Refined crystal structure of $LaSrCoRuO_5$ in $P112_1$ space group (Green: La/Sr, blue: Co, brown: Ru, red: O).

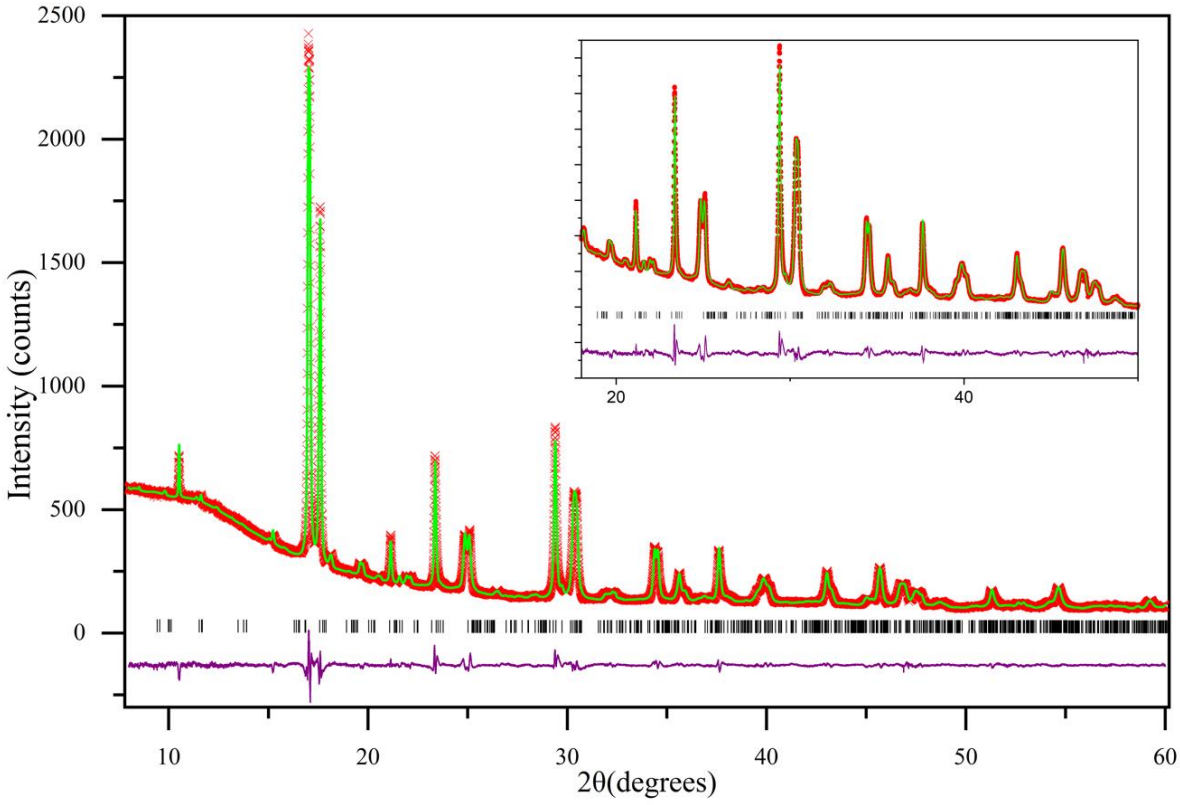


Figure 6.11. Observed, calculated and difference plots from the structural refinement of the large-scale sample of $LaSrCoRuO_5$ against SXRD data collected at room temperature. Inset shows an expanded view of the high angle region.

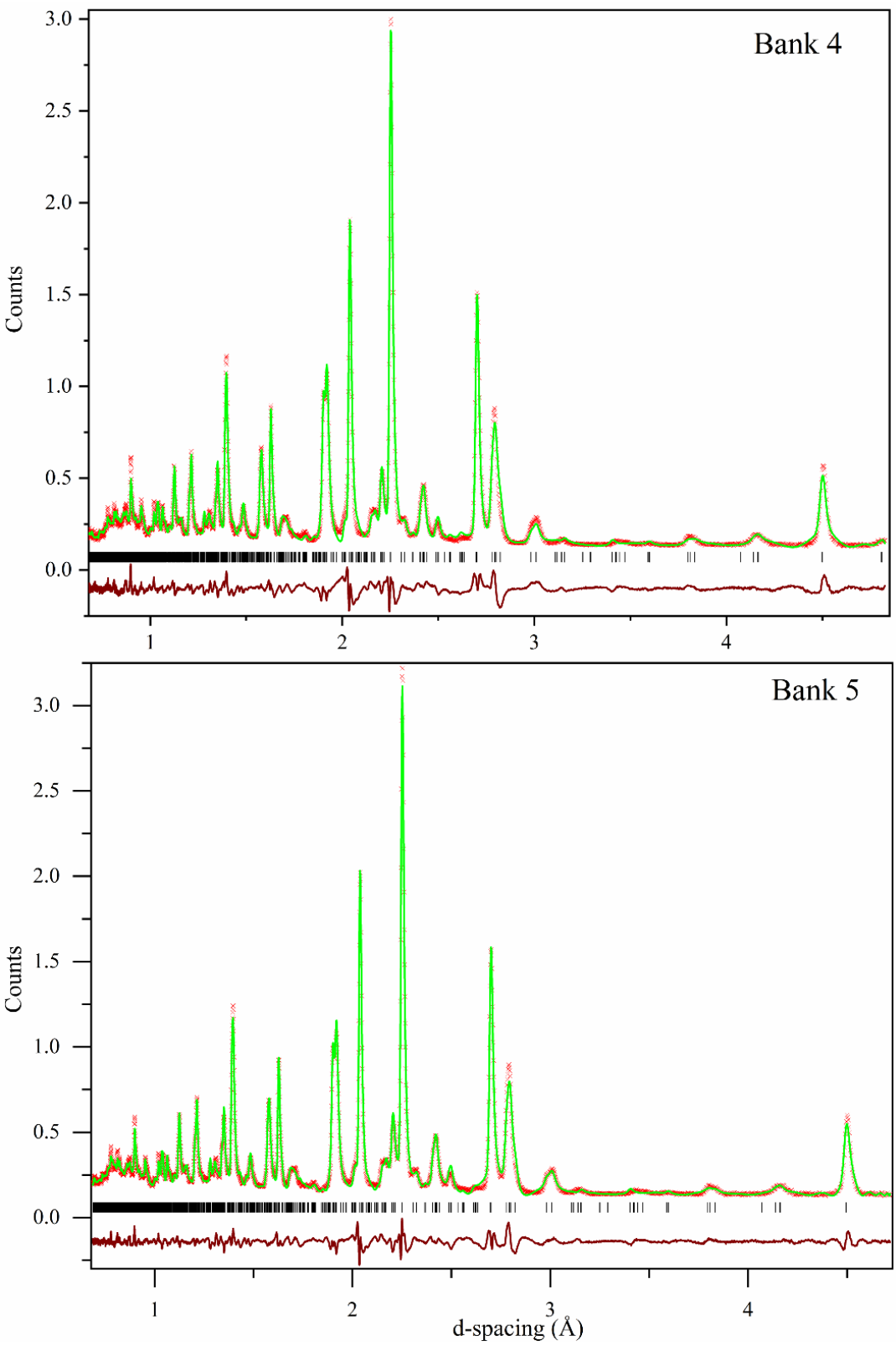


Figure 6.12. Observed, calculated and difference plots from the structural refinements of the large-scale sample of $LaSrCoRuO_5$ against NPD data collected at room temperature.

$LaSrCoRuO_5$, space group $P112_1$ (#4)						
Atom	Wyckoff	*x*	*y*	*z*	Fraction	B_{iso} equiv. (Å^2)
La1/Sr1	2*a*	0.1078(32)	0.3710(39)	0	$^1/_2/^1/_2$	1.62(5)
La2/Sr2	2*a*	0.8850(37)	0.6407(35)	0	$^1/_2/^1/_2$	1.62(5)
La3/Sr3	2*a*	0.3710(39)	0.1078(32)	0	$^1/_2/^1/_2$	1.62(5)
La4/Sr4	2*a*	0.6407(25)	0.8850(37)	0	$^1/_2/^1/_2$	1.62(5)
La5/Sr5	2*a*	0.8582(37)	0.1380(33)	0	$^1/_2/^1/_2$	1.62(5)
La6/Sr6	2*a*	0.1380(33)	0.8582(37)	0	$^1/_2/^1/_2$	1.62(5)
La7/Sr7	2*a*	0.3824(34)	0.6154(31)	0	$^1/_2/^1/_2$	1.62(5)
La8/Sr8	2*a*	0.6154(31)	0.3824(34)	0	$^1/_2/^1/_2$	1.62(5)
Co1	2*a*	$^5/_8$	$^5/_8$	$^3/_4$	1	0.82(2)
Co2	2*a*	0.612(3)	0.136(3)	$^3/_4$	1	0.82(2)
Co3	2*a*	$^1/_8$	$^1/_8$	$^3/_4$	1	0.82(2)
Co4	2*a*	0.136(3)	0.612(3)	$^3/_4$	1	0.82(2)
Ru1	*2a*	0.3648(7)	0.3648(7)	$^3/_4$	1	2.26(10)
Ru2	2*a*	0.8707(8)	0.3793(8)	$^3/_4$	1	2.26(10)
Ru3	2*a*	0.8852(7)	0.8852(7)	$^3/_4$	1	2.26(10)
Ru4	2*a*	0.3793(8)	0.8707(8)	$^3/_4$	1	2.26(10)
O1	2*a*	0.9679(10)	0.5359(9)	$^3/_4$	1	3.15(6)
O2	2*a*	0.2821(10)	0.7140(9)	$^3/_4$	1	3.15(6)
O3	2*a*	0.7140(10)	0.2821(9)	$^3/_4$	1	3.15(6)
O4	2*a*	0.5359(9)	0.9679(10)	$^3/_4$	1	3.15(6)
O5	2*a*	0.0334(8)	0.7865(8)	$^3/_4$	1	3.15(6)
O6	2*a*	0.2165(8)	0.4635(8)	$^3/_4$	1	3.15(6)

O7	2*a*	0.7864(8)	0.0334(8)	¾	1	3.15(6)
O8	2*a*	0.4635(8)	0.2165(8)	¾	1	3.15(6)
O9	2*a*	0.4922(10)	0.4922(10)	¾	1	3.15(6)
O10	2*a*	0.7578(10)	0.7578(10)	¾	1	3.15(6)
O11	2*a*	0.9923(10)	0.2577(10)	¾	1	3.15(6)
O12	2*a*	0.2577(10)	0.9923(10)	¾	1	3.15(6)
O13	2*a*	0.8819(6)	0.8819(6)	0.5093(11)	1	3.15(6)
O14	2*a*	0.8819(6)	0.8819(6)	0.9907(11)	1	3.15(6)
O15	2*a*	0.3681(6)	0.3681(6)	0.9907(11)	1	3.15(6)
O16	2*a*	0.3681(6)	0.3681(6)	0.5093(11)	1	3.15(6)
O17	2*a*	0.6070(16)	0.1430(16)	0.0001(10)	1	3.15(6)
O18	2*a*	0.6193(19)	0.1307(19)	0.4999(10)	1	3.15(6)
O19	2*a*	0.1431(16)	0.6070(16)	0.0001(10)	1	3.15(6)
O20	2*a*	0.1307(19)	0.6193(19)	0.4999(10)	1	3.15(6)
a = 10.813(3) Å, b = 10.823(3) Å, c = 8.1626(1) Å, γ = 90.553(3)°						
wRp = 5.97%; Rp = 5.14%						

Table 6.2. Parameters from the structural refinements of the large-scale sample of $LaSrCoRuO_5$ against NPD data collected at room temperature.

Cation	Anion	Bond length (Å)	Cation	Anion	Bond length (Å)
Co(1)	O9	2.032(11)	Ru(1)	O(6)	1.926(12)
	O10	2.032(11)		O(8)	1.927(12)
	O15	2.119(9)		O(9)	1.949(14)
	O16	2.119(9)		O(15)	1.965(9)
Co(3)	O11	2.030(11)		O(16)	1.965(9)

	O12	2.030(11)	Ru(2)	O(1)	1.994(14)
	O13	2.119(9)		O(3)	1.993(14)
	O14	2.119(9)		O(11)	1.860(14)
Co(2)	O3	1.929(12)		O(19)	2.052(2)
	O4	1.997(12)		O(20)	2.041(1)
	O7	2.189(10)	Ru(3)	O(5)	1.926(12)
	O8	1.827(10)		O(7)	1.927(12)
	O17	2.043(1)		O(10)	1.949(14)
	O18	2.043(1)		O(13)	1.965(9)
Co(4)	O1	1.996(12)		O(14)	1.965(9)
	O2	1.928(12)	Ru(4)	O(2)	1.994(14)
	O5	2.190(10)		O(4)	1.993(14)
	O6	1.828(10)		O(12)	1.860(14)
	O19	2.043(1)		O(17)	2.052(2)
	O20	2.043(1)		O(18)	2.041(1)

Table 6.3. Selected bond lengths from the refined structure of $LaSrCoRuO_5$ at 300 K.

The refined crystal structure of $LaSrCoRuO_5$ shows that the Co cations are located in two different geometries, namely, square-planar sites (occupied by Co1 and Co3) and octahedral sites (occupied by Co2 and Co4). Calculating bond valence sums for the four CoO_x polyhedra yields values consistent with Co^{+} on sites Co(1) and Co(3) (square-planar sites) and Co^{3+} on sites Co(2) and Co(4) (octahedral sites). Bond valence sums calculated for the Ru cations in the square-based pyramidal sites (Ru1, Ru2, Ru3, Ru4) are consistent with the presence of Ru^{3+} centres. This gives an overall formulation of $LaSrCo_{0.5}^{+}Co_{0.5}^{3+}Ru^{3+}O_5$. The presence of a 1:1 ratio of Co^{+} and Co^{3+} centres indicates an effective disproportionation of Co^{2+}, which is highly unusual in the solid state.

Cation	BVS	Cation	BVS
Co(1)	+1.42	Ru(1)	+3.69
Co(2)	+2.69	Ru(2)	+3.35
Co(3)	+1.42	Ru(3)	+3.69
Co(4)	+2.69	Ru(4)	+3.35

Table 6.4. Calculated bond valence sums of the transition metal centres from the refined structure of $LaSrCoRuO_5$.

6.3.3 Magnetic Characterisation of $LaSrCoRuO_5$

6.3.3.1 SQUID Magnetometry

Magnetisation data were collected from the large-scale sample of $LaSrCoRuO_5$ using a ferromagnetic subtraction method (Section 2.8.1). The saturated magnetic moment increases sharply at T ~ 150 K, suggesting an onset of ferromagnetic order. The paramagnetic susceptibility data in the temperature range of 140 K $\leq$ T $\leq$ 300 K obey the Curie-Weiss law ($\chi = C/(T - \theta)$), yielding a value of Curie constant 3.782(7) cm^3 K mol^{-1} and a value of Weiss constant 81.9(4) K. The positive value of the Weiss constant indicates there are ferromagnetic interactions within the sample.

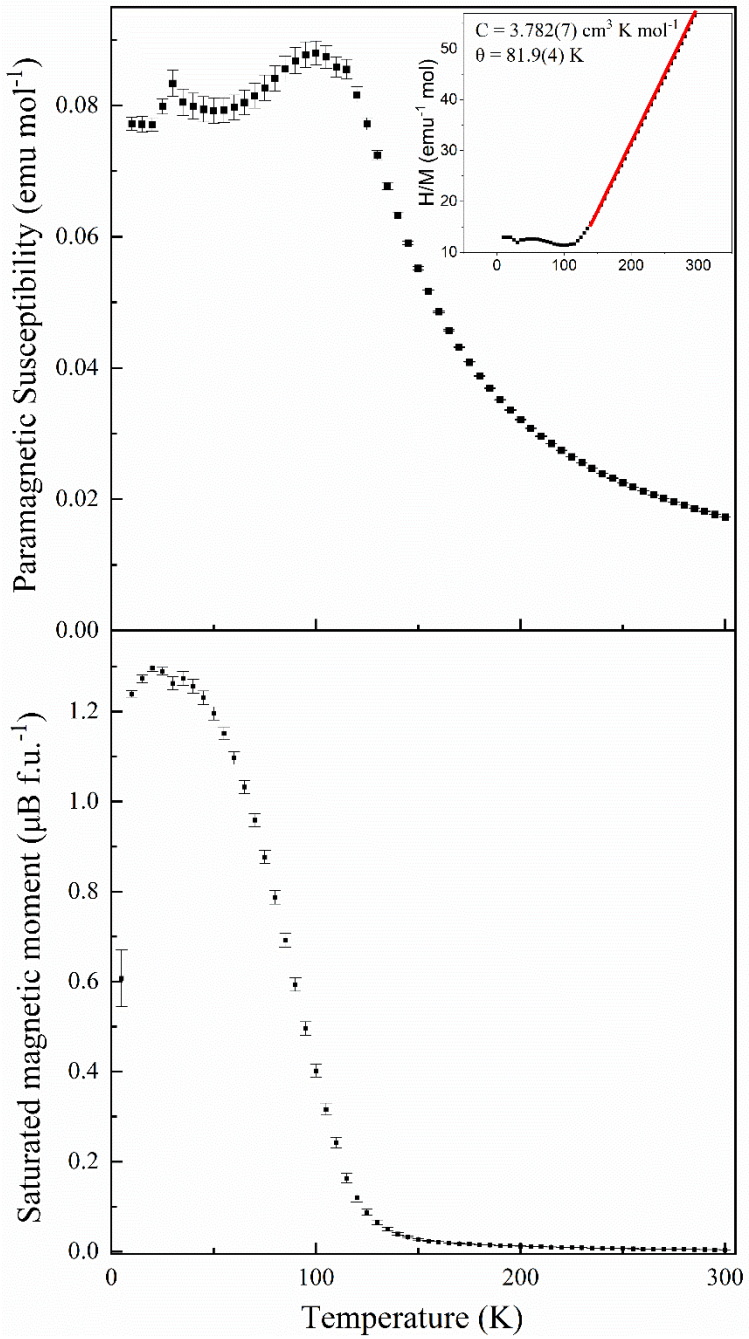


Figure 6.13. Paramagnetic susceptibility (top) and saturated magnetic moment (bottom) of $LaSrCoRuO_5$ collected as a function of temperature. Inset shows the fit to the Curie-Weiss law in the temperature range 140 ≤ T/K ≤ 300.

The magnetisation data collected from $LaSrCoRuO_5$ yield Curie constant 3.782(7) $cm^3 K mol^{-1}$, which corresponds to a μ_{eff}^2 value of 30.256 μB^2. If Co^+ centres at the D_{4h} sites adopt a high spin state (S = 1), Co^{3+} at the O_h sites adopt a low spin state (S = 0) and Ru^{3+} at the C_{4v} sites adopt a low spin state (S = 0.5), the spin-only calculation of the expected magnetic moment of

this combination is 7 μB^2. This value is too small compared with the experimental value even if spin orbit coupling effects are considered. However, even if the Co^{3+} centres at the O_h sites adopt a high spin configuration (S = 2), Co^{+} centres at the D_{4h} sites adopt a high spin state (S = 1) and Ru^{3+} centres at the C_{4v} sites adopt a low spin state (S = 0.5), this combination yields a μ_{eff}^2 value of 19 μB^2, which is still very small compared with the experimental value. This indicates that the 'simple paramagnetic' description is not valid for $LaSrCoRuO_5$ in the temperature range 140 K ≤ T ≤ 300 K. Instead, the magnetic behaviour of the sample is mimicking the Curie-Weiss law rather obeying it. This observation suggests that there are strong magnetic interactions between the transition metal centres in this temperature range.

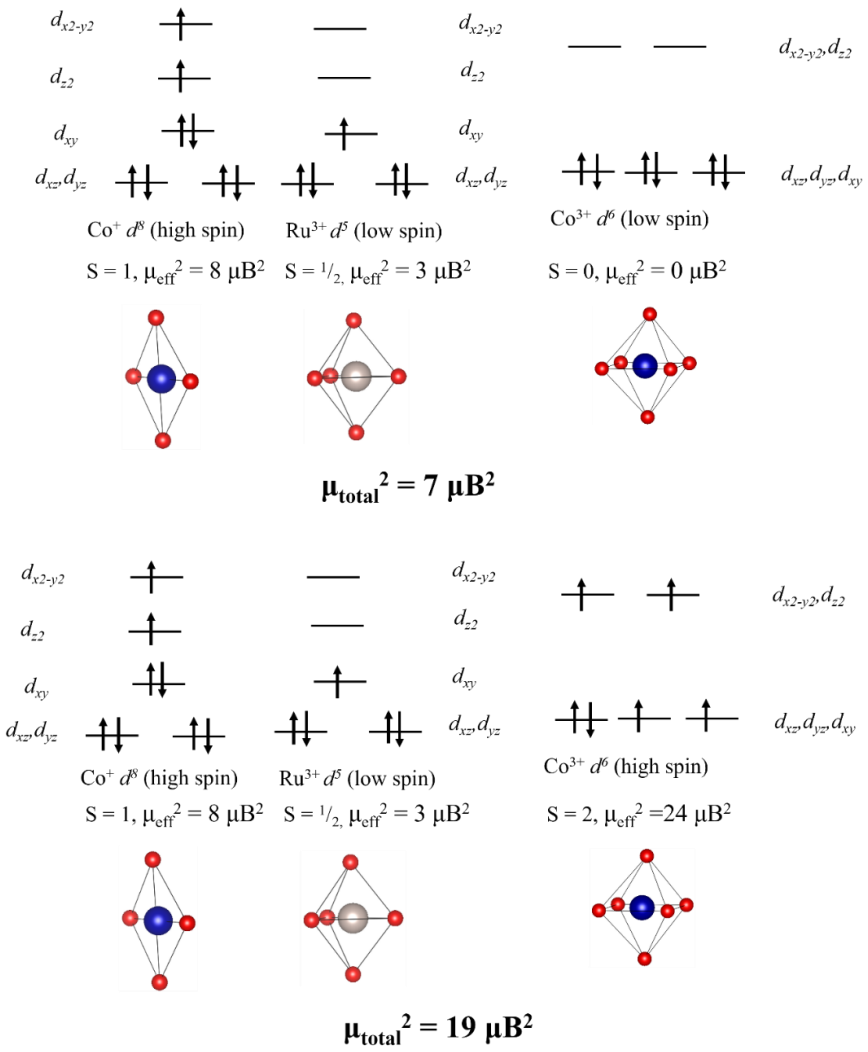


Figure 6.14. Predicted μ_{eff}^2 of $LaSrCoRuO_5$ for Co^{+}, Ru^{3+} and Co^{3+} with different possible electronic configurations.

Magnetisation-field data were collected at 5 K and 300 K. At 5 K, the magnetisation data as a function of applied field exhibit a hysteresis loop, which is consistent with the assignment of ferromagnetic order at low temperature. Close inspection of the hysteresis loop shows a slight displacement from the origin, showing a slight glassy component.

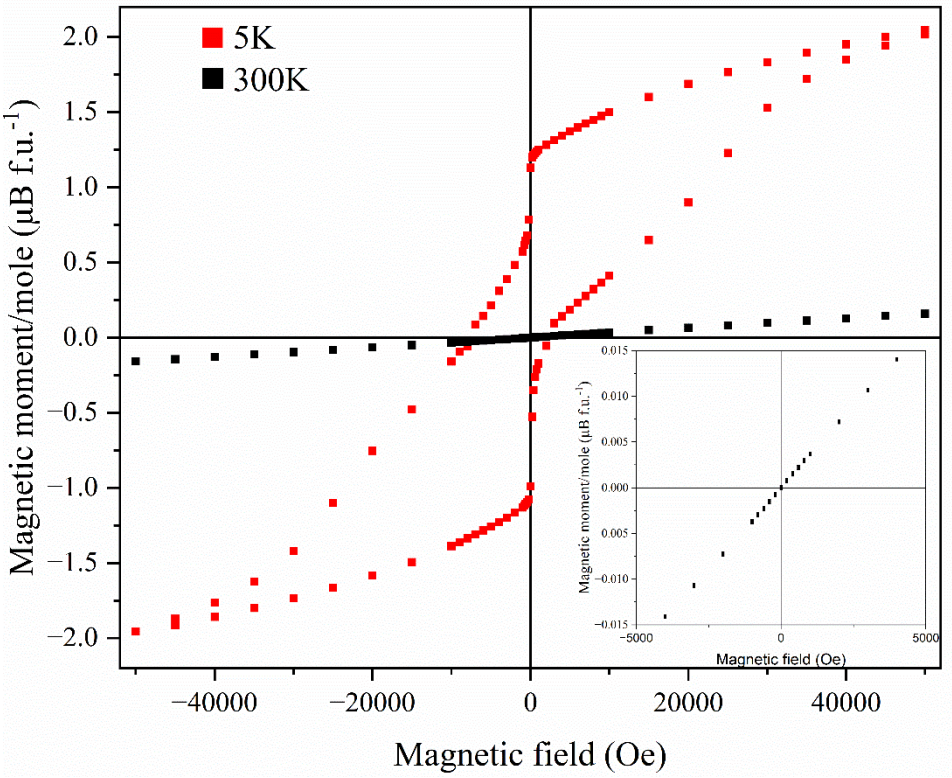


Figure 6.15. Magnetic isotherms collected from the large-scale sample of $LaSrCoRuO_5$ at 5 K and 300 K. Inset shows zoom in region of the room temperature magnetic isotherm plot.

6.3.3.2 Low Temperature Neutron Powder Diffraction Data

The structural model of $LaSrCoRuO_5$ obtained from the refinement of $LaSrCoRuO_5$ against NPD data collected at room temperature (Fig 6.10) was refined against the NPD data collected at 5 K. During the refinement, the oxygen atoms were allowed to move within the constraint imposed (Section 6.3.2.3). The refinements against the NPD data achieved good statistical fits. The observed, calculated and difference plots from the refinements of $LaSrCoRuO_5$ are shown in Fig 6.16. Full structural details from the refinements of $LaSrCoRuO_5$ against NPD data

collected at 5 K are shown in Table 6.5; a comparison of the average bond lengths at 5 K and 300 K is shown in Table 6.6.

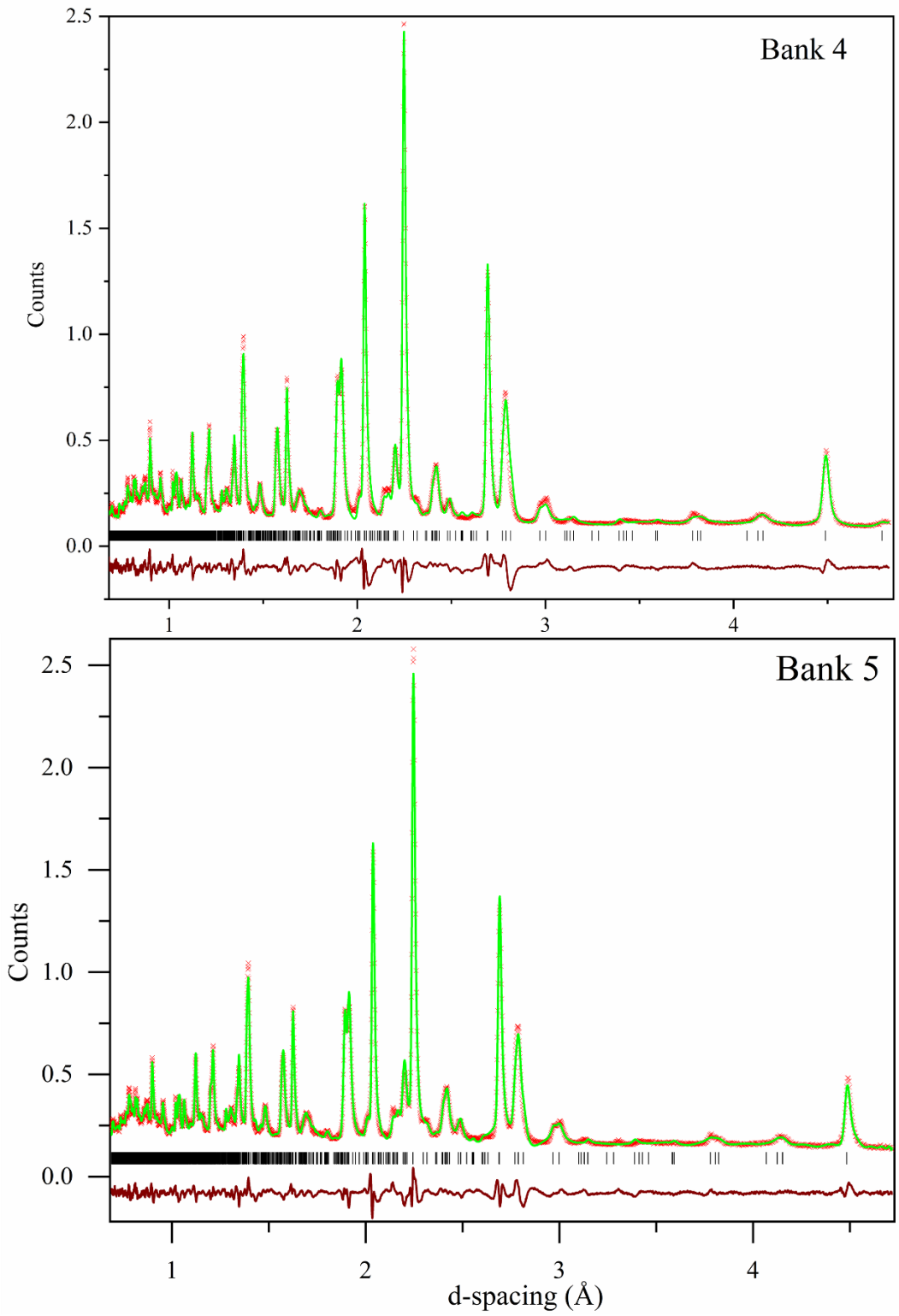


Figure 6.16. Observed, calculated and difference plots from the refinement of $LaSrCoRuO_5$ against NPD data collected at 5 K.

$LaSrCoRuO_5$, space group $P2_1$ (#4)						
Atom	Wyckoff	*x*	*y*	*z*	Fraction	B_{iso} equiv. (Å^2)
La1/ Sr1	2*a*	0.1078(32)	0.3710(39)	0	$^1/_2/^1/_2$	0.32(4)
La2/Sr2	2*a*	0.8850(37)	0.6407(35)	0	$^1/_2/^1/_2$	0.32(4)
La3/Sr3	2*a*	0.3710(39)	0.1078(32)	0	$^1/_2/^1/_2$	0.32(4)
La4/Sr4	2*a*	0.6407(25)	0.8850(37)	0	$^1/_2/^1/_2$	0.32(4)
La5/Sr5	2*a*	0.8582(37)	0.1380(33)	0	$^1/_2/^1/_2$	0.32(4)
La6/Sr6	2*a*	0.1380(33)	0.8582(37)	0	$^1/_2/^1/_2$	0.32(4)
La7/Sr7	2*a*	0.3824(34)	0.6154(31)	0	$^1/_2/^1/_2$	0.32(4)
La8/Sr8	2*a*	0.6154(31)	0.3824(34)	0	$^1/_2/^1/_2$	0.32(4)
Co1	2*a*	$^5/_8$	$^5/_8$	$^3/_4$	1	0.64(28)
Co2	2*a*	0.615(3)	0.136(3)	$^3/_4$	1	0.64(28)
Co3	2*a*	$^1/_8$	$^1/_8$	$^3/_4$	1	0.64(28)
Co4	2*a*	0.136(3)	0.615(3)	$^3/_4$	1	0.64(28)
Ru1	*2a*	0.3643(5)	0.3643(5)	$^3/_4$	1	0.67(9)
Ru2	2*a*	0.8709(6)	0.3791(6)	$^3/_4$	1	0.67(9)
Ru3	2*a*	0.8857(5)	0.8857(5)	$^3/_4$	1	0.67(9)
Ru4	2*a*	0.3791(6)	0.8709(6)	$^3/_4$	1	0.67(9)
O1	2*a*	0.9670(10)	0.5359(9)	$^3/_4$	1	1.80(5)
O2	2*a*	0.2821(10)	0.7141(9)	$^3/_4$	1	1.80(5)
O3	2*a*	0.7141(9)	0.2821(10)	$^3/_4$	1	1.80(5)
O4	2*a*	0.5359(9)	0.9670(10)	$^3/_4$	1	1.80(5)
O5	2*a*	0.0334(8)	0.7864(8)	$^3/_4$	1	1.80(5)
O6	2*a*	0.2166(8)	0.4635(8)	$^3/_4$	1	1.80(5)

O7	2*a*	0.7864(8)	0.0334(8)	¾	1	1.80(5)
O8	2*a*	0.4635(8)	0.2166(8)	¾	1	1.80(5)
O9	2*a*	0.4920(8)	0.4920(8)	¾	1	1.80(5)
O10	2*a*	0.7580(8)	0.7580(8)	¾	1	1.80(5)
O11	2*a*	0.9940(8)	0.2560(8)	¾	1	1.80(5)
O12	2*a*	0.2560(8)	0.9940(8)	¾	1	1.80(5)
O13	2*a*	0.8819(6)	0.8819(6)	0.5093(11)	1	1.80(5)
O14	2*a*	0.8819(6)	0.8819(6)	0.9907(11)	1	1.80(5)
O15	2*a*	0.3681(6)	0.3681(6)	0.9907(11)	1	1.80(5)
O16	2*a*	0.3681(6)	0.3681(6)	0.5093(11)	1	1.80(5)
O17	2*a*	0.6070(16)	0.1431(16)	0.9997(10)	1	1.80(5)
O18	2*a*	0.1431(16)	0.6070(16)	0.9997(10)	1	1.80(5)
O19	2*a*	0.1307(19)	0.6193(19)	0.5003(10)	1	1.80(5)
O20	2*a*	0.6193(19)	0.1307(19)	0.5003(10)	1	1.80(5)
a = 10.776(3) Å, *b* = 10.785(3) Å, *c* = 8.1598(1) Å, *γ* = 90.651(3)°						
wRp = 5.93%; Rp = 4.91%						

Table 6.5. Parameters from the structural refinement of $LaSrCoRuO_5$ against NPD data collected at 5 K.

Cation	**Anion**	**Average Bond lengths/ Å**	
		300 K	**5 K**
Co(1)	O	2.076(10)	2.0674(5)
Co(2)	O	2.0046(10)	1.9984(7)
Co(3)	O	2.075(10)	2.0633(5)

Co(4)	O	2.0046(10)	1.9984(7)
Ru(1)	O	1.9465(11)	1.9445(5)
Ru(2)	O	1.9881(15)	1.9878(5)
Ru(3)	O	1.9465(11)	1.9445(5)
Ru(4)	O	1.9881(13)	1.9878(7)

Table 6.6. Selected bond lengths and bond angles from the refined structure of $LaSrCoRuO_5$ at 300 K and 5 K.

The lattice parameters and the bond lengths extracted from the structural refinement of $LaSrCoRuO_5$ against NPD data collected at 5 K are shorter than those extracted from the structural refinement against NPD data collected at room temperature. This was expected due to the thermal expansion of the unit cell at elevated temperatures.

A direct comparison of the NPD data collected at room temperature and 5 K shows that NPD data collected at 5 K do not have any extra magnetic scattering peaks. This is not surprising as the magnetisation data show evidence of ferromagnetic ordering at low temperature, therefore any additional intensities should be at the same position as the crystallographic peaks. However, there are no obvious intensity mismatches between the data sets collected at room temperature and 5 K, thus the scattering from the ferromagnetic state of $LaSrCoRuO_5$ is not observed.

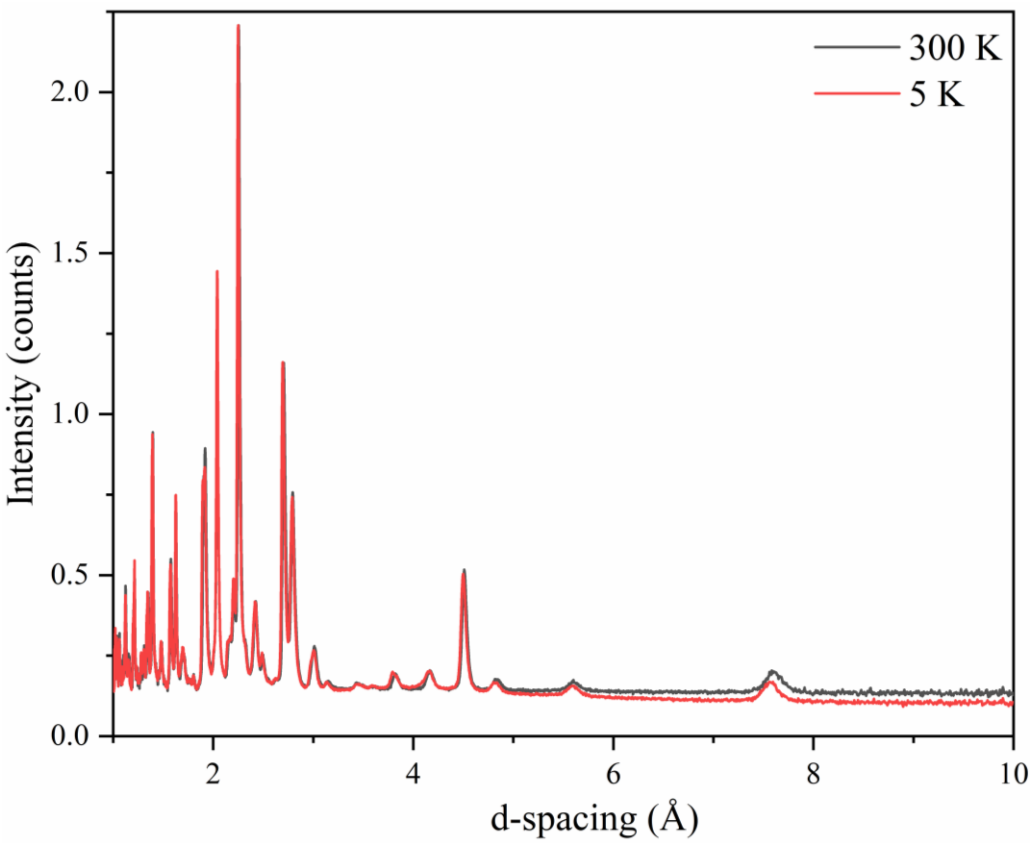


Figure 6.17. Direct comparison of the neutron powder diffraction data of $LaSrCoRuO_5$ collected at 5 K and 300 K.

6.4. Discussion

6.4.1 Crystallographic Structure of $LaSrCoRuO_5$

Reaction between $LaSrCoRuO_6$ and a Zr getter at 450 °C results in a topochemical extraction of oxide anions, yielding an oxygen deficient phase $LaSrCoRuO_5$. The structure of $LaSrCoRuO_5$ is complex and can only be described using a crystallographic unit cell with a $2\sqrt{2} \times 2\sqrt{2} \times 2$ geometric expansion of the aristotype perovskite unit cell (ABO_3). The anion framework is modified such that there are three different transition metal geometries in the structure, namely square-planar, square-based pyramidal and octahedral coordination. The structure of $LaSrCoRuO_5$ consists of a network of corner-sharing polyhedra (CoO_6 octahedra, CoO_4 square-planar units and RuO_5 square-based pyramidal units). There are two distinct RuO_5

units: One is linked to four CoO_6 octahedra and a CoO_4 square-planar unit whilst the other is linked to two CoO_6 octahedra and three CoO_4 square-planar units. There is a ($^1/_4$,$^1/_4$, 0) shift between the layers along the *c* direction so that the B-site rocksalt cation ordering and the anion-vacancy ordering can be preserved (Fig 6.18). It is worth mentioning that the CoO_4 square-planar units exhibit two perpendicular orientations, where they are parallel to [110] and [1-10] directions respectively.

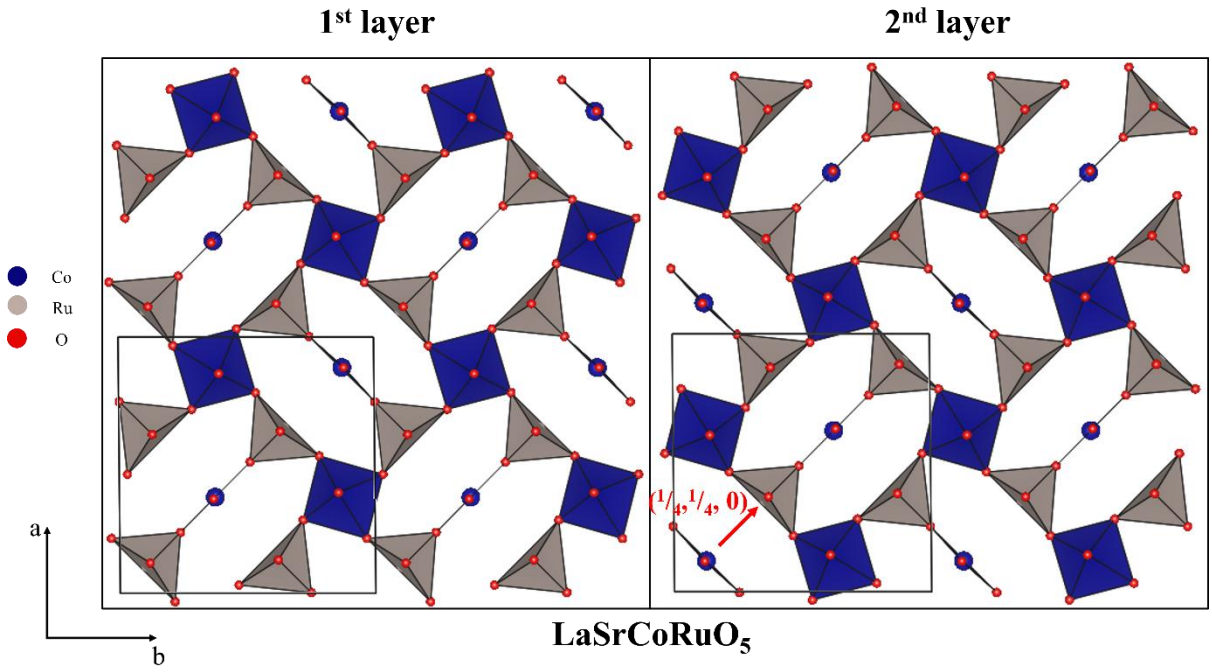


Figure 6.18. A comparison of the 1st layer and 2nd layer of the structure of $LaSrCoRuO_5$, the arrow indicates direction of shifting between layers. La/Sr atoms were omitted for clarity.

The structure of $LaSrCoRuO_5$ raises a question as to why this oxygen deficient phase adopts this type of anion-vacancy ordering. It is likely that the disproportionation of the Co^{2+} centres into a 1:1 ratio of Co^+ and Co^{3+} centres is one of the driving forces for $LaSrCoRuO_5$ to adopt this type of anion-vacancy ordered structure. Since there are three different types of transition metal cation in the structure (Co^+, Co^{3+}, Ru^{3+}), the existence of three different geometries in this structure allows each transition metal cation to reside in its most favourable coordination site. However, it is unclear what factor is aiding the formation of $LaSrCoRuO_5$ phase which

leads to the disproportionation of the Co^{2+} centres. Further investigations on the primary driving force for the $LaSrCoRuO_5$ structural arrangement will be discussed in Chapter 8.

6.4.2 Room Temperature Structural Data

A comparison of the room temperature average Co^{+} – O and Co^{3+} – O bond lengths with other reported compounds are listed below.

Compounds	Bond	Average Bond lengths(Å)
$LaSrCoRuO_5$	Co^{3+} – O	2.0046(9)
$LiCoO_2$[78]	Co^{3+} (LS) – O	1.9213(12)
$LaSrCoRuO_5$	Co^{+} – O	2.075(1)
$LaSrCoRuO_4$	Co^{+} (HS) – O	2.022(1)

Table 6.7. Average Co-O bond lengths in $LaSrCoRuO_5$ and in other selected compounds.

The average bond length of Co^{+}– O in $LaSrCoRuO_5$ is similar to that from $LaSrCoRuO_4$ (Chapter 7), suggesting that the Co^{+} centres in $LaSrCoRuO_5$ adopt a high spin configuration. In addition, the Co^{3+} – O in $LaSrCoRuO_5$ is slightly longer than the reported Co^{3+} (LS) – O in $LiCoO_2$.

6.4.3 Disproportionation in $LaSrCoRuO_5$

In the $LaSrCoRuO_5$ phase, the B-site cations have a summed charge of +5, suggesting that the oxidation states for the B-site transition metal cations are Co^{2+} and Ru^{3+} respectively. The calculated bond valence sums have indicated a disproportionation of Co^{2+} centres into a 1:1 ratio of Co^{+} and Co^{3+} centres, which reside at the D_{4h} sites and O_h sites respectively. As discussed in Section 6.4.2, the average bond length of Co^{+}– O from the refined structure of $LaSrCoRuO_5$ are consistent with the presence of high spin Co^{+} (S = 1) centres. In order to rationalise the disproportionation of Co^{2+} centres, the Co^{3+} centres have to be in a low spin

configuration. As the ligand field stabilisation energy gain by the Co^{3+} d^6, S = 0 in the O_h sites can drive the Co^{2+} disproportionation, which is more favourable compared with locating d^7 Co^{2+} (S = 1) in this site.

Analogous disproportionation to 'avoid' the d^7 electron count has been observed in various 4*d*/5*d* transition metals.[79–82] For example, in $LaSrCo_{0.5}Rh_{0.5}O_{3.25}$, the Rh^{2+} centres disproportionate into a 1:1 ratio of Rh^+ centres and Rh^{3+} centres. This compound contains Rh^+ centres residing at the D_{4h} sites and Rh^{3+} centres residing at the C_{4v} sites. The primary drive for this disproportionation is the ligand field stabilisation energy gained by the Rh^+ (d^8 S = 0) in the square-planar coordination sites and the Rh^{3+} (d^6 S = 0) in the square-based pyramidal sites. This combination is more favourable than Rh^{2+} (d^7 S = 0.5) residing in these two sites.[80] Similar behaviour is also observed in $BiPd_2O_4$, which is better described as $Bi_2Pd^{2+}{}_3Pd^{4+}O_8$. This compound contains square-planar $Pd^{2+}O_4$ (d^8 S = 0) and octahedral $Pd^{4+}O_6$ (d^6 S = 0) units.[81] All these observations suggest that ligand field stabilisation energy gained by d^8 (S = 0) and d^6 (S = 0) is the primary driving force for the disproportionation of transition metal cations that contain d^7 electron count.

However, unlike 4*d*/5*d* transition metals discussed above, 3*d* transition metals have a much weaker ligand field stabilisation energy. This is because 3*d* orbital is more contracted compared with 4*d*/5*d* orbitals, which makes the overlapping between the metal 3*d* and O2*p* less effective. The smaller ligand field provides a smaller energetic stabilization for the d^8 octahedral and d^6 square-planar electron count/coordination combinations. Therefore, it is highly unusual to see the disproportionation of Co^{2+}, a common oxidation state for cobalt cations, undergoes a ligand field stabilization energy driven disproportionation.

There are some examples of 3*d* transition metal cations disproportionation in extended oxides, such as Fe^{4+} and Ni^{3+}. However, in these cases, the driving force of the disproportionation is a metal-to-insulator phase transition, which is driven by the presence of a single electron in the

e_g orbitals in theses oxide phases, rather than the ligand field stabilisation energy gain.[83–86] The unique observation of the ligand field stabilisation energy driven disproportionation of Co^{2+} has shown that low temperature topochemical reduction is a powerful method to synthesise novel material with unusual chemical and physical properties.

6.4.4 Low Temperature Magnetisation Data

The magnetisation data collected from the sample of $LaSrCoRuO_5$ indicate that $LaSrCoRuO_5$ is a ferromagnet at low temperature. However, neutron powder diffraction data collected at 5 K do not show any extra magnetic scattering.

Since the Co^+ centres at the D_{4h} sites are thought to adopt a high spin electronic configuration (S = 1), the Co^{3+} centres at the O_h sites are thought to adopt a low spin electronic configuration (S = 0) and the Ru^{3+} centres at the C_{4v} sites are thought to adopt a low spin electronic configuration (S = 0.5), the magnetic behaviour of $LaSrCoRuO_5$ can be rationalised by considering the magnetic coupling interactions between the Co^+ centres (S = 1) and the Ru^{3+} centres (S = 0.5). The magnetic couplings can be separated into two types, the intralayer coupling (coupling in the *ab* plane) and the interlayer coupling (coupling along the *c* axis). There are two magnetic couplings within the layer to consider between Co^+ D_{4h} and Ru^{3+} C_{4v}: the in-plane coupling is dominated by the σ-type superexchange coupling $(Co\ d_{x2-y2})^1 – O – (Ru\ d_{z2})^0$, which is strongly ferromagnetic. This is followed by a weak contribution from the direct exchange $(Co\ d_{z2})^1 – (Ru\ d_{z2})^0$ (Fig 6.19).

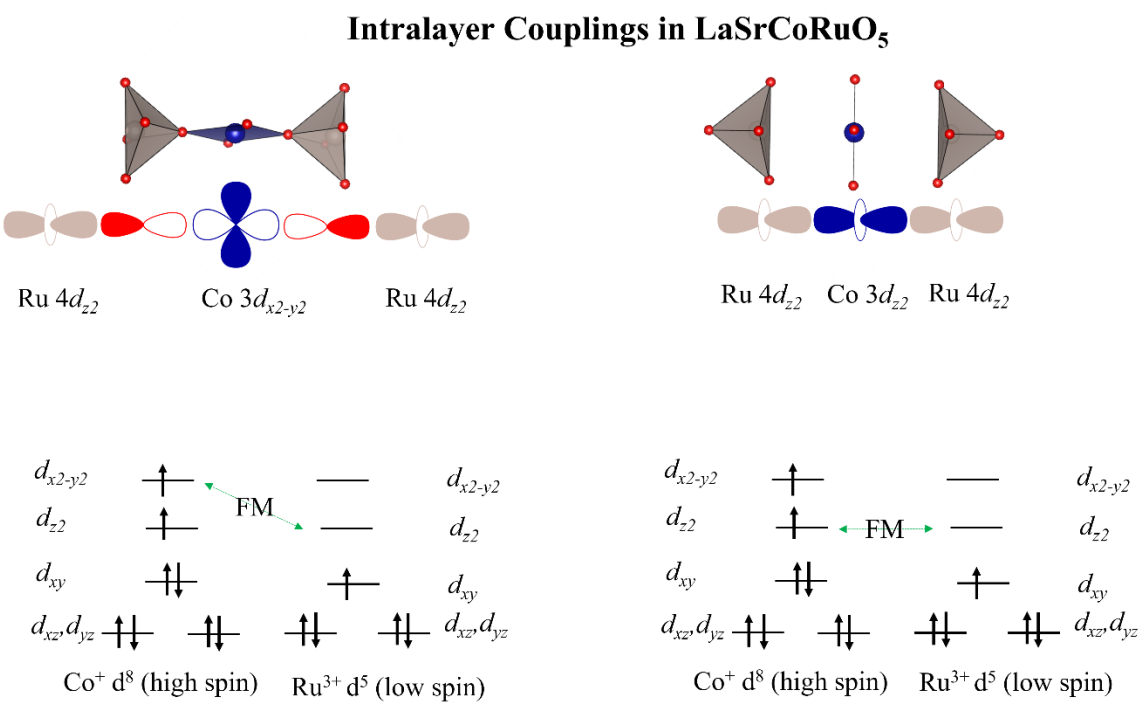


Figure 6.19. Intralayer magnetic couplings between Co^{+} and Ru^{3+} centres in $LaSrCoRuO_5$.

The interlayer couplings between the Co^{+} centres (D_{4h}) and the Ru^{3+} centres (C_{4v}) also need to be considered. As shown in Fig 6.20, there are two magnetic couplings along the *c* direction: The interlayer coupling is dominated by the strong σ-type ferromagnetic superexchange coupling $(Co^{+}\ d_{x2-y2})^1 - O - (Ru^{3+}\ d_{x2-y2})^0$, with weak contributions from the π-symmetry couplings $(Co^{+}\ d_{xy})^2 - O - (Ru^{3+}\ d_{xy})^1$ (Fig 6.20). All the magnetic coupling interactions are ferromagnetic, consistent with the low temperature magnetisation data.

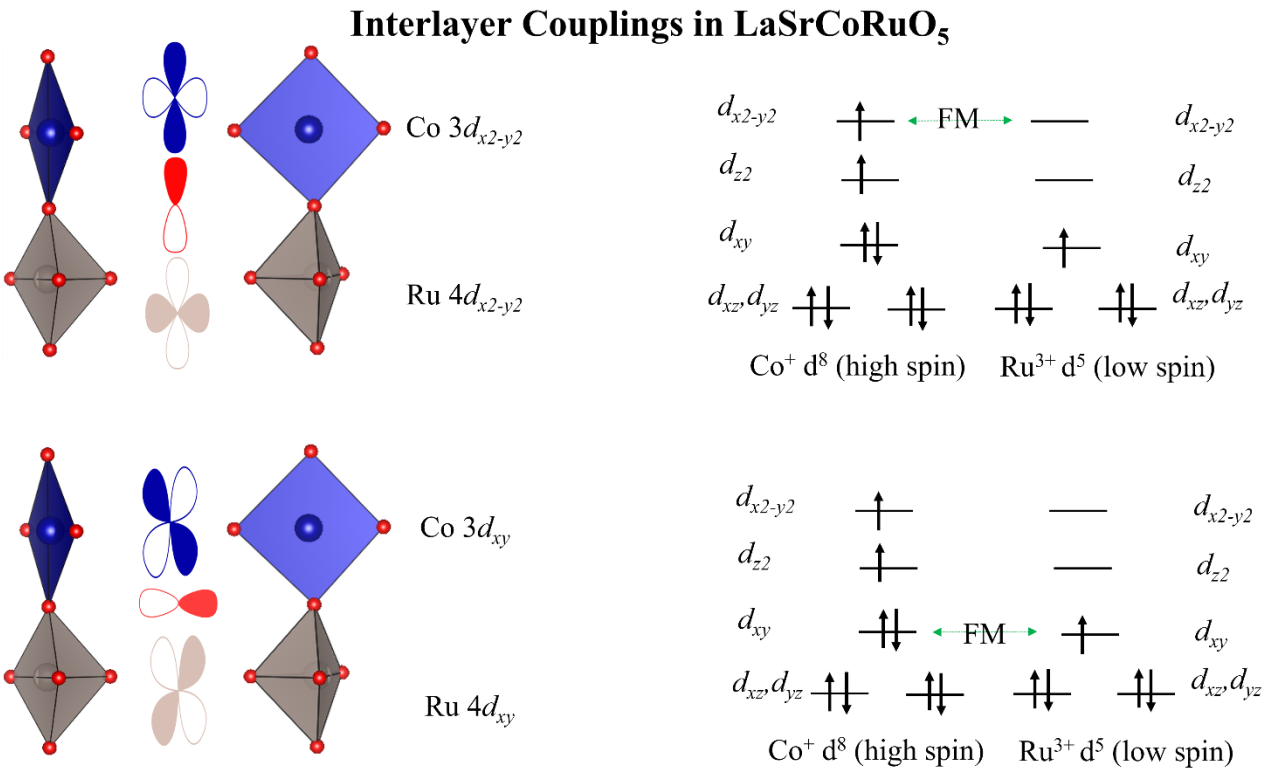


Figure 6.20. Interlayer couplings between Co^{+} and Ru^{3+} centres in $LaSrCoRuO_5$.

6.5 Conclusion

Topochemical reduction of $LaSrCoRuO_6$ with Zr yields $LaSrCoRuO_5$. Electron diffraction, synchrotron X-ray powder diffraction and neutron powder diffraction data collected from this novel reduced phase have justified the need to use a larger unit cell to describe the structure of $LaSrCoRuO_5$. The expansion of the unit cell is a result of the complicated oxygen-vacancy ordering. The reduction process modifies the anion sublattice, and three different transition metal cations geometries result. Bond valence sum calculations show that the Co^{2+} centres have disproportionated into a 1:1 ratio of Co^{+} and Co^{3+} centres, which reside at the D_{4h} and O_h sites respectively.

Low temperature neutron powder diffraction data collected from $LaSrCoRuO_5$ do not show additional magnetic diffraction intensities, despite the magnetisation data collected from SQUID show evidence of ferromagnetic ordering upon cooling to ~ 140 K. The lack of any

long-range magnetic ordering is surprising, and further investigation of the magnetisation properties of $LaSrCoRuO_5$ is needed.

Chapter 7 Synthesis and Characterisation of $LaSrCoRuO_4$

7.1 Introduction

Successful synthesis of $LaSrCoRuO_4$ can be achieved by reacting the B-site cation ordered double perovskite $LaSrCoRuO_6$ with LiH under flowing argon at 375 °C. As discussed in Chapter 5, the reduction of $LaSrCoRuO_6$ to form $LaSrCoRuO_4$ proceeds through an intermediate phase $LaSrCoRuO_5$. Therefore, the reaction equations from the reduction of $LaSrCoRuO_6$ to form $LaSrCoRuO_4$ via $LaSrCoRuO_5$ are proposed below:

$LaSrCoRuO_6 + 2\ LiH \rightarrow LaSrCoRuO_5 + Li_2O + H_2$

$LaSrCoRuO_5 + 2\ LiH \rightarrow LaSrCoRuO_4 + Li_2O + H_2$

In summary, the overall reaction equation is shown as follows:

$LaSrCoRuO_6 + 4\ LiH \rightarrow LaSrCoRuO_4 + 2\ Li_2O + 2\ H_2$

Detailed characterisation of this reduced $LaSrCoRuO_4$ phase will be described in this chapter.

7.2 Experimental

A powdered sample of $LaSrCoRuO_6$ was synthesised through a citrate gel method. A detailed description of the synthesis of $LaSrCoRuO_6$ is shown in Section 5.2.1. A sample of $LaSrCoRuO_4$ suitable for analysis by neutron powder diffraction was prepared: 1 g of quenched $LaSrCoRuO_6$ was ground with 8 mole equivalents of LiH in an argon-filled glove box. The reaction mixture was transferred into an open pyrex ampoule and heated to 375 °C at 1 °C min^{-1} under a constant flow of argon using a flowing tube furnace set-up for a period of 2 days (Section 2.2.2). The reaction progress was monitored by X-ray powder diffraction. Once the reaction was deemed complete, the mixture was washed with methanol under nitrogen to remove the by-product Li_2O and any unreacted LiH. The reduced sample was then dried under vacuum.

7.3 Results

7.3.1 Thermogravimetric Analysis of $LaSrCoRuO_{6-x}$

The oxygen content of the reduced $LaSrCoRuO_{6-x}$ phase was determined using thermogravimetric analysis (TGA). An oxidative TGA measurement was performed by heating a small quantity of the reduced $LaSrCoRuO_{6-x}$ sample to 800 °C under a steady flow of O_2. The reduced $LaSrCoRuO_{6-x}$ sample was kept at 800 °C for 2 hours before being cooled to room temperature. During the reaction, a mass increase of 6.39% was observed, corresponding to a composition of $LaSrCoRuO_{4.07}$ (Fig 7.1). As noted later, the sample contains a small quantity of $LaSrCoRuO_5$. Once this is taken into account, this mass gain corresponds to a composition of $LaSrCoRuO_4$ for the majority phase. X-ray powder diffraction data collected from the re-oxidised $LaSrCoRuO_{6-x}$ after the TGA experiment confirmed a complete re-oxidation to its parent $LaSrCoRuO_6$ phase had taken place. Henceforth, this reduced phase will be referred to as $LaSrCoRuO_4$.

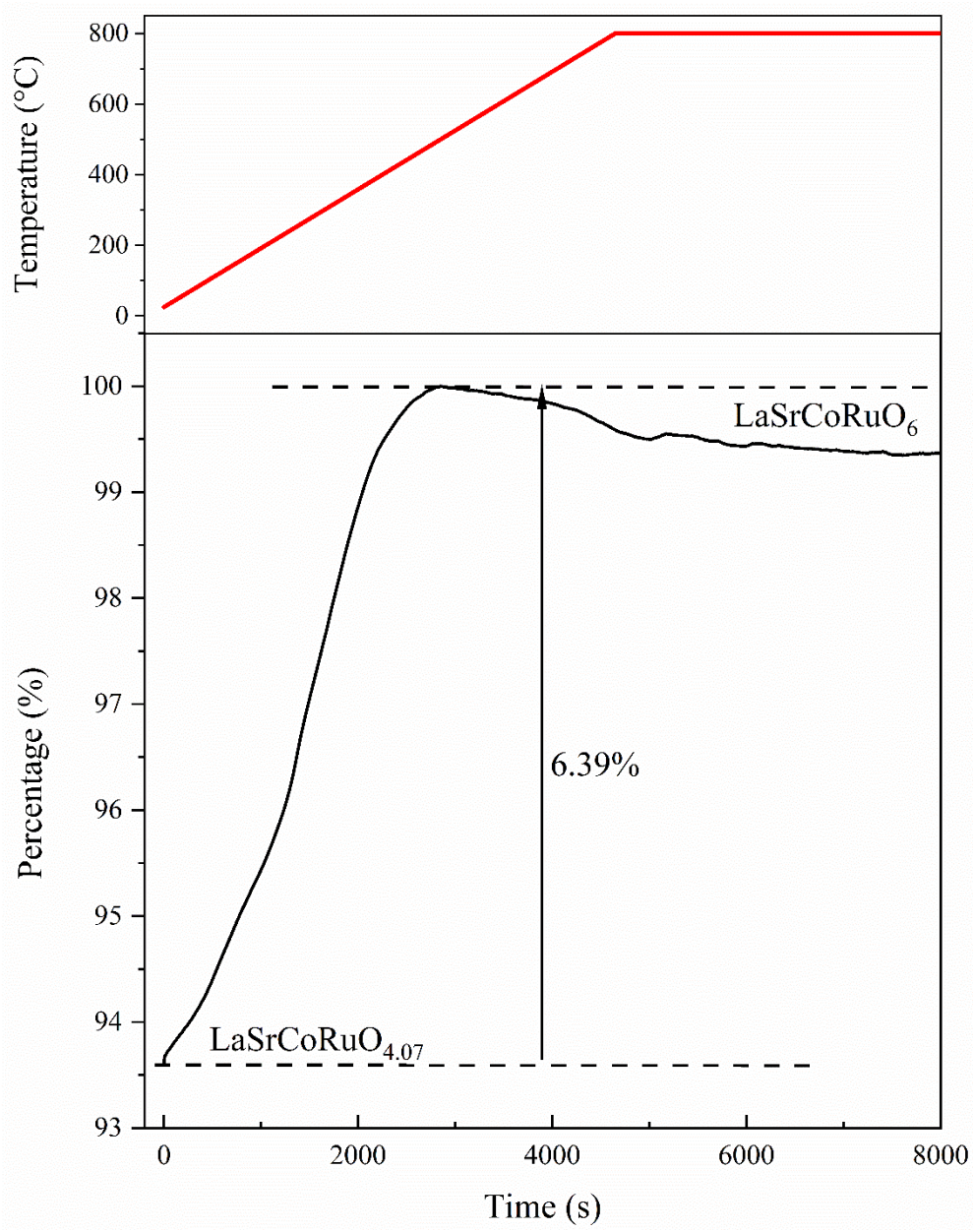


Figure 7.1. Oxidative thermogravimetric analysis of $LaSrCoRuO_{6-x}$, plot shows mass and temperature as a function of time.

7.3.2 Structural Characterisation of $LaSrCoRuO_4$

7.3.2.1 Synchrotron X-ray Powder Diffraction

Synchrotron X-ray powder diffraction (SXRD) data were collected from a large-scale neutron sample of $LaSrCoRuO_4$. These data can be indexed with a body centred tetragonal unit cell (space group *I*4/*mmm*) with lattice parameters: a = 5.66 Å, c = 6.88 Å. The indexed lattice parameters resemble those of $LaSrNiRuO_4$, which adopts an infinite layer structure,[37] suggesting that $LaSrCoRuO_4$ also adopts an infinite layer structure.

A model was constructed based on an $LaSrNiRuO_4$ infinite layer structure, with Co/Ru cation ordering at the B-site, described in space group *I*4/*mmm* with lattice parameters a = 5.66 Å and c = 6.88 Å and refined against the SXRD data. Close inspection of the diffraction data showed the presence of a secondary phase ($LaSrCoRuO_5$, wt%:31.5(5)%), which was then added into the refinement. The refinement of the *I*4/*mmm* model against the SXRD data collected from $LaSrCoRuO_4$ yielded a good statistical fit (wRp = 1.89%; Rp = 1.28%). The observed, calculated and difference plots of the structural refinement of $LaSrCoRuO_4$ against SXRD data collected at room temperature using an *I*4/*mmm* model are shown in Fig 7.2. Full details of the structural parameters obtained from the refinement against SXRD data are shown in Table 7.1. A more detailed structural characterisation of $LaSrCoRuO_4$ with neutron powder diffraction will be described in Section 7.3.2.2.

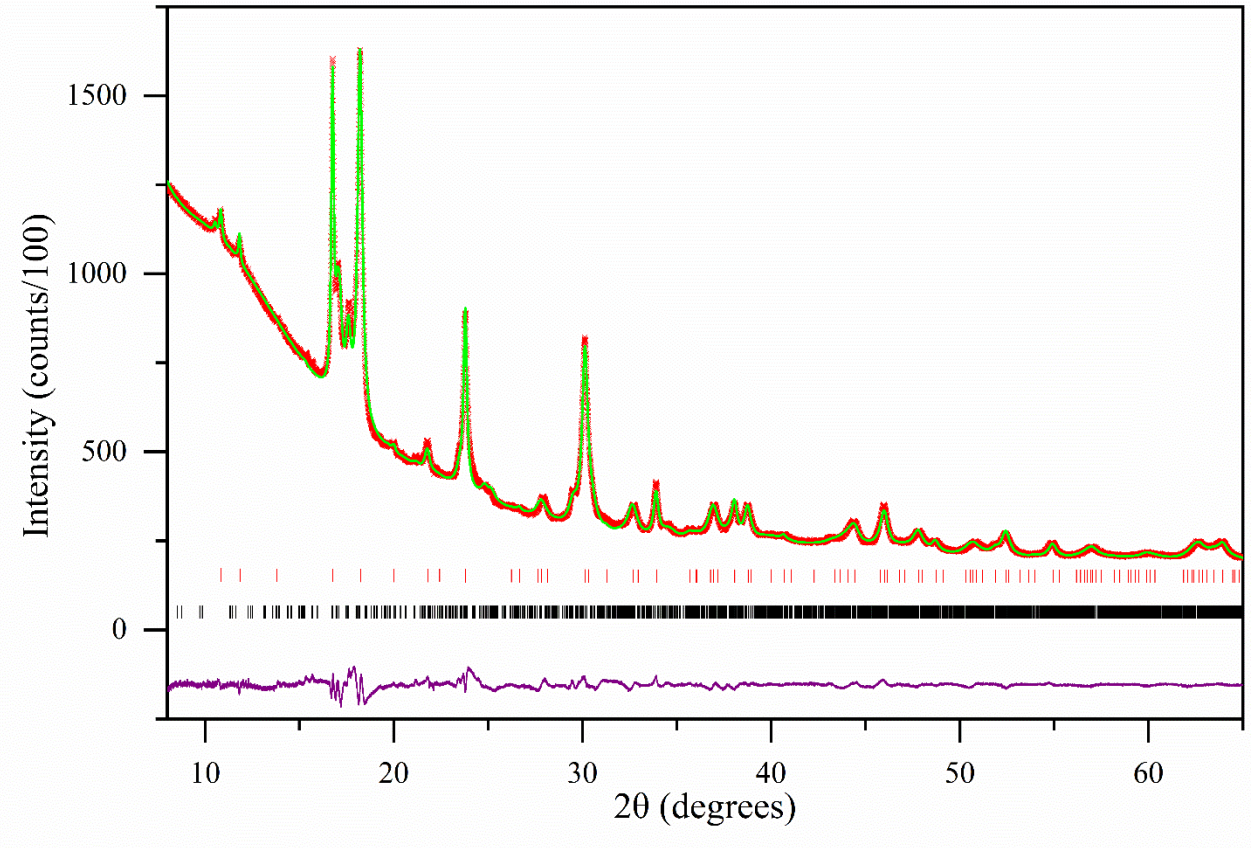


Figure 7.2. Observed, calculated and difference plots from the structural refinement of $LaSrCoRuO_4$ against SXRD data collected at room temperature using an *I4/mmm* structural model. Upper ticks mark the peak positions of the majority phase $LaSrCoRuO_4$ and lower ticks mark the peak positions of the minority phase $LaSrCoRuO_5$.

$LaSrCoRuO_4$, space group *I*4/*mmm* (#139)						
Atom	Wyckoff	*x*	*y*	*z*	Fraction	B_{iso} equiv. ($Å^2$)
La/Sr	4*d*	0	$^1/_2$	$^1/_4$	$^1/_2/^1/_2$	0.01(3)
Co	2*a*	0	0	0	1	0.42(4)
Ru	2*b*	$^1/_2$	$^1/_2$	0	1	0.42(4)
O(2)	8*h*	0.258(1)	0.258(1)	0	1	0.10(8)
a = 5.6690(2) Å, *c* = 6.8778(3) Å						
$LaSrCoRuO_5$: Space group $P112_1$ (#4), *a* = 10.79(2) Å, *b* = 10.80(2) Å, *c* = 8.121(1) Å, γ = 90.82(2)°, wt% 31.5(5)%						
wRp = 1.89%; Rp = 1.28%						

Table 7.1. Parameters from the structural refinement of $LaSrCoRuO_4$ using an *I*4/*mmm* model against SXRD data collected at room temperature.

7.3.2.2 Neutron Powder Diffraction Data Collected from $LaSrCoRuO_4$ at Room Temperature

In an infinite layer structure, the MO_4 square-planar units can undergo cooperative twisting and subtle deformations, which break their 4-fold symmetry. Given these distortions are the result of the displacement of the oxide anions, X-ray diffraction data are not very sensitive to these distortions. Room temperature neutron powder diffraction (NPD) data were collected from $LaSrCoRuO_4$ using the WISH instrument at ISIS (Section 2.4.2.1). Since the oxygen neutron scattering length is comparable to that of the metal elements (e.g. O: 5.80 fm, Co: 2.49 fm),[56] neutron diffraction can accurately determine the positions of the oxide anions, which allows the exact structure of $LaSrCoRuO_4$ to be investigated. The *I4/mmm* tetragonal model obtained from the previous SXRD refinement was refined against the NPD data. During

the refinement, the oxygen positions were allowed to vary. The refinement against the NPD data collected from $LaSrCoRuO_4$ converged rapidly and gave a good statistical fit (wRp = 2.01%; Rp = 1.46%). The observed, calculated and difference plots of the structural refinement of $LaSrCoRuO_4$ are shown in Fig 7.3. Full details of the structural parameters are shown in Table 7.2. The refined structure of $LaSrCoRuO_4$ is shown in Fig 7.4.

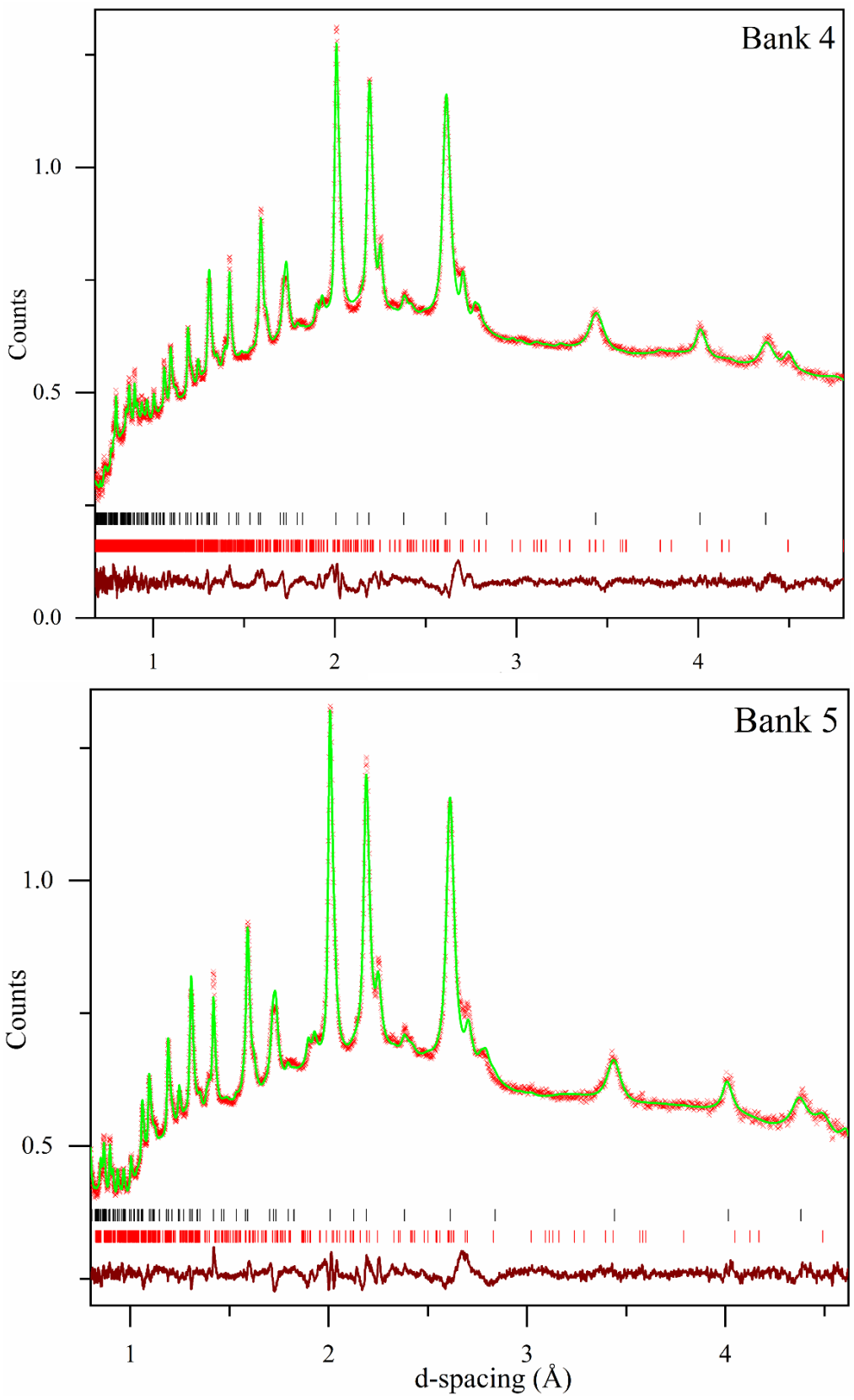


Figure 7.3. Observed, calculated and difference plots from the refinement of $LaSrCoRuO_4$ against NPD data collected at room temperature. Upper ticks mark the peak positions of the majority phase $LaSrCoRuO_4$, lower ticks mark the peak positions of the minority phase $LaSrCoRuO_5$. The presence of incoherent background from hydrogen is likely resulted from over reduced hydride impurities which were also found in ref 71.

$LaSrCoRuO_4$, space group *I*4/*mmm* (#139)						
Atom	Wyckoff	*x*	*y*	*z*	Fraction	B_{iso} equiv. ($Å^2$)
La/Sr	4*d*	0	$^1/_2$	$^1/_4$	$^1/_2/^1/_2$	0.24(4)
Co	2*a*	0	0	0	1	1.94(6)
Ru	2*b*	$^1/_2$	$^1/_2$	0	1	1.94(6)
O	8*h*	0.2519(4)	0.2519(4)	0	1	1.97(5)
a = 5.6786(2) Å, *c* = 6.8823(4) Å						
$LaSrCoRuO_5$: Space group $P112_1$ (#4), *a* = 10.821(9) Å, *b* = 10.828(9) Å, *c* = 8.120(2) Å, *γ* = 91.02(3)°, wt% 18.3(3)%						
wRp = 2.01%; Rp = 1.46%						

Table 7.2. Parameters from the structural refinement of $LaSrCoRuO_4$ against NPD data collected at room temperature.

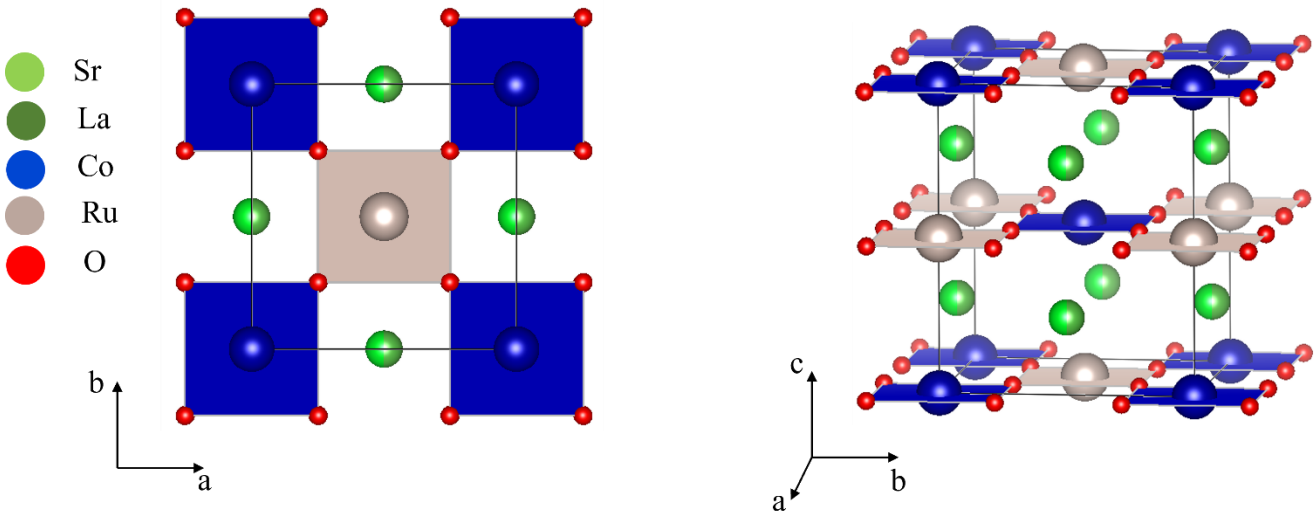


Figure 7.4. Refined structure of $LaSrCoRuO_4$ viewed along different Cartesian axes.

In order to confirm that $LaSrCoRuO_4$ adopts the undistorted tetragonal infinite layer structure, a series of distorted models based on the *I*4/*mmm* infinite layer structural model were

constructed. These structural models allow the subtle distortions of the MO_4 square-planar units (rotation/deformation of the MO_4 square plane) to be described. The *I*4/*m* structural model allows the rotation of the MO_4 square planes around the *c*-axis while keeping the MO_4 units square (4-fold symmetry of the MO_4 square-planar unit is preserved). Further lowering of the symmetry to monoclinic (*I*112/*m* and $P12_11$) distorts the D_{4h} symmetry of the MO_4 square planes to D_{2h} or even C_{2v} symmetry. The structural models described in space group *I*4/*mmm*, *I*4/*m*, *I*112/*m* and $P12_11$ and their corresponding MO_4 square-planar unit distortions are shown in Fig 7.5.[87]

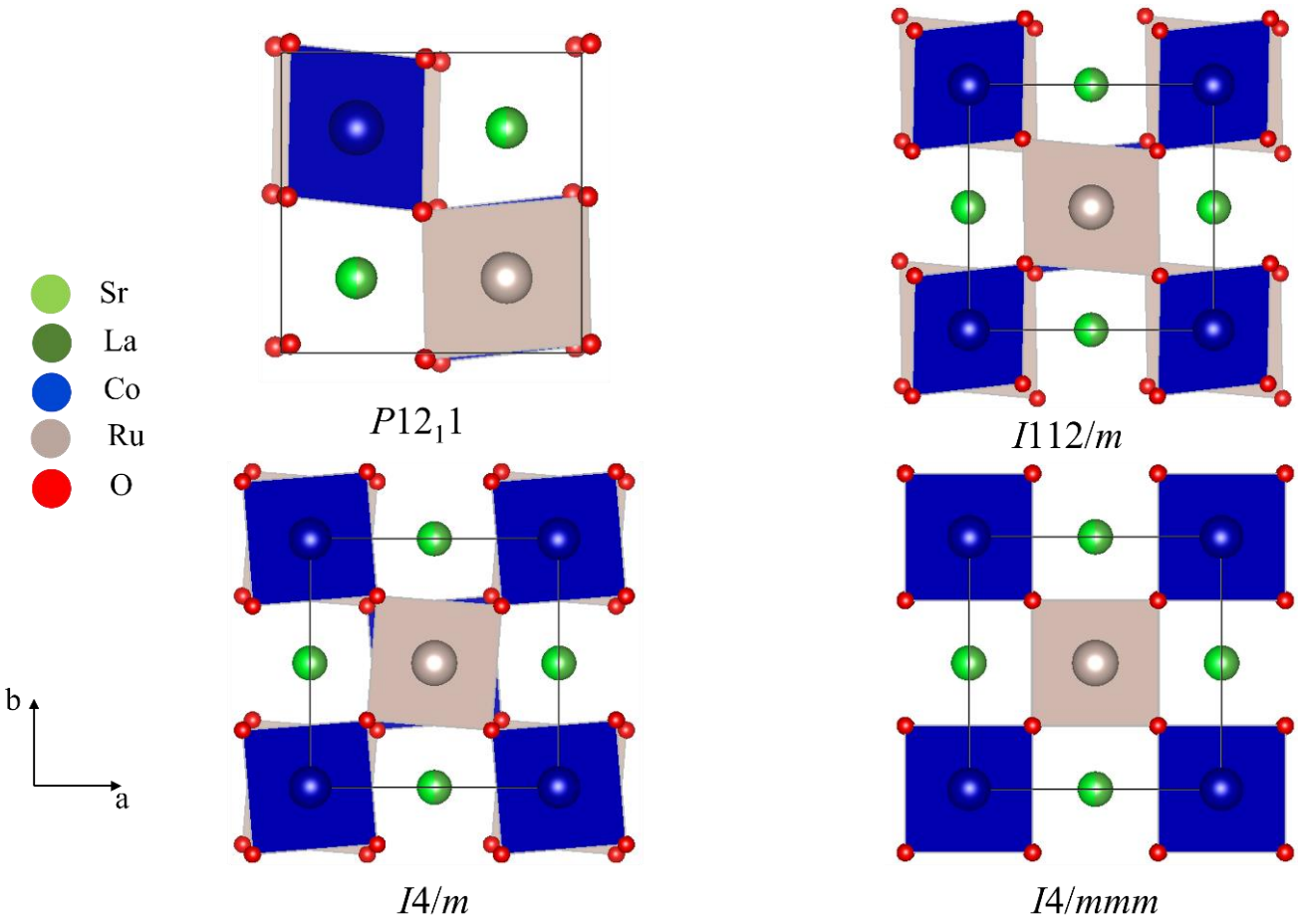


Figure 7.5. The space groups of the infinite layer structure and their corresponding distortions of the MO_4 square-planar unit. The difference between the *P*12$_1$1 and *I*112/*m* structural models is the direction of the rotation of the MO_4 square-planar units. The *I*112/*m* structural model is described as $a^0a^0c^-$ (out-of-phase tilt in the *c* direction) in the Glazer notation, while the *P*12$_1$1 structural model is described as $a^0a^0c^+$ (in-phase tilt in the *c* direction).

These distorted structural models were refined against the NPD data collected at room temperature. The positions of the oxide anions were allowed to move freely during the refinement. The refinements of these distorted structural models gave similar statistical fits to the *I*4/*mmm* model (Table 7.3). In addition, the refined structures of $LaSrCoRuO_4$ obtained from the refinements of the structural models described in space groups *I*4/*m*, *I*112/*m* and $P12_11$ were similar to that obtained from the refined *I*4/*mmm* model (Table 7.4). Therefore, it is reasonable to conclude that $LaSrCoRuO_4$ adopts an undistorted infinite layer structure which can be described in the space group *I*4/*mmm*.

Space Group	*wRp* (%)	*Rp* (%)
*I*4/*mmm* (#139)	2.01	1.46
*I*4/*m* (#87)	2.04	1.49
*I*112/*m* (#12)	2.04	1.45
$P12_11$ (#4)	2.07	1.47

Table 7.3. Fitting statistics obtained from the structural refinements against NPD data collected at room temperature.

Space Group	∠Co-O-Ru (average)/°
*I*4/*mmm* (#139)	180.0
*I*4/*m* (#87)	180.0(1)
*I*112/*m* (#12)	180.0(1)
$P12_11$ (#4)	180.0(3)

Table 7.4. Refined ∠Co-O-Ru obtained from the refinement of different space groups against NPD data collected at room temperature.

7.3.3 Magnetic Characterisation of $LaSrCoRuO_4$

7.3.3.1 SQUID Magnetometry

The ferromagnetic subtraction technique (Section 2.8.1) was used to collect the magnetisation data from $LaSrCoRuO_4$ due to the presence of small amounts (< 2 mol%) of elemental Co present in the sample. A gradual increase in the magnetic susceptibility is observed upon cooling from 350 K. This change is accompanied by a large increase in the saturated magnetic moment, which reaches ~1.72 μB at 10 K. The paramagnetic susceptibility cannot be fitted by the Curie-Weiss law ($\chi = C/(T - \theta) + K$) throughout the whole temperature range, indicating a potential magnetic ordering at room temperature.

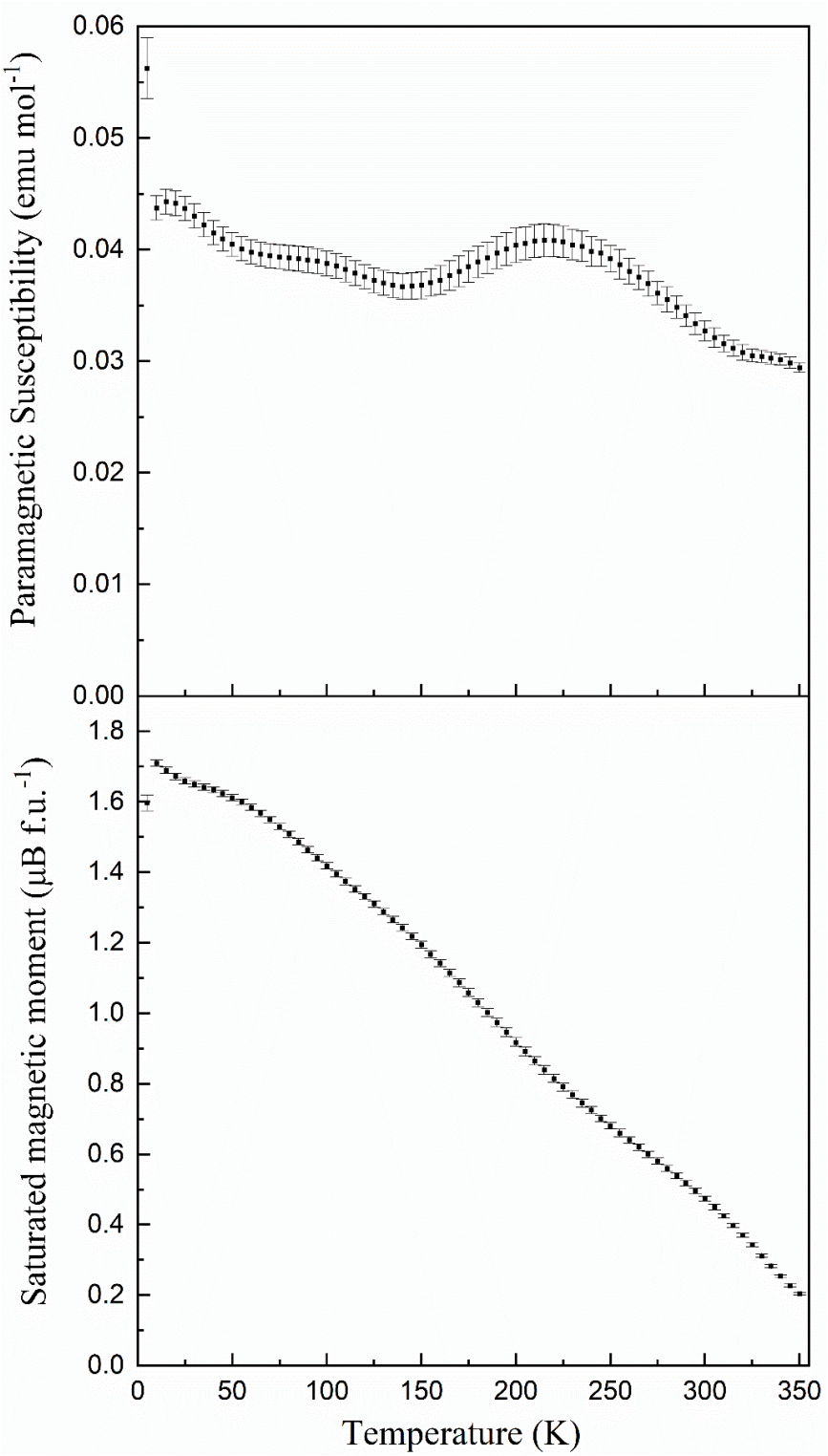


Figure 7.6. The paramagnetic susceptibility and saturated magnetic moment of $LaSrCoRuO_4$ as a function of temperature. The data points at 5 K were considered to be anomalies.

Magnetisation-field data were collected at 5 K, 300 K and 350 K. Both the magnetisation-field data as a function of applied field collected at 5 K and 300 K exhibit a hysteresis loop, indicating the sample is ferromagnetic up to ~ 300 K.

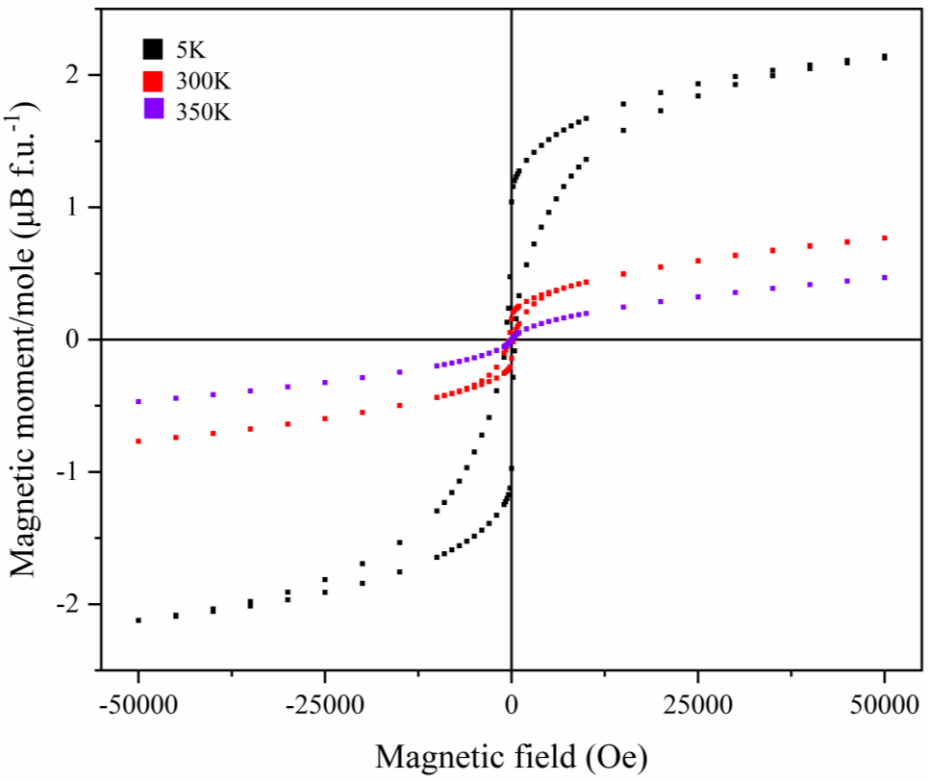


Figure 7.7. Magnetisation-field data collected from $LaSrCoRuO_4$ at 5 K, 300 K and 350 K.

However, attempts to extract magnetic moments of the transition metal centres from the room temperature neutron powder diffraction data set were not successful due to the relatively high background and the relatively low magnetic moment exhibited by the sample (~ 0.5 μB).

7.3.3.2 Low Temperature Neutron Powder Diffraction Data

A direct comparison of the NPD data collected from $LaSrCoRuO_4$ at 5 K and 300 K reveals a subtle enhancement in the intensity of some diffraction peaks in the low temperature data set (Fig 7.8). As the low temperature NPD data collected from the secondary phase $LaSrCoRuO_5$ at 5 K do not show any extra magnetic scattering (Chapter 6), it is reasonable to conclude that the enhancement in the intensity of some diffraction peaks is related to the magnetic ordered

state of $LaSrCoRuO_4$ at 5 K. The additional intensity is at the same position as the crystallographic peaks, which is consistent with the ferromagnetically ordered state observed from the magnetization measurements collected from $LaSrCoRuO_4$.

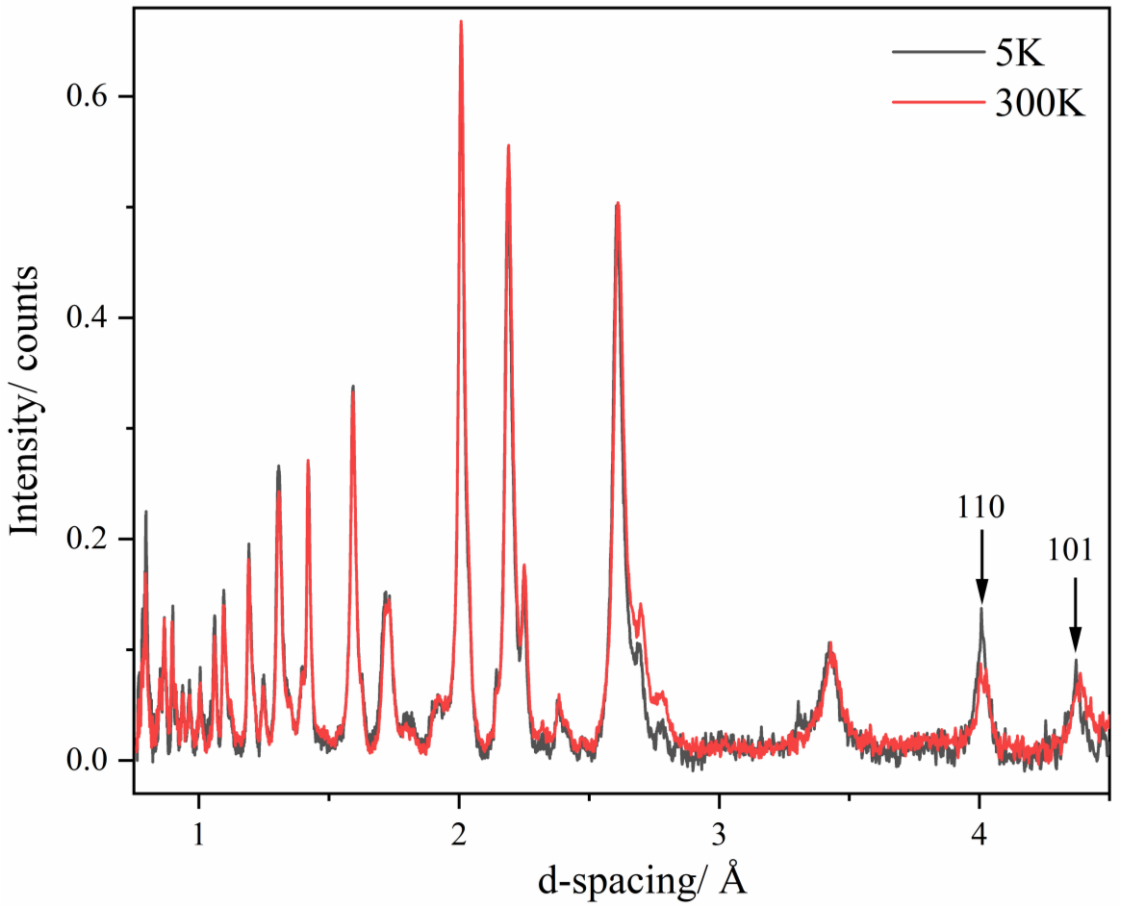


Figure 7.8. NPD data from $LaSrCoRuO_4$ collected at 5 K and 300 K. There is an enhanced magnetic scattering of (101) and (110) diffraction peaks, which is consistent with a magnetic ordered state. Background was subtracted from both sets of the diffraction data.

The magnetic peaks can be indexed using a same unit cell as the crystallographic model, suggesting that the magnetic propagation vector is *k*(0,0,0). Therefore, a series of magnetic models was constructed using the ISODISTORT programme.[88] This procedure yields two magnetic models described by the irreducible representations $m\Gamma^{+}_{3}$ (magnetic space group: 139.537) and $m\Gamma^{+}_{5}$ (magnetic space group 71.536) (Fig 7.9). NPD data of both magnetic

models were simulated (Fig 7.10), the magnetic model described by the irreducible representations $m\Gamma^{+}_{3}$ (magnetic space group: 139.537) gave a better fit to the experimental NPD data. Therefore, the magnetic model with the space group 139.537 was refined against the NPD data collected at 5 K.[55]

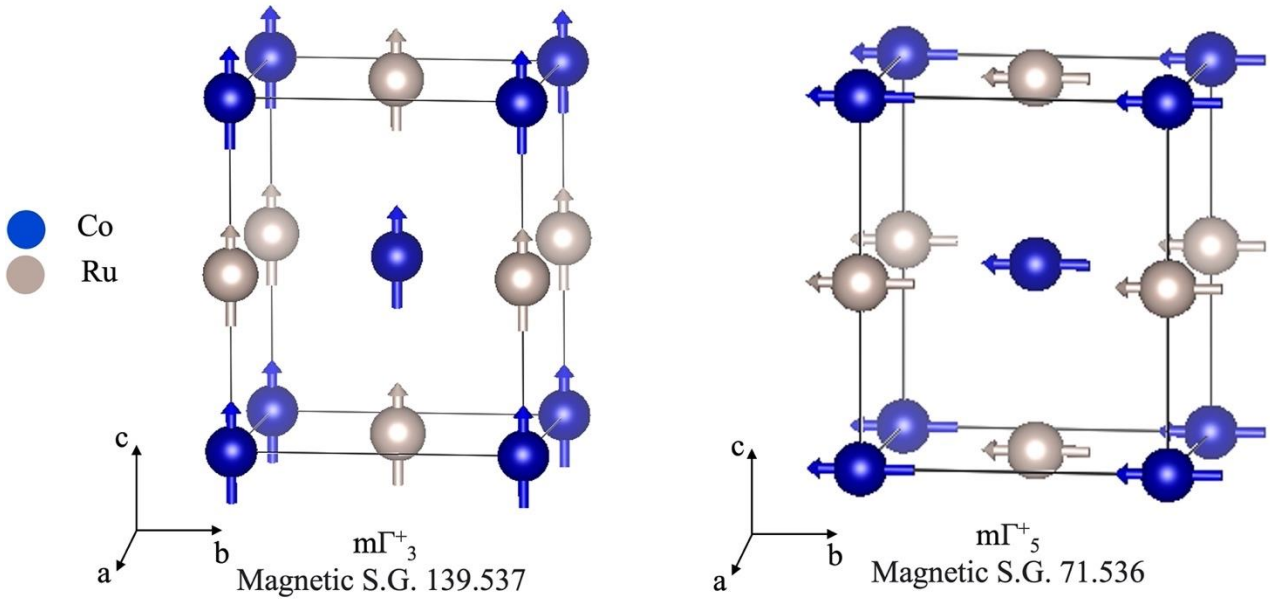


Figure 7.9. Magnetic models described in magnetic space group 139.537 and 71.536 respectively, arrows represent magnetic moment at cobalt and ruthenium sites.

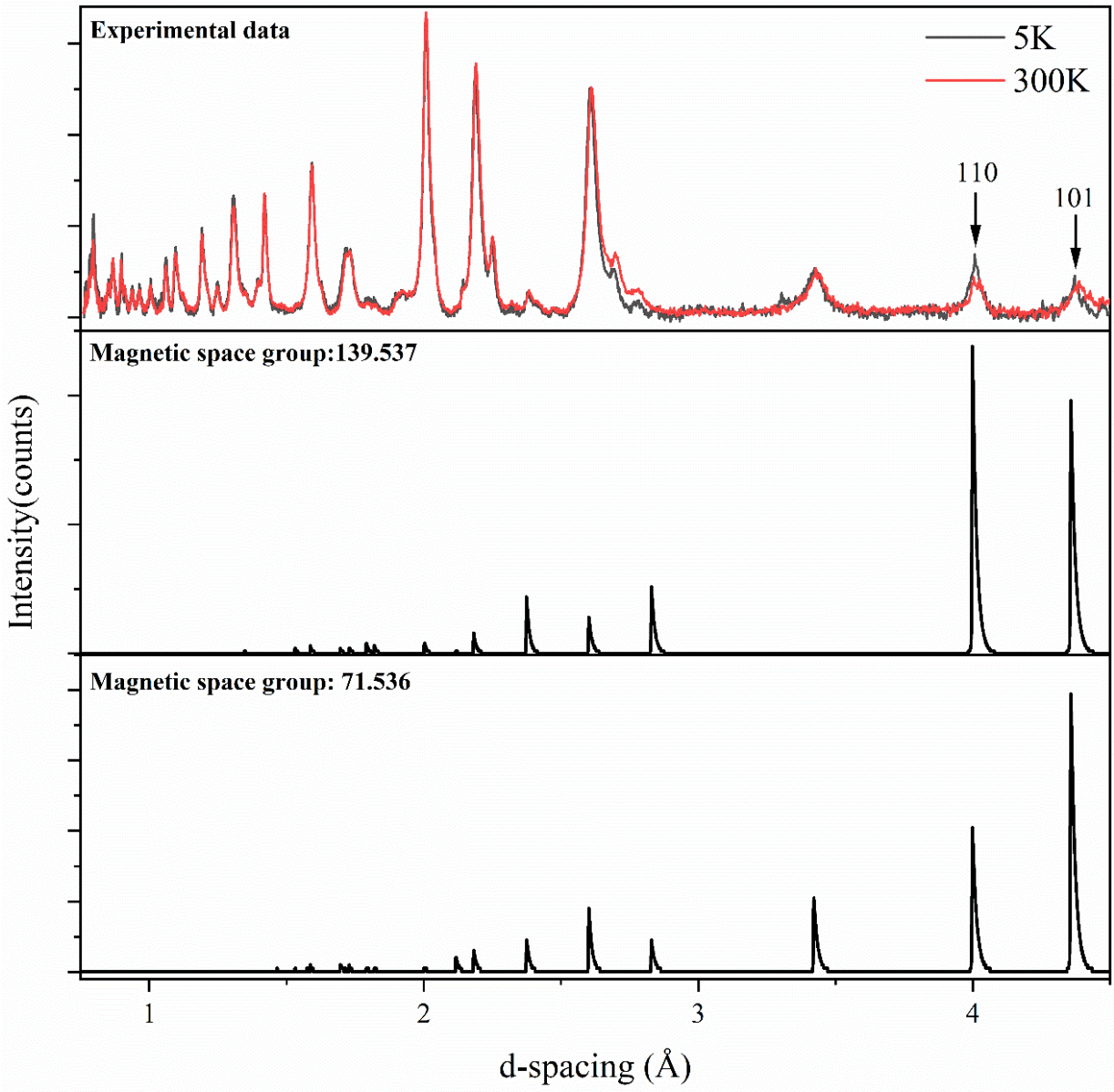


Figure 7.10. Neutron powder diffraction simulation using magnetic models of $LaSrCoRuO_4$ described with space group 139.537 and 71.536.

During the refinement, the magnetic moments at the cobalt and ruthenium centres were allowed to vary independently. This process yielded a magnetic moment of 1.62(6) μB at the cobalt site and 0.21(7) μB at the ruthenium site, with the two magnetic moments aligned parallel to each other along the *z* axis. The refined net moment is 1.83(13) μB, which is slightly larger than the saturated magnetic moment of $LaSrCoRuO_4$ obtained from the magnetisation data at 10 K (Fig 7.6). No structural distortion was observed from the low temperature neutron powder

diffraction data, $LaSrCoRuO_4$ can still be described in space group *I*4/*mmm*. The observed, calculated and difference plots from the refinement of $LaSrCoRuO_4$ against NPD data at 5 K are shown in Fig 7.11. Structural parameters from the refinement of $LaSrCoRuO_4$ are detailed in Table 7.5 and Table 7.6. Selected bond lengths and angles at 5 K and 300 K as a comparison are presented in Table 7.7.

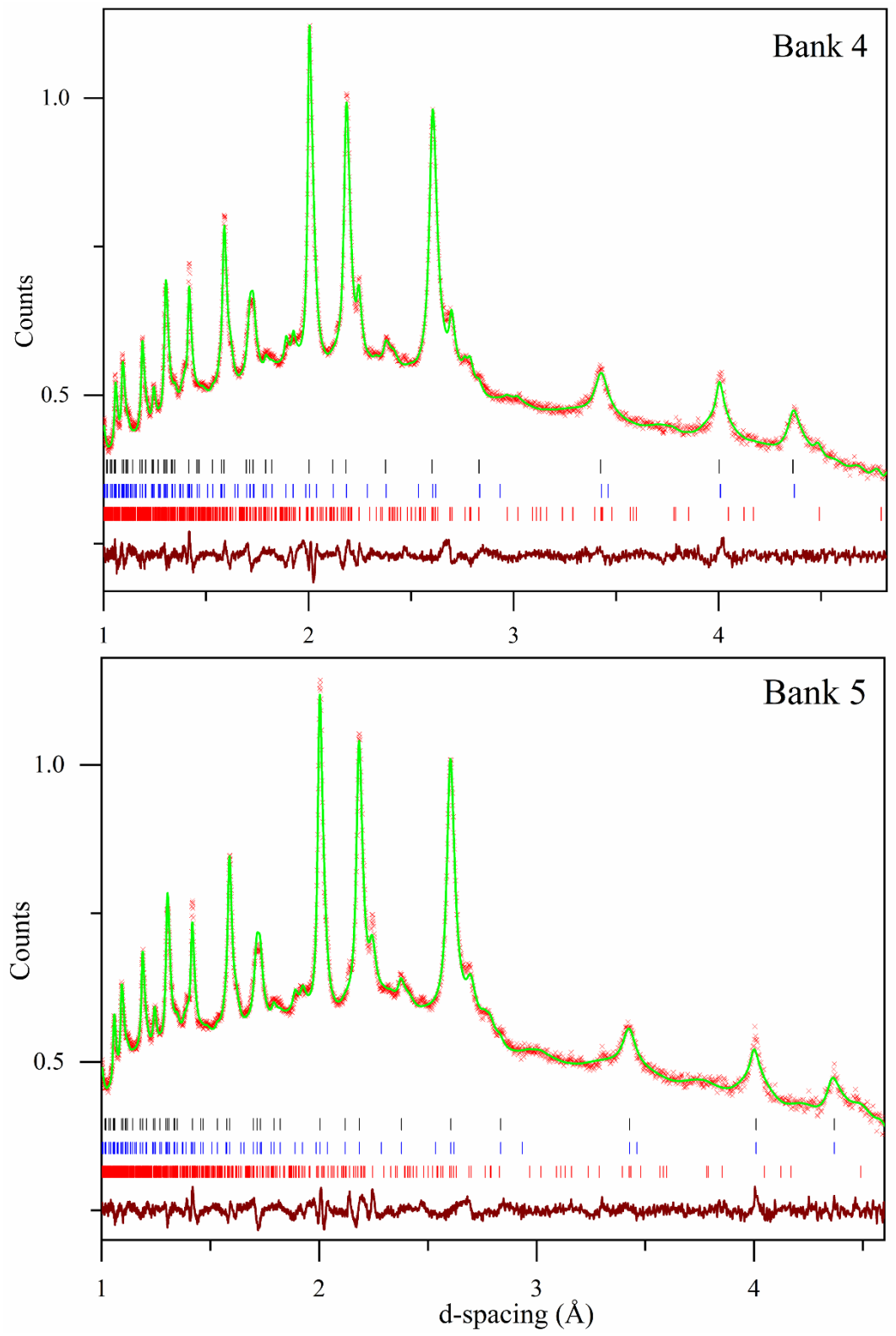


Figure 7.11. Observed, calculated and difference plots from the refinement of $LaSrCoRuO_4$ against NPD data collected at 5 K. Black ticks mark the peak positions of the majority phase $LaSrCoRuO_4$, blue ticks mark the peak positions of the magnetic cell, red ticks mark the peak positions of the secondary phase $LaSrCoRuO_5$.

Atom	*x*	*y*	*z*	M_z (μB)
Co	0	0	0	1.62(6)
Ru	$^1/_2$	$^1/_2$	0	0.21(7)

Table 7.5. The refined magnetic moment on cobalt and ruthenium sites obtained from the refinement against neutron powder diffraction data collected at 5 K.

$LaSrCoRuO_4$, space group *I*4/*mmm* (#139)						
Atom	Wyckoff	*x*	*y*	*z*	Fraction	B_{iso} equiv. (Å^2)
La/Sr	4*d*	0	$^1/_2$	$^1/_4$	$^1/_2$/$^1/_2$	0.25(4)
Co	2*a*	0	0	0	1	1.86(6)
Ru	2*b*	$^1/_2$	$^1/_2$	0	1	1.86(6)
O	8*h*	0.2516(5)	0.2516(5)	0	1	1.89(5)
a = 5.6689(2) Å, *c* = 6.8578(4) Å						
$LaSrCoRuO_5$: Space group $P112_1$ (#4), *a* = 10.79(1) Å, *b* = 10.78(1) Å, *c* = 8.116(2) Å, *γ* = 90.98(3)°, wt% 16.5(3)%						
wRp = 2.06%; Rp = 1.49%						

Table 7.6. Full structural parameters of $LaSrCoRuO_4$ extracted from the refinement against neutron powder diffraction data collected at 5 K.

Cation	Anion	Bond lengths/Å	
		300 K	**5 K**
Co	O	2.023(1)	2.017(1)
Ru	O	1.993(1)	1.991(1)

Table 7.7. Selected bond lengths and angles from the refined structure of $LaSrCoRuO_4$ at 300 K and 5 K.

7.4 Discussion

7.4.1 Electronic Structure of $LaSrCoRuO_4$

The NPD data indicate that $LaSrCoRuO_4$ adopts an infinite layer structure. In the $LaSrCoRuO_4$ phase, the oxygen content gives the transition metal centres a summed charge of +3, which is consistent with the combination of Co^+ and Ru^{2+} centres. Based on previous studies of the analogous infinite layer phase, $LaSrNiRuO_4$, the calculated electronic state for the Ni^+ centres in $LaSrNiRuO_4$ shows that the minority spin at the Ni d_{z2} orbital is at the highest energy level (Fig 7.12).[37] As the Co^+ centres in the $LaSrCoRuO_4$ phase have one fewer electron, the d_{z2} orbital is thought to be no longer doubly occupied. The singly occupied Co d_{z2} orbital reduces the electronic repulsion between the Co d_{z2} - Ru d_{z2} along the *c* direction, which is consistent with the observed contraction of the *c* lattice parameter in $LaSrCoRuO_4$ ($LaSrCoRuO_4$: 6.8823(4) Å, $LaSrNiRuO_4$: 6.9151(4) Å).[37]

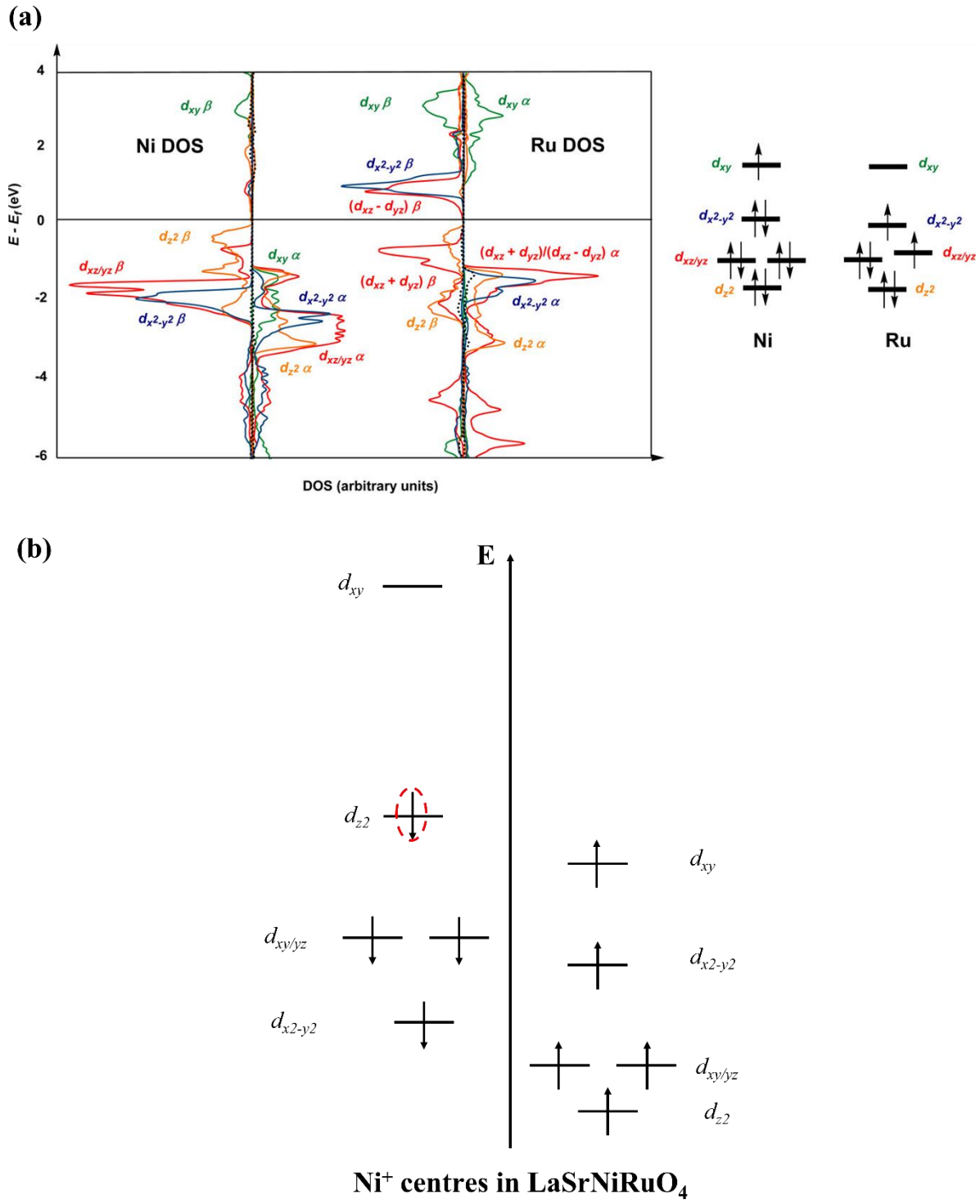


Figure 7.12. (a) Calculated DOS for $LaSrNiRuO_4$, graph taken from ref 37 (b) A schematic representation of filling of the Ni^+ *d*-orbitals. Red circle indicates the highest energy electron located at the d_{z2} orbital. It is worth noting that the axis is defined such that *x* and *y* bisect the M–O–M angles.

Therefore, the electronic structure of $LaSrCoRuO_4$ is proposed as $(d_{xy/yz})^4(d_{xy})^2(d_{z2})^1(d_{x2-y2})^1$ for Co^+ centres, and $(d_{z2})^2(d_{xy/yz})^3(d_{xy})^1(d_{x2-y2})^0$ for Ru^{2+} centres. The proposed electronic structure of Co^+ is consistent with the refined magnetic moment at the cobalt site (1.62(6) μB), which is close to the theoretical high spin Co^+ centres (S = 1). The magnetic moment on the ruthenium site is small compared with its theoretical value (S = 1). The loss of magnetic moment at the ruthenium centres was also observed in $LaSrNiRuO_4$.[37]

7.4.2 Magnetic Behaviour of $LaSrCoRuO_4$

As discussed in Section 7.3.3.2, $LaSrCoRuO_4$ adopts a ferromagnetic ordered state at room temperature with the magnetic moment localised almost entirely on the cobalt centres. Since $LaSrCoRuO_4$ is a ferromagnetic insulator, the magnetism can be explained through the Goodenough-Kanamori rules (Section 1.5.2). The magnetic couplings can be separated into two types: Interlayer coupling (coupling along the *c*-axis) and intralayer coupling (coupling on the *ab* plane). Considering the interlayer couplings first, there are two magnetic couplings to consider between the Co^+ and Ru^{2+} centres. The first coupling is the direct exchange between (Ru d_{z2})^2 – (Co d_{z2})^1, which gives rise to a weak ferromagnetic interaction. The second magnetic coupling is the direct exchange interaction between (Co d_{yz})^2– (Ru d_{yz})^1, which is also weakly ferromagnetic. There are two intralayer couplings, the weak ferromagnetic π-type superexchange interaction between (Co d_{xy})^2 – O – (Ru d_{xy})^1 and the strong ferromagnetic σ-type superexchange interaction between (Co d_{x2-y2})^1 – O – (Ru d_{x2-y2})^0. The resultant interlayer and intralayer ferromagnetic couplings are consistent with the refined magnetic structure.

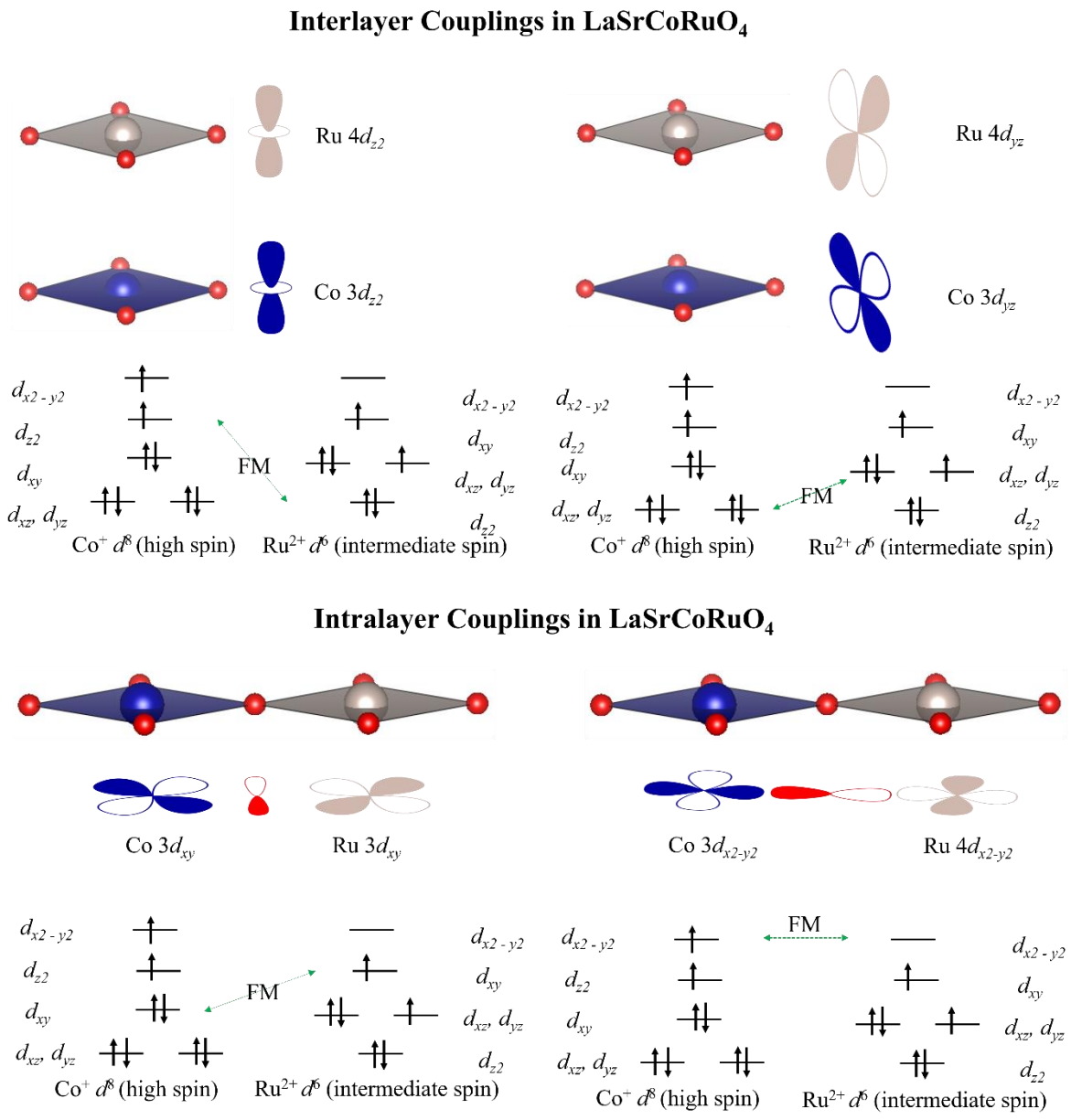


Figure 7.13. Ferromagnetic magnetic exchange interactions in $LaSrCoRuO_4$.

7.5 Conclusion

The topochemical reduction of $LaSrCoRuO_6$ with LiH under flowing argon leads to the formation of $LaSrCoRuO_4$, which adopts an infinite layer structure. This novel reduced oxide phase can be indexed with a body centred tetragonal unit cell with a slight expansion of the *ab* plane and a large contraction of the *c* lattice parameter.

$LaSrCoRuO_4$ is a room temperature ferromagnet, as demonstrated by the magnetisation-field data collected at 300 K. Upon cooling to 10 K, the saturated magnetic moment of $LaSrCoRuO_4$ reaches ~ 1.72 μB, which is localised almost entirely on the Co^{+} centres, with the Ru^{2+} centres contributing a small amount of magnetic moment (0.21(7) μB). Previous computational calculation has ruled out the possibility of Ru^{2+} centres adopting an extreme Jahn-Teller distortion (S = 0) ground state.[89] Therefore, the loss of the magnetic moment at the Ru^{2+} centres could be due to strong covalency or strong spin orbit coupling.

Chapter 8 A-site Substitution of a Reduced Oxide Phase Derived from $LaSrCoRuO_6$

8.1 Introduction

As discussed in Chapter 6, the B-site cation ordered double perovskite $LaSrCoRuO_6$ can be reduced with Zr to form $LaSrCoRuO_5$. This compound adopts a complex anion-vacancy ordered structure, which consists of a network of corner-sharing CoO_6 octahedra, RuO_5 square-based pyramidal units and CoO_4 square-planar units (Fig 8.7). It was found that the cobalt centres in $LaSrCoRuO_5$ exhibit a mixed valence of Co^+ and Co^{3+} centres at a 1:1 ratio, with the Co^+ centres residing at the square-planar sites and the Co^{3+} centres residing at the octahedral sites. It is proposed that the disproportionation of the Co^{2+} centres is driven by the ligand field stabilisation energy gain of the low spin Co^{3+} (S = 0) at the octahedral sites, which is more favourable compared to Co^{2+} centres residing at these sites (Chapter 6). In order to gain a deeper insight into the correlation between the anion-vacancy ordered structure adopted by $LaSrCoRuO_5$ and the disproportionation of the Co^{2+} centres, A-site substitution of $LaSrCoRuO_5$ was investigated.

8.2 Experimental

8.2.1 Synthesis of $La_xSr_{2-x}CoRuO_6$

Samples of $La_xSr_{2-x}CoRuO_6$ ($0.6 \leq x \leq 1.4$) were synthesised through a citrate gel method. Suitable stoichiometric ratios of La_2O_3 (dried at 900 °C), $SrCO_3$, Co and RuO_2 (dried at 800 °C) were weighed out and ground thoroughly in a mortar and pestle. The powders were then dissolved in a minimum quantity of deionised water and 6 M nitric acid at a 1:1 ratio with gentle heating. Then, 3 mole equivalents of citric acid monohydrate and 2 ml of ethylene glycol were added into the mixture. The solution was heated at 200 °C with constant stirring. The

solution became viscous and set into a gel, which then pyrolyzed. The resulting mixture was ground thoroughly into a fine powder. The powder was transferred to an alumina crucible and heated to 900 °C at 5 °C min^{-1}. The powder was held at 900 °C for 12 hours before being reground, pressed into13 mm pellets and heated to 1200 °C at 1 °C min^{-1} for 2 periods of 48 hours in air. After the final heating cycle, the pellets were ground thoroughly and characterised by X-ray powder diffraction. Once the reaction was deemed complete, pellets of $La_xSr_{2-x}CoRuO_6$ ($0.6 \leq x \leq 1.4$) were heated to 1200 °C and kept at this temperature for 12 hours, before subsequently cooling to 450 °C at 5 °C min^{-1}. The pellets were then immediately quenched by placing them into a pre-cooled crucible in dry ice. The pellets were ground thoroughly into powder.

8.2.2 Synthesis of $La_xSr_{2-x}CoRuO_5$

Samples of $La_xSr_{2-x}CoRuO_5$ ($0.6 \leq x \leq 1.4$) were prepared by putting the respective parent $La_xSr_{2-x}CoRuO_6$ ($0.6 \leq x \leq 1.4$) phases in a glass 'thimble' inside an evacuated sealed silica ampoule along with 2 mole equivalents of Zr powder (Section 2.2.4). A series of small-scale reactions were performed in which 200 mg of $La_xSr_{2-x}CoRuO_6$ ($0.6 \leq x \leq 1.4$) was heated along with Zr powder in the temperature range from 375 °C to 470 °C. The reaction progression was monitored by X-ray powder diffraction.

***x* (content of La)**	**Reduction Temperature (°C)**
0.6	375
0.7	425
0.8	435
0.9	435
1.0	450
1.1	450

1.2	450
1.3	450
1.4	470

Table 8.1. Reaction temperatures of $La_xSr_{2-x}CoRuO_6$ ($0.6 \leq x \leq 1.4$) with Zr in a sealed ampoule, yielding respective reduced oxide phases.

Although all the doped parent oxide phases ($La_xSr_{2-x}CoRuO_6$, $0.6 \leq x \leq 1.4$) were synthesised at the same reaction temperature as their undoped analogue $LaSrCoRuO_6$ (1200 °C), their corresponding reduced $La_xSr_{2-x}CoRuO_5$ ($0.6 \leq x \leq 1.4$) phases were formed at slightly different reaction temperatures (Table 8.1). In general, compared with the undoped starting material ($x = 1$), La-deficient parent oxide phases ($x < 1$) were more reactive and formed the corresponding reduced phases at lower reaction temperatures (T < 450 °C); while for the La-rich parent oxide phases ($x > 1$), higher reaction temperatures (T > 450 °C)/more reaction cycles are needed to fully convert the parent oxides into their corresponding reduced phases.

8.3 Results

8.3.1 Characterisation of $La_xSr_{2-x}CoRuO_6$ ($0.6 \leq x \leq 1.4$)

Synchrotron X-ray powder diffraction (SXRD) data were collected from the whole range of A-site doped $La_xSr_{2-x}CoRuO_6$ ($0.6 \leq x \leq 1.4$) double perovskites. These data can be readily indexed with the same monoclinic cell (space group $P2_1/n$),[90] as the undoped $LaSrCoRuO_6$ phase, with slight variations in the lattice parameters. Structural models based on the previously reported Co/Ru, B-site cation ordered double perovskite structure of $LaSrCoRuO_6$ (space group $P2_1/n$) with $(^x/_2)$: $(1-{}^x/_2)$ ratios of La:Sr at the A-site were constructed and refined against the SXRD data. During the refinement, all atoms were allowed to move, and the anti-site disorder (Co/Ru) at the B-site was refined. Refinements of the doped samples of $La_xSr_{2-x}CoRuO_6$ (0.6

$\leq x \leq 1.4$) against SXRD data converged rapidly and gave good statistical fits, indicating that single-phase samples had been prepared. The observed, calculated and difference plots from the structural refinement of $La_{0.8}Sr_{1.2}CoRuO_6$ are shown in Fig 8.1 as a representative, while the rest of the refinement plots can be found in Appendix 2.4. A structural model of $LaSrCoRuO_6$ is shown in Fig 8.1. Full details of the structural parameters obtained from the refinement of $La_{0.8}Sr_{1.2}CoRuO_6$ are shown in Table 8.2.

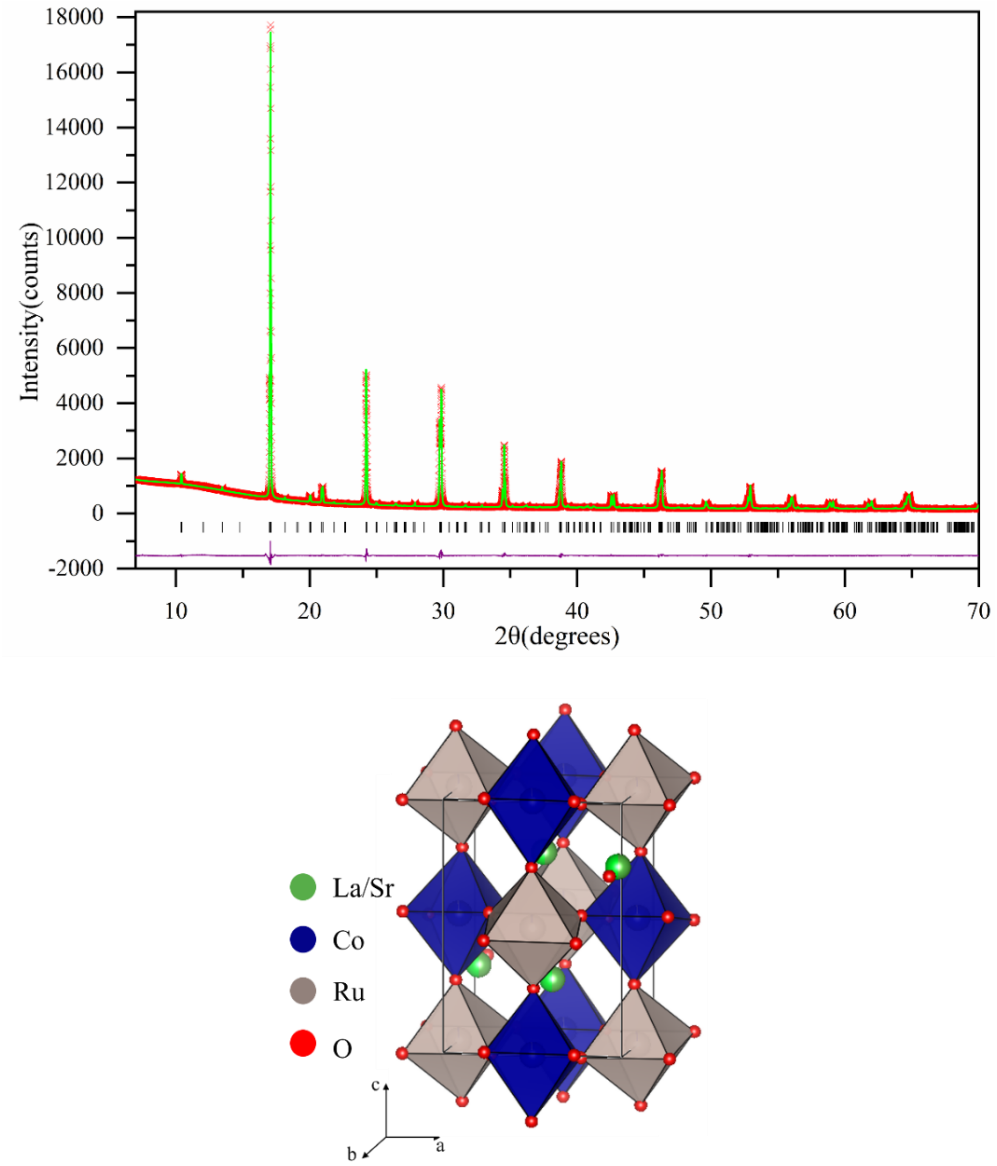


Figure 8.1. Observed, calculated and difference plots from the structural refinement of $La_{0.8}Sr_{1.2}CoRuO_6$ against SXRD data collected at room temperature (top) and a structural model of $LaSrCoRuO_6$ (bottom).

$La_{0.8}Sr_{1.2}CoRuO_6$, space group $P2_1/n$ (#14)						
Atom	Wyckoff	*x*	*y*	*z*	Fraction	B_{iso} equiv. (Å^2)
La(1)	4*e*	0.00482(13)	0.01678(6)	0.25010(11)	$^2/_5$	0.337(7)
Sr(1)	4*e*	0.00482(13)	0.01678(6)	0.25010(11)	$^3/_5$	0.337(7)
Co(1)/Ru(2)	2*c*	$^1/_2$	0	$^1/_2$	0.909(3)/0.092(3)	0.046(8)
Ru(1)/Co(2)	2*d*	$^1/_2$	0	0	0.909(3)/0.092(3)	0.046(8)
O(1)	4*e*	0.2758(9)	0.2653(9)	0.0419(8)	1	0.28(3)
O(2)	4*e*	0.2349(9)	0.7791(9)	0.0192(9)	1	0.28(3)
O(3)	4*e*	0.9363(4)	0.4969(6)	0.2503(9)	1	0.28(3)
a = 5.59117(1) Å, *b* = 5.55730(1) Å, *c* = 7.86680(2) Å *β* = 89.9650(6)° *wRp = 2.21%; Rp = 1.50%*						

Table 8.2. Parameters from the structural refinement of $La_{0.8}Sr_{1.2}CoRuO_6$.

Fig 8.2 shows a plot of the lattice parameters of $La_xSr_{2-x}CoRuO_6$ ($0.6 \leq x \leq 1.4$) phases extracted from the structural refinements as a function of composition (*x*). The black solid line indicates the undoped compound $LaSrCoRuO_6$, the left-hand side represents the La-deficient compounds ($x < 1$, hole doping) and the right-hand side represents the La-rich compounds ($x > 1$, electron doping).

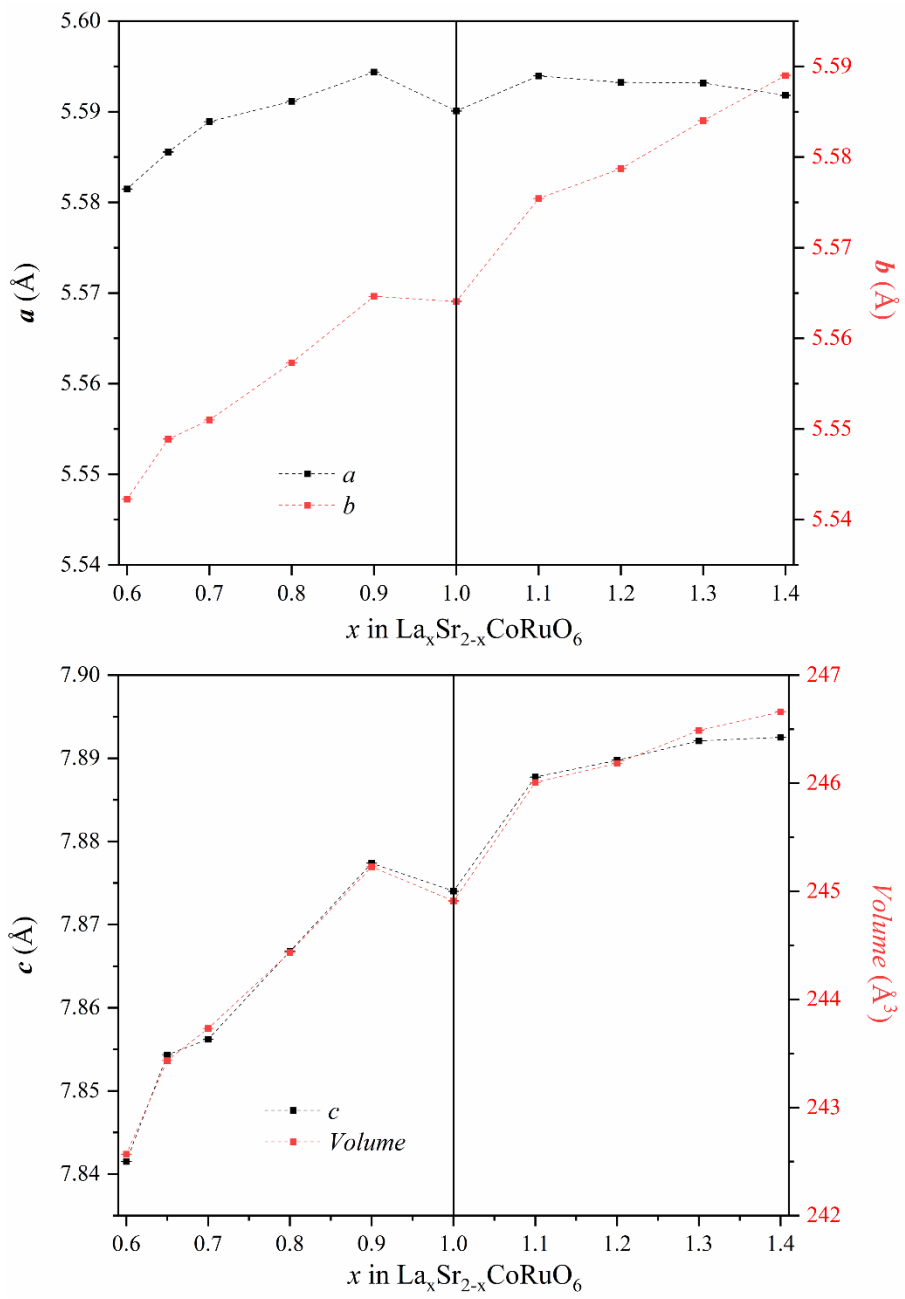


Figure 8.2. *a*, *b* lattice parameters (top); *c* lattice parameter and volume of the unit cell (bottom) against *x* in $La_xSr_{2-x}CoRuO_6$.

As discussed in the literature,[90,91] the doping of $LaSrCoRuO_6$ changes the oxidation states of the transition metal centres. Upon electron doping, the valency of Ru decreases from Ru^{5+} to Ru^{4+}; On the contrary, the substitution of La^{3+} cations with Sr^{2+} cations for the hole doped compounds leads to the oxidation of Co^{2+} centres to Co^{3+} centres (Fig 8.3). The literature also states that upon hole doping the system, the newly formed Co^{3+} centres adopt a high spin state,

which is consistent with the monotonic lattice parameter change upon substitution with Sr^{2+} into the structure.[90]

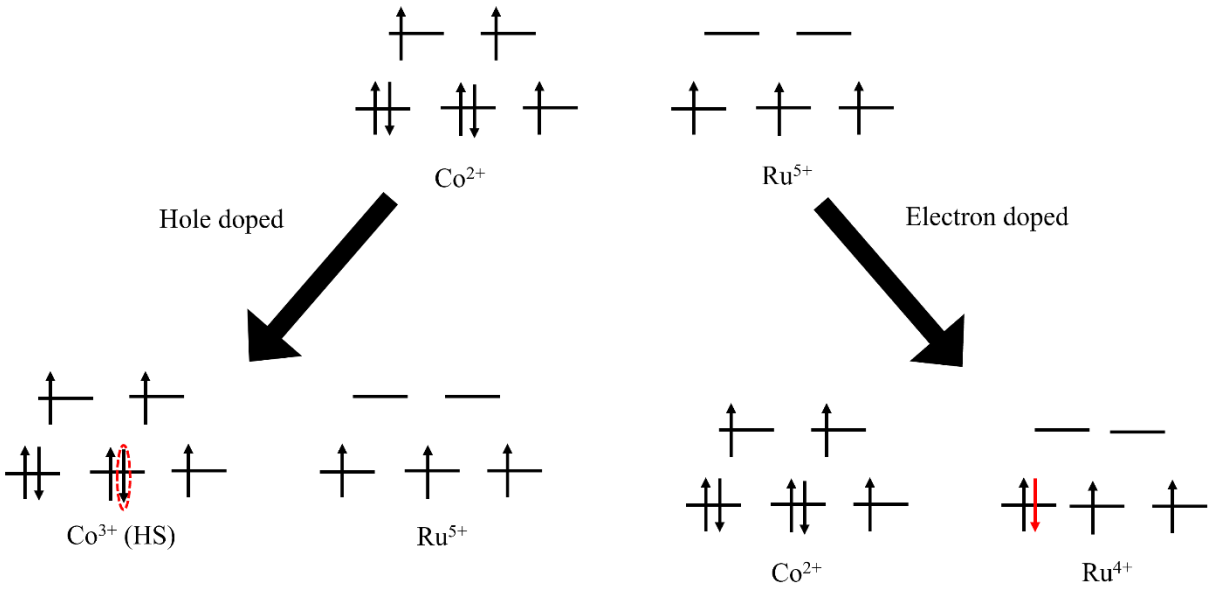


Figure 8.3. Predicted spin states of the B-site transition metal cations in $La_xSr_{2-x}CoRuO_6$ ($0.6 \leq x \leq 1.4$).

As shown in Fig 8.2, the change in the *a* lattice parameter is subtle, while the *b* and *c* lattice parameters increase drastically as the amount of La increases (*x*). There is a slight discontinuity in the lattice parameter at $x = 1$. The monotonic change in the lattice parameters of the $La_xSr_{2-x}CoRuO_6$ ($0.6 \leq x \leq 1.4$) series is consistent with the formation of single phases throughout the whole doping series. The expansion of the *b* and *c* lattice parameters upon electron doping is attributed to the reduction of the Ru^{5+} centres to Ru^{4+} centres, which outweighs the effect from the substitution of smaller La^{3+} cations for larger Sr^{2+} cations; on the contrary, the contraction of the *b* and *c* lattice parameters upon hole doping arises from the oxidation of Co^{2+} centres to Co^{3+} centres, which outweighs the effect from the substitution of larger Sr^{2+} cations for smaller La^{3+} cations. The observed change in the lattice parameters upon doping is consistent with previously reported results. The ionic radii of these A- and B-site cations are summarised in Table 8.3.

Ions	Ionic Radius (pm)
La^{3+}	103.2
Sr^{2+}	118.0
Co^{2+} (HS)	88.5
Co^{2+} (LS)	79.0
Co^{3+} (HS)	75.0
Co^{3+} (LS)	68.5
Ru^{5+}	56.5
Ru^{4+}	62.0

Table 8.3. Ionic radii of A- and B-site cations.[92]

The Co and Ru centres in $LaSrCoRuO_6$ are distributed in a rocksalt ordered arrangement, while the La/Sr cations are randomly distributed over the A-site. The change in the Co/Ru disorder will affect the magnetic properties of the parent oxide phases and their corresponded reduced phases ($La_xSr_{2-x}CoRuO_6$, $0.6 \leq x \leq 1.4$, $La_xSr_{2-x}CoRuO_{6-\delta}$, $0.7 \leq x \leq 1.3$). Therefore, the anti-site disorder of the Co and Ru centres was refined and summarised in Fig 8.4. Upon doping of $LaSrCoRuO_6$, the anti-site disorder increases when the samples become more hole doped ($La_xSr_{2-x}CoRuO_6$, $x < 1$) and remains almost constant for the electron doped samples ($La_xSr_{2-x}CoRuO_6$, $x > 1$). The increase in the anti-site disorder at the B-site is attributed to the reduction in size and oxidation state differences between the Co and Ru transition metal cations.[91] The anti-site disorder of the B-site cations for the electron doped $La_xSr_{2-x}CoRuO_6$ samples are relatively small (< 5%) while anti-site disorder is noticeable for the hole doped samples (~ 15%). Therefore, the anti-site disorder between the Co and Ru centres will not significantly affect the magnetic properties of the electron doped double perovskite oxide phases ($La_xSr_{2-x}CoRuO_6$, $1 < x \leq 1.4$) and the electron doped reduced phases

($La_xSr_{2-x}CoRuO_{6-\delta}$, $1 < x \leq 1.3$) but it might be large enough to play a role in affecting the magnetic properties of the hole doped double perovskite oxide phases ($La_xSr_{2-x}CoRuO_6$, $0.6 \leq x < 1$) and the hole doped reduced phases ($La_xSr_{2-x}CoRuO_{6-\delta}$, $0.7 \leq x < 1$).

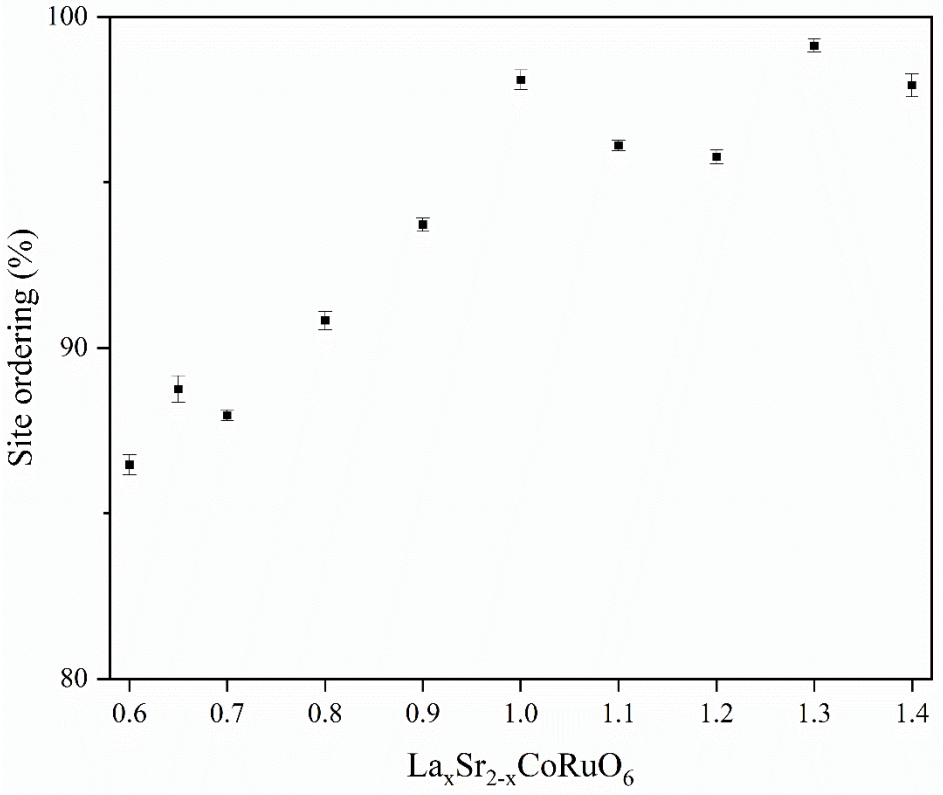


Figure 8.4. Degrees of B-site cation order in $La_xSr_{2-x}CoRuO_6$ ($0.6 \leq x \leq 1.4$) as a function of *x*.

8.3.2. Thermogravimetric Analysis of $La_xSr_{2-x}CoRuO_{6-\delta}$ ($0.6 \leq x \leq 1.4$)

To determine the chemical composition of the reduced $La_xSr_{2-x}CoRuO_{6-\delta}$ ($0.6 \leq x \leq 1.4$) phases, oxidative thermogravimetric analysis (TGA) experiments were conducted for all reduced samples of $La_xSr_{2-x}CoRuO_{6-\delta}$ ($0.6 \leq x \leq 1.4$). A small quantity of reduced samples was heated to 800 °C under a constant flow of O_2, the samples were held at this temperature for 3 hours before cooling to room temperature. The oxygen contents of the reduced samples were calculated from the mass difference between $La_xSr_{2-x}CoRuO_{6-\delta}$ and their respective parent phases $La_xSr_{2-x}CoRuO_6$. X-ray powder diffraction data collected from the re-oxidised products

after the TGA experiments confirmed a complete re-oxidation to their respective parent phases $La_xSr_{2-x}CoRuO_6$ ($0.6 \leq x \leq 1.4$). The oxygen contents of the reduced $La_xSr_{2-x}CoRuO_{6-\delta}$ ($0.6 \leq x \leq 1.4$) samples are summarised in Table 8.4. The TGA data collected from $La_{0.8}Sr_{1.2}CoRuO_{6-\delta}$ are shown below, while the TGA data collected from other phases can be found in Appendix 2.5.

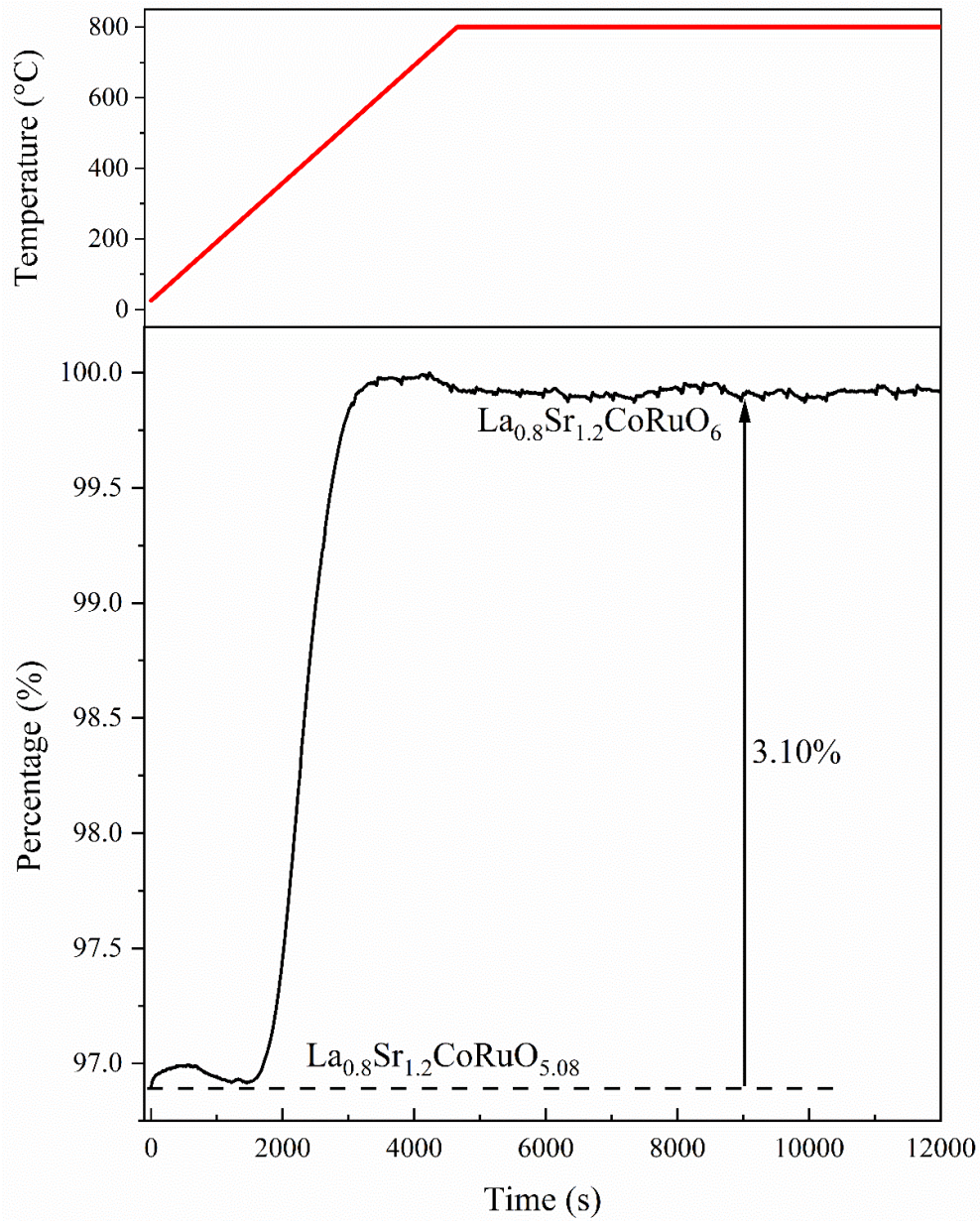


Figure 8.5. Oxidative thermogravimetric data collected from $La_{0.8}Sr_{1.2}CoRuO_{6-\delta}$. Top panel indicates the heating profile, bottom panel indicates the change of mass of the sample as a function of time.

La Content (x)	Oxygen content
1.4	5.08
1.3	5.09
1.2	5.07
1.1	5.05
1.0	5.03
0.9	5.02
0.8	5.08
0.7	5.01
0.6	5.10

Table 8.4. Oxygen content of the doping series $La_xSr_{2-x}CoRuO_{6-\delta}$ ($0.6 \leq x \leq 1.4$).

The TGA data are expected to help distinguish the following two possible scenarios: for the first scenario, it is possible that the hole/electron doping of the reduced $La_xSr_{2-x}CoRuO_{6-\delta}$ ($0.6 \leq x \leq 1.4$) phases changes the oxygen content so that the charges of the transition metal centres are preserved upon doping ($La_xSr_{2-x}CoRuO_{4.5+0.5x}$); for the second scenario, the hole/electron doping of the reduced $La_xSr_{2-x}CoRuO_{6-\delta}$ ($0.6 \leq x \leq 1.4$) phases oxidises/reduces the transition metal cations and hence all the reduced doped phases have a uniform oxygen content ($La_xSr_{2-x}CoRuO_5$). The TGA data obtained from this series of compounds ($La_xSr_{2-x}CoRu_{6-\delta}$ ($0.6 \leq x \leq 1.4$)) are more consistent with the second scenario, where the transition metal cations are oxidised/reduced upon doping. Slight oxygen excess was observed for some samples, which can be attributed to the presence of unreacted parent $La_xSr_{2-x}CoRuO_6$ ($0.6 \leq x \leq 1.4$) phases. The presence of the unreacted parent $La_xSr_{2-x}CoRuO_6$ ($0.6 \leq x \leq 1.4$) phases were confirmed by synchrotron X-ray powder diffraction (SXRD) data collected from this series of compounds (Appendix 2.6). Once this is taken into account, the mass gain

corresponds to a composition of $La_xSr_{2-x}CoRuO_5$ ($0.7 \leq x \leq 1.4$). Henceforth, this series of reduced phases will be referred to as $La_xSr_{2-x}CoRuO_5$ ($0.6 \leq x \leq 1.4$).

8.3.3 Structural Characterisation of $La_xSr_{2-x}CoRuO_5$ ($0.6 \leq x \leq 1.4$)

Synchrotron X-ray powder diffraction (SXRD) data were collected from samples of $La_xSr_{2-x}CoRuO_5$ ($0.6 \leq x \leq 1.4$) prepared by reduction of $La_xSr_{2-x}CoRuO_6$ ($0.6 \leq x \leq 1.4$) with Zr getters. The SXRD data showed that the reduced $La_xSr_{2-x}CoRuO_5$ ($0.7 \leq x \leq 1.4$) samples adopted the same anion-vacancy ordered structure as their undoped reduced phase ($LaSrCoRuO_5$), while $La_{0.6}Sr_{1.4}CoRuO_5$ adopted a different anion-vacancy ordered structure. The difference in the crystal structure between these samples was distinguished by the loss of the superstructure peaks (Fig 8.6). Since the crystal structure of $La_{0.6}Sr_{1.4}CoRuO_5$ is different from the rest of the doping series, it was then excluded from the magnetic characterisation.

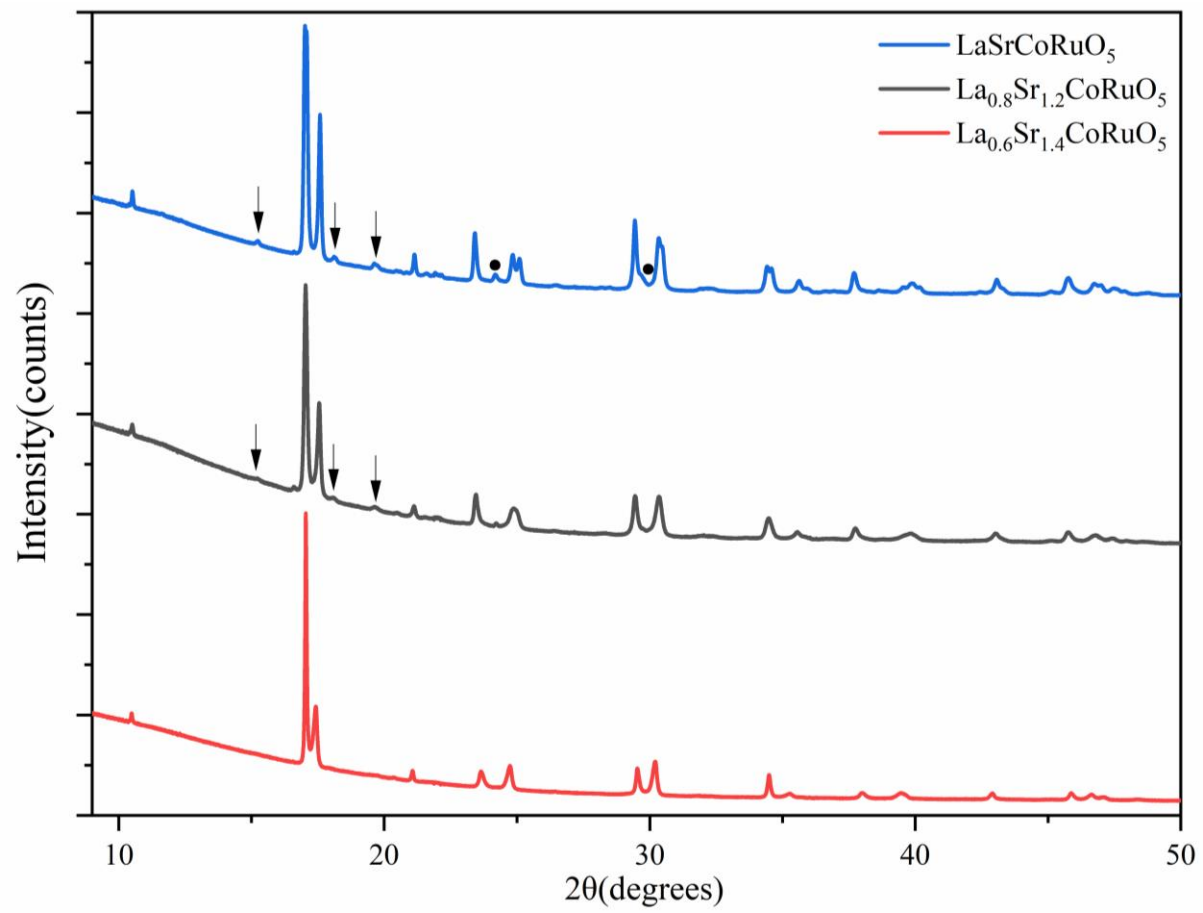


Figure 8.6. Direct comparison of the SXRD data collected from the undoped $LaSrCoRuO_5$, $La_{0.8}Sr_{1.2}CoRuO_5$ and $La_{0.6}Sr_{1.4}CoRuO_5$. Arrows highlight the superstructure peaks, dots represent the unreacted starting material $LaSrCoRuO_6$.

SXRD data collected from samples of $La_xSr_{2-x}CoRuO_5$ ($0.7 \leq x \leq 1.4$) showed that all the reduced phases can be indexed with a $2\sqrt{2} \times 2\sqrt{2} \times 2$ geometric cell expansion described in $P112_1$ space group based on the undoped sample $LaSrCoRuO_5$, mentioned in Chapter 6, with slight variations in the lattice parameters. Structural models based on the refined structure of $LaSrCoRuO_5$, with adjusted La/Sr ratios, were refined against the SXRD data collected from the reduced samples in the doping series ($La_xSr_{2-x}CoRuO_5$, $0.7 \leq x \leq 1.4$). The refinements against the SXRD data converged rapidly and achieved good statistical fits. The observed, calculated and difference plots of $La_{0.8}Sr_{1.2}CoRuO_5$ are shown as a representative, and the rest

of the refinement plots of the doping series can be found in Appendix 2.6. A structural model of $LaSrCoRuO_5$ is also shown in Fig 8.7.

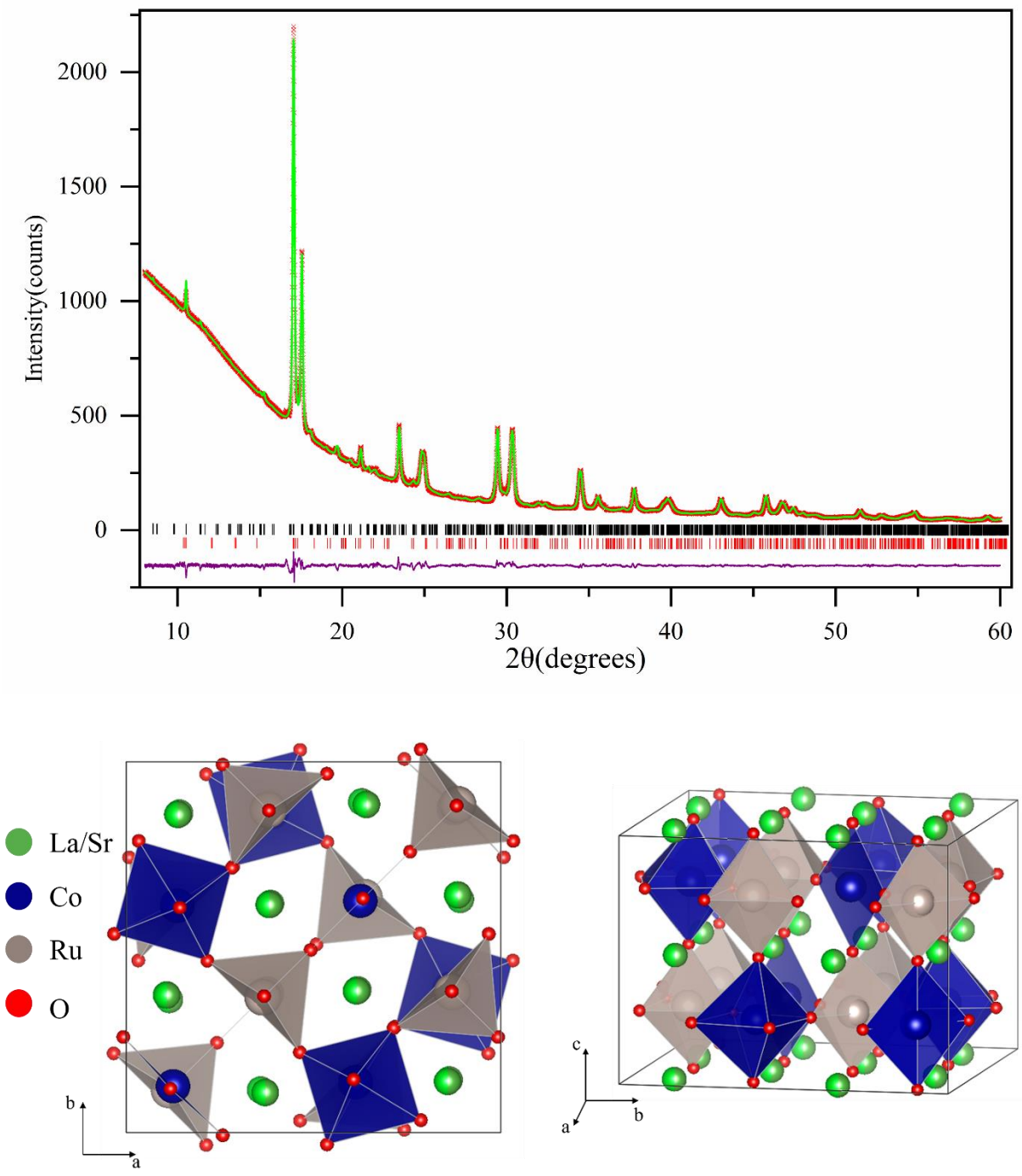


Figure 8.7. Observed, calculated and difference plots from the structural refinement of $La_{0.8}Sr_{1.2}CoRuO_5$ against SXRD data collected at room temperature. Upper ticks mark the peak positions of the majority phase $La_{0.8}Sr_{1.2}CoRuO_5$ and the lower ticks mark the peak positions of the minority phase $La_{0.8}Sr_{1.2}CoRuO_6$.

The lattice parameters extracted from the refinements against SXRD data collected from the reduced samples ($La_xSr_{2-x}CoRuO_5$, $0.7 \leq x \leq 1.4$) are plotted as a function of composition (x) (Fig 8.8). The black solid line represents the undoped reduced phase $LaSrCoRuO_5$, the left-hand side represents the La-deficient samples ($x < 1$, hole doping) and the right-hand side represents the La-rich samples ($x > 1$, electron doping). The lattice parameters extracted from $La_{1.4}Sr_{0.6}CoRuO_5$ are clearly anomalous (circled in red), as this end member approaches the doping limit of the structure. Therefore, this phase ($La_{1.4}Sr_{0.6}CoRuO_5$) was excluded for the magnetic characterisation.

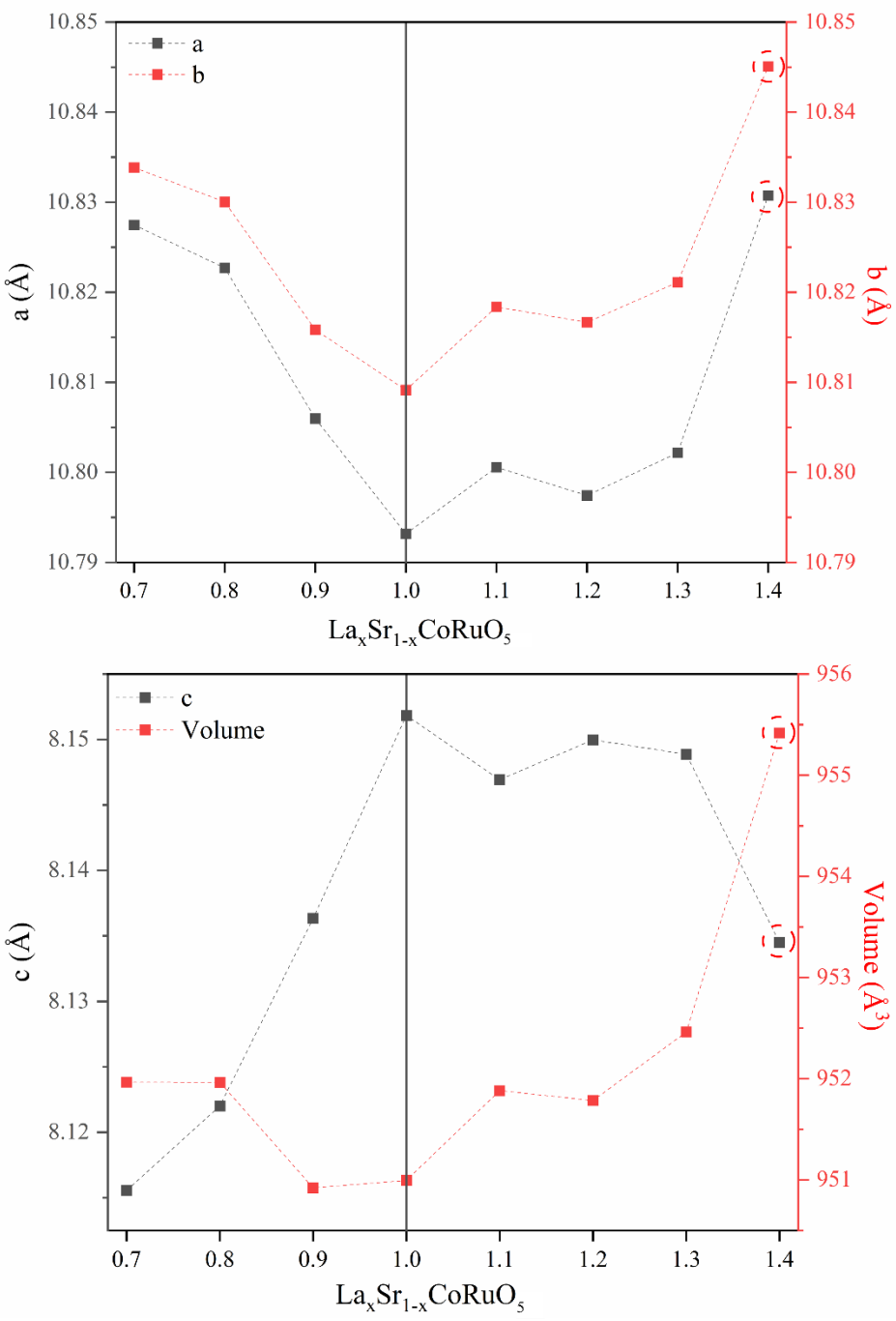


Figure 8.8. *a*, *b* lattice parameters (top), *c* lattice parameter and volume of the unit cell (bottom) against *x* in $La_xSr_{2-x}CoRuO_5$.

As shown in Fig 8.8, the *a* and *b* lattice parameters increase drastically upon hole doping, which is attributed to the substitution of smaller La^{3+} cations with larger Sr^{2+} cations into the structure. The contraction of the *c* lattice parameter upon hole doping arises from the oxidation of the transition metal centres. On the contrary, the slight increase in the *a*, *b* lattice parameters upon

electron doping are attributed to the reduction of the transition metal centres while there is not a significant change in the *c* lattice parameter upon electron doping.

In summary, with combination of the TGA data and the extracted lattice parameters from the structural refinement of the $La_xSr_{2-x}CoRuO_5$ ($0.7 \leq x \leq 1.3$) samples, it is reasonable to conclude that this series of compounds is single-phase and has a uniform oxygen content.

As discussed in Chapter 6, bond valence sum calculations for the transition metal cations in $LaSrCoRuO_5$ reveal a disproportionation of Co^{2+} centres into a 1:1 ratio of Co^{+} and Co^{3+} centres. This structure contains Co^{+} centres that reside at the square-planar coordination sites (D_{4h}) and Co^{3+} centres that locate at the octahedral sites (O_h), suggesting that the disproportionation of the Co^{2+} centres is coupled with the anion-vacancy ordering in $LaSrCoRuO_5$. Upon slight hole/electron doping, $La_xSr_{2-x}CoRuO_5$ ($0.7 \leq x \leq 1.3$) samples are isostructural with the undoped sample $LaSrCoRuO_5$, suggesting that the sophisticated anion-vacancy ordered structure adopted by $LaSrCoRuO_5$ can accommodate a small amount of electronic doping. However, when the system becomes heavily hole doped ($La_{0.6}Sr_{1.4}CoRuO_5$), a change in the crystal structure was observed. This will be further discussed in Section 8.4.2.

8.3.4 Magnetic Characterisation of $La_xSr_{2-x}CoRuO_5$ ($0.7 \leq x \leq 1.4$)

Magnetization data were collected from samples of $La_xSr_{2-x}CoRuO_5$ ($0.7 \leq x \leq 1.3$) using a ferromagnetic subtraction method (Section 2.8.1). The magnetisation data collected from $La_{0.8}Sr_{1.2}CoRuO_5$ are shown in Fig 8.9 as a representative, with the rest of the magnetisation plots found in Appendix 2.7. The paramagnetic susceptibility of $La_{0.8}Sr_{1.2}CoRuO_5$ can be fitted with the Curie-Weiss law ($\chi = C/(T - \theta)$) between $145 \leq T/K \leq 300$ to yield values of C = 3.581(6) cm^3 K mol^{-1} and θ = 71.1(4) K. Below 145 K, the saturated magnetic moment of $La_{0.8}Sr_{1.2}CoRuO_5$ increases sharply, which is suggestive of the onset of ferromagnetic order below T ~ 145 K.

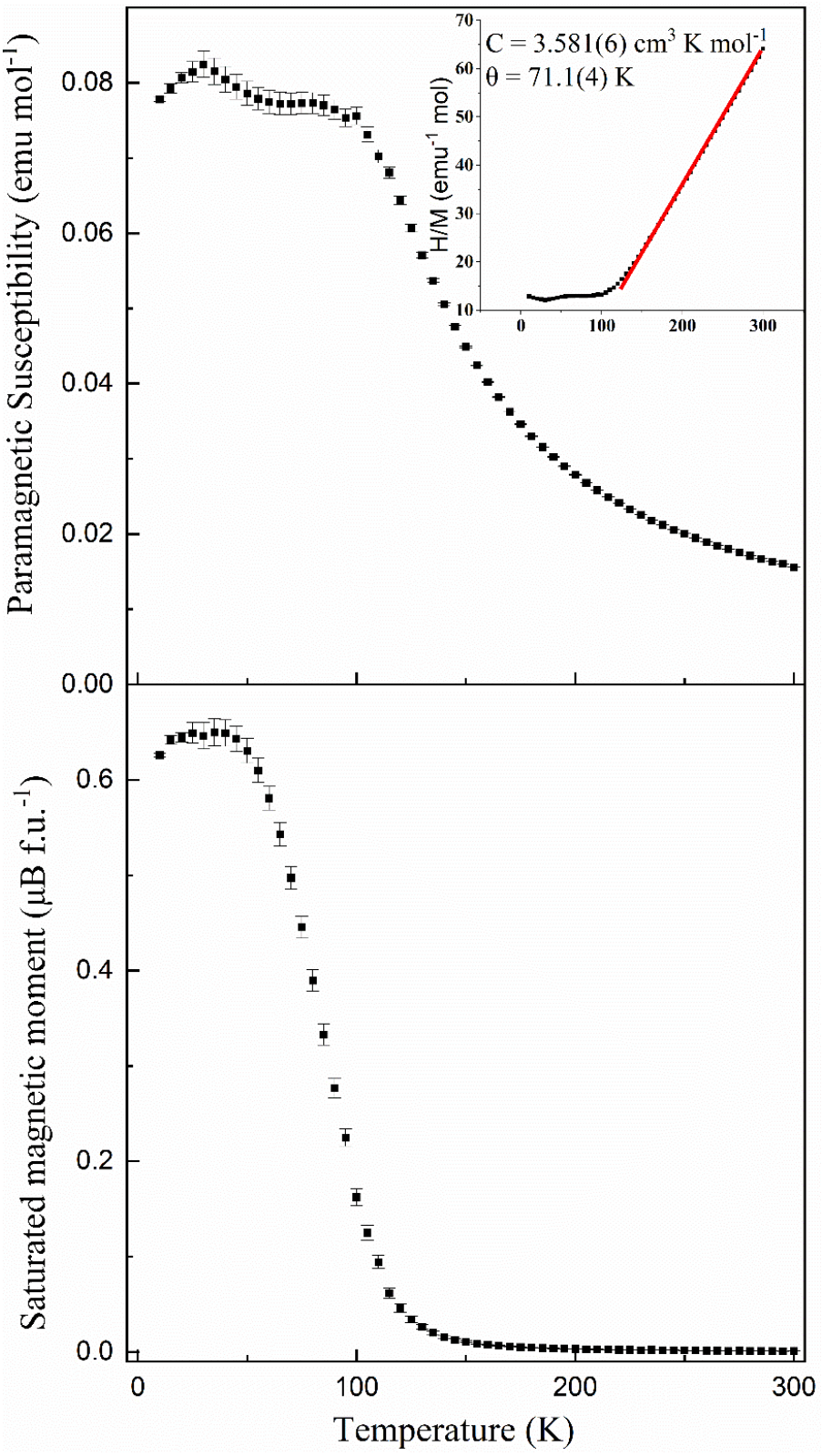


Figure 8.9. The paramagnetic susceptibility and saturated magnetic moment of $La_{0.8}Sr_{1.2}CoRuO_5$ collected as a function of temperature. Inset shows the fit to Curie-Weiss law in the temperature range $145 \leq T/K \leq 300$.

The magnetisation-field data collected from $La_{0.8}Sr_{1.2}CoRuO_5$ are shown in Fig 8.10. A hysteresis loop was observed at 5 K. This observation is consistent with the magnetisation data described above, suggesting the presence of a ferromagnetic ordered state of $La_{0.8}Sr_{1.2}CoRuO_5$ at low temperature. The hysteresis loop at 5 K is slightly displaced from the origin, indicating a possible spin-glass state. The magnetisation-field data collected from other doped reduced phases ($La_xSr_{2-x}CoRuO_5$, $0.7 \leq x \leq 1.3$) are listed in Appendix 2.7.

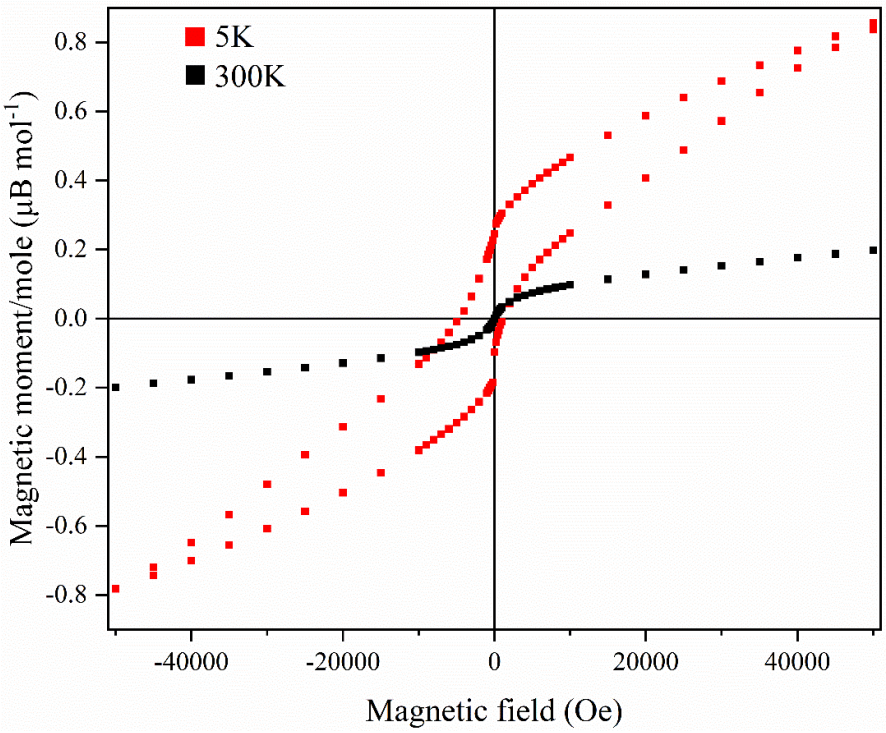


Figure 8.10. Magnetisation data collected as a function of applied field from $La_{0.8}Sr_{1.2}CoRuO_5$.

In general, the magnetisation data collected from all doped reduced oxide phases ($La_xSr_{2-x}CoRuO_5$, $0.7 \leq x \leq 1.3$) suggest a presence of a ferromagnetic ordered state at low temperature which is similar to the undoped $LaSrCoRuO_5$ phase.

The paramagnetic susceptibility of each doped compound ($La_xSr_{2-x}CoRuO_5$, $0.7 \leq x \leq 1.3$) can be fitted by the Curie-Weiss law ($\chi = C/(T - \theta)$) within a slightly different temperature range. The Curie constants and the Weiss constants extracted from the magnetisation data are summarised in Fig 8.11. The black line represents the undoped $LaSrCoRuO_5$ phase; the left-

hand side represents the La-deficient compounds ($x < 1$, hole doping) and the right-hand side represents the La-rich compounds ($x > 1$, electron doping). The Curie constant increases slightly when the sample becomes more electron doped and decreases slightly upon hole doping. At the meantime, the Weiss constant extracted decreases when x deviates from 1. Throughout the whole doping series, the Weiss constant remains positive, indicating that a net ferromagnetic interaction is present in all the doped reduced oxide phases ($La_xSr_{2-x}CoRuO_5$, $0.7 \leq x \leq 1.3$).

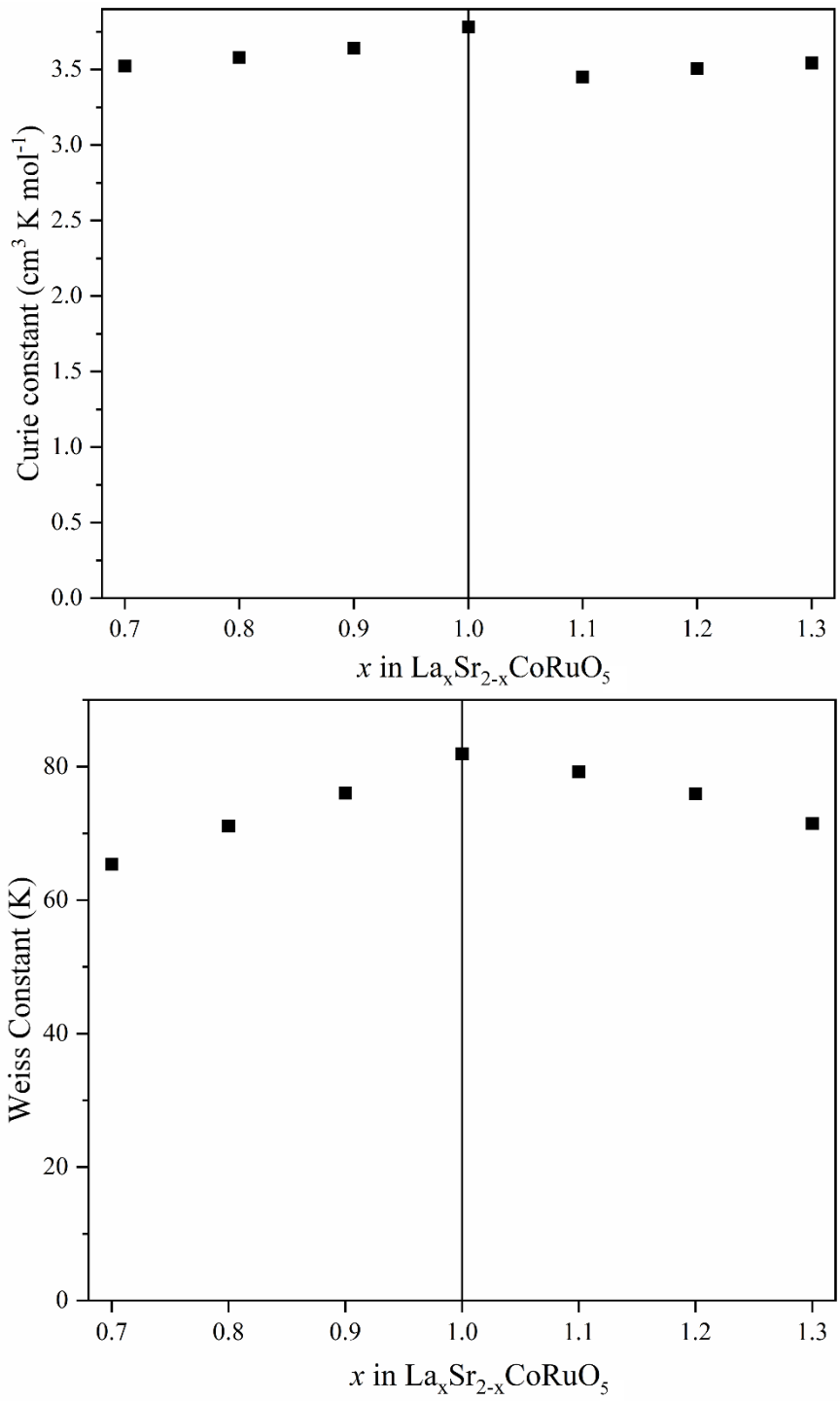


Figure 8.11. Curie constant (top) and Weiss constant (bottom) against *x* in $La_xSr_{2-x}CoRuO_5$.

The Curie constants extracted from the doped reduced phases ($La_xSr_{2-x}CoRuO_5$, $0.7 \leq x \leq 1.3$) are inconsistent with a simple weakly interacting paramagnetic model, similar to their undoped $LaSrCoRuO_5$ phase (Section 6.3.3.1), where the Curie-Weiss law is mimicked by the sample. Thus, the Curie constants extracted from the doped reduced phases ($La_xSr_{2-x}CoRuO_5$, $0.7 \leq x$

≤ 1.3) cannot accurately depict the number of unpaired electrons in the Co/Ru cations centres. Therefore, the saturated magnetic moment of the doped reduced oxide phases is plotted as a function of temperature (Fig 8.12), as the saturated magnetic moment can also provide information about the number of unpaired electrons in the transition metal centres in a compound.

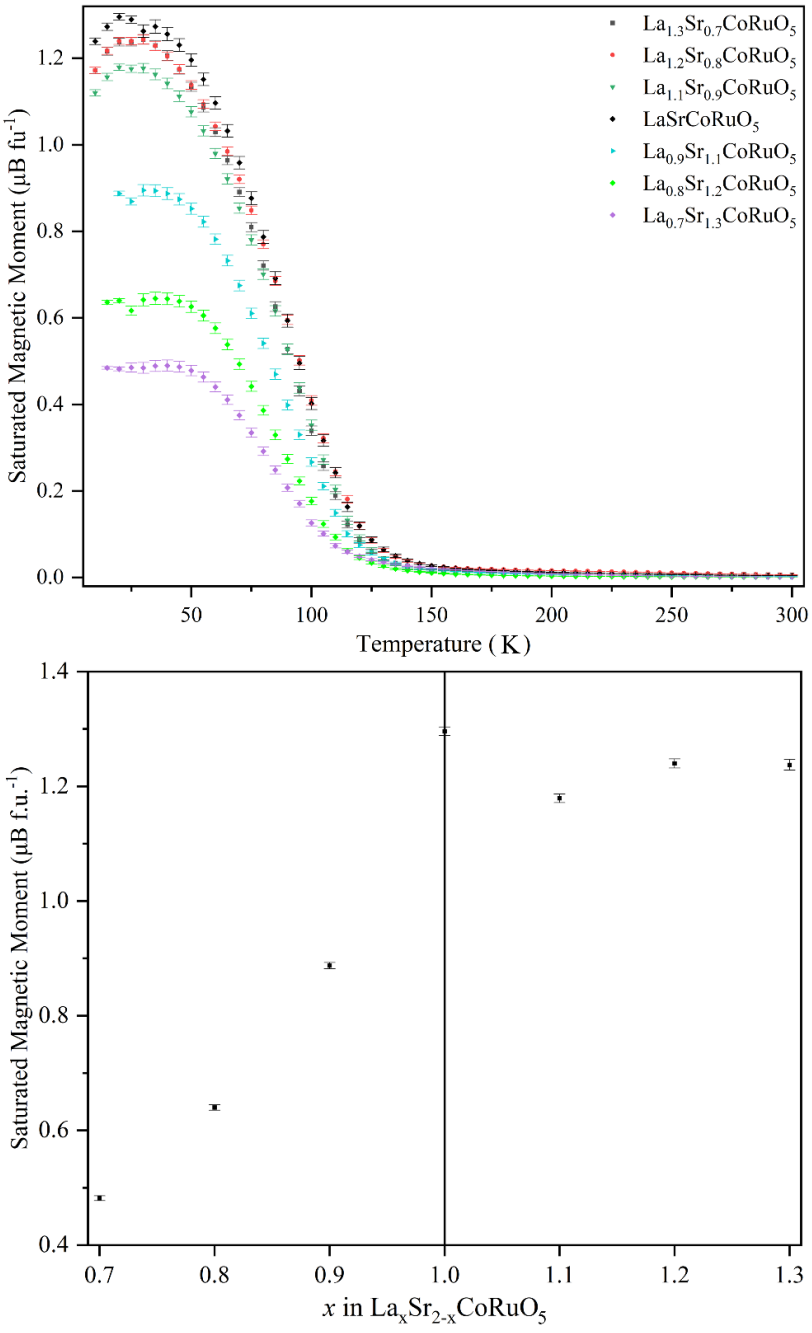


Figure 8.12. Saturated magnetic moment of $La_xSr_{2-x}CoRuO_5$ against temperature (top) and saturated magnetic moment of $La_xSr_{2-x}CoRuO_5$ (bottom) against *x* at 20 K.

The saturated magnetic moments of the doped reduced oxide phases ($La_xSr_{2-x}CoRuO_5$, $0.7 \leq x \leq 1.3$) decrease drastically upon hole doping ($x < 1$) but remain almost unchanged upon electron doping ($x > 1$). The magnetic properties of the doped reduced phases ($La_xSr_{2-x}CoRuO_5$, $0.7 \leq x \leq 1.3$) can be explained by examining the electronic structures of the B-site transition metal centres. In principle, there is an ambiguity over which transition metal cations are oxidised (Co/Ru) in $La_xSr_{2-x}CoRuO_5$ when $x < 1$. Hole doping of the system could oxidise Co^+ centres to Co^{2+} centres or Ru^{3+} centres to Ru^{4+} centres. The oxidation of the Co^+ to Co^{2+} centres removes an electron from the t_{2g} level, introducing an extra unpaired electron (Fig 8.13 bottom). This extra electron would not significantly affect the magnetic couplings between the transition metal centres, the magnetic interaction in the hole doped samples would still be dominated by the σ-type ferromagnetic superexchange couplings between (Co d_{x2-y2})^1 – O – (Ru d_{z2})^0, (Co d_{x2-y2})^1 – O – (Ru d_{x2-y2})^0 and the weak ferromagnetic direct exchange between (Co d_{z2})^1-(Ru d_{z2})^0. However, the saturated magnetic moment of the reduced phases would be expected to increase upon hole doping due to the presence of an extra unpaired electron, this is not consistent with the experimental data.

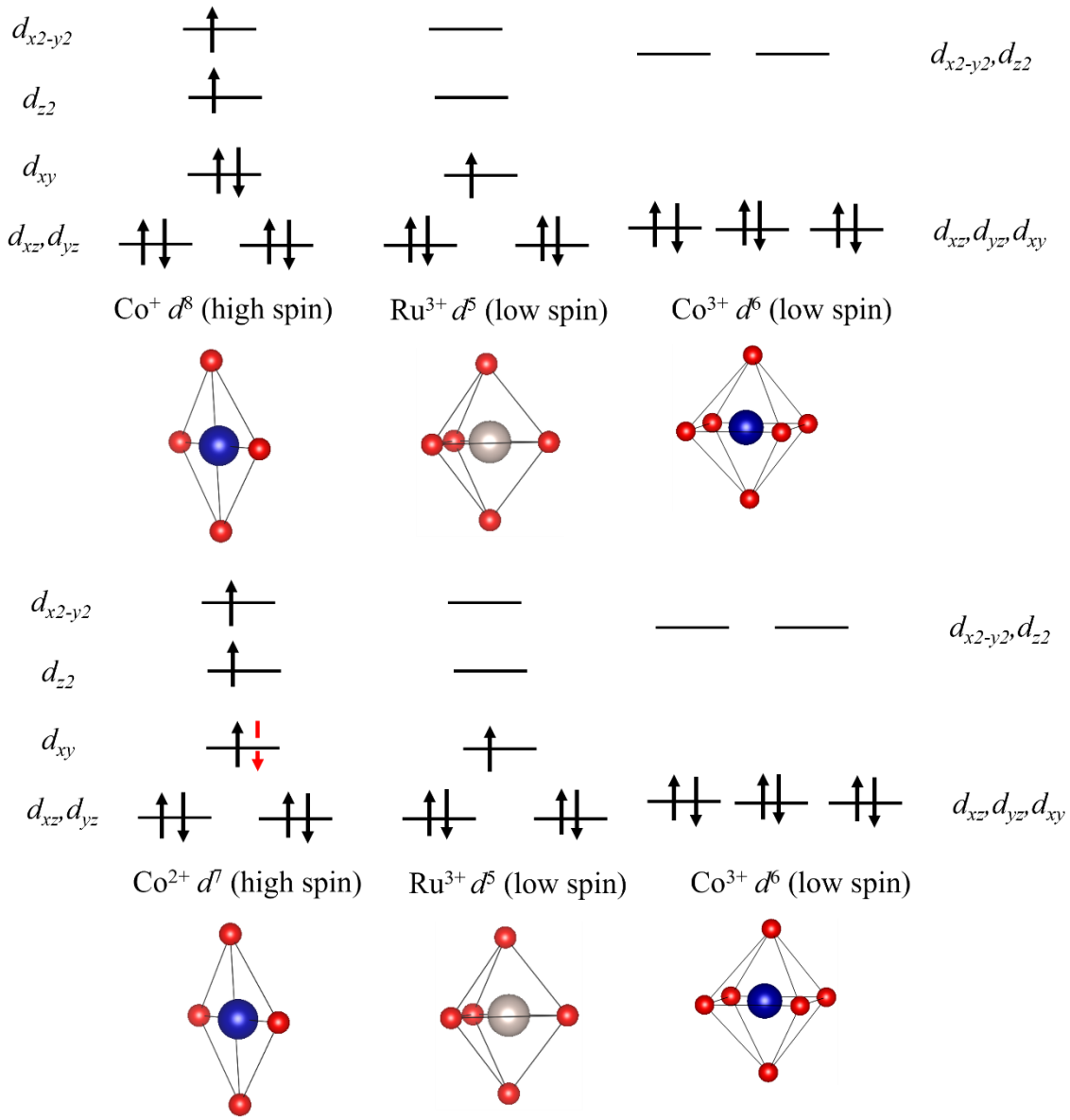


Figure 8.13. Predicted electronic states of B-site transition metal cations in $LaSrCoRuO_5$ (top); predicted electronic states of B-site transition metal cations in hole doped $La_xSr_{2-x}CoRuO_5$ ($0.7 \leq x < 1$), red dashed arrow indicates the electron removed upon oxidation (bottom).

For the second possibility, the oxidation of Ru^{3+} centres to Ru^{4+} centres removes an electron from the t_{2g} level, introducing an extra unpaired electron in the Ru t_{2g} level. The introduction of an extra unpaired electron in the Ru t_{2g} level would not significantly affect the magnetic couplings between the transition metal centres (the strong σ-type superexchange couplings between (Co d_{x2-y2})^1 – O – (Ru d_{x2-y2})^0 and (Co d_{x2-y2})^1 – O – (Ru d_{z2})^0 are still preserved).

However, the saturated magnetic moment of the samples would also expect to increase upon hole doping, which is also not consistent with the experimental data.

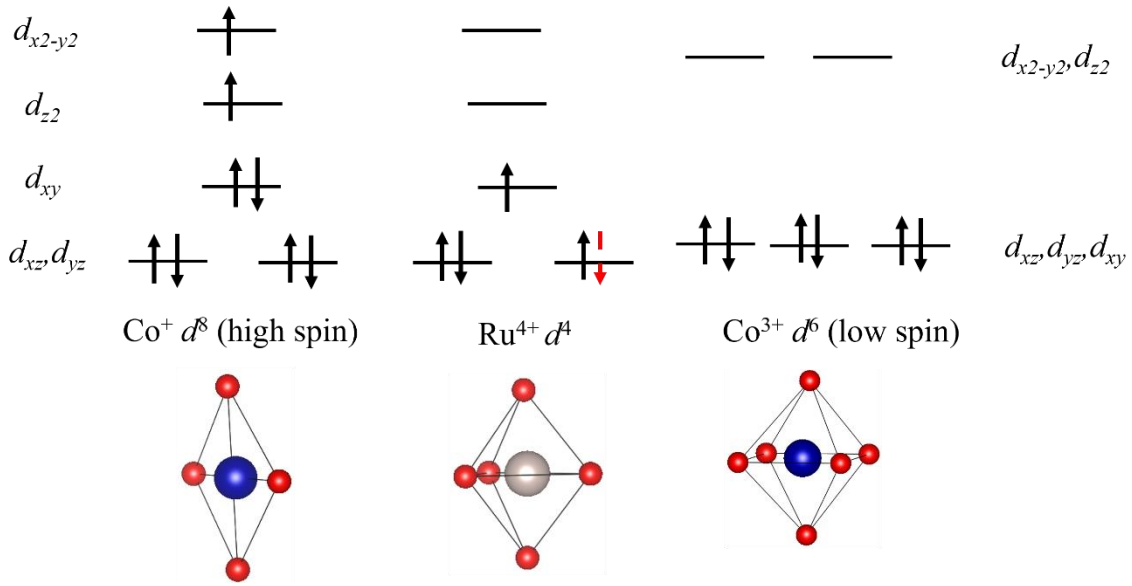


Figure 8.14. Predicted spin states of B-site transition metal cations in hole doped $La_xSr_{2-x}CoRuO_5$ ($0.7 \leq x < 1$), red dashed arrow indicates the electron removed upon oxidation.

In summary, it is unclear what factors cause the decrease in the saturated magnetic moment of these hole doped oxygen deficient phases ($La_xSr_{2-x}CoRuO_5$, $0.7 \leq x < 1$). It is worth noting that an increase in the anti-site disorder was observed at the B-site for the hole doped $La_xSr_{2-x}CoRuO_6$ ($0.7 \leq x < 1$) phases (Section 8.3.1). It is likely that the increase in the anti-site disorder upon hole doping plays a role in affecting the magnetic properties of these hole doped reduced phases. Further investigations are needed to understand this hole-doped $La_xSr_{2-x}CoRuO_5$ ($0.7 \leq x < 1$) system.

For the electron doped samples ($x > 1$), the saturated magnetic moment remains almost unchanged upon electron doping. Previous studies have shown that the 4*d*/5*d* transition metal centres do not contribute strongly to the total magnetic moment of a sample. Therefore, in this case, it is likely that the reduction takes place at the Ru^{3+} centres to yield Ru^{2+} centres. The lack

of Ru centres contribution to the overall saturated magnetic moments was also observed in $LaSrCoRuO_4$ and $LaSrNiRuO_4$.[37]

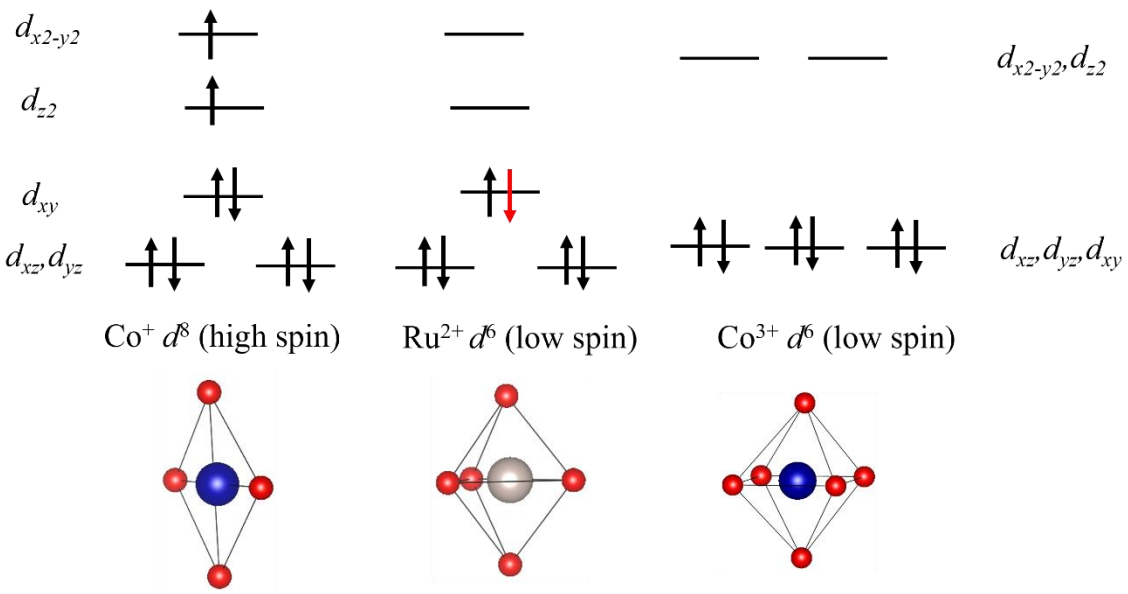


Figure 8.15. Predicted spin states of B-site transition metal cations in electron doped $La_xSr_{2-x}CoRuO_5$ ($1 < x \leq 1.3$). The red arrow indicates the extra electron added into the system upon electron doping.

8.4 Discussion

8.4.1 Doping Limits of $La_xSr_{2-x}CoRuO_6$ and $La_xSr_{2-x}CoRuO_5$ ($0.6 \leq x \leq 1.4$)

The chemical doping concept by varying ratio of the A-site cations in oxide or oxyhydride phases to introduce either holes or electrons into the system has been explored widely in solid-state chemistry.[93,94] By introducing more 'holes' or 'electrons' into the system, the charges of the transition metal cations can be altered. This may lead to a change in the structure of a material, or even its electronic and magnetic properties.[95–97]

The B-site cation ordered double perovskite $LaSrNiRuO_6$ can be doped to a very wide extent, in which $La_{1+x}Sr_{1-x}NiRuO_6$ ($-0.25 \leq x \leq 0.375$) can be achieved. However, for the reduction of $La_{1+x}Sr_{1-x}NiRuO_6$ with CaH_2 under flowing argon to form $La_{1+x}Sr_{1-x}NiRuO_4$, was only

successful when x = -0.15, -0.05, +0.1 and +0.25, which reduces the doping limit of the reduced phase.[93]

Similarly, the double perovskite $La_xSr_{2-x}CoRuO_6$ can be doped in a large degree, as both end members La_2CoRuO_6 and Sr_2CoRuO_6 have been reported.[98,99] The topochemical reduction of the doped $LaSrCoRuO_6$ compounds could be reduced to their respective reduced oxide phases in a similar manner. However, for the electron doped samples of $La_xSr_{2-x}CoRuO_6$ ($x > 1$), the activation energy associated with the reduction reactions with Zr increases as the reactions occur at a higher temperature. On the contrary, the reduction of the hole doped samples of $La_xSr_{2-x}CoRuO_6$ ($x < 1$) with Zr at 450 °C leads to the formation of a secondary phase, $La_xSr_{2-x}CoRuO_4$ ($x < 1$), which can only be avoided by using a lower reaction temperature. Therefore, the hole doped samples of $La_xSr_{2-x}CoRuO_5$ ($x < 1$) become more fragile as reflected in the lowering of the reduction temperatures. In addition, SXRD data collected from the heavily hole-doped reduced phase $La_{0.6}Sr_{1.4}CoRuO_5$ suggest a change in the anion-vacancy ordered structure. This has demonstrated that the doping range for $La_xSr_{2-x}CoRuO_5$ phases is narrower compared with their parent oxide phases ($La_xSr_{2-x}CoRuO_6$).

In conclusion, the starting material $La_xSr_{2-x}CoRuO_6$ shows a great ability to accommodate chemical doping. The large extent of electronic doping does not significantly compromise the B-site cation ordering. The topochemical reduced oxide $La_xSr_{2-x}CoRuO_5$ phase is also stable in a relatively wide doping range, with a structural change observed when a large amount of Sr^{2+} is introduced into the structure ($La_{0.6}Sr_{1.4}CoRuO_5$).

8.4.2 Magnetic Behaviours of the Reduced Oxide Phases

The crystal structures are generally preserved for all doped parent oxide phases and oxygen deficient phases. The magnetic properties of the hole doped reduced $La_xSr_{2-x}CoRuO_5$ ($0.7 \leq x < 1$) phases are very different from the undoped compound $LaSrCoRuO_5$.

For the La-rich (electron doped) compounds, the magnitude of the change of the saturated magnetic moment is unexpectedly small. This observation is attributed to the reduction of the Ru^{3+} centres, where the Ru centres contribute little towards the saturated magnetic moment of the samples, which has been observed in many mixed 3*d* and 4*d*/5*d* double perovskites.[16] For the La-deficient (hole doped) compounds, the saturated magnetic moments of the materials decrease drastically upon hole doping. It is unclear what factor causes this drastic change in the saturated magnetic moment upon hole doping.

The change in the anion-vacancy ordered structure upon a large degree of hole doping is surprising ($La_{0.6}Sr_{1.4}CoRuO_5$). This observation has indicated that the crystal structure is coupled with the oxidation states of the transition metal centres, suggesting that the complex anion-vacancy ordered structure adopted by $LaSrCoRuO_5$ is coupled with the oxidation states of the transition metal centres.

8.5 Conclusion

The double perovskite $LaSrCoRuO_6$ phase can accommodate a large degree of chemical doping. A series of doped parent oxide $La_xSr_{2-x}CoRuO_6$ ($0.6 \leq x \leq 1.4$) phases can be reduced with Zr to form $La_xSr_{2-x}CoRuO_5$ ($0.6 \leq x \leq 1.4$) at different reaction temperatures. The TGA data collected from the reduced doped $La_xSr_{2-x}CoRuO_5$ ($0.7 \leq x \leq 1.3$) phases confirmed a uniform oxygen content throughout the whole reduced series ($La_xSr_{2-x}CoRuO_5$ ($0.7 \leq x \leq 1.3$)), indicating that the transition metal centres were oxidised/reduced upon doping. SXRD data collected from the reduced doped $La_xSr_{2-x}CoRuO_5$ ($0.7 \leq x \leq 1.3$) phases confirmed the successful synthesis of single-phase reduced compounds. Upon slight electron/hole doping, $La_xSr_{2-x}CoRuO_5$ ($0.7 \leq x \leq 1.3$) phases are isostructural with the undoped $LaSrCoRuO_5$ phase. However, upon heavy hole doping the system ($La_{0.6}Sr_{1.4}CoRuO_5$), a structural change was observed. This observation suggests that the anion-vacancy ordered structure of $LaSrCoRuO_5$ is coupled with the oxidation states of the transition metal centres. Further works are needed to

investigate this doping series. For example, the stoichiometries of the reduced doped phases ($La_xSr_{2-x}CoRuO_5$, $0.7 \leq x \leq 1.3$) can be further confirmed by neutron powder diffraction; In addition, it is possible to solve the crystal structure of $La_{0.6}Sr_{1.4}CoRuO_5$ using neutron powder diffraction technique; Moreover, DFT calculations may also help to rationalise the interesting magnetic behaviour of the hole-doped compounds ($La_xSr_{2-x}CoRuO_5$, $0.7 \leq x < 1$).

Although all the doped reduced compounds ($La_xSr_{2-x}CoRuO_5$, $0.7 \leq x \leq 1.3$) are structurally indistinguishable, their magnetic properties differ vastly, indicating that a small amount of chemical doping can be used to tune the magnetic and physical properties of materials.

Chapter 9 Synthesis and Characterisation of $LaSrCoRuO_{6-x}H_y$

9.1 Introduction

The topochemical reduction of the B-site cation ordered double perovskite $LaSrCoRuO_6$ with LiH and CaH_2 in a sealed ampoule yields novel oxyhydride phases with different stoichiometries $LaSrCoRuO_{6-x}H_y$. In this chapter, a detailed structural and magnetic characterisation of these oxyhydride phases will be discussed.

9.2 Experimental

9.2.1 Reduction of $LaSrCoRuO_6$ with CaH_2

A quenched sample of $LaSrCoRuO_6$ was prepared via a citrate gel method as described in Section 5.2.1. 1.5 g of quenched $LaSrCoRuO_6$ was ground thoroughly with 4 mole equivalents of CaH_2 in an argon-filled glove box. The reaction mixture was then transferred into a pyrex ampoule and sealed under vacuum. The pyrex ampoule was then heated to 360 °C at 1 °C min^{-1} for 3 periods of 8 days. The rection mixtures were ground between each cycle and the reaction progression was monitored by X-ray powder diffraction. Once the reaction was deemed finished, the reaction mixture was washed under nitrogen with 0.1 M NH_4Cl in methanol to get rid of the calcium-containing by-products formed during the reaction, and any unreacted CaH_2. This was followed by 5 × 25 ml of clean methanol to dissolve any NH_4Cl residues. The sample was then dried in vacuum. This phase will be referred to as 'Sample A (CaH_2)'.

9.2.2 Reduction of $LaSrCoRuO_6$ with LiH

A quenched sample of $LaSrCoRuO_6$ was prepared via a citrate gel method as described in Section 5.2.1. A sample suitable for analysis by neutron powder diffraction was prepared by mixing 1.5 g of the quenched sample of $LaSrCoRuO_6$ with 8 mole equivalents of LiH in an

argon-filled glove box. The reaction mixture was then transferred into a pyrex ampoule and the pyrex ampoule was sealed under vacuum. The pyrex ampoule was heated to 320 °C at 1 °C min^{-1} for 3 periods of 8 days. Intermediate grinding was performed between each reaction cycle. X-ray powder diffraction was used to monitor the reaction progression. Once the reaction was deemed finished, the reaction mixture was washed under nitrogen with methanol to remove the Li_2O formed as by-product of the reaction and unreacted LiH. The washed product was dried in vacuum. This phase will be referred to as 'Sample B (LiH)'.

9.3 Results

9.3.1 Chemical Analysis of 'Sample A (CaH_2)'

9.3.1.1 Thermogravimetric Analysis of 'Sample A (CaH_2)'

The composition of 'Sample A (CaH_2)' ($LaSrCoRuO_{6-x}$) obtained from the reaction with CaH_2 was determined by conducting an oxidative thermogravimetric analysis (TGA). A small quantity of the reduced sample was heated to 800 °C under a constant flow of O_2 and kept at this temperature for 2 hours before cooling. During the TGA experiment, a mass gain of 9.27% was recorded, corresponding to a chemical formula $LaSrCoRuO_{3.20}$ (Fig 9.1). X-ray powder diffraction data collected from the re-oxidised product after the TGA experiment confirmed a complete re-oxidation back to the starting material $LaSrCoRuO_6$.

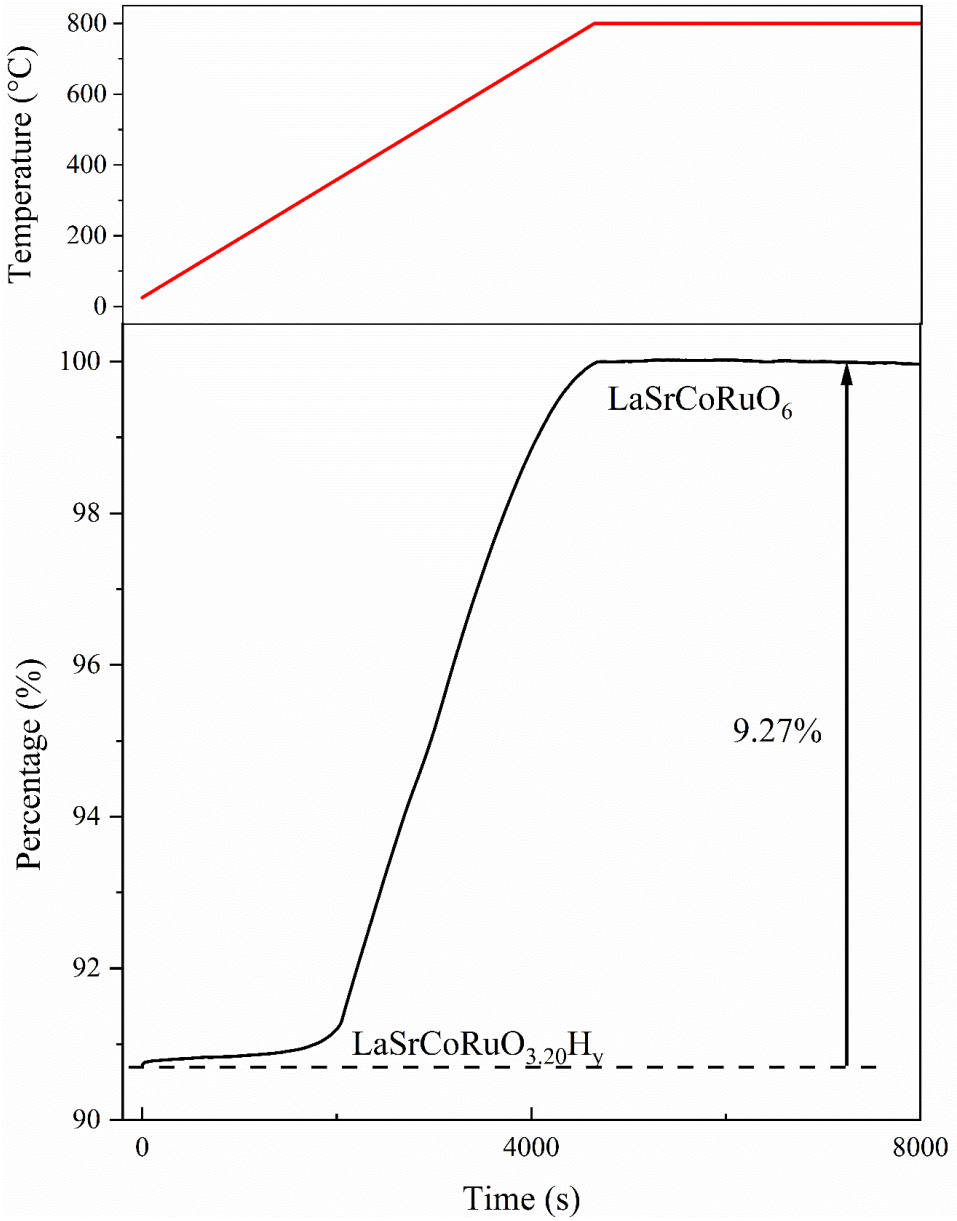


Figure 9.1. Oxidative thermogravimetric data collected from 'Sample A (CaH_2)'. Top panel indicates the heating profile, bottom panel shows the relative mass of the sample.

However, it is chemically unreasonable to have a chemical composition of '$LaSrCoRuO_{3.20}$' as the transition metal centres will have a summed charge of +1.4. Therefore, 'Sample A (CaH_2)' is considered as an oxyhydride phase.

9.3.1.2 Iodometric Titration of 'Sample A (CaH_2)'

The hydride content of 'Sample A (CaH_2)' was determined by performing iodometric titrations (Section 2.12). Iodometric titration allows the combined oxidation states of the transition metal centres to be determined. Combining the overall oxidation states of the transition metal centres with the oxygen content obtained from the TGA measurement, the hydride content of 'Sample A (CaH_2)' can then be calculated. The hydride content calculated from each titration is listed in Table 9.1.

Mass of 'Sample A (CaH_2)' (mg)	**I_2 reacted with the sample (mmol)**	**Volume of thiosulphate used for titration (ml) (concentration: 0.0098 M)**	**H^- content**
29.1	0.02233	5.85	1.925
44.3	0.03508	3.25	1.904
23.1	0.02086	6.15	1.806
43.9	0.02895	4.50	2.019

Table 9.1. Results of hydride content obtained from the iodometric titration of 'Sample A (CaH_2)'.

The average hydride content obtained from the titration was 1.91, which gave an approximate chemical composition of 'Sample A (CaH_2)' $LaSrCoRuO_{3.20}H_{1.91}$.

9.3.1.3 Structural Characterisation of 'Sample A (CaH_2)'

Synchrotron X-ray powder diffraction (SXRD) data were collected from 'Sample A (CaH_2)'. The SXRD data can be indexed with a cubic unit cell described in space group *Fm*-3*m* with the lattice parameter a = 7.67 Å. A structural model was constructed based on a Co/Ru B-site cation ordered double perovskite described in space group *Fm*-3*m* and refined against the

SXRD data. The oxygen occupancy was allowed to vary during the refinement. The refinement against SXRD data converged rapidly and gave a good statistical fit (*wRp* = 4.52%; *Rp* = 3.01%). The occupancy of the oxygen site declined dramatically and gave a value of 0.48(2). The refinement gave a composition of $LaSrCoRuO_{2.88(12)}$. However, SXRD data could not provide an accurate information about the anion content, as the light anions are weakly scattered by X-ray. Since the unit cell described 'Sample A (CaH_2)' has a cubic symmetry, it is likely that the oxide and the hydride anions are arranged in a completely disordered manner. The observed, calculated and difference plots of the structural refinement against SXRD data are shown in Fig 9.2, full details of the structural parameters are given in Table 9.2.

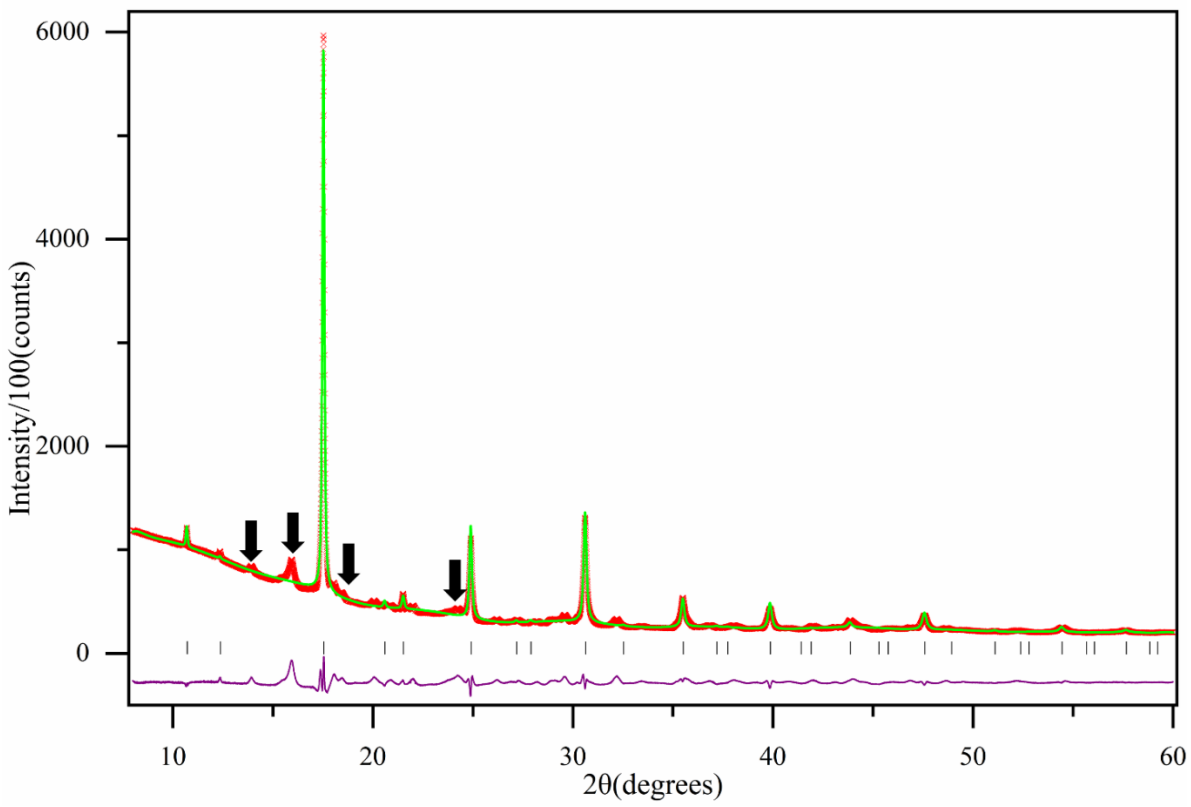


Figure 9.2. Observed, calculated and difference plots from the refinement of 'Sample A (CaH_2)' against SXRD data collected at room temperature. Arrows indicate unknown impurities present in the sample.

'Sample A (CaH_2)' $LaSrCoRuO_{3.20}H_{1.91}$, space group *Fm*-3*m* (#225)						
Atom	Wyckoff	*x*	*y*	*z*	Fraction	B_{iso} equiv. ($Å^2$)
La/Sr	8*c*	$^1/_4$	$^1/_4$	$^1/_4$	$^1/_2/^1/_2$	3.09(5)
Co	4*a*	0	0	0	1	3.08(7)
Ru	4*b*	$^1/_2$	0	0	1	3.08(7)
O(1)	24*e*	$^1/_2$	0	$^1/_4$	0.48(2)	4.13(70)
a = 7.6679(2) Å						
wRp = 4.52%; Rp = 3.01%						

Table 9.2. Structural parameters obtained from the refinement against SXRD data collected from 'Sample A (CaH_2)'.

9.3.1.4 SQUID Magnetometry of 'Sample A (CaH_2)'

A 'ferromagnetic subtraction' method (Section 2.8.1) was used to collect the magnetisation data from 'Sample A (CaH_2)' due to trace amounts of elemental Co (< 2 mol%) present in the sample. The paramagnetic susceptibility of 'Sample A (CaH_2)' fits with the Curie-Weiss law ($\chi = C/(T - \theta) + K$) in the temperature range 125 K ≤ T ≤ 300 K. This process yields values of C = 2.82(8) cm^3 K mol^{-1}, Weiss constant -162(5) K and K = 0.0009(1) $cm^3\,K\,mol^{-1}$. The saturated magnetic moment increases gradually upon cooling, which indicate a potential onset to canted antiferromagnetic ordering at low temperatures.

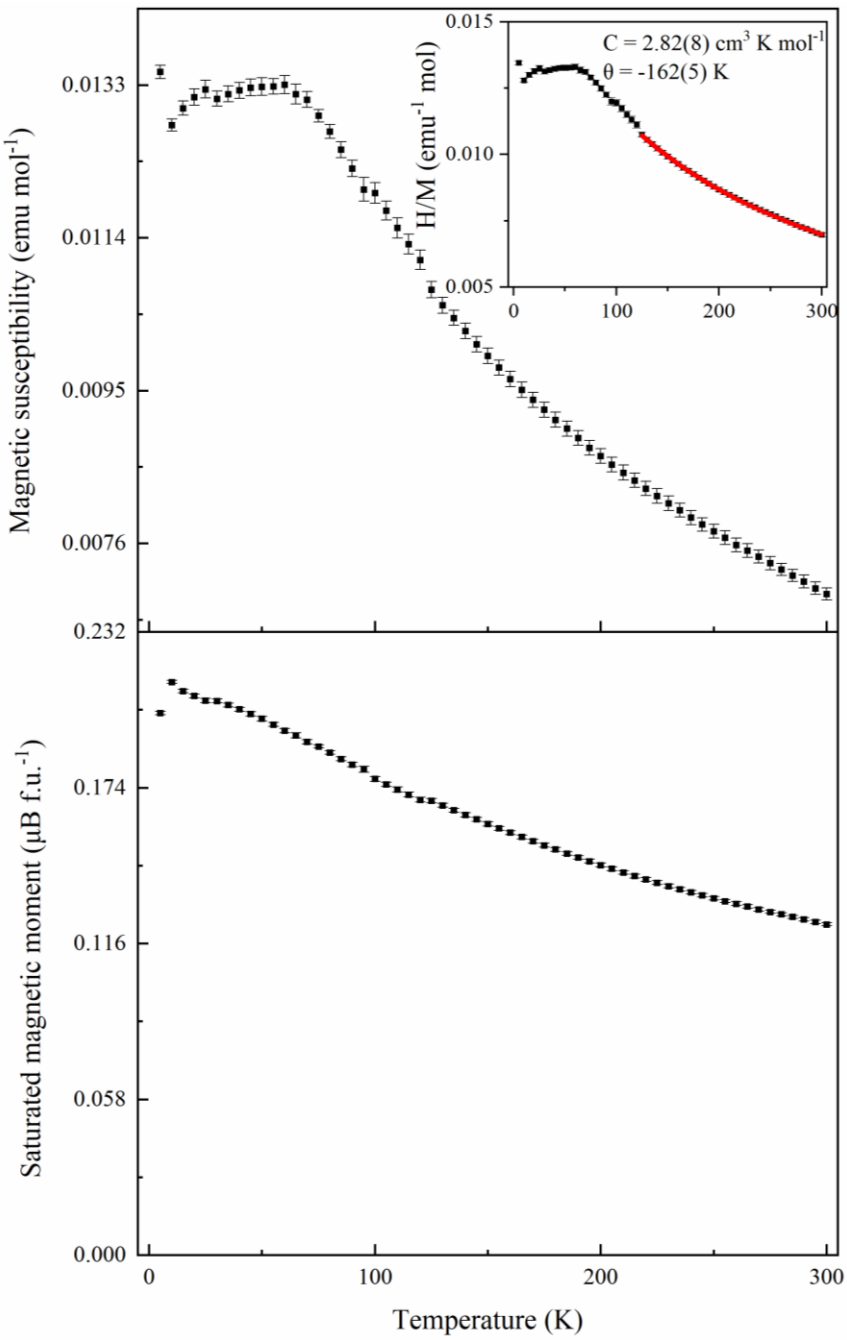


Figure 9.3. The paramagnetic susceptibility (top) and saturated magnetic moment (bottom) of 'Sample A (CaH_2)' collected as a function of temperature.

9.3.2 Thermogravimetric Analysis of 'Sample B (LiH)'

The composition of 'Sample B (LiH)' ($LaSrCoRuO_{6-x}$) obtained from the reaction with LiH was determined by conducting an oxidative TGA experiment. A small quantity of the reduced sample was heated to 800 °C under a constant flow of O_2. The sample was kept at this

temperature for 5 hours before cooling to room temperature. During the reaction, a mass gain of 5.86% was observed. The increase in the mass is consistent with the chemical formula $LaSrCoRuO_{4.23}$ (Fig 9.4). X-ray powder diffraction data collected from the re-oxidised product after the TGA experiment confirmed a complete re-oxidation to the starting material $LaSrCoRuO_6$.

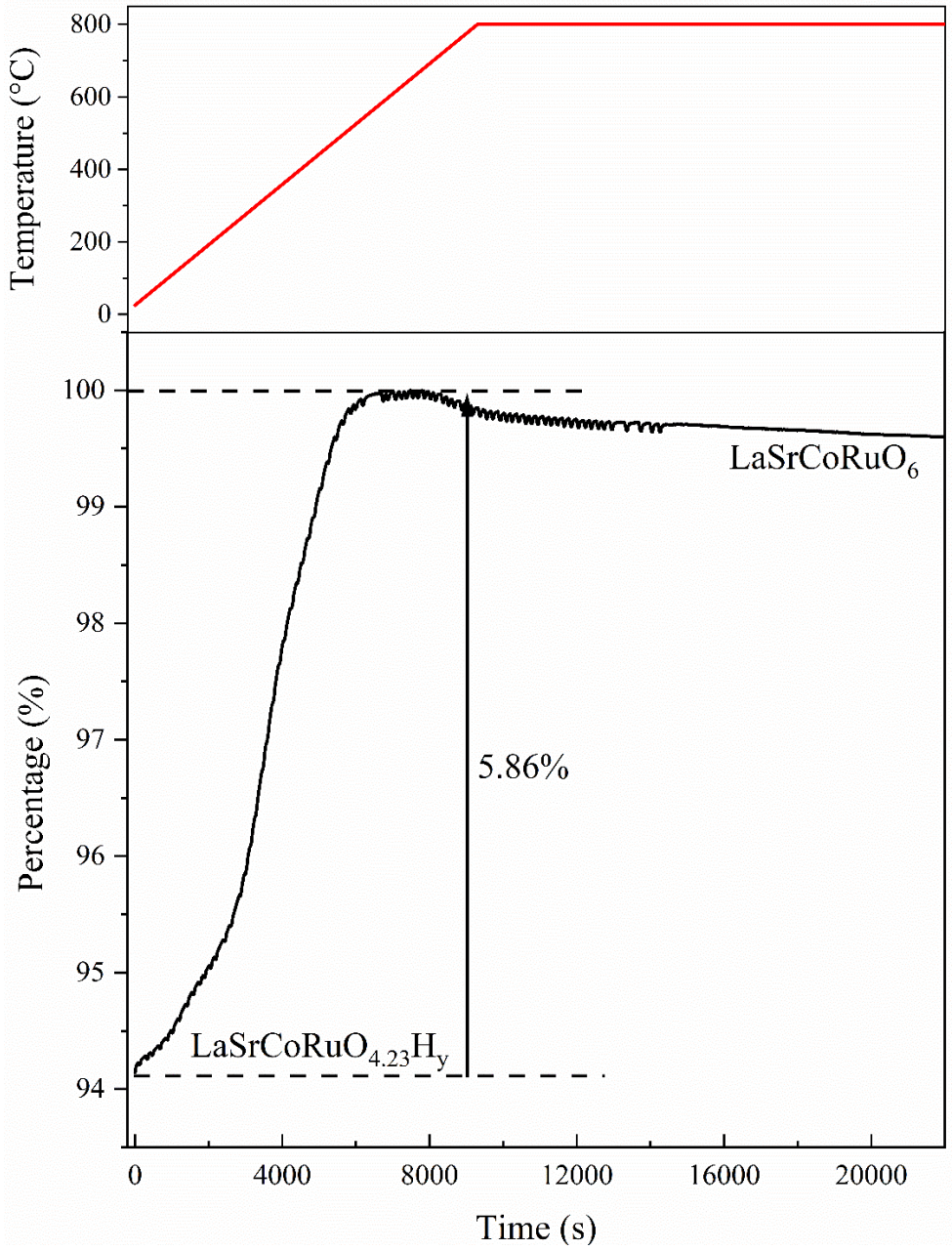


Figure 9.4. Oxidative thermogravimetric data collected from 'Sample B (LiH)'. Top panel indicates the heating profile, bottom panel indicates the relative mass of the sample as a function of time.

In order to investigate whether 'Sample B (LiH)' is an oxyhydride phase, TGA-MS data were collected from this sample. The sample was heated to 800 °C under a constant flow of O_2. A H_2O signal was observed at ~ 350 °C accompanied with a dramatic mass increase. There was another H_2O signal at ~ 800 °C, this was later found to be related to the TGA-MS instrument (Appendix 2.8). This measurement indicates that 'Sample B (LiH)' is an oxyhydride phase with a chemical formula $LaSrCoRuO_{4.23}H_y$.

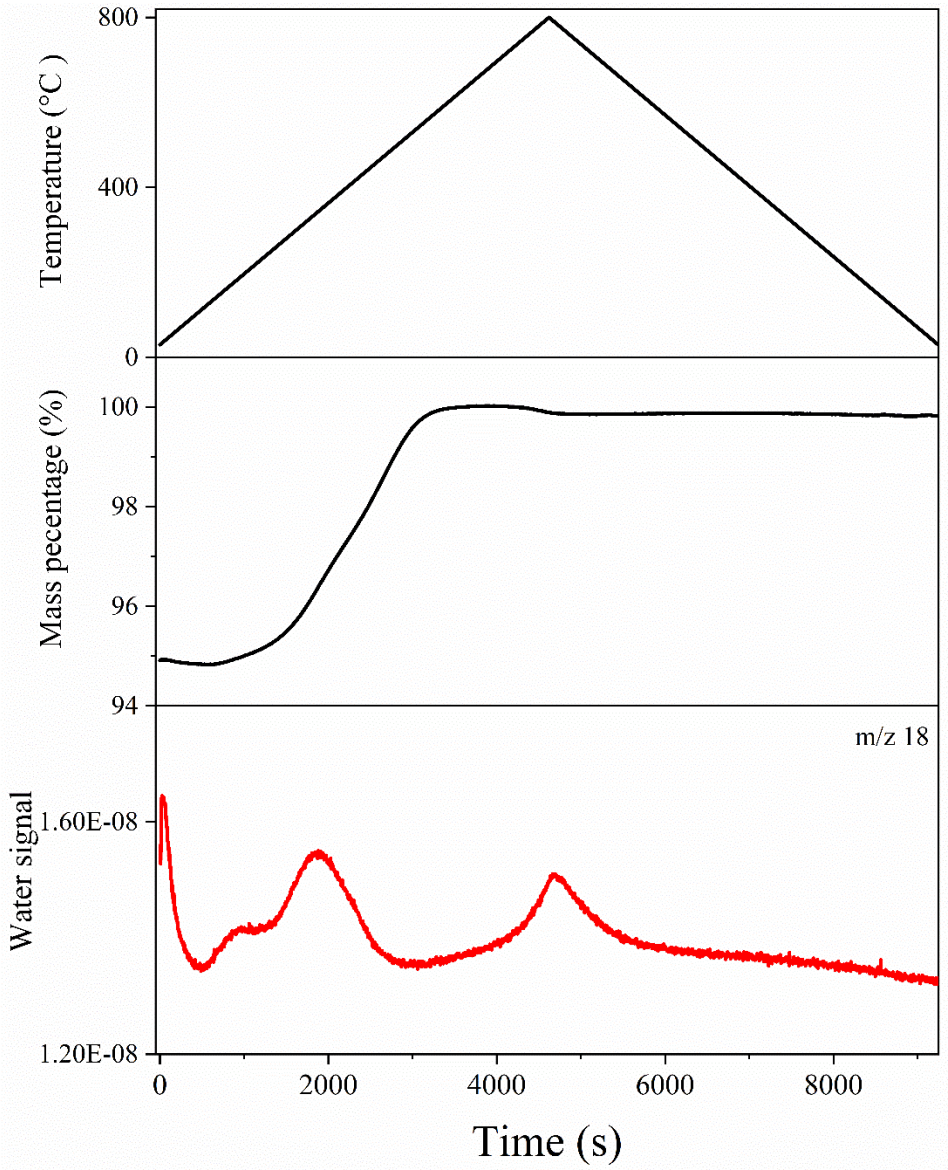


Figure 9.5. TGA-MS data collected from 'Sample B (LiH)'.

9.3.3 Structural Characterisation of 'Sample B (LiH)'

9.3.3.1 Neutron Powder Diffraction Data Collected from 'Sample B (LiH)' at Room Temperature

Neutron powder diffraction (NPD) data from 'Sample B (LiH)' were collected using the WISH instrument at ISIS (Section 2.4.2.1). Since hydride has a negative neutron scattering length (-3.7 fm), neutron powder diffraction can distinguish hydride anions from the oxide anions and the heavy metal cations.[56] The collected NPD data had a relatively high background, which is consistent with the formation of an oxyhydride phase, as hydride anions have a large incoherent cross section.

NPD data collected from 'Sample B (LiH)' can be indexed using a body centred tetragonal unit cell with the lattice parameters a = 5.43 Å, b = 5.43 Å, c = 7.96 Å. A structural model based on the B-site cation ordered double perovskite described in space group $I4/m$ was constructed and refined against the NPD data (Fig 9.6). The oxygen occupancies were refined. This process yielded an occupancy of 0.415 of the oxygen atom at the O1 equatorial site, while no appreciable oxygen vacancy was detected at the O2 apical site (Fig 9.7). The refinements against NPD data gave a composition of $LaSrCoRuO_{3.28(1)}$, which is not consistent with the oxygen content of 4.23 obtained from the TGA data (Section 9.3.2). Therefore, hydride anions were added into the structural model. Since the equatorial anion site is occupied by both O^{2-} and H^- anions, the observed neutron scattering length is the weighted average of the neutron scattering lengths of both O^{2-} and H^- anions. Therefore, considering the neutron scattering length of O^{2-} and H^- anions (5.8 fm, -3.7 fm),[56] the O:H ratio consistent with the refined neutron scattering length of the O1 equatorial site can be defined as $O_mH_{(5.8m-2.407)/3.7}$. Since the value of m was already known from the TGA measurement (m = 4.23), the hydride content at the O1 site can be calculated. This process gives an equatorial anion site occupancy of O1/H1 = 0.558/0.371. The anion occupancies were then refined. This process yielded a refined

occupancy of O1/H1 = 0.559(2):0.370(3) at the equatorial anion site, corresponding to a chemical composition of $LaSrCoRuO_{4.24(1)}H_{1.48(1)}$, with a small amount of anion vacancies present. The oxygen content refined from the NPD data is consistent with the oxygen content obtained from the TGA data ($LaSrCoRuO_{4.23}H_y$). However, the refinement did not yield a good statistical fit. Close inspection of the refinement plot showed some diffraction peaks with intensity mismatches, which are particularly obvious at d = 4.1 Å, 1.6 Å (Fig 9.6).

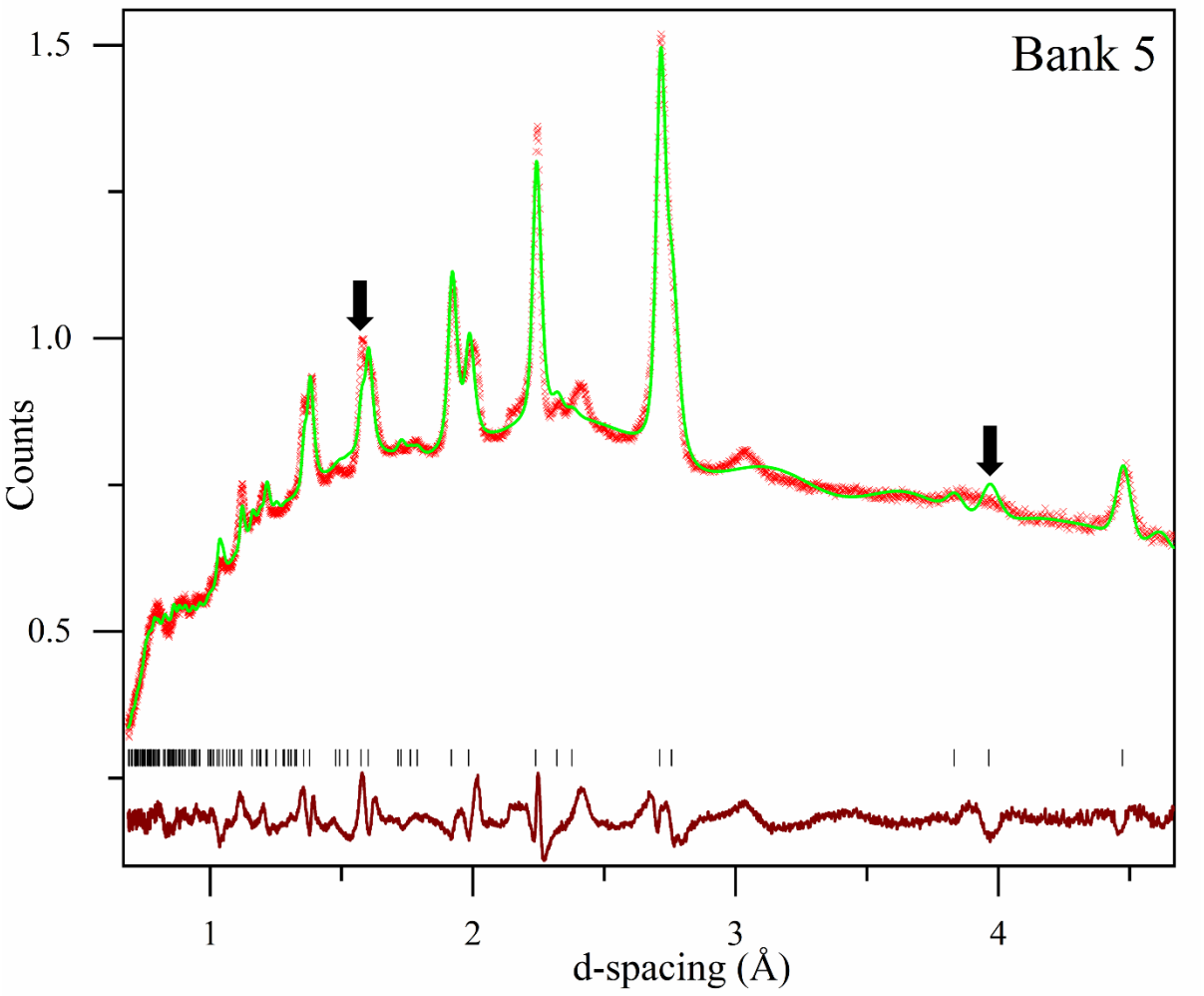


Figure 9.6. Observed, calculated and difference plots from the refinement of 'Sample B (LiH)' against NPD data collected at room temperature. Refinement of an *I*4/*m* symmetry model. Arrows indicate diffraction peaks intensity mismatches at d ~ 4.1, 1.6 Å.

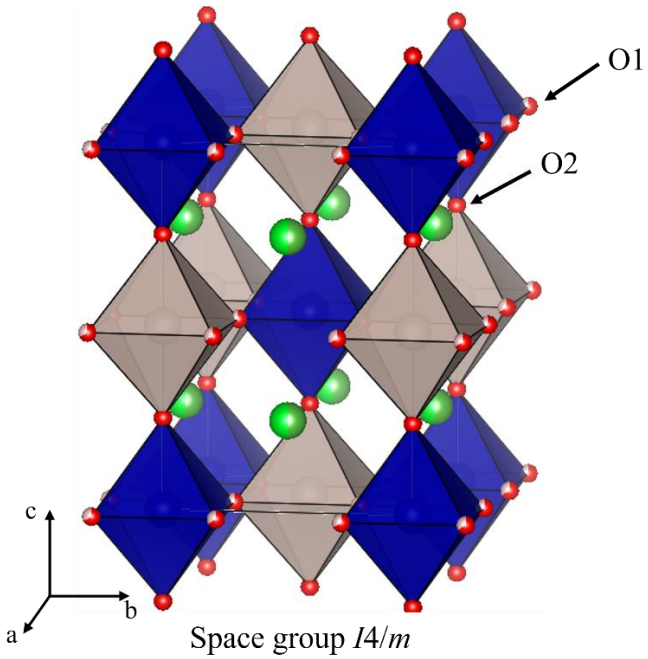


Figure 9.7. Structural model of $LaSrCoRuO_{6-x}H_y$ used for the refinement. O1 is the equatorial anion site and O2 is the apical anion site.

In combination, these observations suggest that 'Sample B (LiH)' is a mixture of two phases. A second phase described in the space group *Fm*-3*m*, resembles the structure obtained from the refinement of 'Sample A (CaH_2)', was added into the refinement. A two-phase model utilising both the *I*4/*m* structure and *Fm*-3*m* structure was refined against the NPD data. The occupancies of the oxygen sites of both phases were refined. The refinement converged rapidly and yielded an improved statistical fit. This process yielded '$LaSrCoRuO_{1.98(18)}$' (space group *Fm*-3*m*, 36.74% wt%, henceforth referred to as the *Fm*-3*m* phase) and '$LaSrCoRuO_{4.12(8)}$' (space group *I*4/*m*, 63.26% wt%, henceforth referred to as the *I*4/*m* phase) respectively. Hydride anions were then added into both of the structural models, the ratio of the O/H was calculated using the same method discussed before. Since the refined lattice parameters of the *Fm*-3*m* phase are similar to those of the 'Sample A (CaH_2)', the oxygen content of this phase was assumed to be 3.2 (similar to the oxygen content of 'Sample A (CaH_2)'). The oxygen content of the *I*4/*m* phase was then calculated so that the overall oxygen content of this two-phase sample ('Sample B (LiH)') is consistent with the TGA data ('$LaSrCoRuO_{4.23}H_y$'). This

process yielded a O:H ratio for the *Fm*-3*m* phase 0.53:0.32, and a O1:H1 ratio for the *I*4/*m* phase 0.72:0.28. The occupancies of the oxide and hydride of both phases were then set to these values and subsequently refined freely without any constraints imposed on the anion occupancies. This process yielded $LaSrCoRuO_{3.30(6)}H_{2.13(9)}$ (space group *Fm*-3*m*, 35(1)% wt%) and $LaSrCoRuO_{4.80(1)}H_{1.20(2)}$ (space group *I*4/*m*, 65(2)% wt%). The mixture of these two compounds gives a nominal chemical formula of '$LaSrCoRuO_{4.23(3)}H_{1.55(4)}$', which is consistent with the oxygen content obtained from the TGA data ($LaSrCoRuO_{4.23}H_y$). It is worth noting that the refined compositions of these phases are not very reliable, as there are a large number of strongly correlated variables in the refinement and the quality of the NPD data is inadequate. This makes the determination of the exact compositions of these two phases difficult. Henceforth, these two oxyhydride phases presented in 'Sample B (LiH)' will be referred to as the *I*4/*m* phase (refined composition: $LaSrCoRuO_{4.80(1)}H_{1.20(2)}$) and the *Fm*-3*m* phase (refined composition: $LaSrCoRuO_{3.30(6)}H_{2.13(9)}$). The refined structures of both oxyhydride phases are shown in Fig 9.8. The observed, calculated and difference plots of the two-phase model against NPD data collected at room temperature are shown in Fig 9.9. Full details of the two-phase model are given in in Table 9.3.

Sample B (LiH)

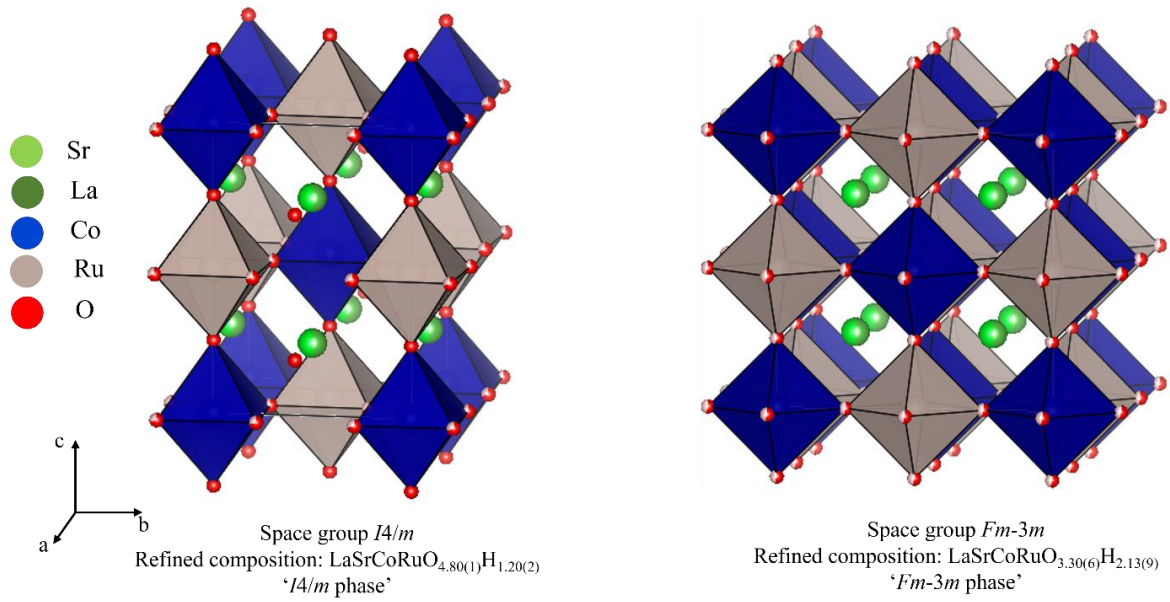


Figure 9.8. Refined structure of *I*4/*m* phase and *Fm*-3*m* phase.

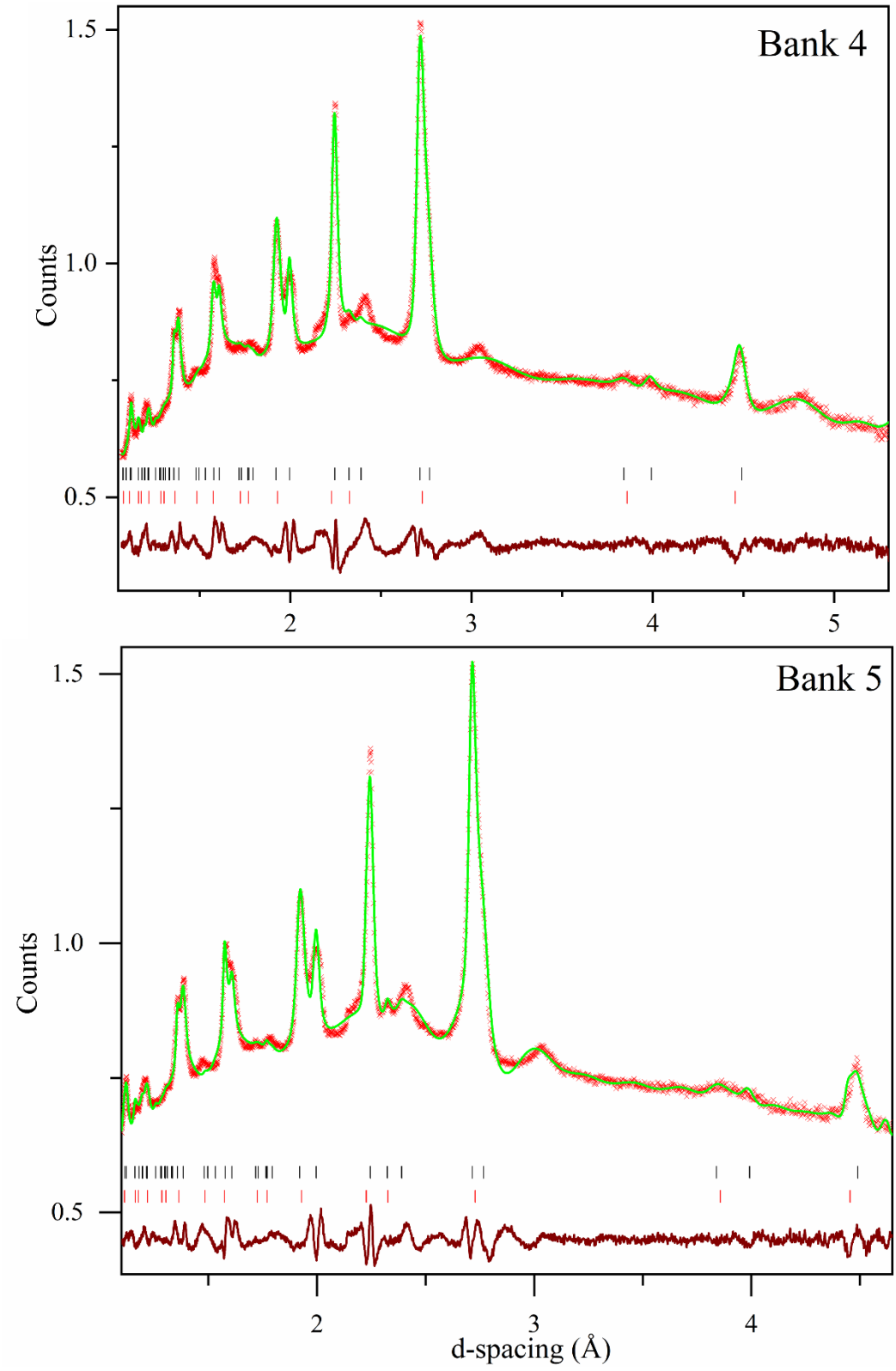


Figure 9.9. Observed, calculated and difference plots from the two-phase refinement against NPD data collected from 'Sample B (LiH)'. Upper ticks mark the peak positions of $LaSrCoRuO_{4.80(1)}H_{1.20(2)}$ (*I*4/*m* phase), lower ticks mark the peak positions of $LaSrCoRuO_{3.30(6)}H_{2.13(9)}$ (*Fm*-3*m* phase).

Structural parameters summary for 'Sample B (LiH)'						
$LaSrCoRuO_{4.80(1)}H_{1.20(2)}$, space group *I*4/*m* (#87)						
Atom	Wyckoff	*x*	*y*	*z*	Fraction	B_{iso} equiv. ($Å^2$)
La/Sr	4*d*	$^1/_2$	0	$^1/_4$	$^1/_2/^1/_2$	0.46(14)
Co	2*a*	0	0	0	1	0.97(14)
Ru	2*b*	$^1/_2$	$^1/_2$	0	1	0.97(14)
O(1)	8*h*	0.243(7)	0.257(8)	0	0.700(3)	2.75(16)
H(1)	8*h*	0.243(7)	0.257(8)	0	0.300(5)	2.75(16)
O(2)	*4e*	0	0	$^1/_2$	1	2.75(16)
a = 5.4307(3) Å, *c* = 7.9842(8) Å wt% = 65(2)%						
$LaSrCoRuO_{3.30(6)}H_{2.13(9)}$, space group *Fm*-3*m* (#225)						
Atom	Wyckoff	*x*	*y*	*z*	Fraction	B_{iso} equiv. ($Å^2$)
La/Sr	8*c*	$^1/_4$	$^1/_4$	$^1/_4$	$^1/_2/^1/_2$	0.46(14)
Co	4*a*	0	0	0	1	0.97(14)
Ru	4*b*	$^1/_2$	0	0	1	0.97(14)
O(1)	24*e*	$^1/_2$	0	$^1/_4$	0.55(1)	2.75(16)
H(1)	24*e*	$^1/_2$	0	$^1/_4$	0.36(2)	2.75(16)
a = 7.7154(7) Å wt% = 35(1)%						
wRp=1.88%; Rp=1.37%						

Table 9.3. Structural parameters from the two-phase refinements against NPD data collected from 'Sample B (LiH)'.

Close inspection of the neutron powder diffraction refinement plots showed diffuse scattering at d ≈ 4.85 Å, 3.05 Å, 2.41 Å and 2.14 Å (Fig 9.10). A two-phase Pawley refinement utilising an *I*4/*m* unit cell with a √2 × √2 × 2 geometric cell expansion and an *Fm*-3*m* model with a 2 × 2 × 2 geometric cell expansion was performed, none of those peaks were indexed. These broad, diffuse scattering peaks may be a result of short-range anion ordering between the oxide and hydride anions in the *I*4/*m* phase.

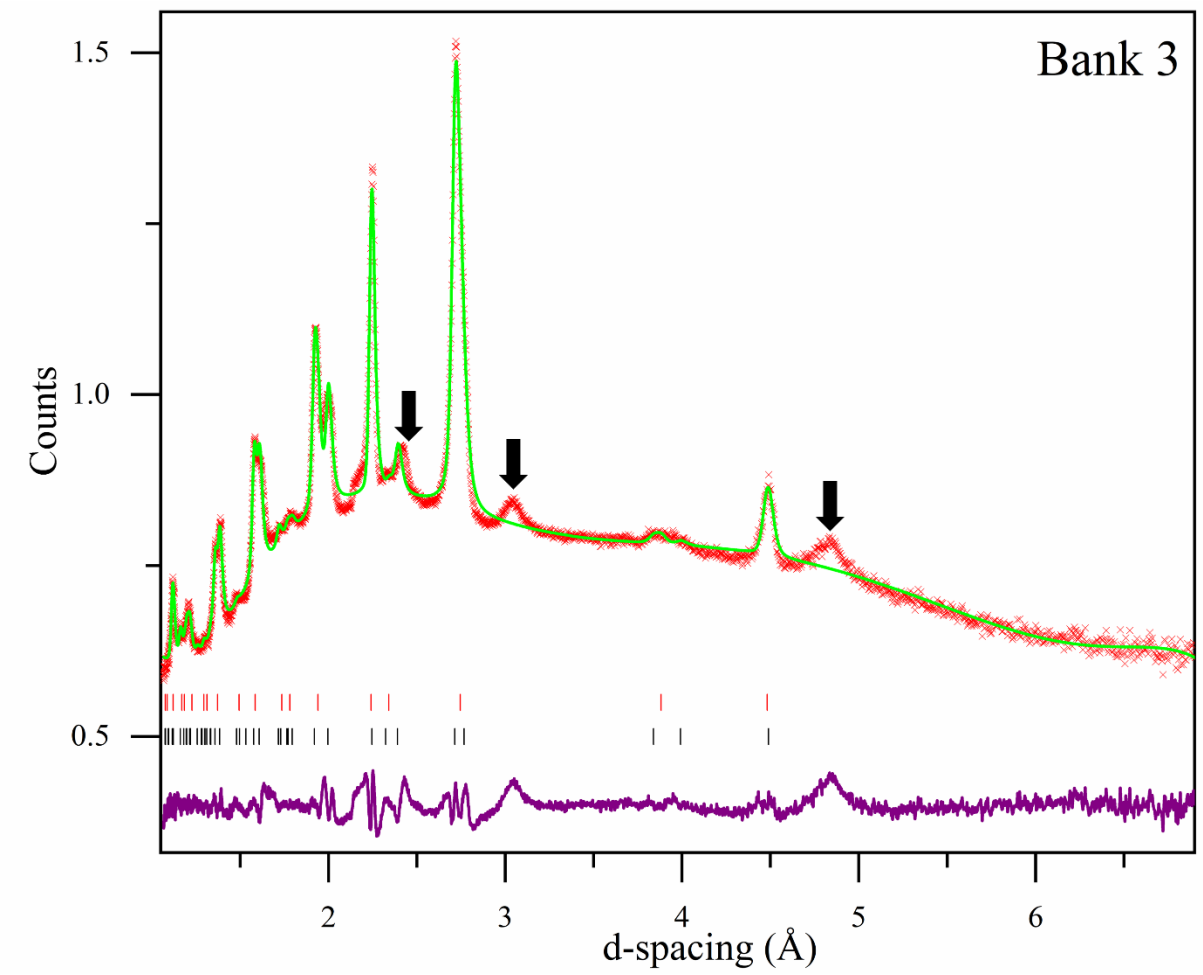


Figure 9.10. Two-phase Pawley refinement against NPD data collected from 'Sample B (LiH)' at room temperature. Lower ticks mark the peak positions of the phase described in space group *I*4/*m* with a unit cell dimension $\sqrt{2}a_p \times \sqrt{2}a_p \times 2a_p$, upper ticks mark the peak positions of the phase described in space group *Fm*-3*m* with a unit cell dimension $2a_p \times 2a_p \times 2a_p$; Arrows indicate diffraction peaks that cannot be properly indexed by the small $\sqrt{2}a_p \times \sqrt{2}a_p \times 2a_p$ unit cell.

The two-phase model utilising both the *I*4/*m* structure and *Fm*-3*m* structure was then refined against SXRD data collected from 'Sample B (LiH)'. The refinement converged rapidly and gave a good statistical fit (wRp = 1.94%; Rp = 1.42%). The observed, calculated and difference plots of the refinement against SXRD collected at room temperature are shown in Fig 9.11.

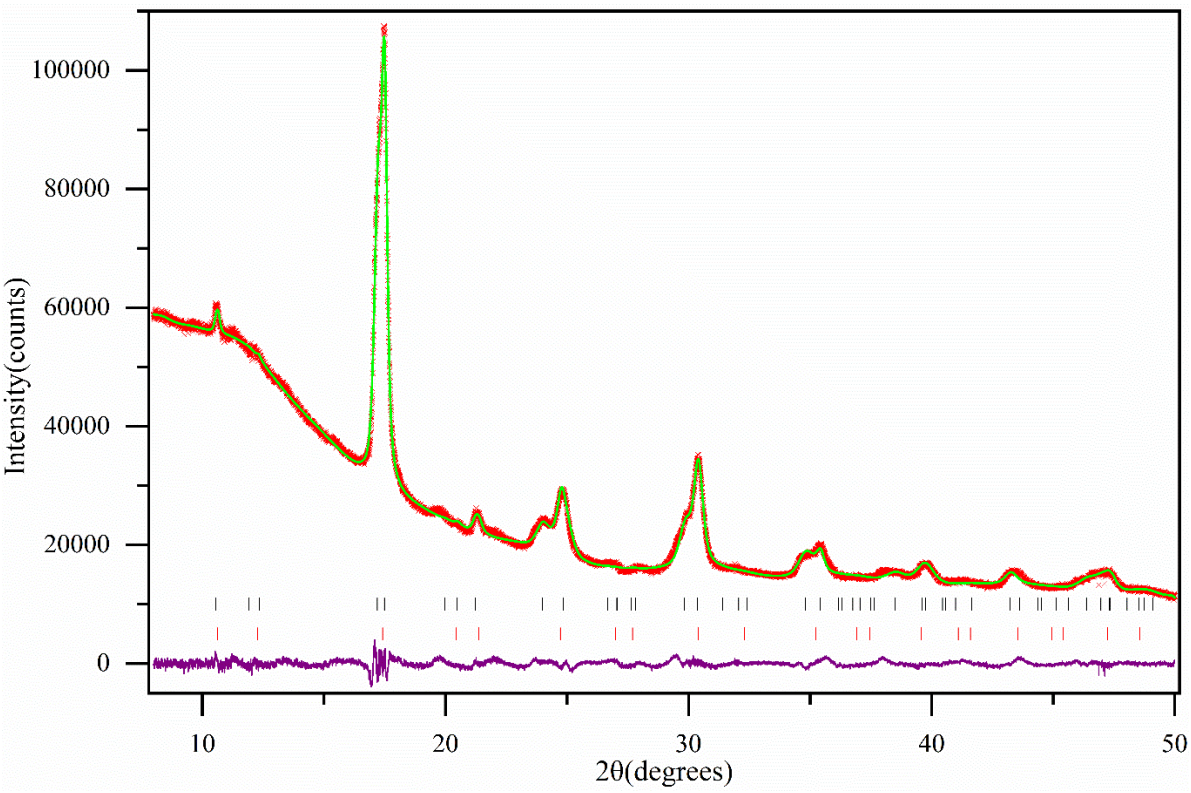


Figure 9.11. Observed, calculated and difference plots of two-phase refinement of 'Sample B (LiH)' against SXRD data. Upper ticks mark the peak positions of $LaSrCoRuO_{4.80(1)}H_{1.20(2)}$ (*I*4/*m* phase), lower ticks mark the peak positions of $LaSrCoRuO_{3.30(6)}H_{2.13(9)}$ (*Fm*-3*m* phase)

9.3.3.2 Electron Diffraction Characterisation of 'Sample B (LiH)'

In order to investigate the possibility of hydride and oxide ordering, electron diffraction (ED) data were collected from 'Sample B (LiH)'. The ED data presented in this thesis were collected by Dr Maria Batuk and Prof. Joke Hadermann at the University of Antwerp. The electron diffraction collection process and sample preparation are detailed in Section 2.10. The orange unit cell represents a unit cell with a $\sqrt{2} \times \sqrt{2} \times 2$ cell expansion of the aristotype perovskite

unit cell that was used in neutron and synchrotron powder diffraction refinements. The presence of bright reflections along [001] zone axis indicates that there may be a superstructure of the *I*4/*m* phase. The extensive streaking parallel to the [100] and [010] direction in the electron diffraction data suggest that the *I*4/*m* phase may have a short-range ordering between the oxide and the hydride anions. The large unit cell can be indexed with a $2\sqrt{2} \times 2\sqrt{2} \times 2$ cell expansion.

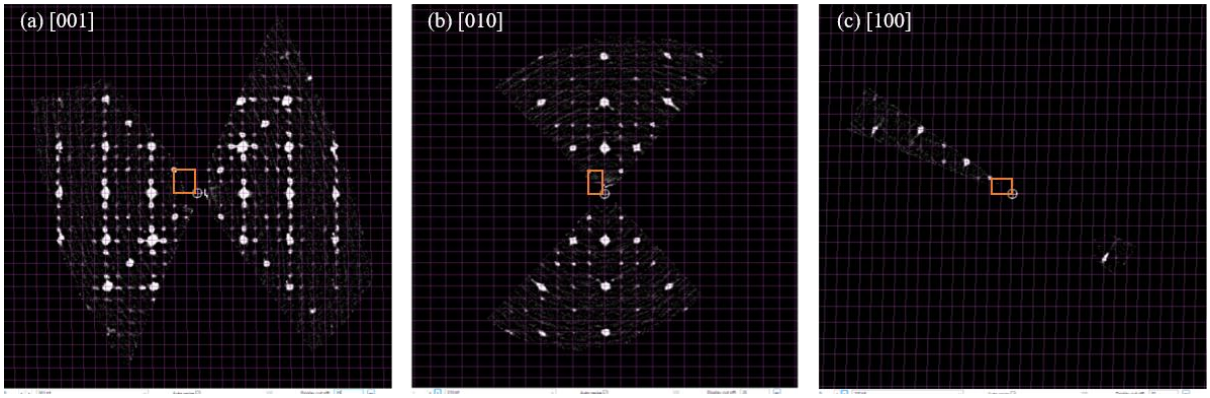


Figure 9.12. Electron diffraction data collected from 'Sample B (LiH)'. Orange cell indicates the small unit cell with a $\sqrt{2} \times \sqrt{2} \times 2$ cell dimension.

A two-phase Pawley refinement against the NPD data collected from 'Sample B (LiH)' utilising a tetragonal model with a $2\sqrt{2} \times 2\sqrt{2} \times 2$ geometric cell expansion and an *Fm*-3*m* model with a $2 \times 2 \times 2$ geometric cell expansion was performed. The two-phase Pawley refinement converged rapidly and gave a good statistical fit (Fig 9.13). Those extra diffuse scattering that was not indexed by the small unit cell can now be indexed by the expanded unit cell. However, close inspection of the Pawley refinement shows there were significant peak shape mismatches, as indicated in Fig 9.13 inset. This observation indicates that the diffuse scattering was likely a result of short-range anion ordering, which is consistent with the electron diffraction data.

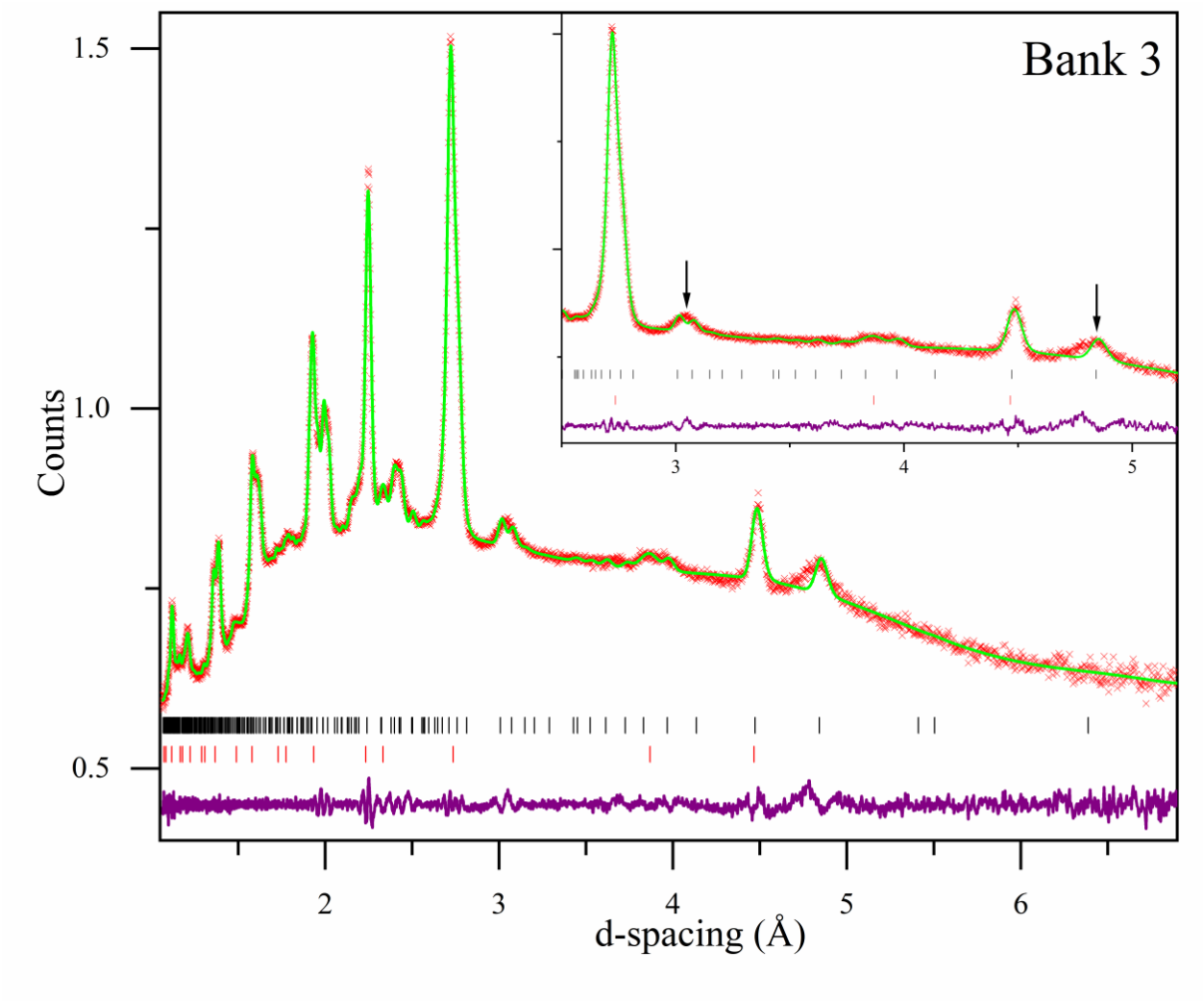


Figure 9.13. Two-phase Pawley refinement against NPD data collected from 'Sample B (LiH)' at room temperature. Upper ticks mark the peak positions of the tetragonal unit cell with a cell dimension $2\sqrt{2}a_p \times 2\sqrt{2}a_p \times 2a_p$, lower ticks mark the peak positions of the unit cell described in the space group *Fm*-3*m* with a $2a_p \times 2a_p \times 2a_p$ dimension. Inset shows expanded view of the high d-spacing region.

9.3.4 Magnetic Characterisation

9.3.4.1 SQUID Magnetometry of 'Sample B (LiH)'

Due to the presence of trace amounts of elemental Co (< 2 mol%) in the sample, magnetisation data of 'Sample B (LiH)' were collected using a technique called 'ferromagnetic subtraction'. The saturated magnetic moment increased sharply around 100 K, indicating an onset of canted antiferromagnetic order. The paramagnetic susceptibility of 'Sample B (LiH)'can be fitted by

the Curie-Weiss law ($\chi = C/(T - \theta) + K$) in the temperature range 110 K ≤ T ≤ 300 K to yield Curie constant 2.36(2) cm^3 K mol^{-1}, Weiss constant 13.0(6) K and K = 0.00217(6) cm^3 K mol^{-1}. The slight positive value of the Weiss constant indicates an overall weak ferromagnetic interaction within the sample.

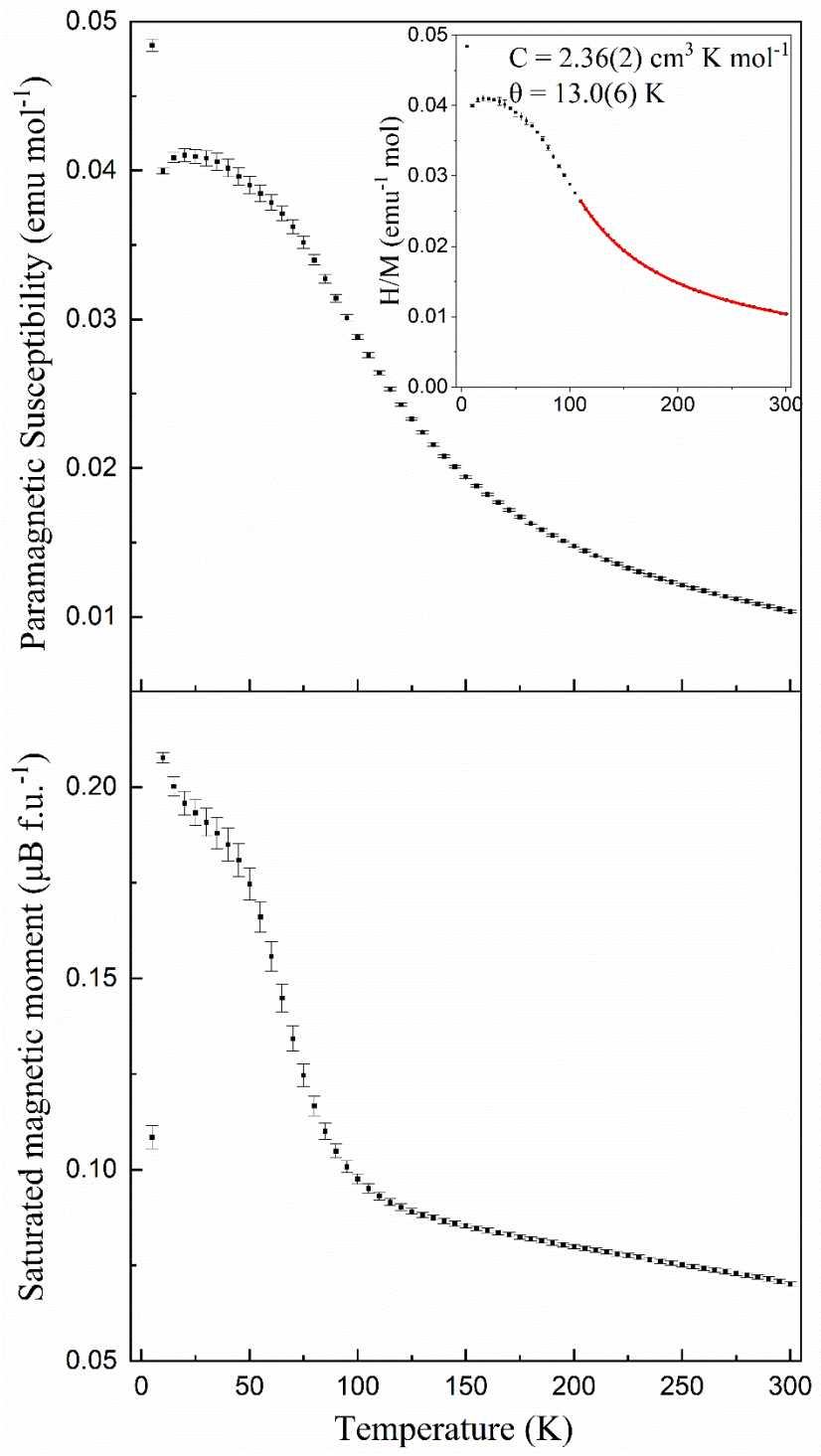


Figure 9.14. The paramagnetic susceptibility (top) and saturated ferromagnetic moment (bottom) of 'Sample B (LiH)' collected as a function of temperature.

Magnetisation-field data from 'Sample B (LiH)' were collected at 5 K and 300 K. At 5 K, the magnetisation data as a function of applied field exhibit a hysteresis loop. The magnetisation did not saturate even under an applied field of 50000 Oe, indicating a canted antiferromagnetic state of 'Sample B (LiH)' at 5 K.

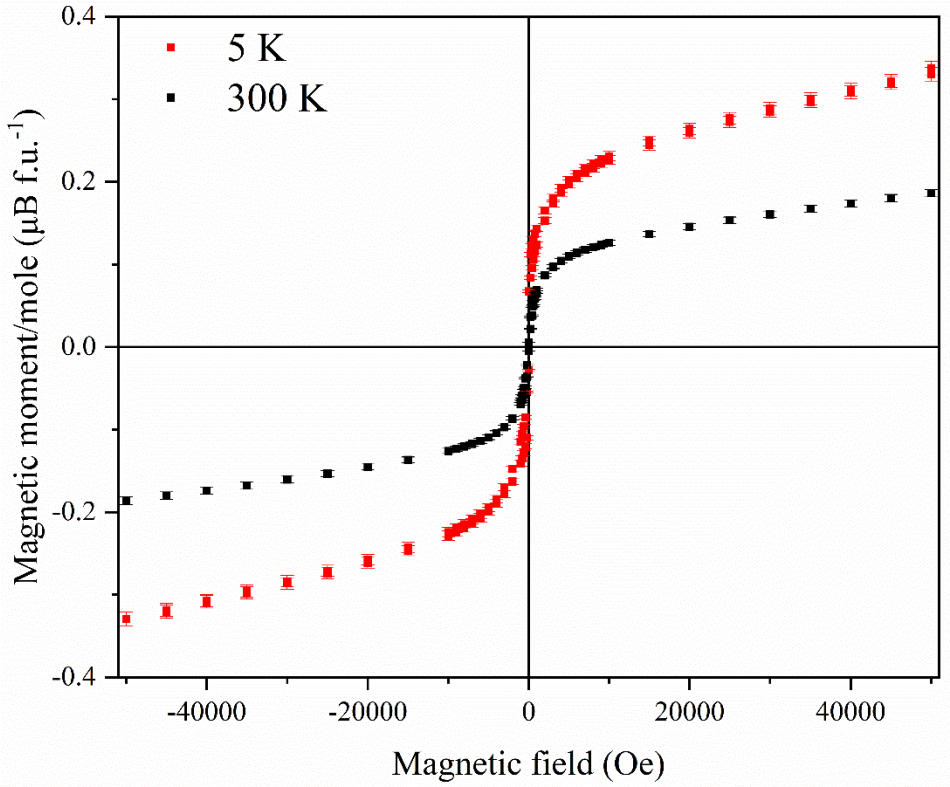


Figure 9.15. Magnetisation-field data collected from 'Sample B (LiH)' at 5 K and 300 K.

9.3.4.2 Low Temperature Neutron Powder Diffraction Data of 'Sample B (LiH)'

The two-phase model utilising both the *I*4/*m* and *Fm*-3*m* models obtained from the room temperature NPD refinement was refined against the NPD data collected at 5 K. Anions were allowed to move freely during the refinement, but the occupancy of the hydride and oxide anions were fixed. The refinements converged rapidly and gave good statistical fits. The observed, calculated and difference plots of the refinements against NPD collected at 5 K are shown in Fig 9.16, full details of the two-phase model are shown in Table 9.4 and the selected bond length comparison at 5 K and 300 K is shown in Table 9.5.

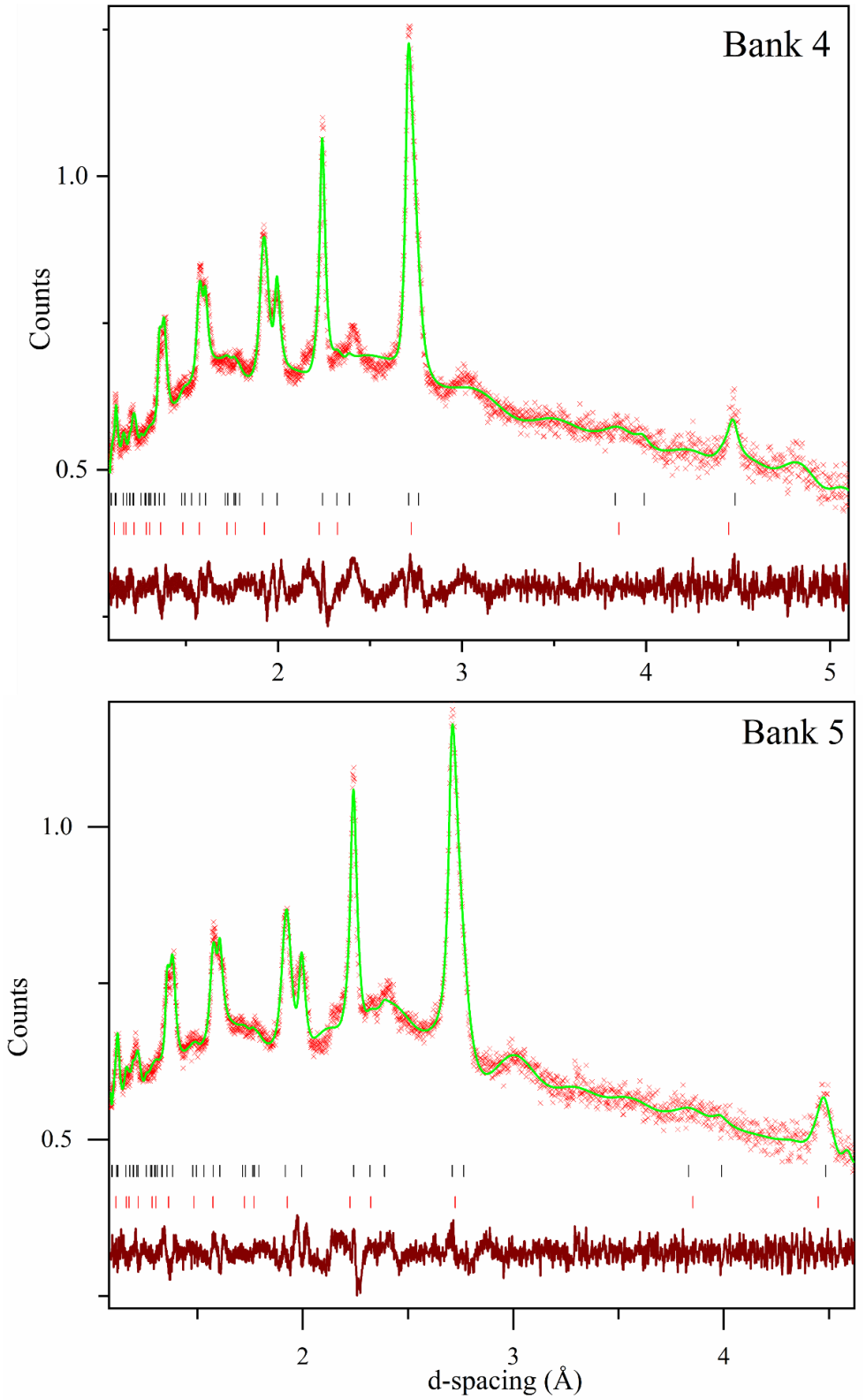


Figure 9.16. Observed, calculated and difference plots from the two-phase refinement of 'Sample B (LiH)' against NPD data collected at 5 K. Upper ticks mark the peak positions of $LaSrCoRuO_{4.80(1)}H_{1.20(2)}$ (*I*4/*m* phase), lower ticks mark the peak positions of $LaSrCoRuO_{3.30(6)}H_{2.13(9)}$ (*Fm*-3*m* phase).

Structural parameters summary for 'Sample B (LiH)'						
$LaSrCoRuO_{4.80(1)}H_{1.20(2)}$, space group *I*4/*m* (#87)						
Atom	Wyckoff	*x*	*y*	*z*	Fraction	B_{iso} equiv. ($Å^2$)
La/ Sr	4*d*	$^1/_2$	0	$^1/_4$	$^1/_2/^1/_2$	0.45(27)
Co	2*a*	0	0	0	1	0.77(22)
Ru	2*b*	$^1/_2$	$^1/_2$	0	1	0.77(22)
O(1)	8*h*	0.243(7)	0.257(8)	0	0.700	2.68(24)
H(1)	8*h*	0.243(7)	0.257(8)	0	0.300	2.68(24)
O(2)	4*e*	0	0	$^1/_2$	1	2.68(24)
a = 5.4205(5) Å, *c* = 7.9791(13) Å w% = 63(2)%						
$LaSrCoRuO_{3.30(6)}H_{2.13(9)}$, space group *Fm*-3*m* (#225)						
Atom	Wyckoff	*x*	*y*	*z*	Fraction	B_{iso} equiv. ($Å^2$)
La/Sr	8*c*	$^1/_4$	$^1/_4$	$^1/_4$	$^1/_2/^1/_2$	0.45(27)
Co	4*a*	0	0	0	1	0.77(22)
Ru	4*b*	$^1/_2$	0	0	1	0.77(22)
O(1)	24*e*	$^1/_2$	0	$^1/_4$	0.55	2.68(24)
H(1)	24*e*	$^1/_2$	0	$^1/_4$	0.36	2.68(24)
a = 7.7055(11) Å w% = 37(2)%						
wRp = 2.51%; Rp = 1.98%						

Table 9.4. Structural parameters of $LaSrCoRuO_{4.80(1)}H_{1.20(2)}$ (*I*4/*m* phase) and $LaSrCoRuO_{3.30(6)}H_{2.13(9)}$ (*Fm*-3*m* phase) obtained from the two-phase refinement of 'Sample B (LiH)' against NPD data collected at 5 K.

Bond lengths summary for 'Sample B (LiH)'			
$LaSrCoRuO_{4.80(1)}H_{1.20(2)}$, *I*4/*m* phase			
Cation	**Anion**	**Bond lengths/Å**	
		300 K	**5 K**
Co	O	1.9482(2)	1.9447(3)
Ru	O	1.9434(2)	1.9416(3)
Bond		**Bond Angles**	
		300 K	**5 K**
Co-O-Ru		176.8(1)°	176.7(1)°
$LaSrCoRuO_{3.30(6)}H_{2.13(9)}$, *Fm*-3*m* phase			
Cation	**Anion**	**Bond lengths/Å**	
		300 K	**5 K**
Co	O	1.9289(3)	1.9262(3)
Ru	O	1.9289(3)	1.9262(3)
Bond		**Bond Angles**	
		300 K	**5 K**
Co-O-Ru		180.0°	180.0°

Table 9.5. Selected bond lengths/bond angles from the refined structure of $LaSrCoRuO_{4.80(1)}H_{1.20(2)}$ (*I*4/*m* phase), and $LaSrCoRuO_{3.30(6)}H_{2.13(9)}$ (*Fm*-3*m* phase) at 5 K and 300 K.

The lattice parameters and the bond lengths extracted from the two-phase structural refinement against NPD data collected from 'Sample B (LiH)' at 5 K are shorter than those extracted from the refinement against NPD data collected at room temperature. This was expected due to the thermal expansion of the unit cell at elevated temperatures.

Apart from the information of the crystallographic structure, low temperature neutron powder diffraction data also give information about the magnetic structure of the sample. A direct comparison of the NPD data collected at room temperature and 5 K shows that the NPD data collected at 5 K lose paramagnetic scattering as reflected in the lowering of the background at the high d-spacing region. However, no extra diffraction peaks and intensity mismatches were observed in the NPD data collected at 5 K. Thus, NPD data collected at 5 K show no evidence of long-range magnetic order of 'Sample B (LiH)'.

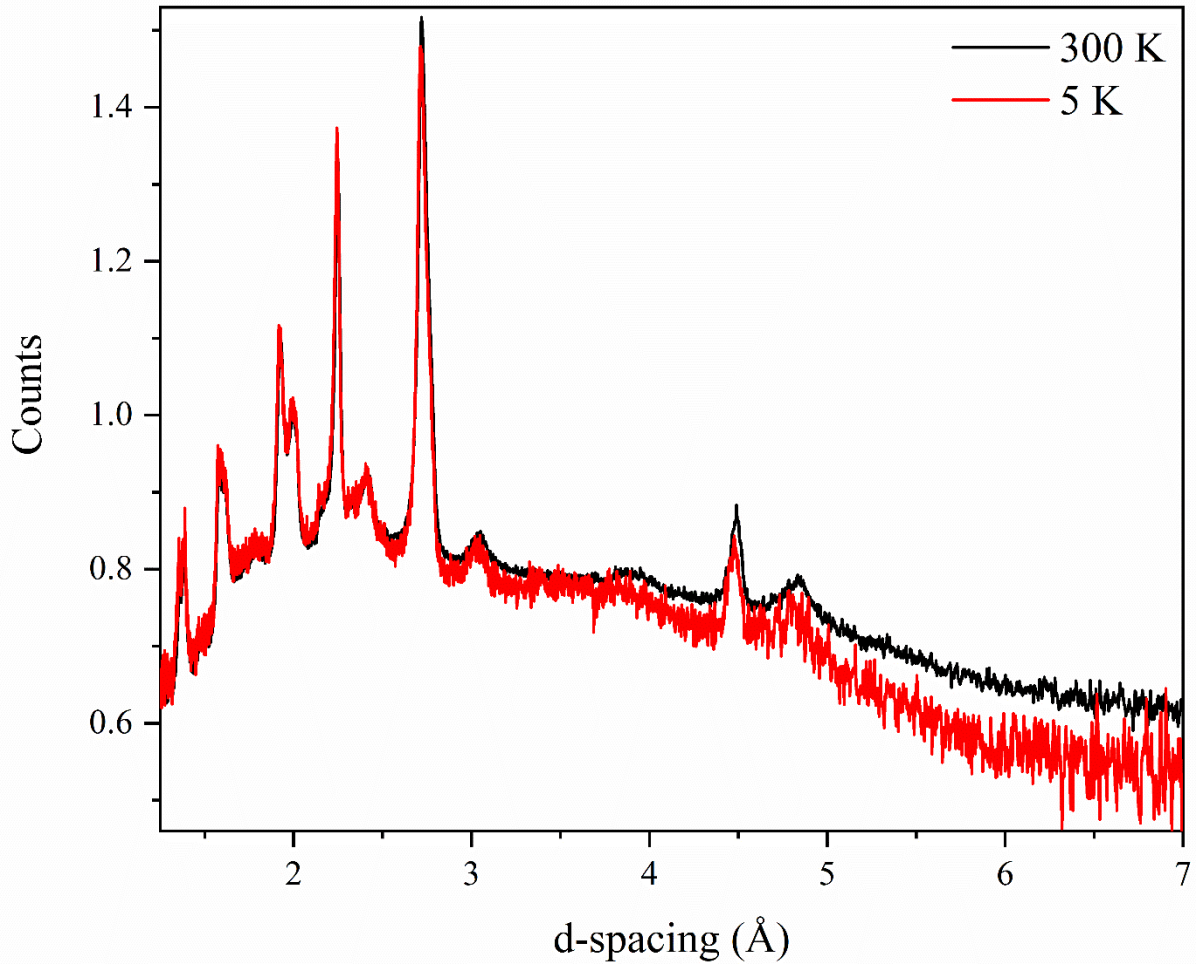


Figure 9.17. Comparison of NPD data collected from 'Sample B (LiH)' at 300 K and 5 K.

9.4 Discussion

9.4.1 Compositions of $LaSrCoRuO_{6-x}H_y$

Reactions of $LaSrCoRuO_6$ with CaH_2 yielded an oxyhydride phase with an approximate chemical composition of $LaSrCoRuO_{3.20}H_{1.91}$ ('Sample A (CaH_2)'). The structure of 'Sample A (CaH_2)' can be described in the space group *Fm*-3*m* ($LaSrCoRuO_{3.20}H_{1.91}$); Meanwhile, reactions with LiH yielded two oxyhydride phases ('Sample B (LiH)'), namely, the *Fm*-3*m* phase (refined composition: $LaSrCoRuO_{3.30(6)}H_{2.13(9)}$) and the *I*4/*m* phase (refined composition: $LaSrCoRuO_{4.80(1)}H_{1.20(2)}$). The oxyhydride phases synthesised via reduction of $LaSrCoRuO_6$ with CaH_2 ('Sample A (CaH_2)') and LiH ('Sample B (LiH)') in sealed ampoules are summarised in Fig 9.18.

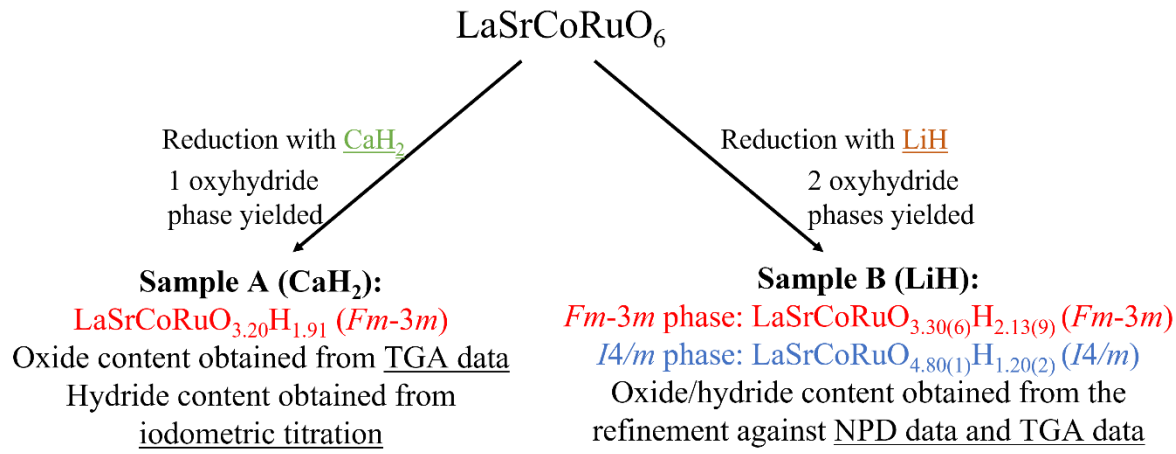


Figure 9.18. A summary of oxyhydride phases yielded from the reduction of $LaSrCoRuO_6$ with CaH_2/LiH in sealed ampoules.

Unlike the reduction of the *n* = 1 Ruddlesden-Popper phase $LaSr_3CoRuO_8$ with CaH_2, where only one oxyhydride phase was yielded ($LaSr_3CoRuO_4H_4$), the reduction of $LaSrCoRuO_6$ with different binary hydrides yielded different oxyhydride phases with a range of oxide and hydride contents.[100] The difference in the reduction behaviour of $LaSr_3CoRuO_8$ and $LaSrCoRuO_6$ can be attributed to the structures of the oxyhydride phases formed: $LaSr_3CoRuO_4H_4$ adopts a fully anion ordered structure, where all the hydride anions reside at the equatorial site of the MO_2H_4

octahedra, while the oxide anions are located at the apical site of the MO_2H_4 octahedra. The anion ordering in $LaSr_3CoRuO_4H_4$ was thought to stabilise this particular oxyhydride phase, as anion ordering could potentially optimise the bonding between the transition metal cations and the oxide/hydride anions. On the contrary, the oxyhydride phases obtained from the reduction of $LaSrCoRuO_6$ do not adopt long-range anion ordered structures. The origin of the oxide/hydride ordering will be discussed in Section 9.4.2. Due to the lack of long-range oxide/hydride ordering in $LaSrCoRuO_{6-x}H_y$, there is little stabilisation for any particular oxyhydride composition. As a result, it is likely that a series of oxyhydride phases with different compositions can be yielded through the reduction of $LaSrCoRuO_6$ with binary metal hydrides by varying reaction conditions (reaction temperatures, the duration of the heating period, hydrogen partial pressure built-up in the sealed ampoule etc.).

9.4.2 Anion Order in Oxyhydride Phases

The broad diffuse scattering observed in the NPD data collected from 'Sample B (LiH)' indicates a potential short-range ordering of the oxide and the hydride anions in the *I*4/*m* oxyhydride phase. This idea was further supported by the electron diffraction data, where extra diffraction peaks were observed. The electron diffraction data are consistent with a unit cell with $2\sqrt{2} \times 2\sqrt{2} \times 2$ cell expansion of the aristotype perovskite unit cell, which is considered as a result of anion ordering. A two-phase Pawley refinement of a tetragonal unit cell with a $2\sqrt{2} \times 2\sqrt{2} \times 2$ geometric cell expansion shows that those diffuse peaks have significant peak shape mismatches (Fig 9.13), indicating that the anion ordering is short-ranged.

An expansion of the *ab* plane observed from the electron diffraction data of the *I*4/*m* phase (refined composition: $LaSrCoRuO_{4.80(1)}H_{1.20(2)}$) indicates that the short-ranged anion ordering should be along the *ab* plane. This is consistent with the refined structure of the *I*4/*m* phase (refined composition: $LaSrCoRuO_{4.80(1)}H_{1.20(2)}$), where the apical anion site is only occupied

by oxide ions while both oxide and hydride anions are distributed in a disordered manner at the equatorial anion site. The short-range ordering of the oxide and hydride anions in the *I*4/*m* phase along the *ab* plane can be attributed to a mix of *trans* and *cis*-MO_4H_2 coordination preference: First, hydride anions are strong σ-donating ligands. Two strongly σ bonding ligands in an octahedral complex prefer to adopt a *cis*- configuration due to the '*trans* influence'.[101] Therefore, one would expect the hydride anions to prefer a *cis*-MO_2H_2 arrangement over the *trans*- arrangement in the *I*4/*m* phase.[102] However, certain *d* electron counts such as d^2 and high spin d^7 can overcome this effect and stabilise the *trans* coordination by optimising the π-bonding interactions. For example, $SrVO_2H$, which has V^{3+} d^2 centres, the VO_4H_2 octahedra adopt the *trans*-coordination.[74] Regarding to the *I*4/*m* phase (refined composition: $LaSrCoRuO_{4.80(1)}H_{1.20(2)}$) that contains Co^{2+} d^7(HS) centres, it is likely that *trans*-CoO_4H_2 octahedra will be favoured due to the d^7 electron count of the Co^{2+} centres. In an ideal, fully ordered arrangement of hydride and oxide anions, the H-M-H chains have a regular arrangement and give rise to anion ordering along the *ab* plane. However, since a *cis*-RuO_4H_2 arrangement is preferred, there are two equivalent arrangements related to each other by a 90° rotation for the H-Ru-H chains to conserve in a *cis* configuration (Fig 9.19), which could lead to anion disorder within the *ab* plane. On the contrary, since a *trans*-CoO_4H_2 arrangement is preferred, there is only one way to organise the H-Co-H chains which conserves a trans configuration (there is only one choice regarding the 180° turn). As a result, it is likely that the *trans* preference of CoO_4H_2 stabilises a short-range ordering between the oxide and hydride anions observed in the *I*4/*m* phase (refined composition: $LaSrCoRuO_{4.80(1)}H_{1.20(2)}$).

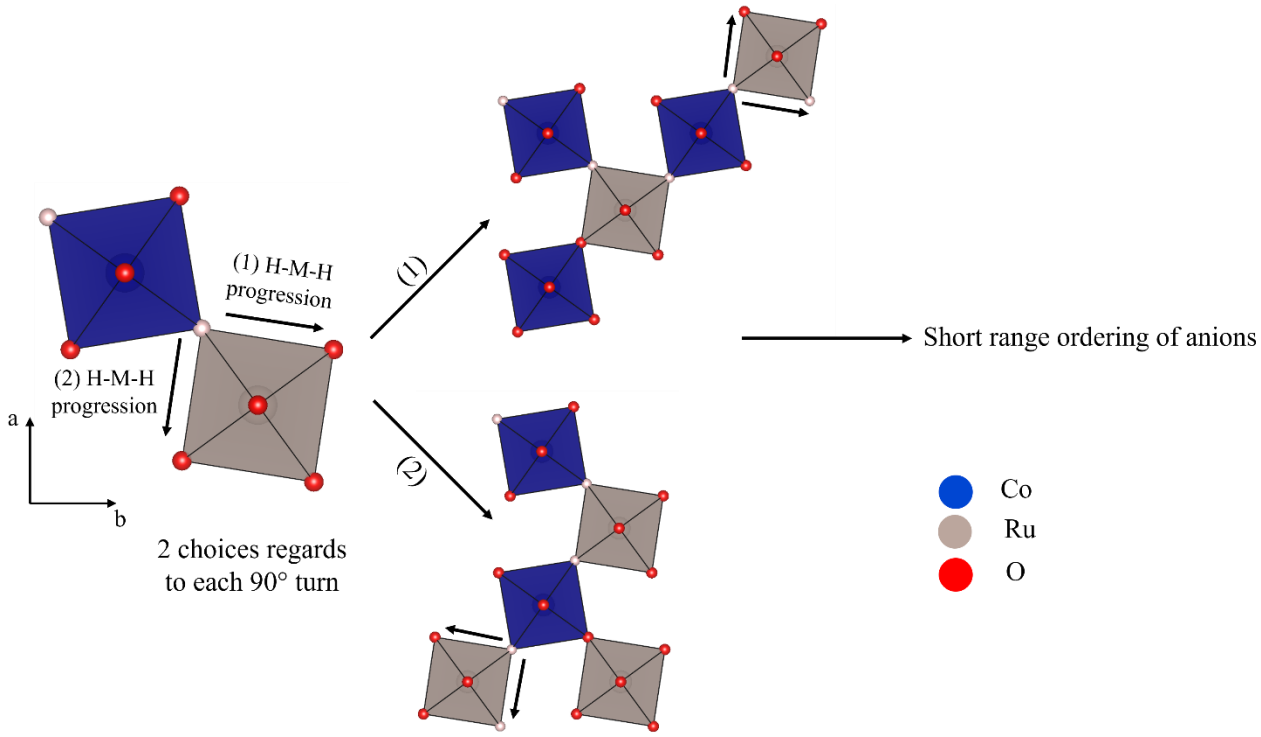


Figure 9.19. Schematic representation of *cis* RuO_4H_2 leads to 2 choices of -H-Ru-H- chain progression.

9.5 Conclusion

The reduction of $LaSrCoRuO_6$ with binary metal hydrides (CaH_2 or LiH) yields a series of oxyhydride phases with various O/H contents. Short-range anion ordering was observed in one of the oxyhydride phases (refined composition: $LaSrCoRuO_{4.80(1)}H_{1.20(2)}$, space group: *I*4/*m*), which is attributed to a mix of *cis*- and *trans*-MO_4H_2 coordination preference. The reduction behaviour of the Co/Ru double perovskite is significantly different from that of the n = 1 Ruddelsden-Popper phase, where the latter yields only one oxyhydride phase with a fully anion-ordered structure ($LaSr_3CoRuO_4H_4$). This observation has marked a distinction in the topochemical reduction of double perovskite and Ruddelsden-Popper complex metal oxide phases.

Chapter 10 Conclusion

In this thesis, the topochemical reaction of Ru-containing double perovskites phases was conducted using various reducing agents (binary metal hydrides, finely divided Zr powder). The objective of this work was to synthesise novel metastable materials with novel chemical and physical properties, while understanding the correlation between their properties and crystal structures.

Chapters 3 and 4 discussed the microstructure and the microstructure-dependent reactivity of $LaSrNiRuO_6$. Previous work had shown that the reduction of $LaSrNiRuO_6$ with CaH_2 yielded an oxygen deficient phase, $LaSrNiRuO_4$. The progress of this reduction reaction was found to be related to the synthesis conditions of the parent oxide $LaSrNiRuO_6$ phase: samples of $LaSrNiRuO_6$ that had been rapidly cooled from the synthesis temperature appeared to react much faster than samples of $LaSrNiRuO_6$ that were slowly cooled. The reactivity difference can be attributed to the microstructure of $LaSrNiRuO_6$, which was observed to be coupled with the final cooling step of its synthesis. The quenched samples of $LaSrNiRuO_6$ were observed to have a much smaller average crystalline domain size and higher microstructural strain compared with the slow-cooled samples of $LaSrNiRuO_6$. The formation of the small and highly strained crystalline domains was thought to be coupled with a phase transition of $LaSrNiRuO_6$ from *R*-3 to $P2_1/n$ (T ~ 400 °C) upon cooling from high temperature. The microstructure-dependent reactivity of $LaSrNiRuO_6$ is ascribed to the large strain built-up between the reaction interface ($LaSrNiRuO_6$-$LaSrNiRuO_4$), which adds to the activation energy barrier of the reduction reaction. Since small crystalline domains have enhanced plasticity, they can better accommodate the strain between the reaction interface compared with large crystalline domains. In addition, the enhanced microstructural strain in the small crystalline domains also acts to destabilise $LaSrNiRuO_6$. As a result, the activation energy of the reduction is smaller for the quenched samples of $LaSrNiRuO_6$, which makes them more reactive. These

observations suggest that the microstructure of a starting material plays an important role in topochemical reductions.

Similarly, the analogous Ru-containing $LaSrCoRuO_6$ double perovskite phase undergoes a *R*-3 to $P2_1/n$ phase transition (T ~ 450 °C) upon cooling from the synthesis temperature. The topochemical reduction of $LaSrCoRuO_6$ was previously studied but no novel reduced phases were found. Therefore, samples of $LaSrCoRuO_6$ were rapidly cooled so that their reactivity could be enhanced. Then, several novel reduced phases were successfully prepared via the topochemical reduction of the quenched samples of $LaSrCoRuO_6$. Chapter 5 has discussed the reduction pathway of $LaSrCoRuO_6$ with LiH and Zr to yield two novel oxygen deficient phases, $LaSrCoRuO_5$ and $LaSrCoRuO_4$. The reduction of $LaSrCoRuO_6$ with Zr as an oxygen getter led to the formation of $LaSrCoRuO_5$, while the more metastable phase $LaSrCoRuO_4$, could only be prepared via LiH under flowing argon. This observation highlights an important distinction between binary metal hydrides and Zr as reducing agents. Reduction with binary metal hydrides is under kinetic control while reduction with Zr as an oxygen getter is under thermodynamic control. Reduction with Zr as an oxygen getter thus requires a higher reaction temperature, which precludes the formation of the most metastable compounds.

Chapter 6 and 7 discussed the structural and magnetic characterisation of the reduced phases derived from $LaSrCoRuO_6$. The reduction of $LaSrCoRuO_6$ with Zr as an oxygen getter yielded an oxygen deficient phase $LaSrCoRuO_5$. $LaSrCoRuO_5$ adopts a complex anion-vacancy ordered structure consisting of corner-sharing CoO_6 octahedra, RuO_5 square-based pyramidal units and CoO_4 square-planar units. The cobalt cations are located at the octahedral and square-planar sites and the ruthenium cations are exclusively located at the square-based pyramidal sites. BVS calculations have indicated that the Co^{2+} centres disproportionate into Co^{+} and Co^{3+} centres at a 1:1 ratio, with Co^{+} centres residing at the square-planar sites and Co^{3+} centres locating at the octahedral sites. The disproportionation of Co^{2+} centres is thought to be driven

by the gain in ligand field stabilisation energy of the low spin Co^{3+} centres. At low temperature, $LaSrCoRuO_5$ exhibits a ferromagnetic state consistent with the predictions from the Goodenough-Kanamori superexchange rules.

The reduction of $LaSrCoRuO_6$ with LiH yielded $LaSrCoRuO_4$, and the structural and magnetic properties of $LaSrCoRuO_4$ were discussed in Chapter 7. $LaSrCoRuO_4$ adopts an infinite layer structure that resembles the structure of $LaNiO_2$. This reduced phase is ferromagnetic up to room temperature, with most of the magnetic moments concentrated on the cobalt centres. The ferromagnetic ground state of $LaSrCoRuO_4$ can also be explained via the Goodenough-Kanamori superexchange rules.

There are several questions that arise from the observation of Co^{2+} disproportionation in $LaSrCoRuO_5$: what is the correlation between the anion-vacancy ordered structure adopted by $LaSrCoRuO_5$ and the disproportionation of the Co^{2+} centres, and which factors control the disproportionation of the Co^{2+} centres? In order to gain a deeper insight into this unusual Co^{2+} disproportionation behaviour, A-site doping of the parent compound $LaSrCoRuO_6$ and the reduced phase $LaSrCoRuO_5$ were investigated and discussed in Chapter 8. The reduction of $La_xSr_{2-x}CoRuO_6$ ($0.6 \leq x \leq 1.3$) with Zr yielded reduced $La_xSr_{2-x}CoRuO_5$ ($0.7 \leq x \leq 1.3$) phases. The reduced $La_xSr_{2-x}CoRuO_5$ ($0.7 \leq x \leq 1.3$) phases are isostructural with the undoped reduced $LaSrCoRuO_5$ phase, suggesting that the disproportionation of Co^{2+} is preserved throughout the doping range. However, the heavily hole doped ($La_{0.6}Sr_{1.4}CoRuO_5$) phase adopts a different anion-vacancy ordered structure as reflected from the SXRD data. This observation suggests that the complicated anion-vacancy ordered structure adopted by $LaSrCoRuO_5$ is coupled with the oxidation states of the transition metal centres.

Oxyhydride phases were also successfully synthesised via the topochemical reduction of quenched $LaSrCoRuO_6$ with binary metal hydrides (CaH_2, LiH) in sealed ampoules. The structural and magnetic characterisation of the resulting oxyhydride phases were discussed in

Chapter 9. Oxyhydride phases with different oxide and hydride contents were prepared, two of which adopt an anion disordered structure (space group: *Fm*-3*m*), while the other phase is found to have short-range anion ordering (space group: *I*4/*m*). The reduction of $LaSrCoRuO_6$ with binary metal hydrides yielded oxyhydride phases with a range of oxide and hydride contents, which is markedly distinct from the reduction of the $n = 1$ Ruddlesden-Popper phase, $LaSr_3CoRuO_8$, where only one oxyhydride phase is yielded ($LaSr_3CoRuO_4H_4$). The difference in the reduction behaviour of the Co/Ru double perovskite and the $n = 1$ Ruddlesden-Popper phases is attributed to the lack of long-range anion ordering in $LaSrCoRuO_{6-x}H_y$, which fails to stabilise a particular oxide/hydride composition. As a result, it is likely that a series of $LaSrCoRuO_{6-x}H_y$ phases with different oxide/hydride contents could be prepared via reactions with binary metal hydrides (CaH_2, LiH) by varying the reaction conditions (e.g. reaction temperatures, the duration of the heating period, partial pressure of hydrogen built-up inside the sealed ampoule etc.).

The phase diagram of $LaSrCoRuO_aH_b$ phases that had been successfully synthesised and characterised in this thesis is shown in Fig 10.1. This work has demonstrated the importance of the H_2 partial pressure built-up within the experimental set-up: when the H_2 partial pressure is low within the experimental set-up, the formation of the oxygen-deficient phases is favoured. If the target products are oxyhydride phases, then a large H_2 partial pressure built-up within the experimental set-up is needed to stabilise the formation of oxyhydride phases.

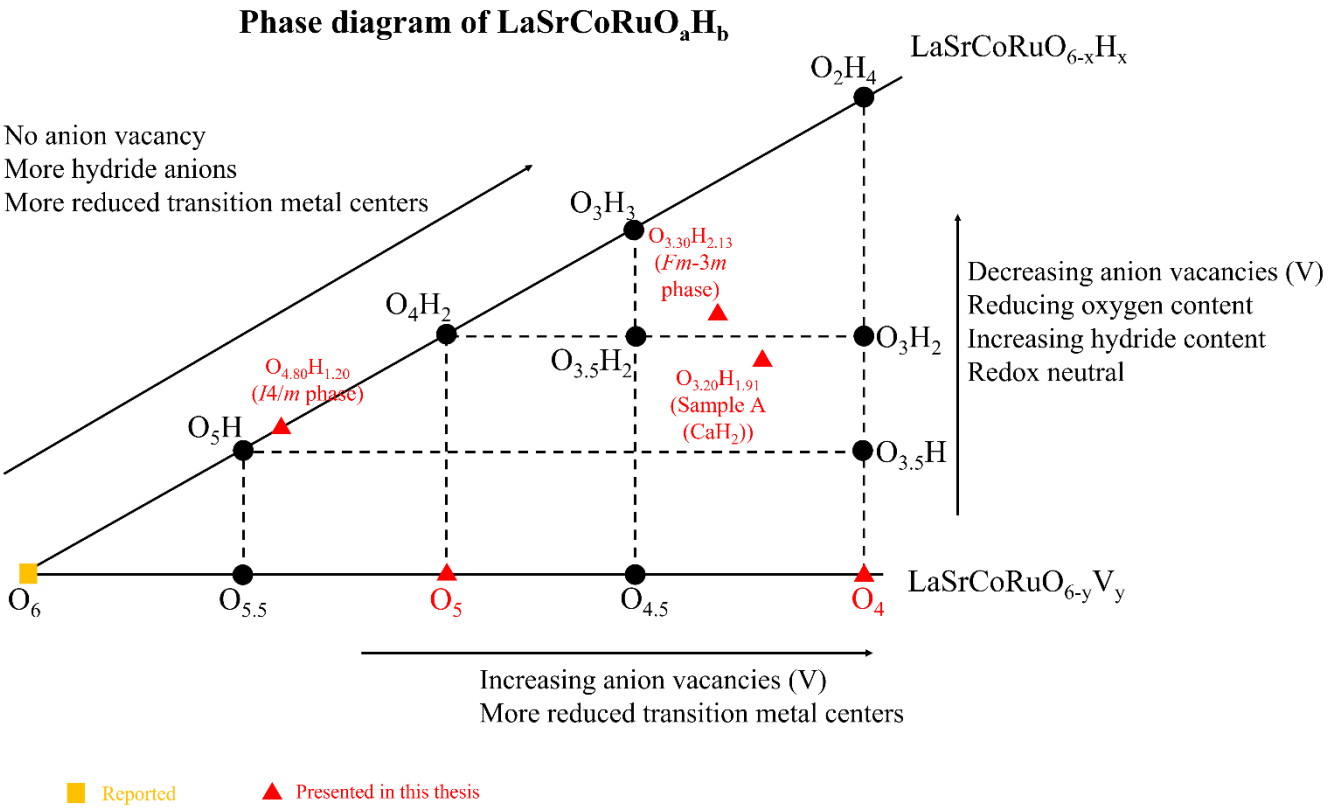


Figure 10.1. Phase diagram of LaSrCoRuO$_a$H$_b$.

Building on this work, further research ideas can be conducted to gain a deeper insight into the mixed Co/Ru transition metal oxide system. First of all, it would be interesting to investigate whether the disproportionation of Co^{2+} can be controlled using chemical pressure. For example, the reduction of similar Ru-containing oxides such as $LaBaCoRuO_6$ can be conducted. In addition, it would be worth investigating the crystal structure of the heavily hole-doped reduced phase $La_{0.6}Sr_{1.4}CoRuO_5$ and even the reduction of Sr_2CoRuO_6 to gain a deeper insight into the unusual Co^{2+} disproportionation. Furthermore, it would be also interesting to investigate the phase diagram of $LaSrCoRuO_{6-x}H_y$ and the magnetic properties of this series of oxyhydride phases.

In conclusion, the work presented in this thesis demonstrates a rich topochemical reduction chemistry of Ru-containing double perovskites which allows the synthesis of a series of novel

metastable phases. However, as mentioned above, there remain some unanswered questions, and further investigations are still needed in this series of ruthenium containing compounds.

Appendix 1 Index of Figures

Figure 1.1. (a) A cubic *Pm*-3*m* unit cell of $SrTiO_3$; (b) <*A*-*O*> and <*B*-*O*> bond lengths in a ABO_3 perovskite structure. 3
Figure 1.2. The ABO_3 structures with different tolerance factors: $CaTiO_3$ (space group: *Pbmn*) (t < 1);[14] $SrTiO_3$ (space group: *Pm*-3*m*) (t = 1);[12] $BaNiO_3$ (space group: $P6_3/mmc$) (t > 1).[18] ..4
Figure 1.3. Table of ordering schemes in double perovskite.[19] 5
Figure 1.4. Topochemical reduction of $LaSrNiRuO_6$ with CaH_2 at 360 °C under flowing argon to form $LaSrNiRuO_4$.[37] 9
Figure 1.5. Topochemical reduction of $LaSr_3NiRuO_8$ with CaH_2 at 450 °C in a sealed ampoule to form $LaSr_3NiRuO_4H_4$. [38].....10
Figure 1.6. Topochemical reduction of $Ba_{0.5}Sr_{0.5}MnO_{3-x}$ with LiH in a sealed ampoule to form $Ba_{0.5}Sr_{0.5}MnO_{2.03}$.[39] 11
Figure 1.7. Topochemical reduction of $LaNiO_3$ with NaH to yield $LaNiO_2$, this oxygen deficient phase adopts an infinite layer structure.[24] 11
Figure 1.8. Topochemical reduction of $LaCoO_3$ with Zr as an oxygen getter to form $La_2Co_2O_5$.[40] 12
Figure 1.9. An example of d^6 Co^{3+} centres in an octahedral environment in high spin configuration (left) and low spin configuration (right). Schematic representations of filling of the *d*-orbitals with paring energy (*P*) shown explicitly. 13
Figure 1.10. A schematic representation of the orbital energies of (a) an atom, (b) a diatomic molecule, (c) a small molecule, (d) a large molecule and (e) an infinite periodic solid. 15
Figure 1.11. (a) A 1D chain of equally spaced atoms with partially filled 1*s* orbitals. The electrons are localised in each orbital; (b) Electron hopping introduces on-site electron repulsion due to the doubly occupied orbital. 16
Figure 1.12. Schematic representation of Hubbard sub-bands as a function of band width *W*. -*I* represents the ionisation energy and -*A* represents electron affinity.[45].....18
Figure 1.13. A schematic representation of superexchange interactions of M-O-M in 180° (top) and in 90°(bottom). 20
Figure 2.1. Schematic representation of a flowing tube system with flowing argon. Arrows indicate the direction of the argon flow during the reaction 26
Figure 2.2. Schematic representation of a zirconium getter set up. 27
Figure 2.3. (a) Air-sensitive X-ray sample holder for Panalytical Empyrean and Panalytical X'Pert diffractometers; (b) Air-sensitive X-ray sample holder for Bruker AXS D8 Advance Pro diffractometers.....29
Figure 2.4. Bragg's law reflection. Bragg's construction for diffraction of monochromatic beams by a set of parallel lattice beam. 30
Figure 2.5 Schematic representation of the principle component in a SQUID magnetometer.[64] 41
Figure 2.6 Graphic representation of the principles of 'ferrosubtraction' measurements. 43
Figure 3.1. X-ray powder diffraction data collected from the first cycle of reduction of quenched and slow-cooled samples of $LaSrNiRuO_6$ with CaH_2 (Q: Quenched, SC: Slow-cooled).....47

Figure 3.2. Observed, calculated, and difference plots from the structural refinements of quenched (top) and slow-cooled (bottom) samples of $LaSrNiRuO_6$ against SXRD data collected at room temperature. Insets show an expanded view of the high angle region. 50
Figure 3.3. Diffraction peaks from selected angles of SXRD data collected from quenched and slow-cooled samples of $LaSrNiRuO_6$ at (a) $2\theta \approx 17.1°$ and (b) $2\theta \approx 29.8°$. 52
Figure 3.4. A plot of peak *fwhm* against 2θ of SXRD diffraction peaks collected from quenched and slow-cooled samples of $LaSrNiRuO_6$. 53
Figure 3.5. The observed, calculated and difference plots from the structural refinement of the $LaSrNiRuO_6$ sample quenched from 425 °C against SXRD data collected at room temperature. 55
Figure 3.6. A plot of peak *fwhm* of SXRD diffraction peaks against 2θ collected from different quenched samples of $LaSrNiRuO_6$. Inset shows the peak *fwhm* of the diffraction peak at $2\theta = 92°$ as a function of quenching temperature. 56
Figure 3.7. Observed, calculated, and difference plots from the refinement of $LaSrNiRuO_6$ with *R*-3 symmetry model against SXRD data collected at 950 °C. Insets show an expanded view of the high angle region. 57
Figure 3.8. Direct peak shape comparison of the quenched and slow-cooled samples of $LaSrNiRuO_6$ before and after the heating cycle at selected angle $2\theta \approx 17.1°$. 58
Figure 3.9. Plot of phase fraction against temperature for quenched and slow-cooled samples of $LaSrNiRuO_6$ extracted from the refinement against the SXRD data sets. 59
Figure 3.10. SXRD diffraction peaks collected from (a) quenched sample before and after annealing at 360 °C and (b) slow-cooled sample before and after annealing at 360 °C. 60
Figure 3.11. The low temperature structure ($P2_1/n$) and high temperature structure (*R*-3) of $LaSrNiRuO_6$ viewed along different Cartesian axes. 63
Figure 3.12. Schematic representation of (a) domains evolution during the cooling process of $LaSrNiRuO_6$ below the phase transition temperature and (b) crystalline domains in slow-cooled and quenched $LaSrNiRuO_6$. 64
Figure 4.1. Schematic illustration of particle and crystalline domain of $LaSrNiRuO_6$. 68
Figure 4.2. X-ray powder diffraction data collected from the products of reaction between CaH_2 and the quenched and slow-cooled samples of $LaSrNiRuO_6$ after 48 hours of heating at 360 °C under flowing argon. Analogous data collected from $LaSrNiRuO_6$ and $LaSrNiRuO_4$ are shown as a comparison. 71
Figure 4.3. Estimated fraction of the reduced phase $LaSrNiRuO_4$ from the reduction of quenched and slow-cooled samples of $LaSrNiRuO_6$ with CaH_2 calculated from the relative area of the main reflections of each phase as a function of heating cycle. 72
Figure 4.4. A summary of the particle size and microstructure of quenched, slow-cooled, slow-cooled-quenched and quenched-slow-cooled samples of $LaSrNiRuO_6$. 75
Figure 4.5. Observed, calculated and difference plots from structural refinements of quenched-slow-cooled (top) and slow-cooled-quenched (bottom) samples of $LaSrNiRuO_6$ against XRD data collected at room temperature. 76
Figure 4.6. Plot of peak *fwhm* against 2θ of XRD data collected from the quenched, slow-cooled, quenched-slow-cooled and slow-cooled-quenched samples of $LaSrNiRuO_6$. Inset shows the peak *fwhm* of XRD diffraction peak at $2\theta = 50.4°$ from four samples. 78

Figure 4.7. XRD data collected from the products of reaction between CaH_2 and slow-cooled-quenched and quenched-slow-cooled samples of $LaSrNiRuO_6$ after 48 hours of heating at 360 °C under flowing argon. Analogous data collected from $LaSrNiRuO_6$ and $LaSrNiRuO_4$ are shown in comparison. 80
Figure 4.8. Estimated fractions of the reduced phase $LaSrNiRuO_4$ from reduction of quenched-slow-cooled and slow-cooled-quenched samples of $LaSrNiRuO_6$ with CaH_2 calculated from the relative area of the main reflections of each phase. 81
Figure 4.9. Schematic diagram of the interface between $LaSrNiRuO_6$ and $LaSrNiRuO_4$ during the topochemical reduction. Arrows indicate the strain arising from the parameter mismatch at the interface. 82
Figure 4.10. A schematic diagram showing the influence of microstructural effects on the activation energy of reduction of $LaSrNiRuO_6$ with CaH_2. 83
Figure 4.11. A schematic diagram showing how the influence of microstructural effects on the activation energy of the reduction of $LaSrNiRuO_6$ with CaH_2 can lead to the observed differences in the reactivity of quenched and slow-cooled samples of $LaSrNiRuO_6$. 84
Figure 5.1. Topochemical reduction profile of $LaSrCoRuO_6$ with Zr at different temperatures to form two compositions of $LaSrCoRuO_{6-x}$. The lower part of the diagram shows X-ray diffraction data from $LaSrCoRuO_4$ synthesised via the reduction with LiH. 92
Figure 5.2. Topochemical reduction progression of $LaSrCoRuO_6$ with LiH to form two compositions of $LaSrCoRuO_{6-x}$. 93
Figure 5.3. Reduction of a substrate using a Zr getter as a reducing agent. 96
Figure 5.4. Reduction profile of $LaSrCoRuO_6$ with a Zr getter. 97
Figure 5.5. Proposed reaction pathway for the topochemical reduction of $LaSrCoRuO_6$ using LiH as a reducing agent. 99
Figure 5.6. Structural transformation of (a) reduction of $LaSrCoRuO_6$ to $LaSrCoRuO_4$ via the intermediate phase $LaSrCoRuO_5$ and (b) reduction of $SrFeO_3$ to form $SrFeO_2$ via the intermediate phase $SrFeO_{2.5}$. 101
Figure 6.1. Oxidative thermogravimetric analysis of $LaSrCoRuO_{6-x}$, plot shows temperature and mass as a function of time. 104
Figure 6.2. Observed, calculated and difference plots of the Pawley refinement of $LaSrCoRuO_5$ against SXRD data using a body centred unit cell with a $\sqrt{2} \times \sqrt{2} \times 2$ geometric cell expansion of the aristotype perovskite unit cell; Inset shows additional diffraction peaks that cannot be indexed using this cell. 105
Figure 6.3. Electron diffraction data collected from $LaSrCoRuO_5$ sample. Orange unit cell indicates the basic cell with $\sqrt{2}a_p$ x $\sqrt{2}a_p$ x $2a_p$ 106
Figure 6.4. Observed, calculated and difference plots of the Pawley refinement of $LaSrCoRuO_5$ against SXRd data using a monoclinic unit cell described in space group $P112_1$ with a $2\sqrt{2} \times 2\sqrt{2} \times 2$ geometric cell expansion of the aristotype perovskite unit cell. 107
Figure 6.5. Observed, calculated and difference plots from the Pawley refinements of $LaSrCoRuO_5$ using unit cells with different symmetries. 108
Figure 6.6. Structure of $LaNi_{0.9}Co_{0.1}O_{2.5}$ (top),[76] and two structural models of $LaSrCoRuO_5$ constructed based on the anion-vacancy ordering of $LaNi_{0.9}Co_{0.1}O_{2.5}$ (bottom). 109
Figure 6.7. A direct comparison of (a) experimental NPD data collected from $LaSrCoRuO_5$ at room temperature and simulated NPD data for (b) model 1 and (c) model 2. 110

Figure 6.8. Schematic representation of the tilting system within the structure. La/Sr atoms were omitted for clarity.....111
Figure 6.9. Schematic representation of the mirror planes constraint within the structure. La/Sr atoms were omitted for clarity. 114
Figure 6.10. Refined crystal structure of $LaSrCoRuO_5$ in $P112_1$ space group (Green: La/Sr, blue: Co, brown: Ru, red: O). 115
Figure 6.11. Observed, calculated and difference plots from the structural refinement of the large-scale sample of $LaSrCoRuO_5$ against SXRD data collected at room temperature. Inset shows an expanded view of the high angle region. 115
Figure 6.12. Observed, calculated and difference plots from the structural refinements of the large-scale sample of $LaSrCoRuO_5$ against NPD data collected at room temperature.....116
Figure 6.13. Paramagnetic susceptibility (top) and saturated magnetic moment (bottom) of $LaSrCoRuO_5$ collected as a function of temperature. Inset shows the fit to the Curie-Weiss law in the temperature range $140 \leq T/K \leq 300$.....121
Figure 6.14. Predicted μ_{eff}^2 of $LaSrCoRuO_5$ for Co^+, Ru^{3+} and Co^{3+} with different possible electronic configurations.....122
Figure 6.15. Magnetic isotherms collected from the large-scale sample of $LaSrCoRuO_5$ at 5 K and 300 K. Inset shows zoom in region of the room temperature magntic isotherm plot. 123
Figure 6.16. Observed, calculated and difference plots from the refinement of $LaSrCoRuO_5$ against NPD data collected at 5 K. 124
Figure 6.17. Direct comparison of the neutron powder diffraction data of $LaSrCoRuO_5$ collected at 5 K and 300 K.....128
Figure 6.18. A comparison of the 1st layer and 2nd layer of the structure of $LaSrCoRuO_5$, the arrow indicates direction of shifting between layers. La/Sr atoms were omitted for clarity. 129
Figure 6.19. Intralayer magnetic couplings between Co^+ and Ru^{3+} centres in $LaSrCoRuO_5$. 133
Figure 6.20. Interlayer couplings between Co^+ and Ru^{3+} centres in $LaSrCoRuO_5$. 134
Figure 7.1. Oxidative thermogravimetric analysis of $LaSrCoRuO_{6-x}$, plot shows mass and temperature as a function of time.....139
Figure 7.2. Observed, calculated and difference plots from the structural refinement of $LaSrCoRuO_4$ against SXRD data collected at room temperature using an *I*4/*mmm* structural model. Upper ticks mark the peak positions of the majority phase $LaSrCoRuO_4$ and lower ticks mark the peak positions of the minority phase $LaSrCoRuO_5$. 141
Figure 7.3. Observed, calculated and difference plots from the refinement of $LaSrCoRuO_4$ against NPD data collected at room temperature. Upper ticks mark the peak positions of the majority phase $LaSrCoRuO_4$, lower ticks mark the peak positions of the minority phase $LaSrCoRuO_5$. The presence of incoherent background from hydrogen is likely resulted from over reduced hydride impurities which were also found in ref 71. 144
Figure 7.4. Refined structure of $LaSrCoRuO_4$ viewed along different Cartesian axes. 145
Figure 7.5. The space groups of the infinite layer structure and their corresponding distortions of the MO_4 square-planar unit. The difference between the $P12_11$ and $I112/m$ structural models is the direction of the rotation of the MO_4 square-planar units. The $I112/m$ structural model is

described as $a^0a^0c^-$ (out-of-phase tilt in the *c* direction) in the Glazer notation, while the $P12_11$ structural model is described as $a^0a^0c^+$ (in-phase tilt in the *c* direction).....146
Figure 7.6. The paramagnetic susceptibility and saturated magnetic moment of $LaSrCoRuO_4$ as a function of temperature. The data points at 5 K were considered to be anomalies. 149
Figure 7.7. Magnetisation-field data collected from $LaSrCoRuO_4$ at 5 K, 300 K and 350 K. 150
Figure 7.8. NPD data from $LaSrCoRuO_4$ collected at 5 K and 300 K. There is an enhanced magnetic scattering of (101) and (110) diffraction peaks, which is consistent with a magnetic ordered state. Background was subtracted from both sets of the diffraction data. 151
Figure 7.9. Magnetic models described in magnetic space group 139.537 and 71.536 respectively, arrows represent magnetic moment at cobalt and ruthenium sites. 152
Figure 7.10. Neutron powder diffraction simulation using magnetic models of $LaSrCoRuO_4$ described with space group 139.537 and 71.536. 153
Figure 7.11. Observed, calculated and difference plots from the refinement of $LaSrCoRuO_4$ against NPD data collected at 5 K. Black ticks mark the peak positions of the majority phase $LaSrCoRuO_4$, blue ticks mark the peak positions of the magentic cell, red ticks mark the peak positions of the secondary phase $LaSrCoRuO_5$. 155
Figure 7.12. (a) Calculated DOS for $LaSrNiRuO_4$, graph taken from ref 37 (b) A schematic representation of filling of the Ni^+ *d*-orbitals. Red circle indicates the highest energy electron at the d_{z2} orbital. It is worth noting that the axis is defined such that *x* and *y* bisect the M–O–M angles. 158
Figure 7.13. Ferromagnetic magnetic exchange interactions in $LaSrCoRuO_4$. 160
Figure 8.1. Observed, calculated and difference plots from the structural refinement of $La_{0.8}Sr_{1.2}CoRuO_6$ against SXRD data collected at room temperature (top) and a structural model of $LaSrCoRuO_6$ (bottom). 166
Figure 8.2. *a*, *b* lattice parameters (top); *c* lattice parameter and volume of the unit cell (bottom) against *x* in $La_xSr_{2-x}CoRuO_6$. 168
Figure 8.3. Predicted spin states of the B-site transition metal cations in $La_xSr_{2-x}CoRuO_6$ ($0.6 \leq x \leq 1.4$). 169
Figure 8.4. Degrees of B-site cation ordering in $La_xSr_{2-x}CoRuO_6$ ($0.6 \leq x \leq 1.4$) as a function of *x*. 171
Figure 8.5. Oxidative thermogravimetric data collected from $La_{0.8}Sr_{1.2}CoRuO_{6-\delta}$. Top panel indicates the heating profile, bottom panel indicates the change of mass of the sample as a function of time. 172
Figure 8.6. Direct comparison of the SXRD data collected from the undoped $LaSrCoRuO_5$, $La_{0.8}Sr_{1.2}CoRuO_5$ and $La_{0.6}Sr_{1.4}CoRuO_5$. Arrows highlight the superstructure peaks, dots represent the unreacted starting material $LaSrCoRuO_6$. 175
Figure 8.7. Observed, calculated and difference plots from the structural refinement of $La_{0.8}Sr_{1.2}CoRuO_5$ against SXRD data collected at room temperature. Upper ticks mark the peak positions of the majority phase $La_{0.8}Sr_{1.2}CoRuO_5$ and the lower ticks mark the peak positions of the minority phase $La_{0.8}Sr_{1.2}CoRuO_6$. 176
Figure 8.8. *a*, *b* lattice parameters (top), *c* lattice parameter and volume of the unit cell (bottom) against *x* in $La_xSr_{2-x}CoRuO_5$. 178

Figure 8.9. The paramagnetic susceptibility and saturated magnetic moment of $La_{0.8}Sr_{1.2}CoRuO_5$ collected as a function of temperature. Inset shows the fit to Curie-Weiss law in the temperature range $145 \leq T/K \leq 300$. 180
Figure 8.10. Magnetisation data collected as a function of applied field from $La_{0.8}Sr_{1.2}CoRuO_5$. 181
Figure 8.11. Curie constant (top) and Weiss constant (bottom) against *x* in $La_xSr_{2-x}CoRuO_5$. 183
Figure 8.12. Saturated magnetic moment of $La_xSr_{2-x}CoRuO_5$ against temperature (top) and saturated magnetic moment of $La_xSr_{2-x}CoRuO_5$ (bottom) against *x* at 20 K. 184
Figure 8.13. Predicted electronic states of B-site transition metal cations in $LaSrCoRuO_5$ (top); predicted electronic states of B-site transition metal cations in hole doped $La_xSr_{2-x}CoRuO_5$ ($0.7 \leq x < 1$), red dashed arrow indicates the electron removed upon oxidation (bottom). 186
Figure 8.14. Predicted spin states of B-site transition metal cations in hole doped $La_xSr_{2-x}CoRuO_5$ ($0.7 \leq x < 1$), red dashed arrow indicates the electron removed upon oxidation. 187
Figure 8.15. Predicted spin states of B-site transition metal cations in electron doped $La_xSr_{2-x}CoRuO_5$ ($1 < x \leq 1.3$). The red arrow indicates the extra electron added into the system upon electron doping....188
Figure 9.1. Oxidative thermogravimetric data collected from 'Sample A (CaH_2)'. Top panel indicates the heating profile, bottom panel shows the relative mass of the sample....195
Figure 9.2. Observed, calculated and difference plots from the refinement of 'Sample A (CaH_2)' against SXRD data collected at room temperature. Arrows indicate unknown impurities present in the sample. 197
Figure 9.3. The paramagnetic susceptibility (top) and saturated magnetic moment (bottom) of 'Sample A (CaH_2)' collected as a function of temperature. 199
Figure 9.4. Oxidative thermogravimetric data collected from 'Sample B (LiH)'. Top panel indicates the heating profile, bottom panel indicates the relative mass of the sample as a function of time.....200
Figure 9.5. TGA-MS data collected from 'Sample B (LiH)'. 201
Figure 9.6. Observed, calculated and difference plots from the refinement of 'Sample B (LiH)' against NPD data collected at room temperature. Refinement of an *I*4/*m* symmetry model. Arrows indicate diffraction peaks intensity mismatches at d ~ 4.1, 1.6 Å. 203
Figure 9.7. Structural model of $LaSrCoRuO_{6-x}H_y$ used for the refinement. O1 is the equatorial anion site and O2 is the apical anion site. 204
Figure 9.8. Refined structure of *I*4/*m* phase and *Fm*-3*m* phase. 206
Figure 9.9. Observed, calculated and difference plots from the two-phase refinement against NPD data collected from 'Sample B (LiH)'. Upper ticks mark the peak positions of $LaSrCoRuO_{4.80(1)}H_{1.20(2)}$ (*I*4/*m* phase), lower ticks mark the peak positions of $LaSrCoRuO_{3.30(6)}H_{2.13(9)}$ (*Fm*-3*m* phase). 207
Figure 9.10. Two-phase Pawley refinement against NPD data collected from 'Sample B (LiH)' at room temperature. Lower ticks mark the peak positions of the phase described in space group *I*4/*m* with a unit cell dimension $\sqrt{2}a_p \times \sqrt{2}a_p \times 2a_p$, upper ticks mark the peak positions of the phase described in space group *Fm*-3*m* with a unit cell dimension $2a_p \times 2a_p \times 2a_p$; Arrows

indicate diffraction peaks that cannot be properly indexed by the small $\sqrt{2}a_p \times \sqrt{2}a_p \times 2a_p$ unit cell. 209
Figure 9.11. Observed, calculated and difference plots of two-phase refinement of 'Sample B (LiH)' against SXRD data. Upper ticks mark the peak positions of $LaSrCoRuO_{4.80(1)}H_{1.20(2)}$ (*I*4/*m* phase), lower ticks mark the peak positions of $LaSrCoRuO_{3.30(6)}H_{2.13(9)}$ (*Fm*-3*m* phase) 210
Figure 9.12. Electron diffraction data collected from 'Sample B (LiH)'. Orange cell indicates the small unit cell with a $\sqrt{2} \times \sqrt{2} \times 2$ cell dimension. 211
Figure 9.13. Two-phase Pawley refinement against NPD data collected from 'Sample B (LiH)' at room temperature. Upper ticks mark the peak positions of the tetragonal unit cell with a cell dimension $2\sqrt{2}a_p \times 2\sqrt{2}a_p \times 2a_p$, lower ticks mark the peak positions of the unit cell described in the space group *Fm*-3*m* with a $2a_p \times 2a_p \times 2a_p$ dimension. Inset shows expanded view of the high d-spacing region. 212
Figure 9.14. The paramagnetic susceptibility (top) and saturated ferromagnetic moment (bottom) of 'Sample B (LiH)' collected as a function of temperature. 213
Figure 9.15. Magnetisation-field data collected from 'Sample B (LiH)' at 5 K and 300 K. . 214
Figure 9.16. Observed, calculated and difference plots from the two-phase refinement of 'Sample B (LiH)' against NPD data collected at 5 K. Upper ticks mark the peak positions of $LaSrCoRuO_{4.80(1)}H_{1.20(2)}$ (*I*4/*m* phase), lower ticks mark the peak positions of $LaSrCoRuO_{3.30(6)}H_{2.13(9)}$ (*Fm*-3*m* phase). 215
Figure 9.17. Comparison of NPD data collected from 'Sample B (LiH)' at 300 K and 5 K. 218
Figure 9.18. A summary of oxyhydride phases yielded from the reduction of $LaSrCoRuO_6$ with CaH_2/LiH in sealed ampoules. 219
Figure 9.19. Schematic representation of *cis* RuO_4H_2 leads to 2 choices of -H-Ru-H- chain progression. 222
Figure 10.1. Phase diagram of $LaSrCoRuO_aH_b$. 227
Figure A2-1. Observed, calculated and difference plots from the structural refinement of $LaSrNiRuO_6$ sample quenched from 350 °C against SXRD data collected at room temperature. 238
Figure A2-2. Observed, calculated and difference plots from the structural refinement of $LaSrNiRuO_6$ sample quenched from 375 °C against SXRD data collected at room temperature. 239
Figure A2-3. Observed, calculated and difference plots from the structural refinement of $LaSrNiRuO_6$ sample quenched from 450 °C against SXRD data collected at room temperature. 239
Figure A2-4. Observed, calculated and difference plots from the structural refinement of $LaSrNiRuO_6$ sample quenched from 500 °C against SXRD data collected at room temperature. 240
Figure A2-5. Observed, calculated and difference plots from the structural refinement of $LaSrNiRuO_6$ sample quenched from 600 °C against SXRD data collected at room temperature. 240
Figure A2-6. The particle size distribution of the (top) quenched sample of $LaSrNiRuO_6$, obtained from 1135 particles and (bottom) slow-cooled sample of $LaSrniRuO_6$, obtained from 991 particles. 242

Figure A2-7. SEM images of the particles of (top) quenched sample of $LaSrNiRuO_6$ and (bottom) slow-cooled sample of $LaSrNiRuO_6$.....243
Figure A2-8. Observed, calculated and difference plots from the structural refinement of a quenched sample of $LaSrNiRuO_6$ against XRD data collected at room temperature.....244
Figure A2-9. Observed, calculated and difference plots from the structural refinement of a slow-cooled sample of $LaSrNiRuO_6$ against XRD data collected at room temperature. 245
Figure A2-10. Observed, calculated and difference plots from the structural refinement of $La_{0.6}Sr_{1.4}CoRuO_6$ against XRD data collected at room temperature. 246
Figure A2-11. Observed, calculated and difference plots from the structural refinement of $La_{0.65}Sr_{1.35}CoRuO_6$ against XRD data collected at room temperature.....247
Figure A2-12. Observed, calculated and difference plots from the structural refinement of $La_{0.7}Sr_{1.3}CoRuO_6$ against XRD data collected at room temperature. 247
Figure A2-13. Observed, calculated and difference plots from the structural refinement of $La_{0.9}Sr_{1.1}CoRuO_6$ against XRD data collected at room temperature. 248
Figure A2-14. Observed, calculated and difference plots from the structural refinement of $La_{1.1}Sr_{0.9}CoRuO_6$ against XRD data collected at room temperature. 248
Figure A2-15. Observed, calculated and difference plots from the structural refinement of $La_{1.2}Sr_{0.8}CoRuO_6$ against XRD data collected at room temperature. 249
Figure A2-16. Observed, calculated and difference plots from the structural refinement of $La_{1.3}Sr_{0.7}CoRuO_6$ against XRD data collected at room temperature. 249
Figure A2-17. Observed, calculated and difference plots from the structural refinement of $La_{1.4}Sr_{0.6}CoRuO_6$ against XRD data collected at room temperature. 250
Figure A2-18. Oxidative thermogravimetric data collected from $La_{0.6}Sr_{1.4}CoRuO_{6-\delta}$. Top panel indicates the heating profile, bottom panel indicates the change of mass in the sample as a function of time.....251
Figure A2-19. Oxidative thermogravimetric data collected from $La_{0.7}Sr_{1.3}CoRuO_{6-\delta}$. Top panel indicates the heating profile, bottom panel indicates the change of mass in the sample as a function of time.....252
Figure A2-20. Oxidative thermogravimetric data collected from $La_{0.9}Sr_{1.1}CoRuO_{6-\delta}$. Top panel indicates the heating profile, bottom panel indicates the change of mass in the sample as a function of time.....253
Figure A2-21. Oxidative thermogravimetric data collected from $La_{1.1}Sr_{0.9}CoRuO_{6-\delta}$. Top panel indicates the heating profile, bottom panel indicates the change of mass in the sample as a function of time.....254
Figure A2-22. Oxidative thermogravimetric data collected from $La_{1.2}Sr_{0.8}CoRuO_{6-\delta}$. Top panel indicates the heating profile, bottom panel indicates the change of mass in the sample as a function of time.....255
Figure A2-23. Oxidative thermogravimetric data collected from $La_{1.3}Sr_{0.7}CoRuO_{6-\delta}$. Top panel indicates the heating profile, bottom panel indicates the change of mass in the sample as a function of time.....256
Figure A2-24. Oxidative thermogravimetric data collected from $La_{1.4}Sr_{0.6}CoRuO_{6-\delta}$. Top panel indicates the heating profile, bottom panel indicates the change of mass in the sample as a function of time.....257

Figure A2-25. Observed, calculated and difference plots from the structural refinement of $La_{0.7}Sr_{1.3}CoRuO_5$ against XRD data collected at room temperature. Upper ticks mark the peak positions of the majority phase $La_{0.7}Sr_{1.3}CoRuO_5$ and lower ticks mark the peak positions of the minority phase $La_{0.7}Sr_{1.3}CoRuO_6$.....258
Figure A2-26. Observed, calculated and difference plots from the structural refinement of $La_{0.9}Sr_{1.1}CoRuO_5$ against XRD data collected at room temperature. Upper ticks mark the peak positions of the majority phase $La_{0.9}Sr_{1.1}CoRuO_5$ and lower ticks mark peak positions of the the minority phase $La_{0.9}Sr_{1.1}CoRuO_4$.....258
Figure A2-27. Observed, calculated and difference plots from the structural refinement of $La_{1.1}Sr_{0.9}CoRuO_5$ against XRD data collected at room temperature. Upper ticks mark the peak positions of the majority phase $La_{1.1}Sr_{0.9}CoRuO_5$ and lower ticks mark the peak positions of the minority phase $La_{1.1}Sr_{0.9}CoRuO_6$.....259
Figure A2-28. Observed, calculated and difference plots from the structural refinement of $La_{1.2}Sr_{0.8}CoRuO_5$ against XRD data collected at room temperature. Upper ticks mark the peak positions of the majority phase $La_{1.2}Sr_{0.8}CoRuO_5$ and lower ticks mark the peak positions of the minority phase $La_{1.2}Sr_{0.8}CoRuO_6$.....259
Figure A2-29. Observed, calculated and difference plots from the structural refinement of $La_{1.3}Sr_{0.7}CoRuO_5$ against XRD data collected at room temperature. Upper ticks mark the peak positions of the majority phase $La_{1.3}Sr_{0.7}CoRuO_5$ and lower ticks mark the peak positions of the minority phase $La_{1.3}Sr_{0.7}CoRuO_6$.....260
Figure A2-30. The paramagnetic susceptibility and saturated magnetic moment of $La_{0.7}Sr_{1.3}CoRuO_5$ as a function of temperature.....261
Figure A2-31. The paramagnetic susceptibility and saturated magnetic moment of $La_{0.9}Sr_{1.1}CoRuO_5$ as a function of temperature.....262
Figure A2-32. The paramagnetic susceptibility and saturated magnetic moment of $La_{1.1}Sr_{0.9}CoRuO_5$ as a function of temperature.....263
Figure A2-33. The paramagnetic susceptibility and saturated magnetic moment of $La_{1.2}Sr_{0.8}CoRuO_5$ as a function of temperature.....264
Figure A2-34. The paramagnetic susceptibility and saturated magnetic moment of $La_{1.3}Sr_{0.7}CoRuO_5$ as a function of temperature.....265
Figure A2-35. Magnetisation-field data collected from $La_{0.7}Sr_{1.3}CoRuO_5$ at 5 K.....266
Figure A2-36. Magnetisation-field data collected from $La_{0.9}Sr_{1.1}CoRuO_5$ at 5 K and 300 K 266
Figure A2-37. Magnetisation-field data collected from $La_{1.1}Sr_{0.9}CoRuO_5$ at 5 K and 300 K. 267
Figure A2-38. Magnetisation-field data collected from $La_{1.2}Sr_{0.8}CoRuO_5$ at 5 K and 300 K. 267
Figure A2-39. Magnetisation-field data collected from $La_{1.3}Sr_{0.7}CoRuO_5$ at 5 K and 300 K. 268
Figure A2-40. TGA-MS data collected from $LaSrCoRuO_6$ under a constant flow of oxygen. Arrow indicates the H_2O signal related to the TGA-MS machine.....269

Appendix 2 Additional Data for Chapter 3-9

Appendix 2.1 Synchrotron X-ray diffraction data (SXRD) from $LaSrNiRuO_6$ Quenched at Different Temperatures

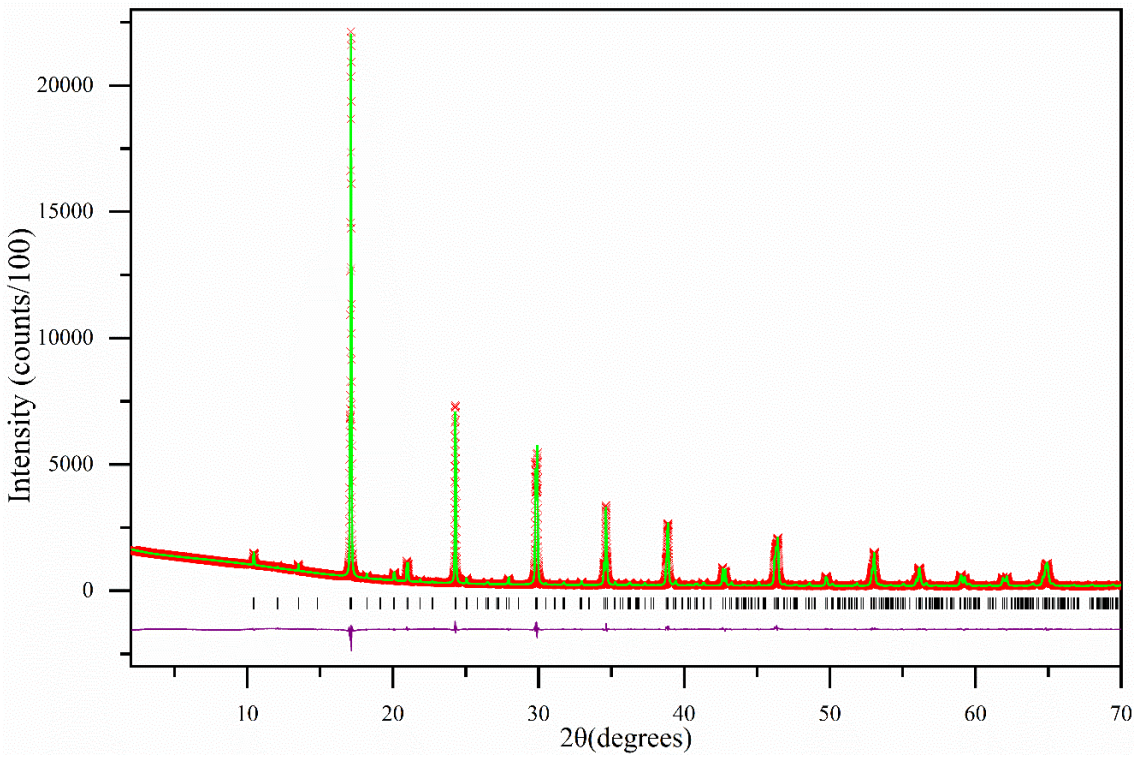


Figure A2-1. Observed, calculated and difference plots from the structural refinement of $LaSrNiRuO_6$ sample quenched from 350 °C against SXRD data collected at room temperature.

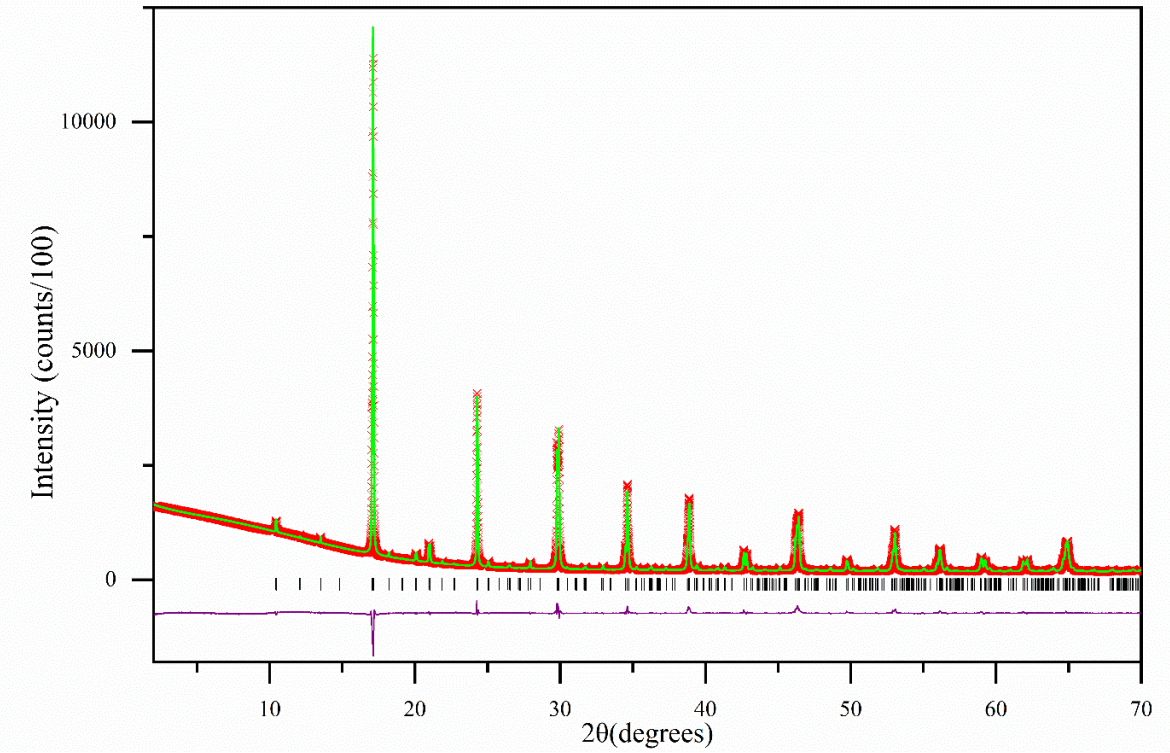


Figure A2-2. Observed, calculated and difference plots from the structural refinement of $LaSrNiRuO_6$ sample quenched from 375 °C against SXRD data collected at room temperature.

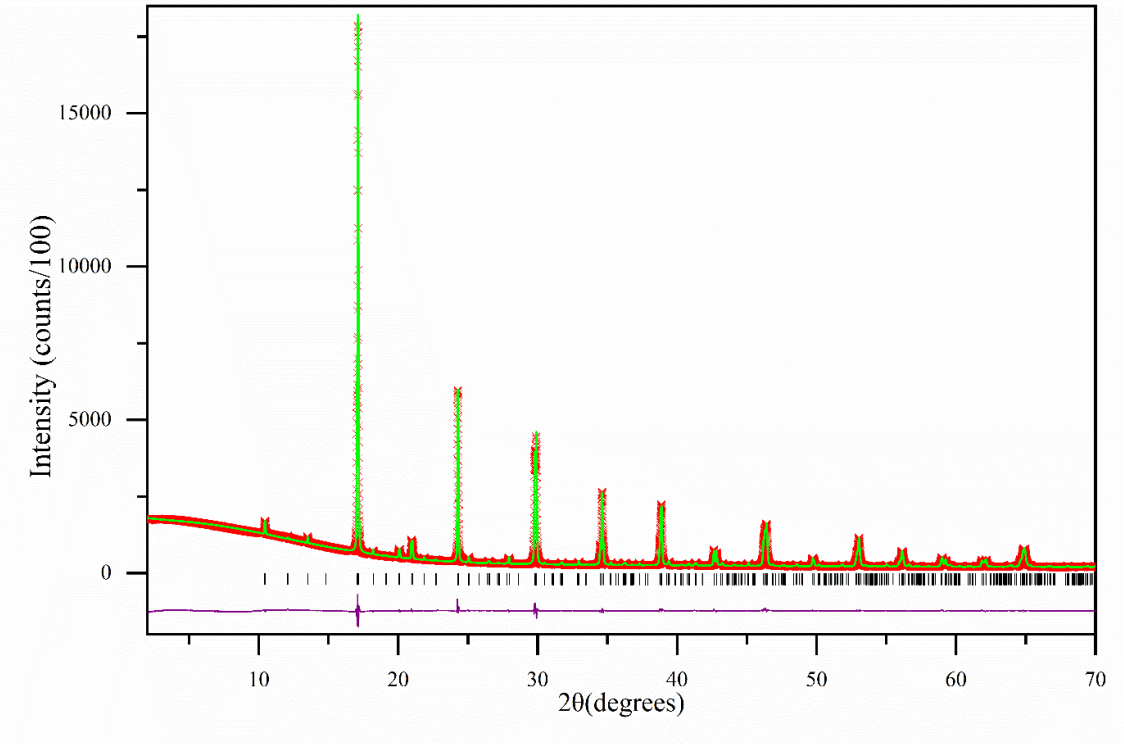


Figure A2-3. Observed, calculated and difference plots from the structural refinement of $LaSrNiRuO_6$ sample quenched from 450 °C against SXRD data collected at room temperature.

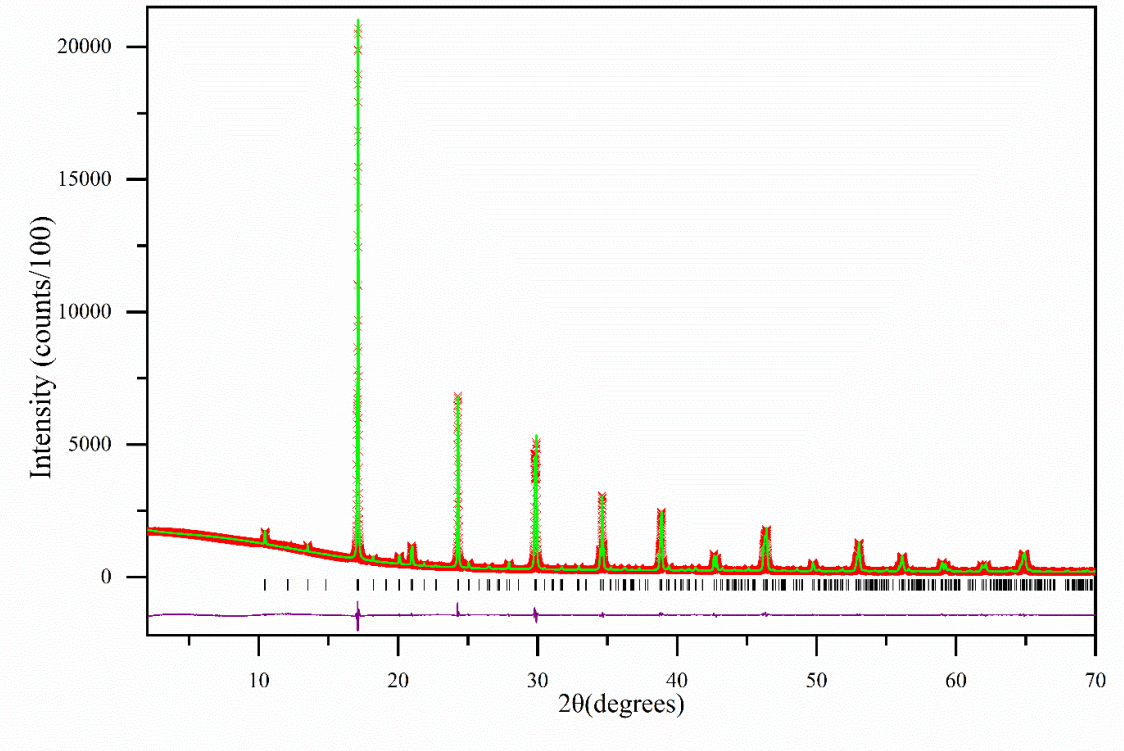


Figure A2-4. Observed, calculated and difference plots from the structural refinement of $LaSrNiRuO_6$ sample quenched from 500 °C against SXRD data collected at room temperature.

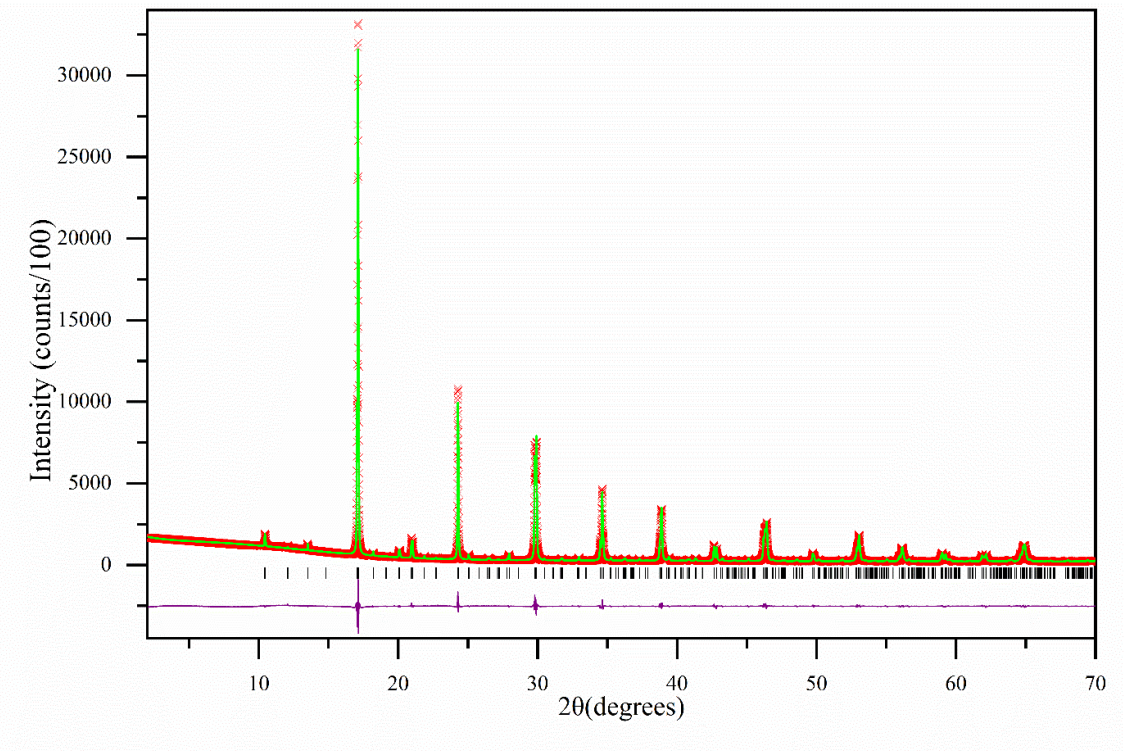


Figure A2-5. Observed, calculated and difference plots from the structural refinement of $LaSrNiRuO_6$ sample quenched from 600 °C against SXRD data collected at room temperature.

Appendix 2.2 SEM Particle size Analysis of Quenched and Slow-cooled samples of $LaSrNiRuO_6$

In this thesis, scanning electron microscopy was used to characterise the particle size distributions of a starting material. The SEM data presented in this thesis were performed by Dr Mylene Hendrickx and Prof. Joke Hadermann from the University of Antwerp. SEM images were collected using a Thermofisher Quanta FEG 250 microscope. The samples were directly transferred onto the SEM sample holder without grinding.

The SEM images were analysed using the commercial software DigitalMicrograph (GATAN). This software uses a threshold function to locate the particles and determine the area, perimeter, length and minimum and maximum radius for each particle located. In order to account for the irregular shape of particles, two different particle size distributions were calculated. The first distribution is the mean particle diameter (Fig A2-6 left), and the second one is the distribution of diameter calculated form the measured area of particle using the assumption that they are spherical ($A = \pi(d/2)^2$) (Fig A2-6 right).

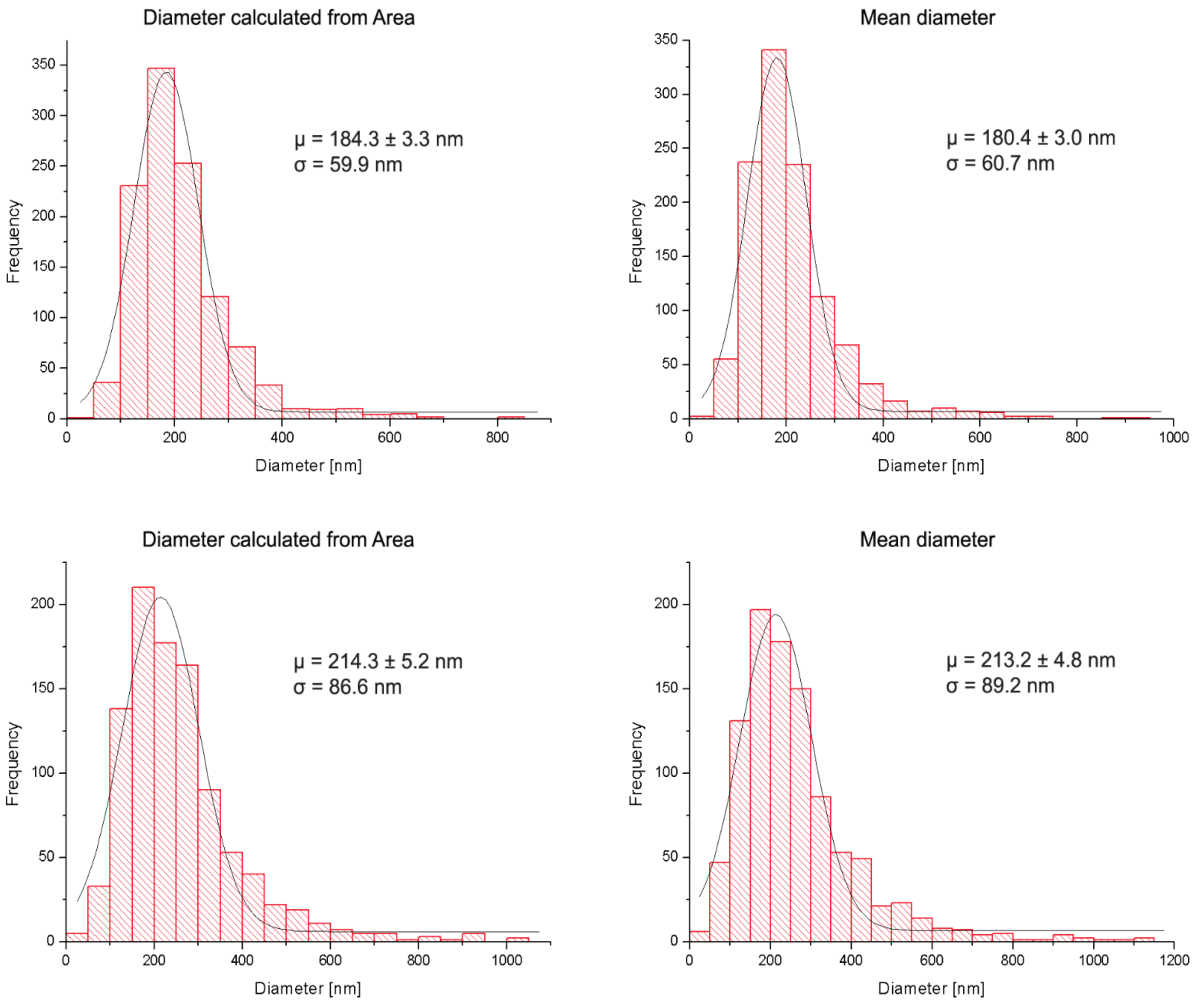


Figure A2-6. The particle size distribution of the (top) quenched sample of $LaSrNiRuO_6$, obtained from 1135 particles and (bottom) slow-cooled sample of $LaSrniRuO_6$, obtained from 991 particles.

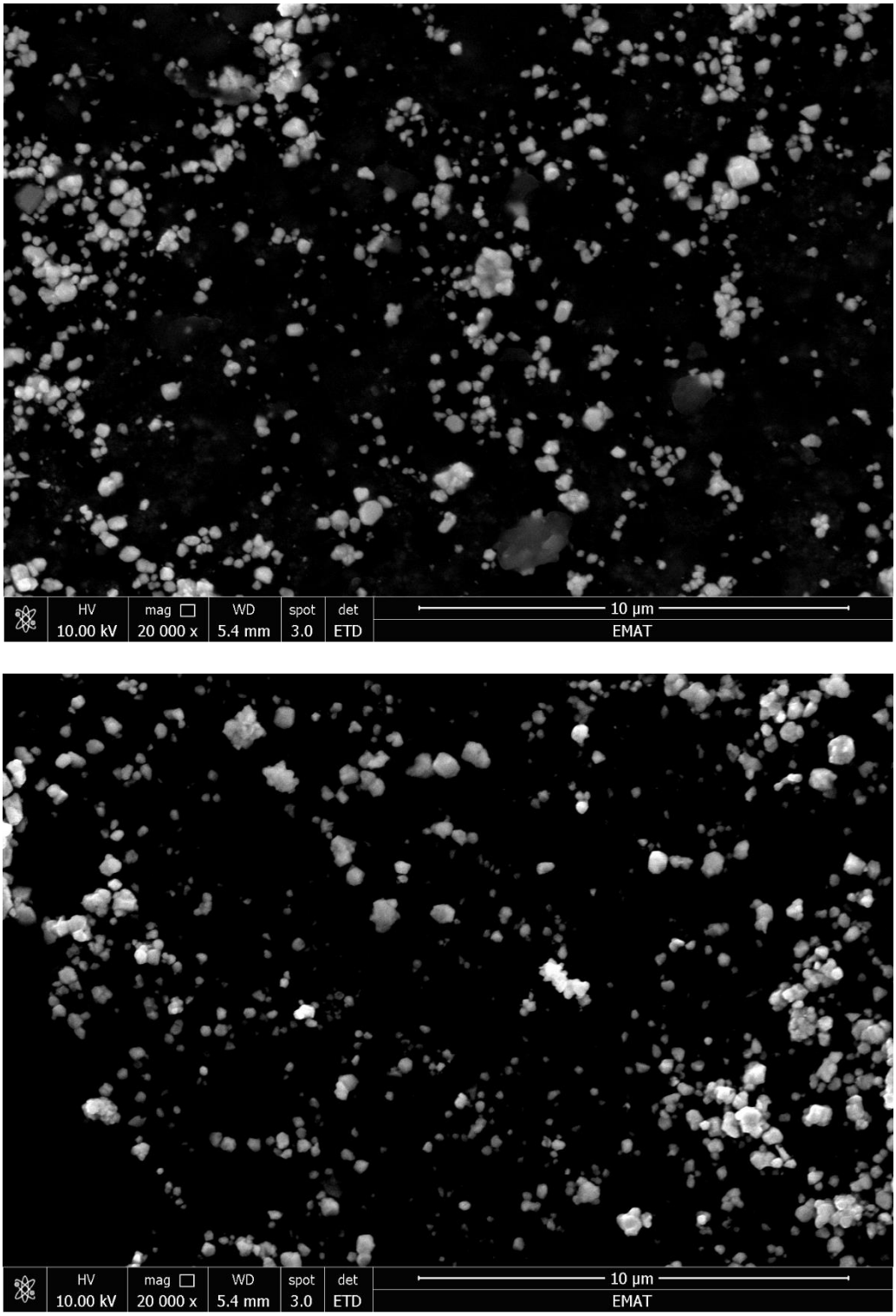


Figure A2-7. SEM images of the particles of (top) quenched sample of $LaSrNiRuO_6$ and (bottom) slow-cooled sample of $LaSrNiRuO_6$.

Appendix 2.3 X-ray diffraction data (XRD) from Quenched and Slow-cooled Samples of $LaSrNiRuO_6$

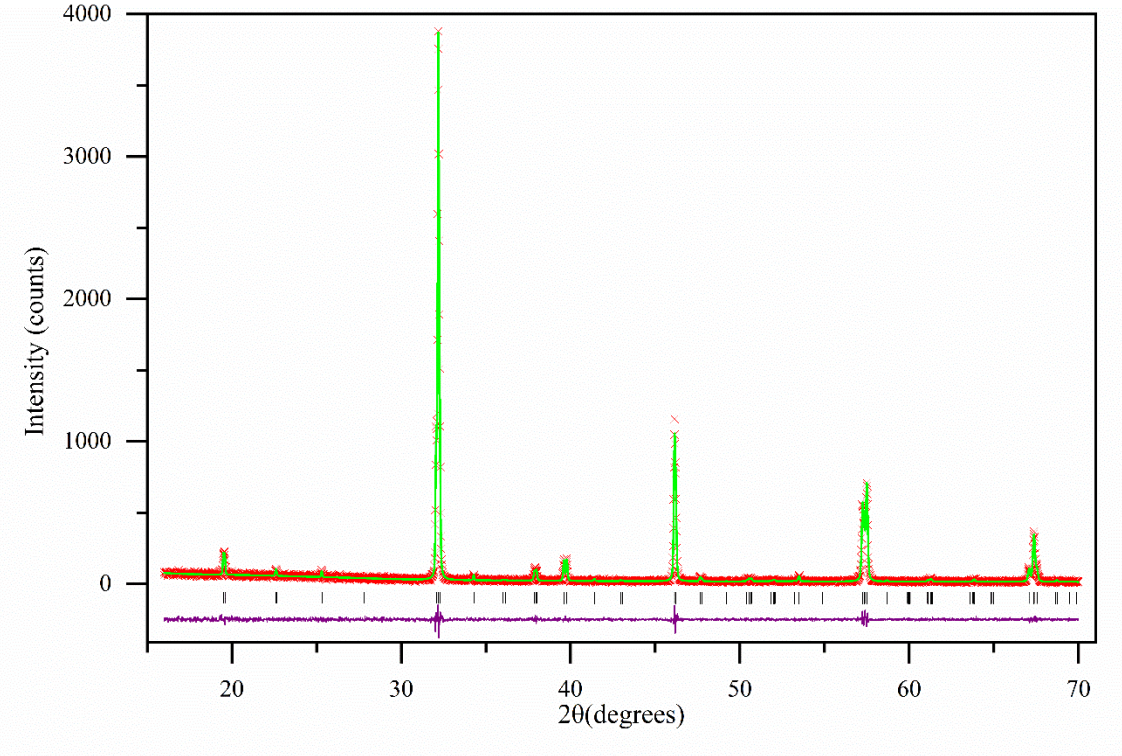


Figure A2-8. Observed, calculated and difference plots from the structural refinement of a quenched sample of $LaSrNiRuO_6$ against XRD data collected at room temperature.

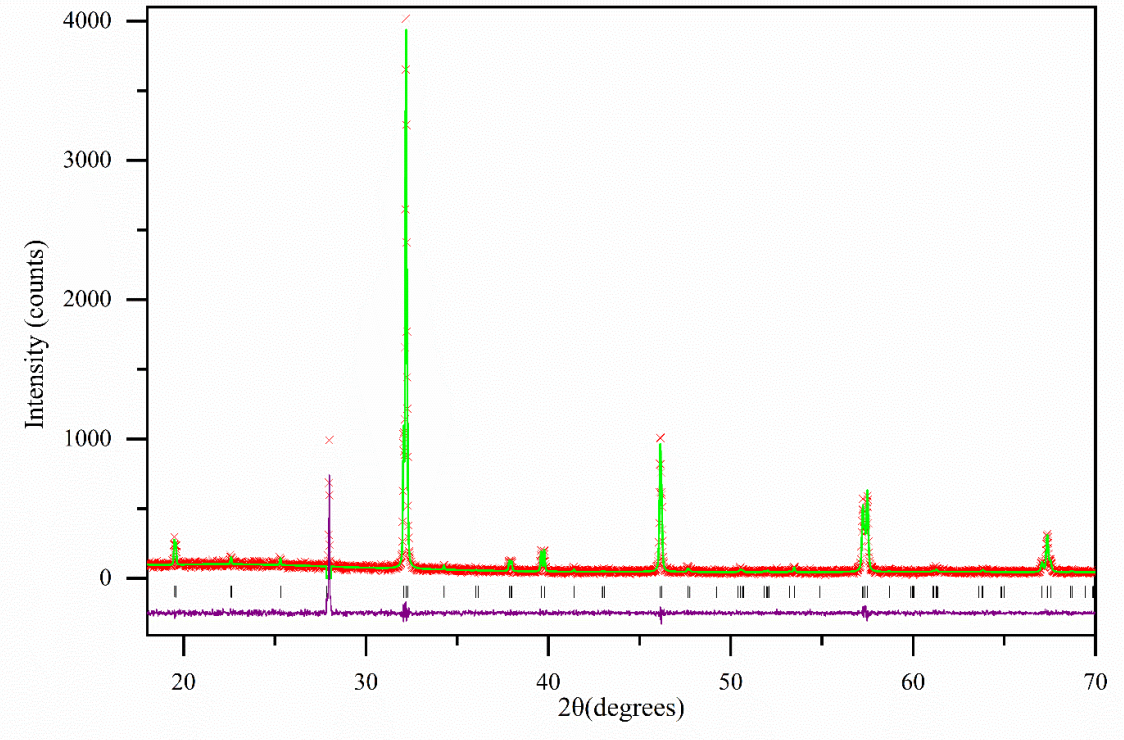


Figure A2-9. Observed, calculated and difference plots from the structural refinement of a slow-cooled sample of $LaSrNiRuO_6$ against XRD data collected at room temperature.

Appendix 2.4 Synchrotron X-ray Diffraction Data (SXRD) from $La_xSr_{2-x}CoRuO_6$ ($0.6 \leq x \leq 1.4$)

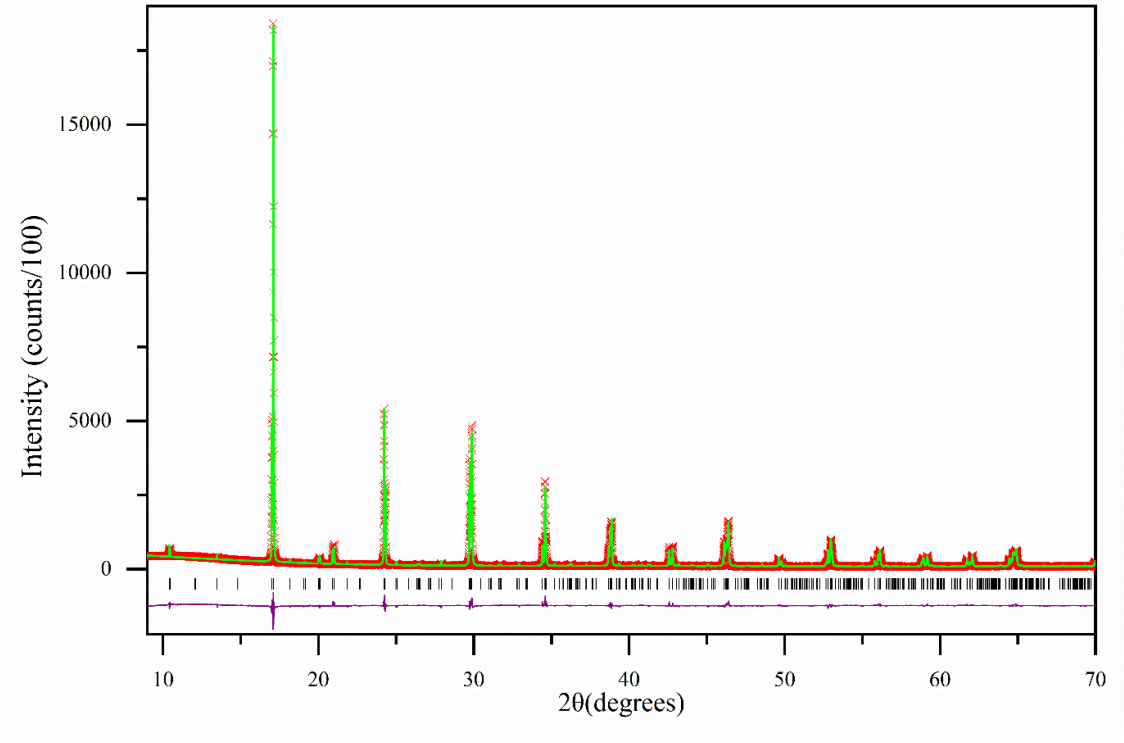


Figure A2-10. Observed, calculated and difference plots from the structural refinement of $La_{0.6}Sr_{1.4}CoRuO_6$ against XRD data collected at room temperature.

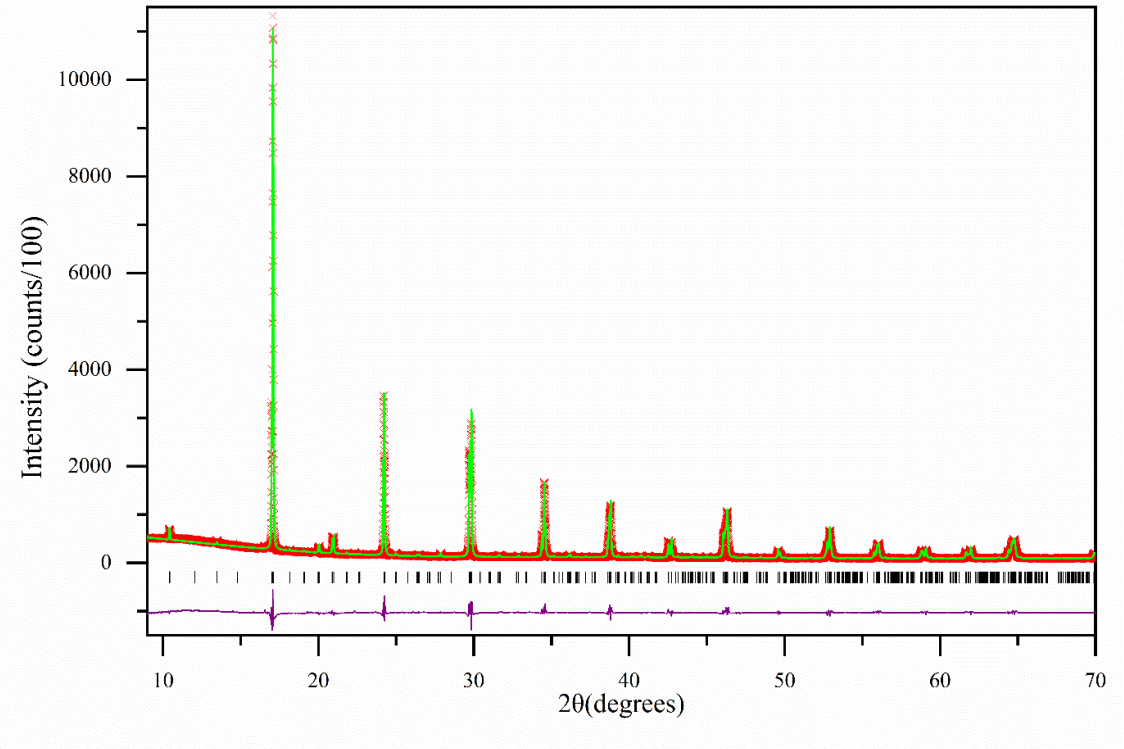


Figure A2-11. Observed, calculated and difference plots from the structural refinement of $La_{0.65}Sr_{1.35}CoRuO_6$ against XRD data collected at room temperature.

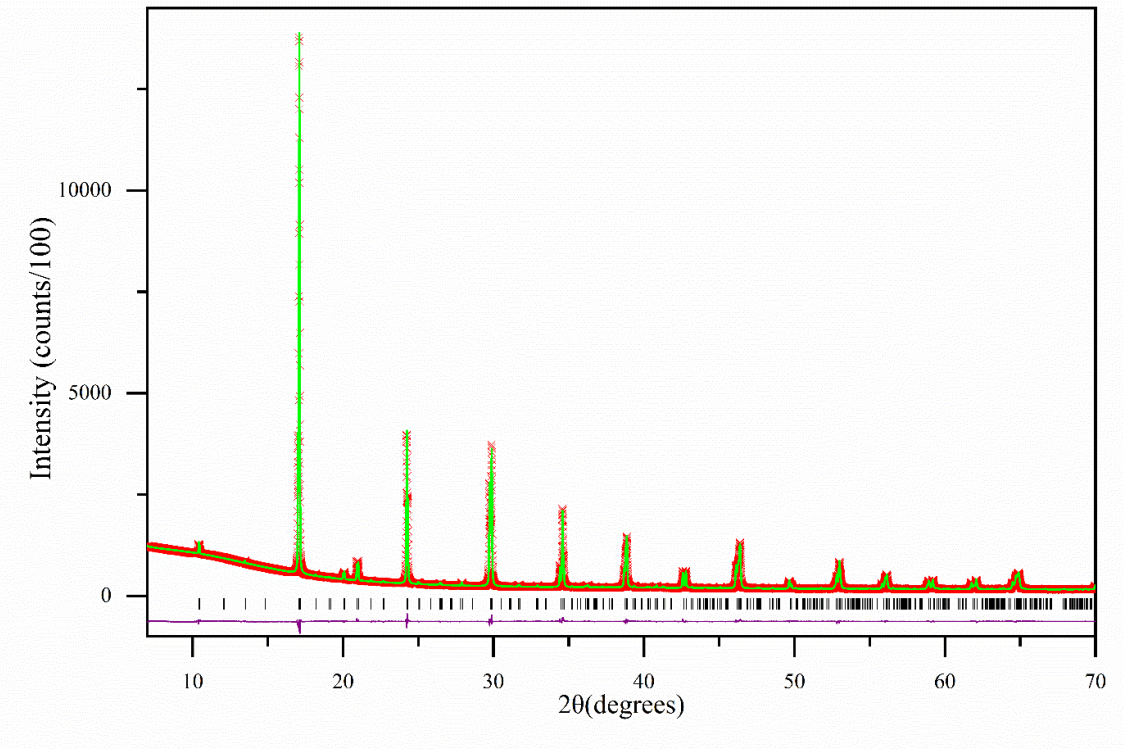


Figure A2-12. Observed, calculated and difference plots from the structural refinement of $La_{0.7}Sr_{1.3}CoRuO_6$ against XRD data collected at room temperature.

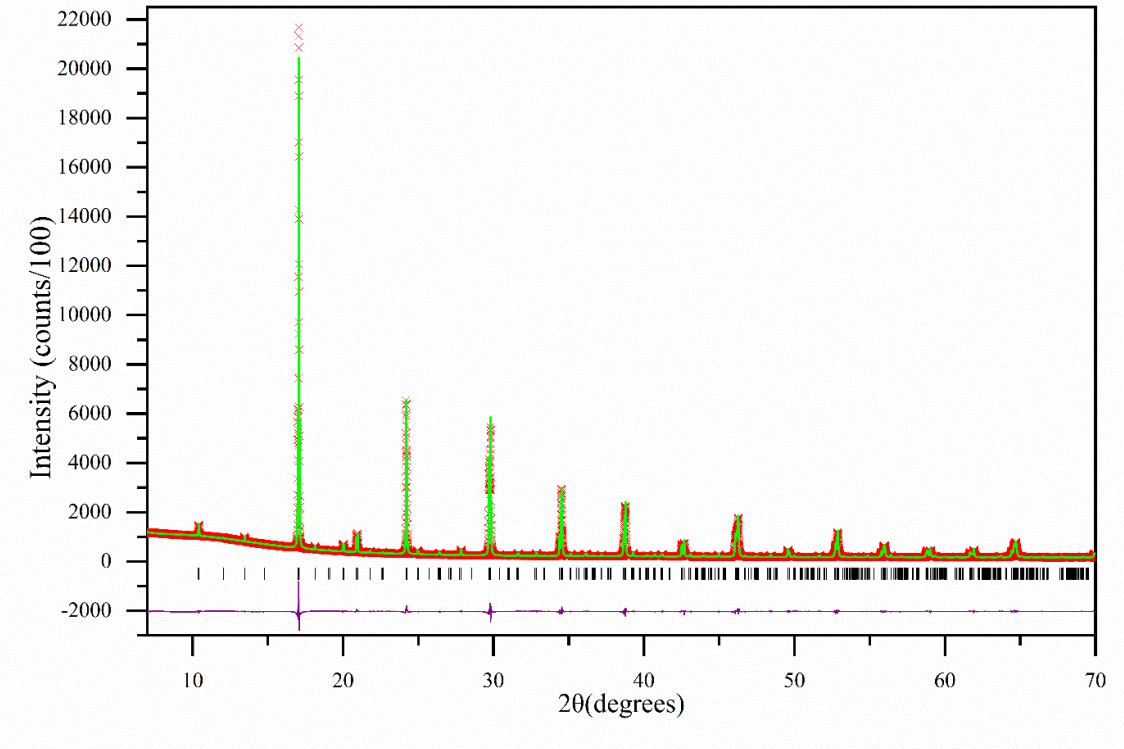


Figure A2-13. Observed, calculated and difference plots from the structural refinement of $La_{0.9}Sr_{1.1}CoRuO_6$ against XRD data collected at room temperature.

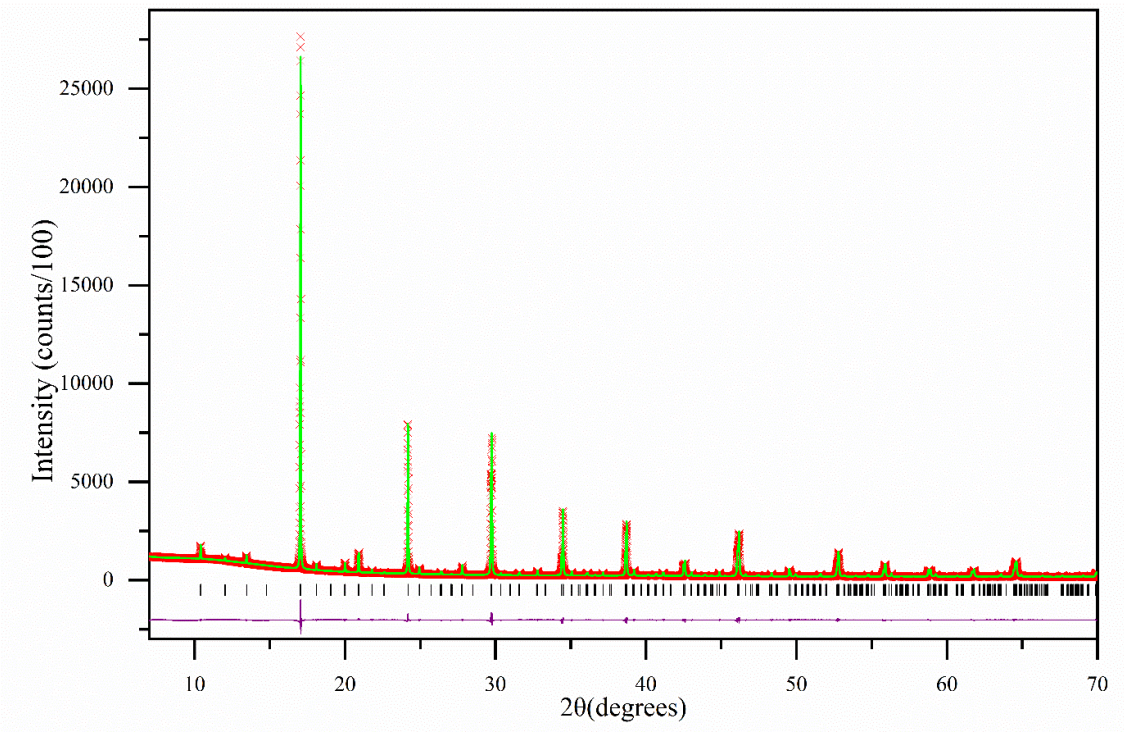


Figure A2-14. Observed, calculated and difference plots from the structural refinement of $La_{1.1}Sr_{0.9}CoRuO_6$ against XRD data collected at room temperature.

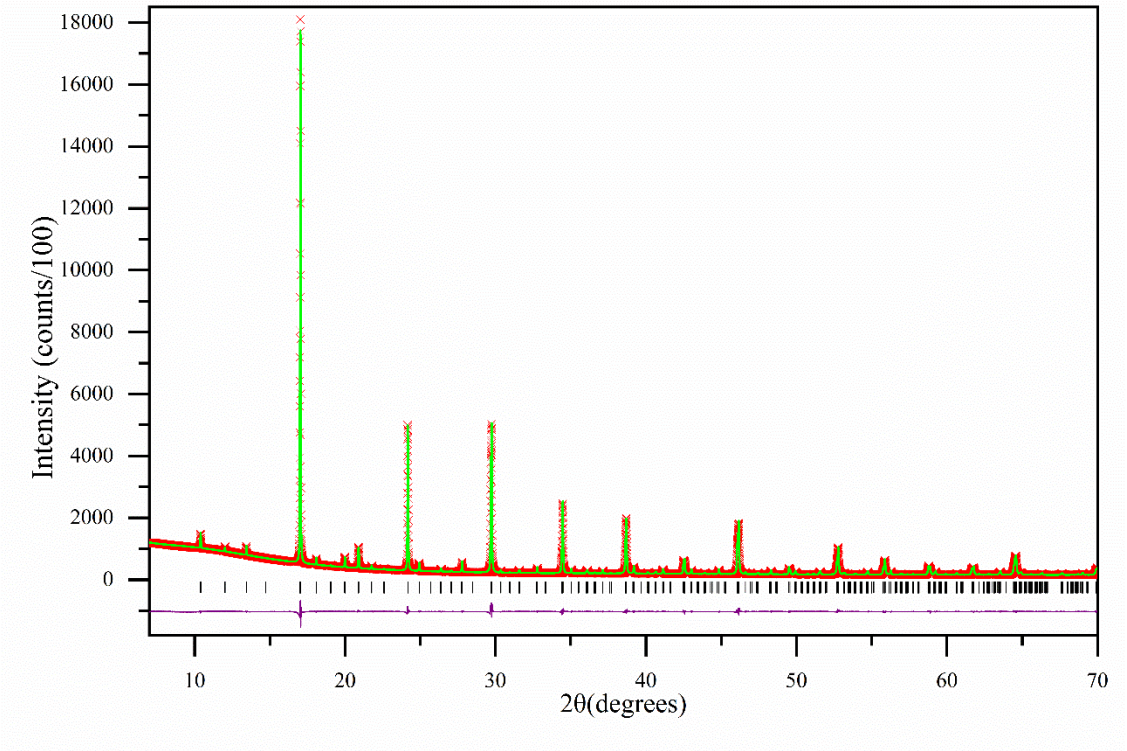


Figure A2-15. Observed, calculated and difference plots from the structural refinement of $La_{1.2}Sr_{0.8}CoRuO_6$ against XRD data collected at room temperature.

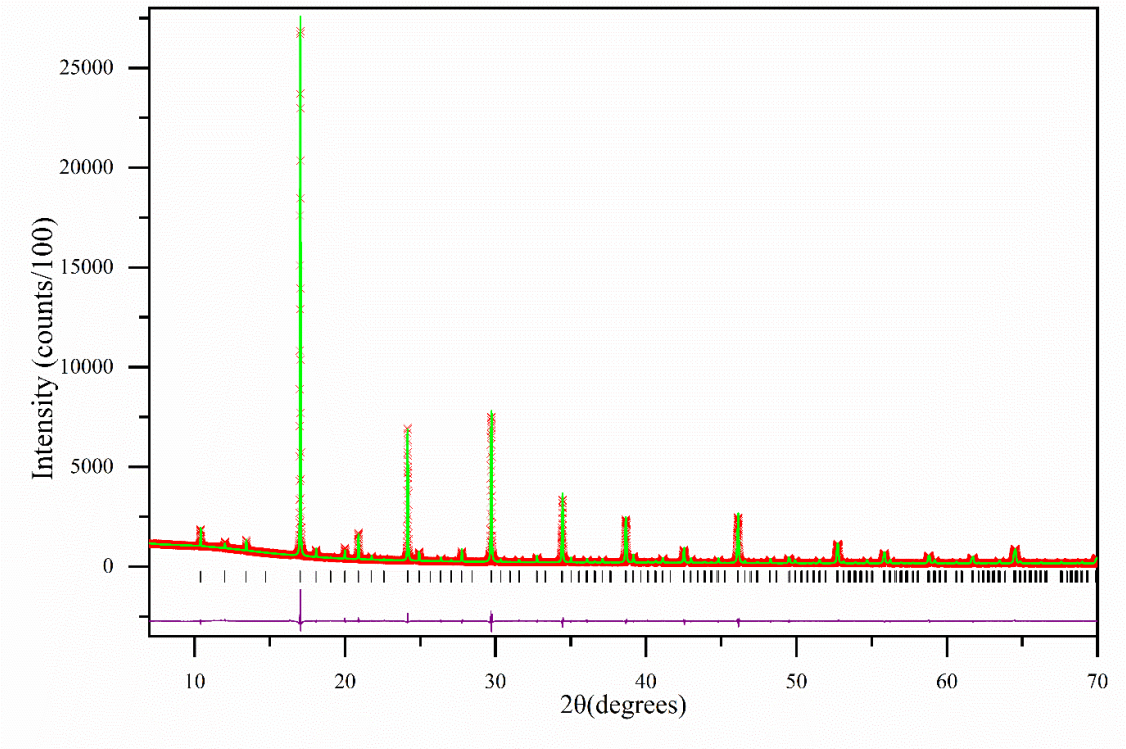


Figure A2-16. Observed, calculated and difference plots from the structural refinement of $La_{1.3}Sr_{0.7}CoRuO_6$ against XRD data collected at room temperature.

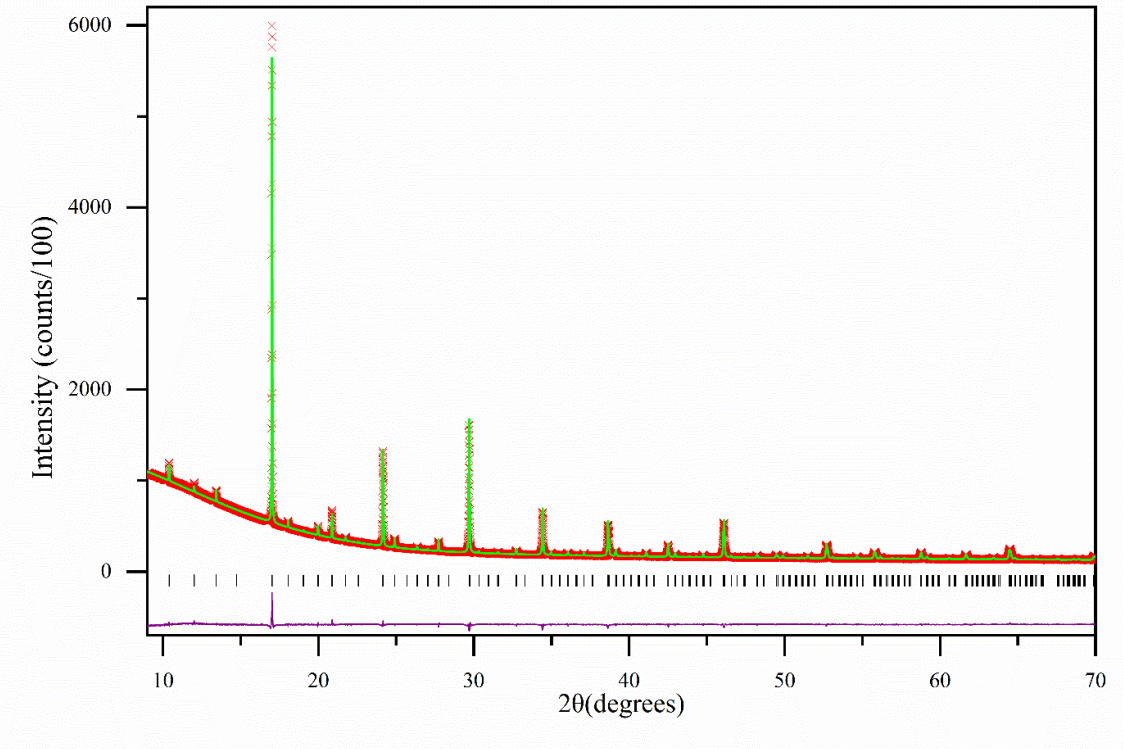


Figure A2-17. Observed, calculated and difference plots from the structural refinement of $La_{1.4}Sr_{0.6}CoRuO_6$ against XRD data collected at room temperature.

Appendix 2.5 Thermogravimetric Analysis (TGA) Data from $La_xSr_{2-x}CoRuO_{6-\delta}$ ($0.6 \leq x \leq 1.4$)

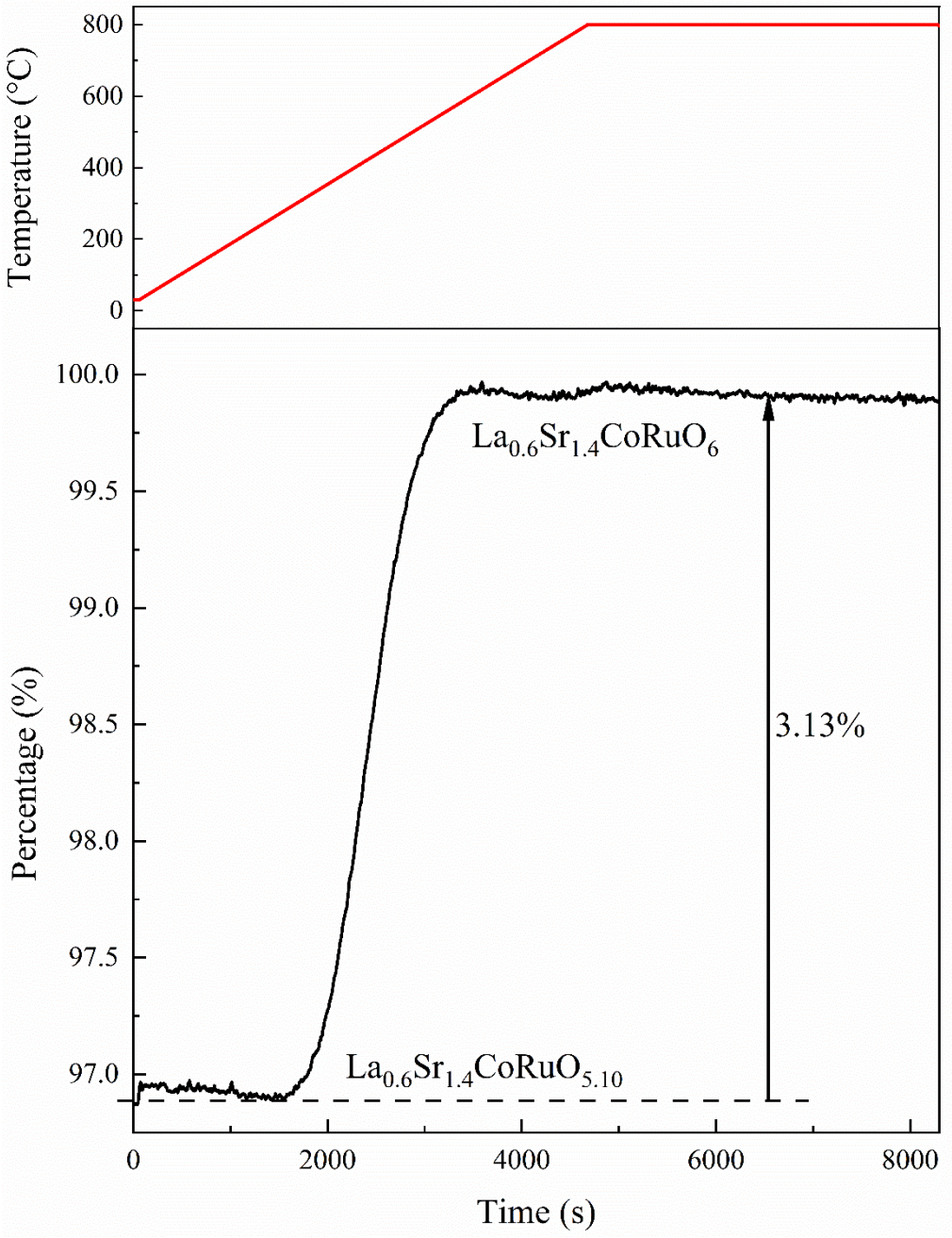


Figure A2-18. Oxidative thermogravimetric data collected from $La_{0.6}Sr_{1.4}CoRuO_{6-\delta}$. Top panel indicates the heating profile, bottom panel indicates the change of mass in the sample as a function of time.

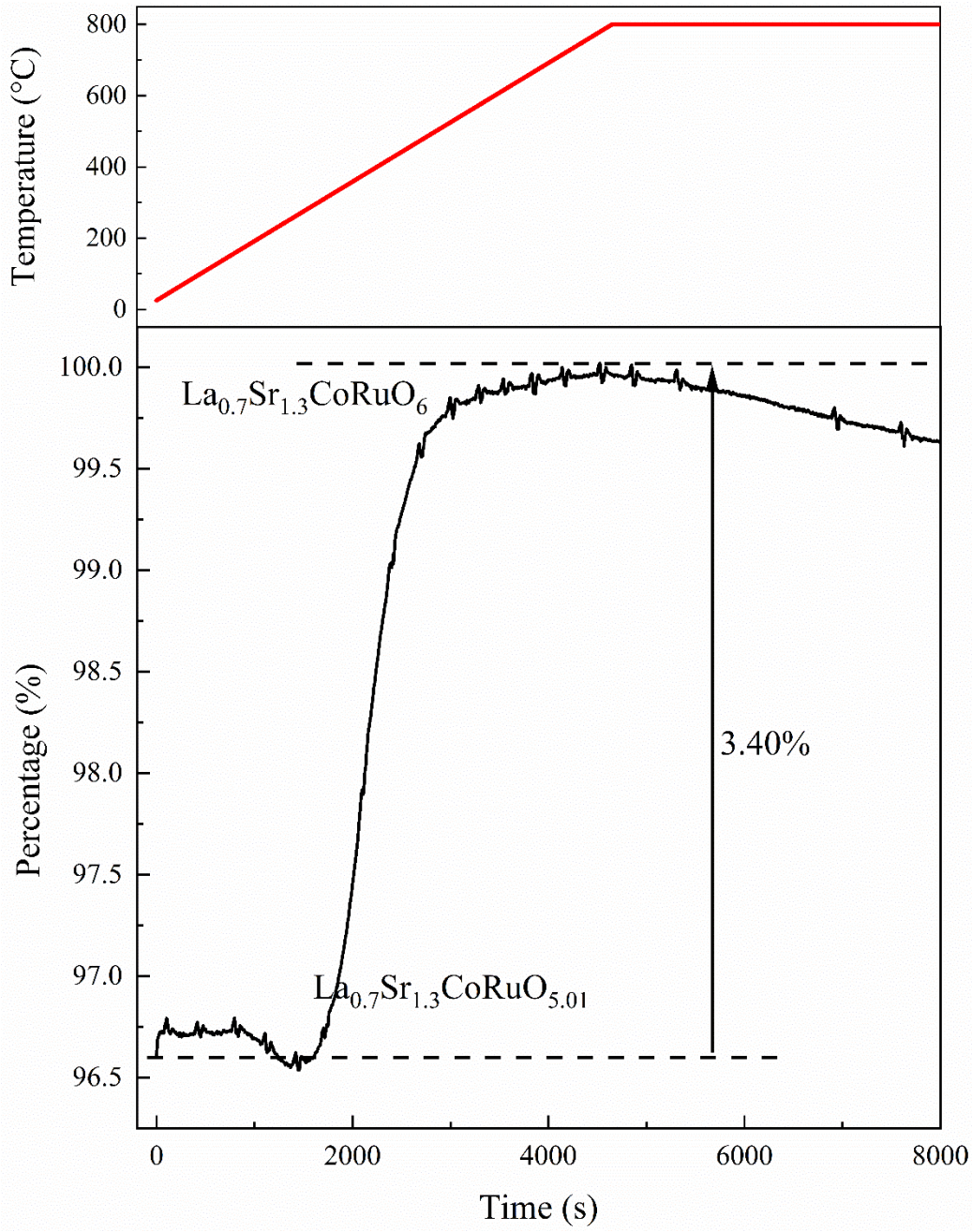


Figure A2-19. Oxidative thermogravimetric data collected from $La_{0.7}Sr_{1.3}CoRuO_{6-\delta}$. Top panel indicates the heating profile, bottom panel indicates the change of mass in the sample as a function of time.

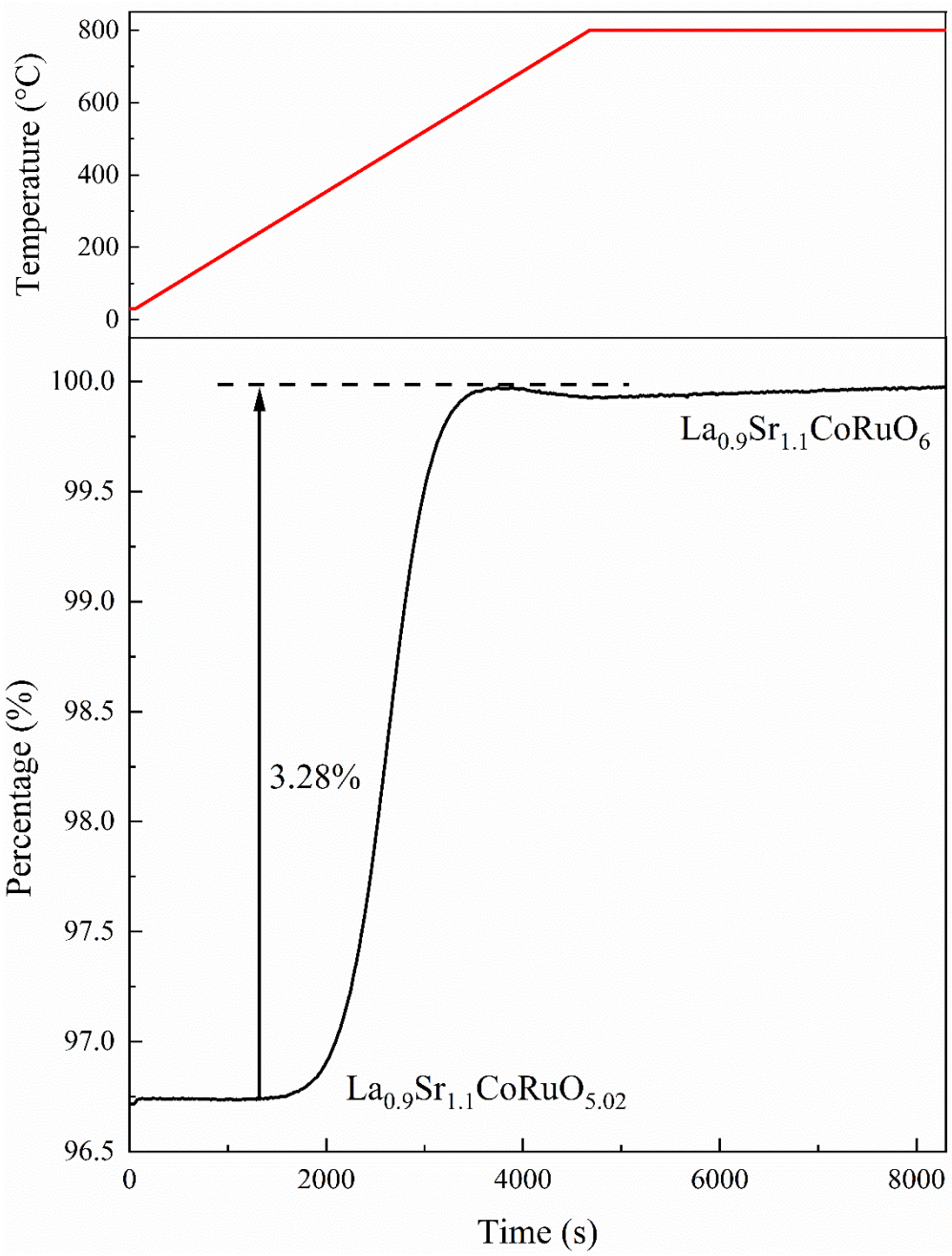


Figure A2-20. Oxidative thermogravimetric data collected from $La_{0.9}Sr_{1.1}CoRuO_{6-\delta}$. Top panel indicates the heating profile, bottom panel indicates the change of mass in the sample as a function of time.

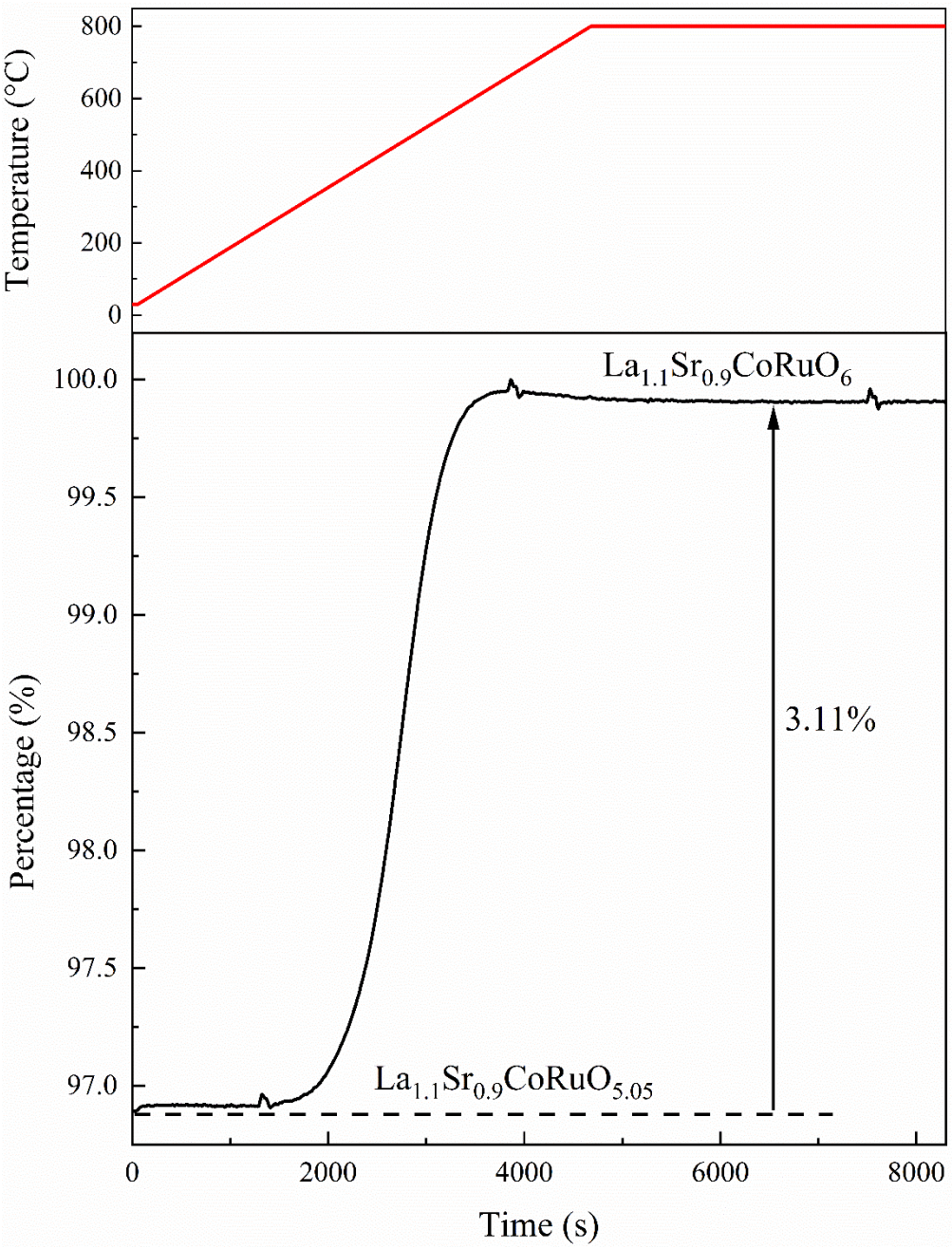


Figure A2-21. Oxidative thermogravimetric data collected from $La_{1.1}Sr_{0.9}CoRuO_{6-\delta}$. Top panel indicates the heating profile, bottom panel indicates the change of mass in the sample as a function of time.

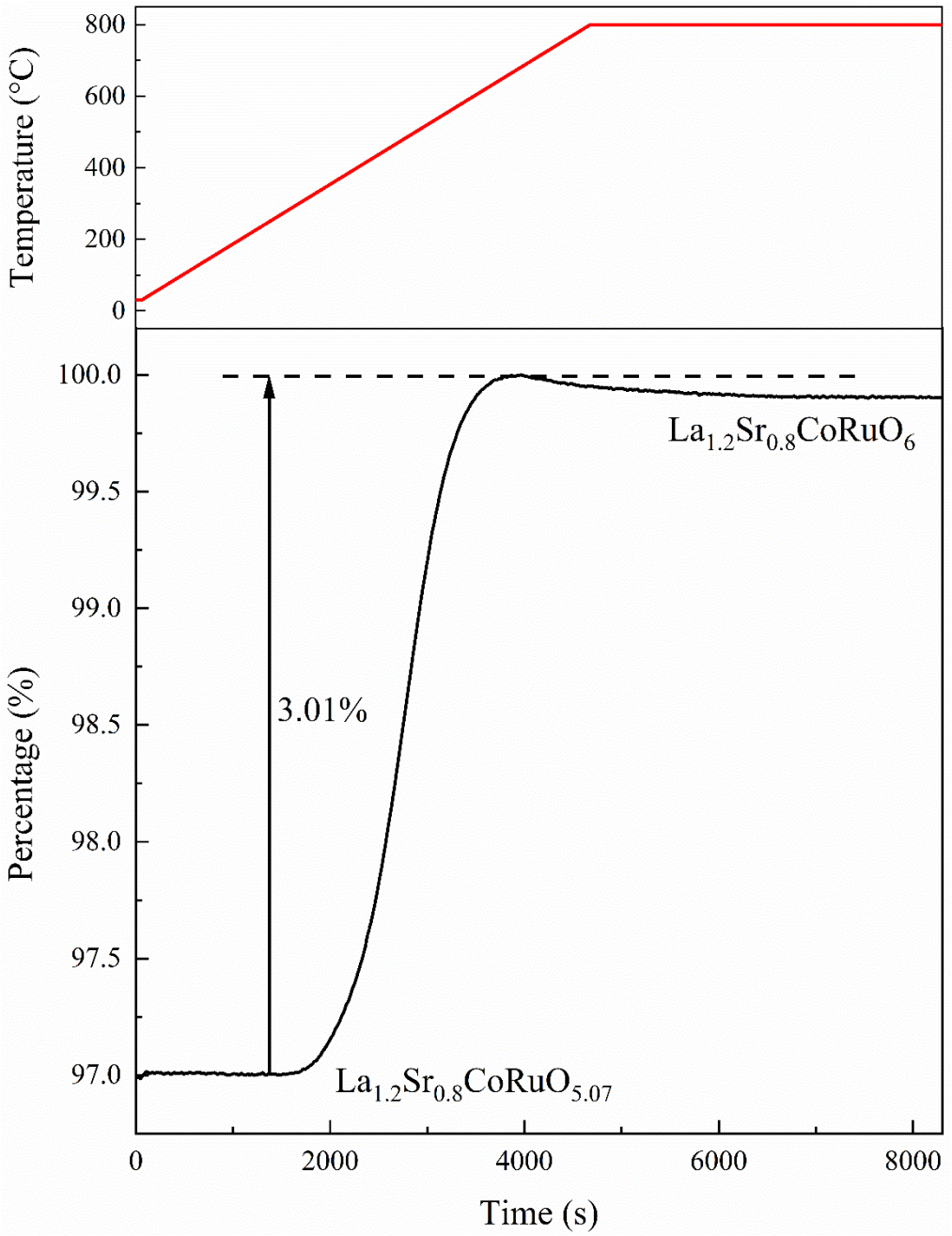


Figure A2-22. Oxidative thermogravimetric data collected from $La_{1.2}Sr_{0.8}CoRuO_{6-\delta}$. Top panel indicates the heating profile, bottom panel indicates the change of mass in the sample as a function of time.

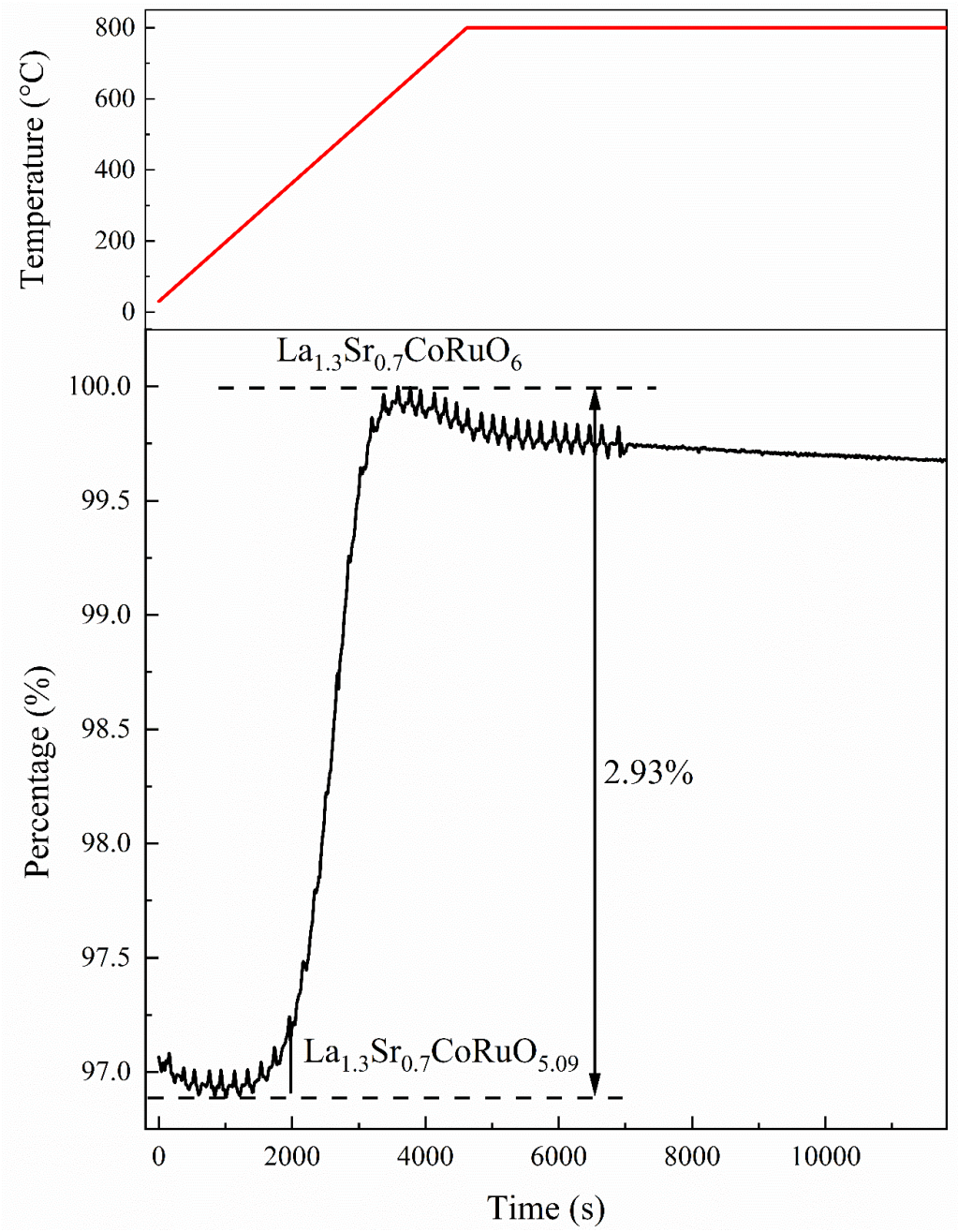


Figure A2-23. Oxidative thermogravimetric data collected from $La_{1.3}Sr_{0.7}CoRuO_{6-\delta}$. Top panel indicates the heating profile, bottom panel indicates the change of mass in the sample as a function of time.

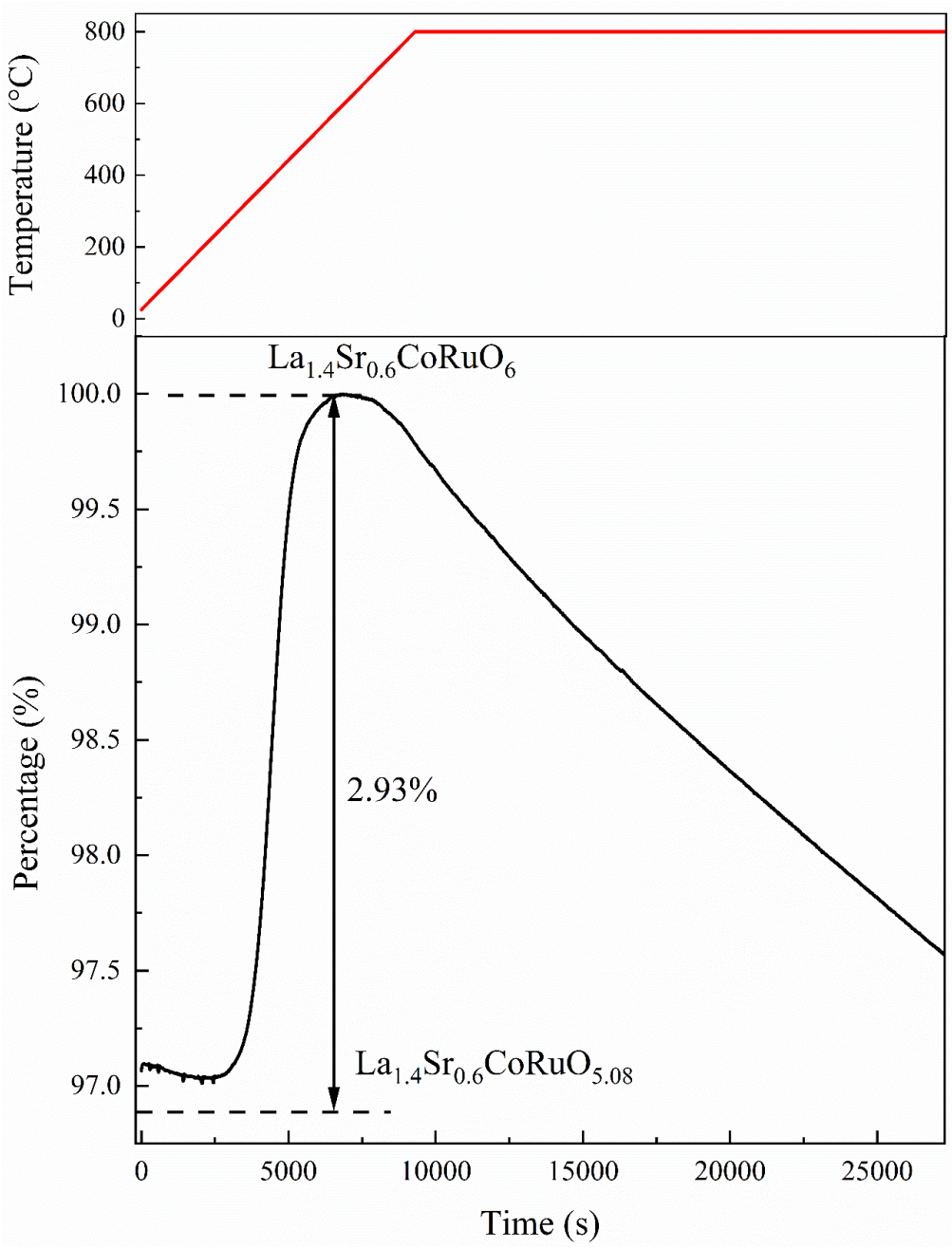


Figure A2-24. Oxidative thermogravimetric data collected from $La_{1.4}Sr_{0.6}CoRuO_{6-\delta}$. Top panel indicates the heating profile, bottom panel indicates the change of mass in the sample as a function of time.

Appendix 2.6 Synchrotron X-ray Diffraction data (SXRD) from $La_xSr_{2-x}CoRuO_5$ ($0.7 \leq x \leq 1.4$)

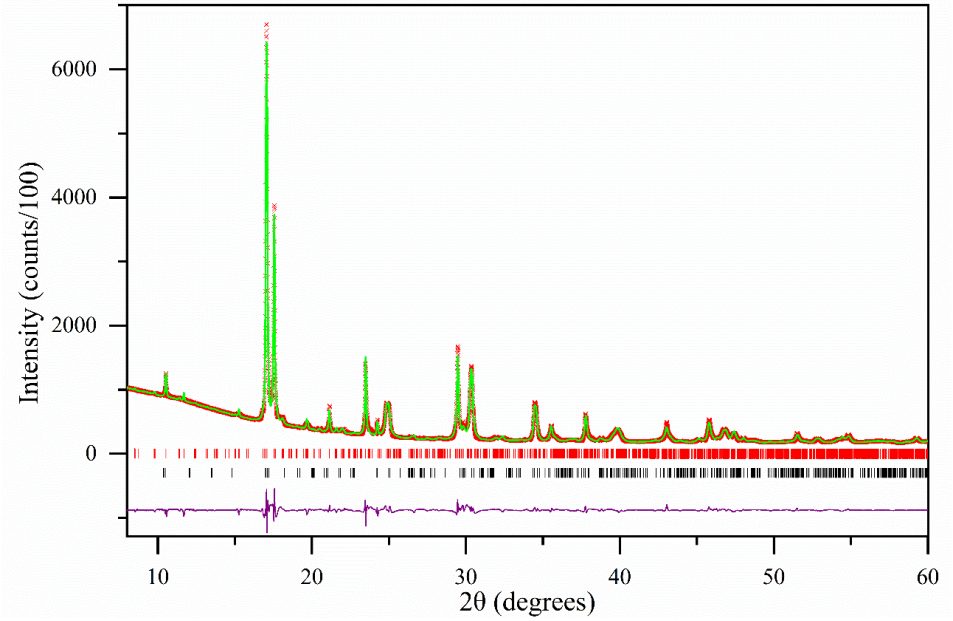


Figure A2-25. Observed, calculated and difference plots from the structural refinement of $La_{0.7}Sr_{1.3}CoRuO_5$ against XRD data collected at room temperature. Upper ticks mark the peak positions of the majority phase $La_{0.7}Sr_{1.3}CoRuO_5$ and lower ticks mark the peak positions of the minority phase $La_{0.7}Sr_{1.3}CoRuO_6$.

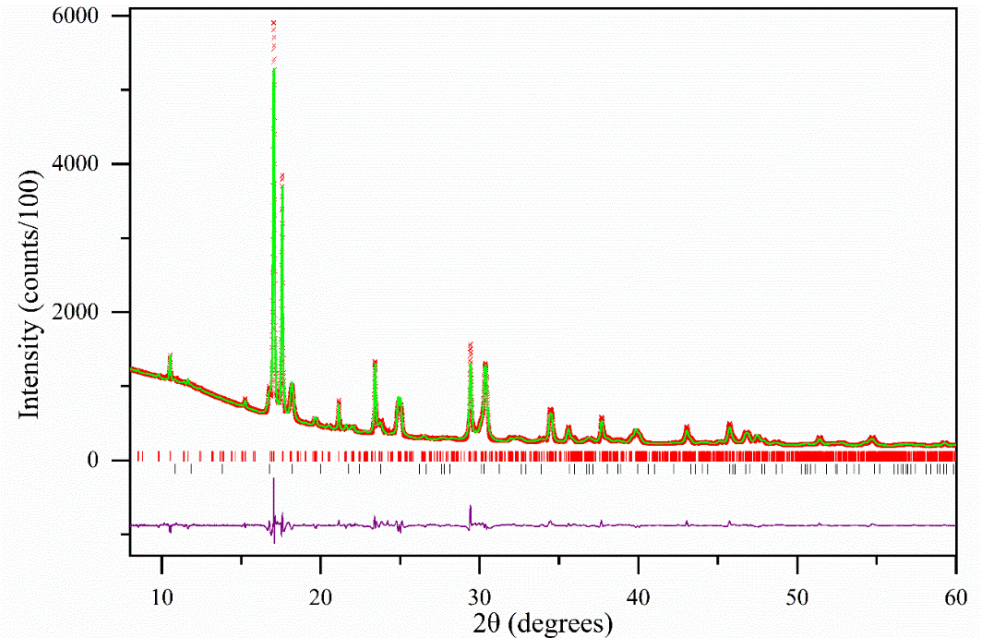


Figure A2-26. Observed, calculated and difference plots from the structural refinement of $La_{0.9}Sr_{1.1}CoRuO_5$ against XRD data collected at room temperature. Upper ticks mark the peak positions of the majority phase $La_{0.9}Sr_{1.1}CoRuO_5$ and lower ticks mark the peak positions of the minority phase $La_{0.9}Sr_{1.1}CoRuO_4$.

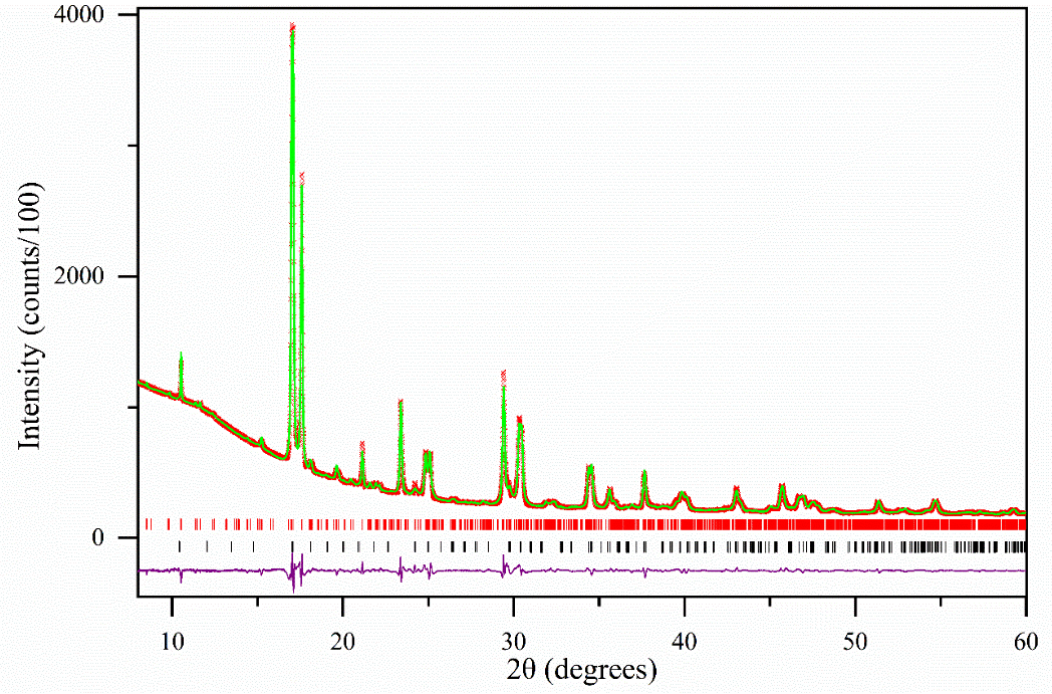


Figure A2-27. Observed, calculated and difference plots from the structural refinement of $La_{1.1}Sr_{0.9}CoRuO_5$ against XRD data collected at room temperature. Upper ticks mark the peak positions of the majority phase $La_{1.1}Sr_{0.9}CoRuO_5$ and lower ticks mark the peak positions of the minority phase $La_{1.1}Sr_{0.9}CoRuO_6$.

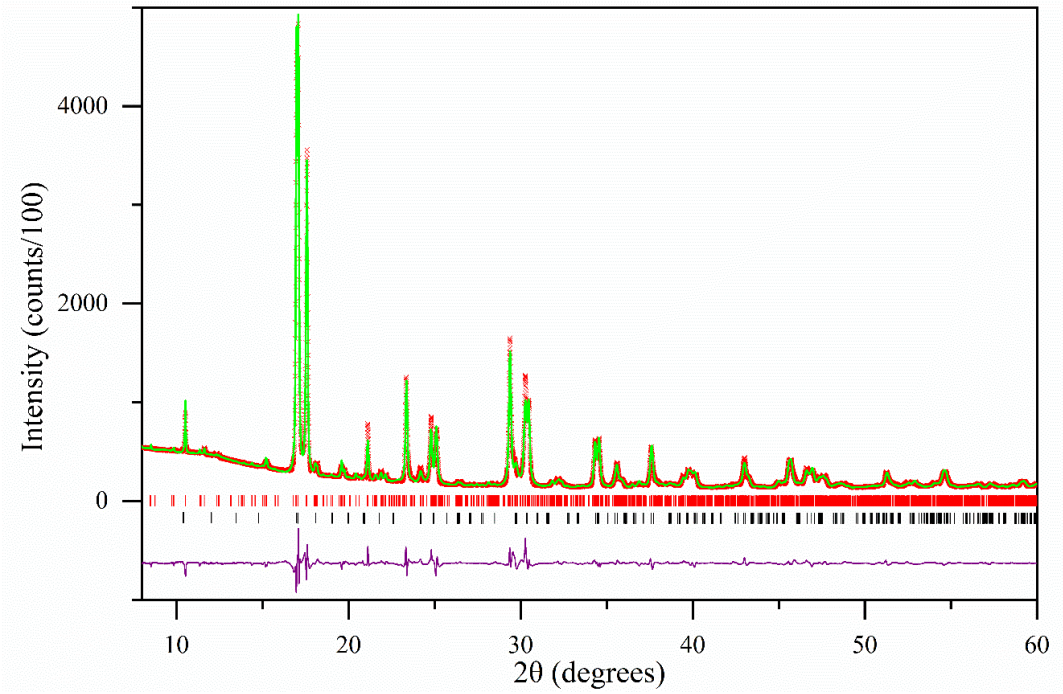


Figure A2-28. Observed, calculated and difference plots from the structural refinement of $La_{1.2}Sr_{0.8}CoRuO_5$ against XRD data collected at room temperature. Upper ticks mark the peak

positions of the majority phase $La_{1.2}Sr_{0.8}CoRuO_5$ and lower ticks mark the peak positions of the minority phase $La_{1.2}Sr_{0.8}CoRuO_6$.

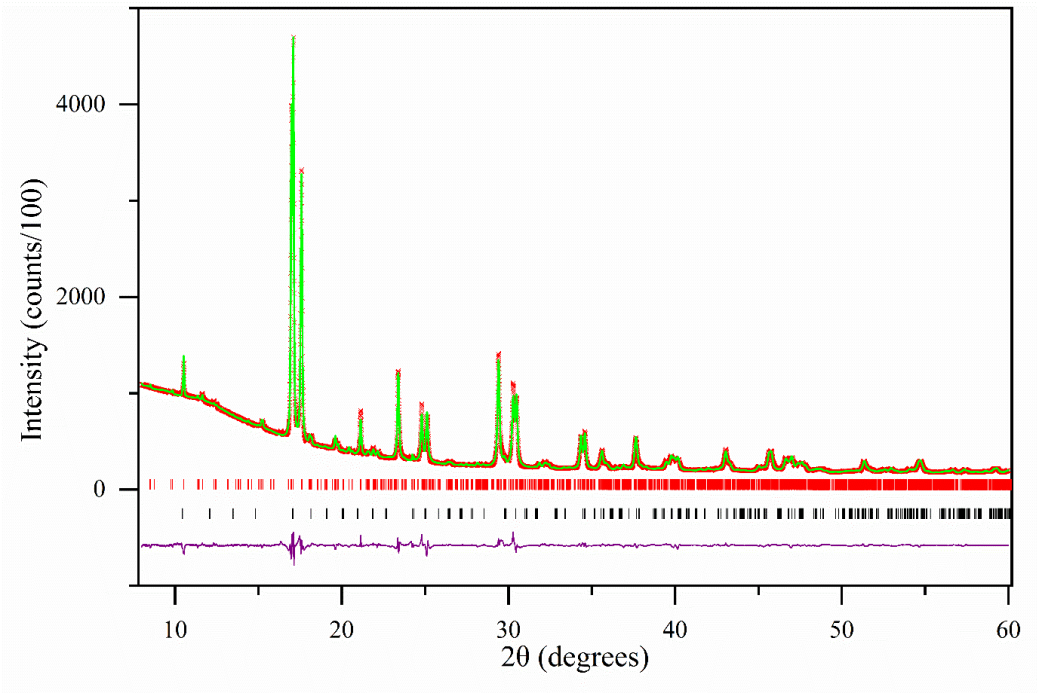


Figure A2-29. Observed, calculated and difference plots from the structural refinement of $La_{1.3}Sr_{0.7}CoRuO_5$ against XRD data collected at room temperature. Upper ticks mark the peak positions of the majority phase $La_{1.3}Sr_{0.7}CoRuO_5$ and lower ticks mark the peak positions of the minority phase $La_{1.3}Sr_{0.7}CoRuO_6$.

Appendix 2.7 Magnetisation Data from $La_xSr_{2-x}CoRuO_5$ ($0.7 \leq x \leq 1.3$)

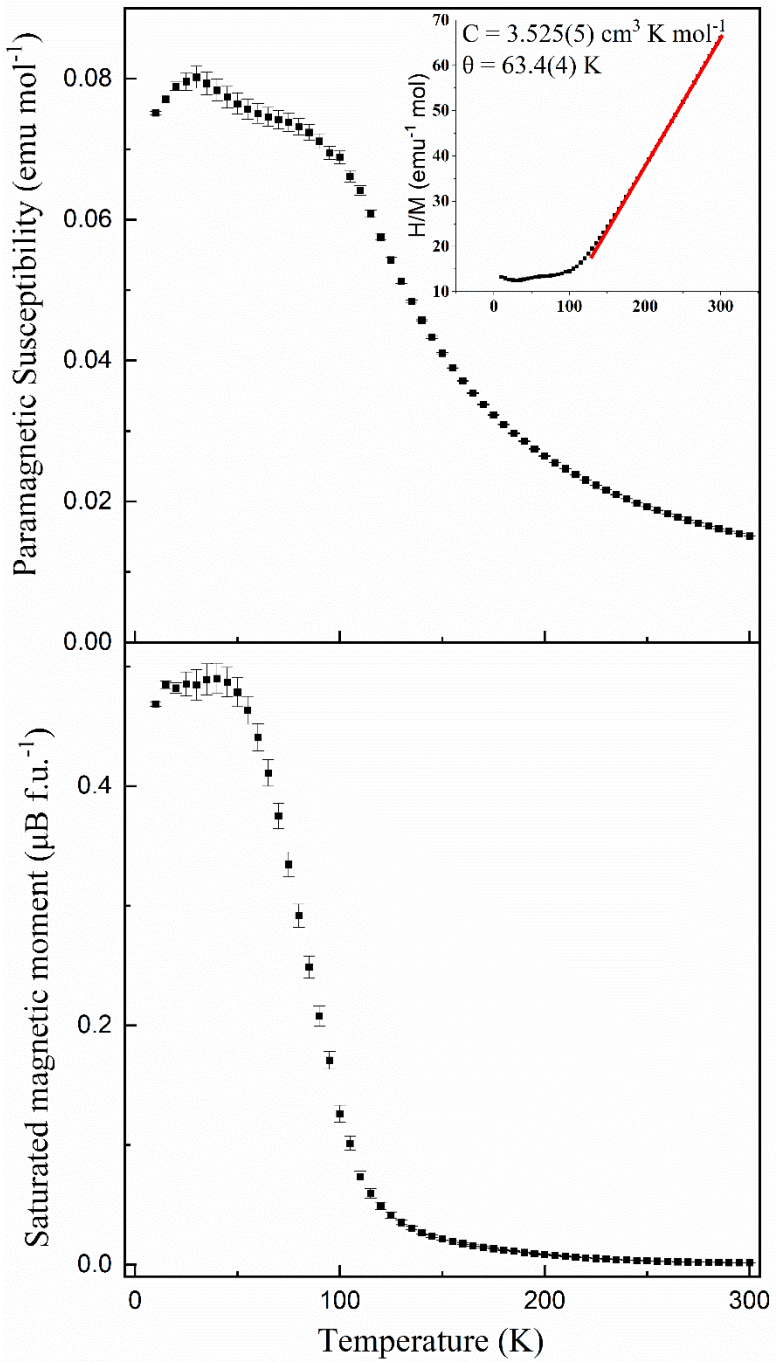


Figure A2-30. The paramagnetic susceptibility and saturated magnetic moment of $La_{0.7}Sr_{1.3}CoRuO_5$ as a function of temperature.

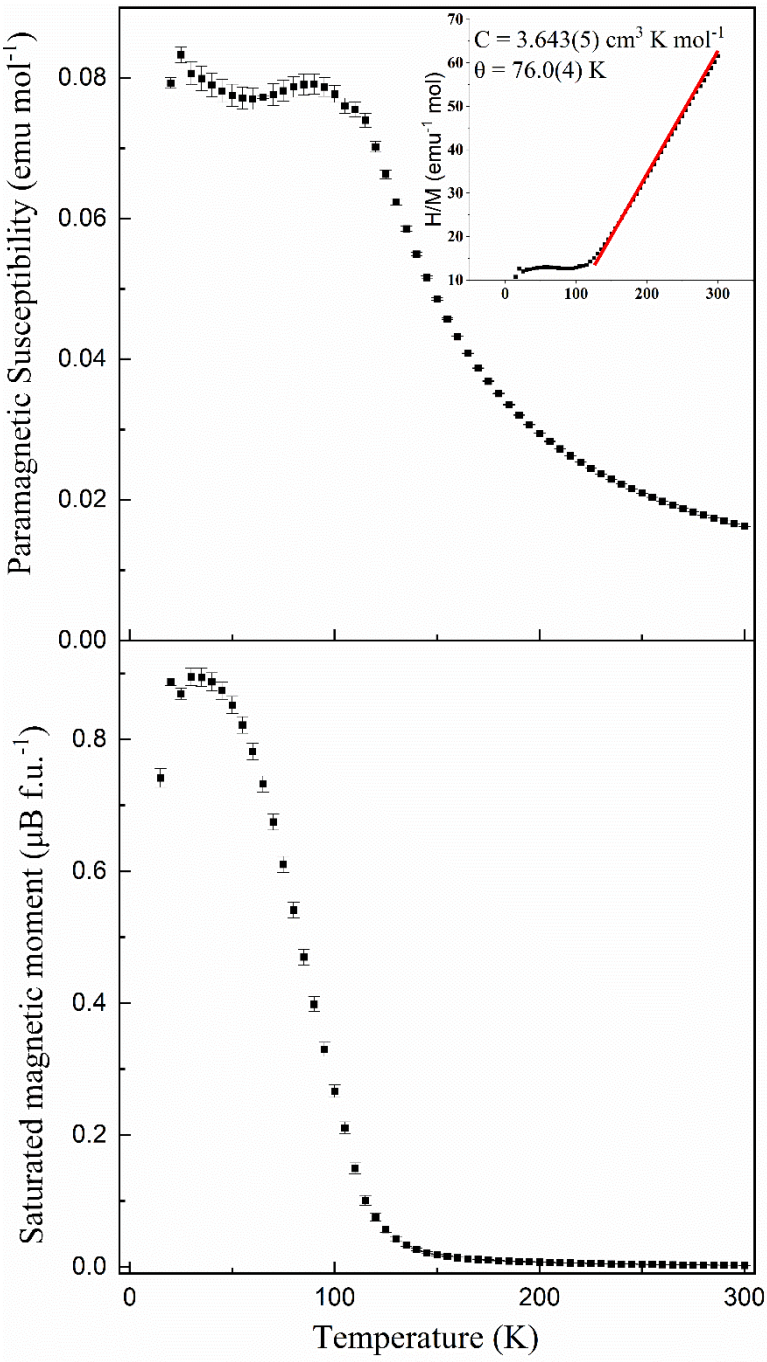


Figure A2-31. The paramagnetic susceptibility and saturated magnetic moment of $La_{0.9}Sr_{1.1}CoRuO_5$ as a function of temperature.

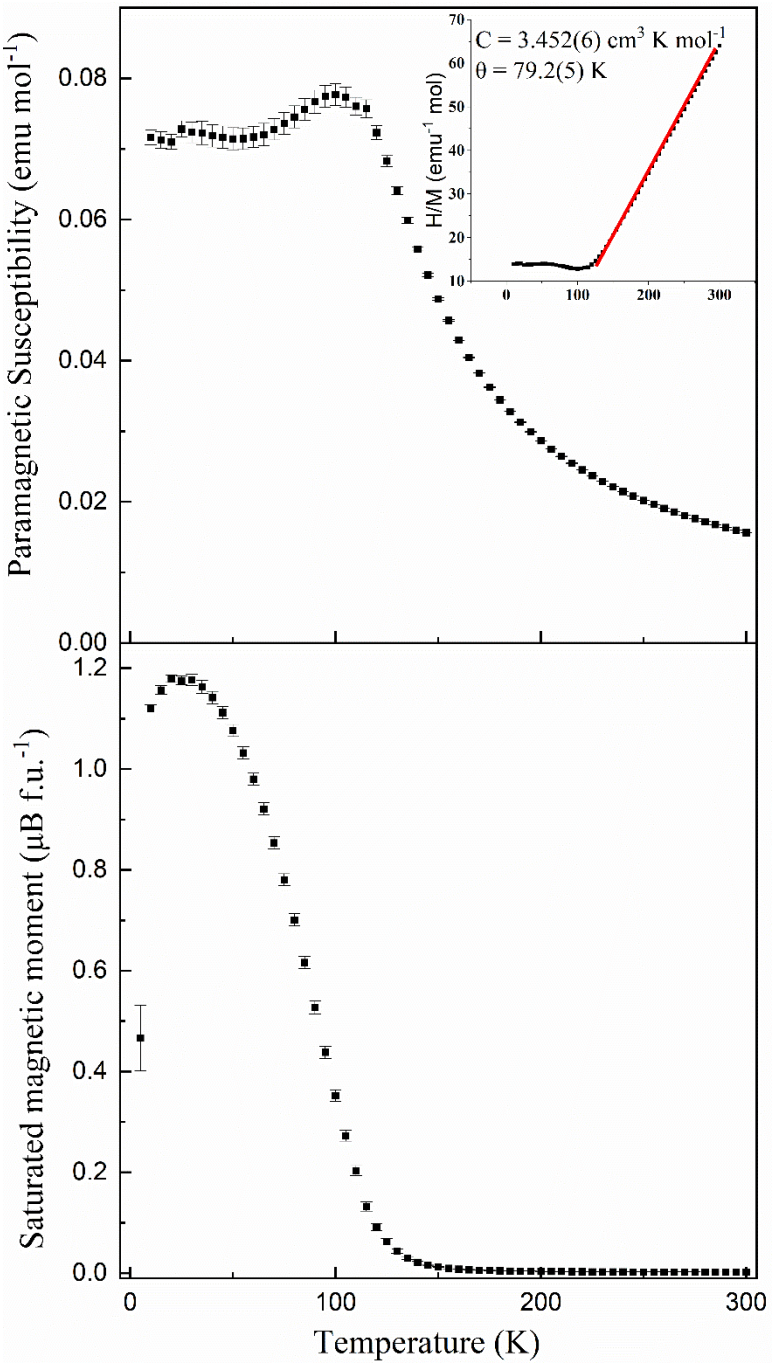


Figure A2-32. The paramagnetic susceptibility and saturated magnetic moment of $La_{1.1}Sr_{0.9}CoRuO_5$ as a function of temperature.

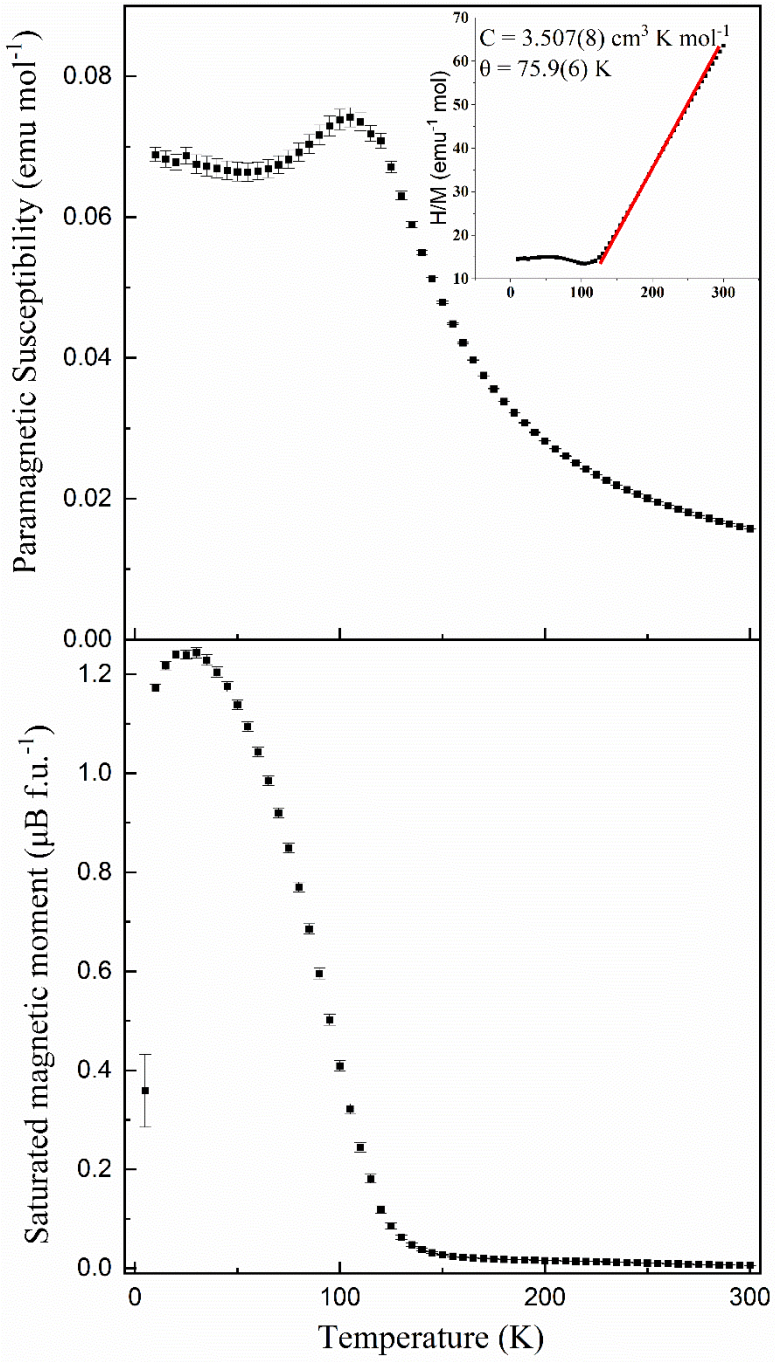


Figure A2-33. The paramagnetic susceptibility and saturated magnetic moment of $La_{1.2}Sr_{0.8}CoRuO_5$ as a function of temperature.

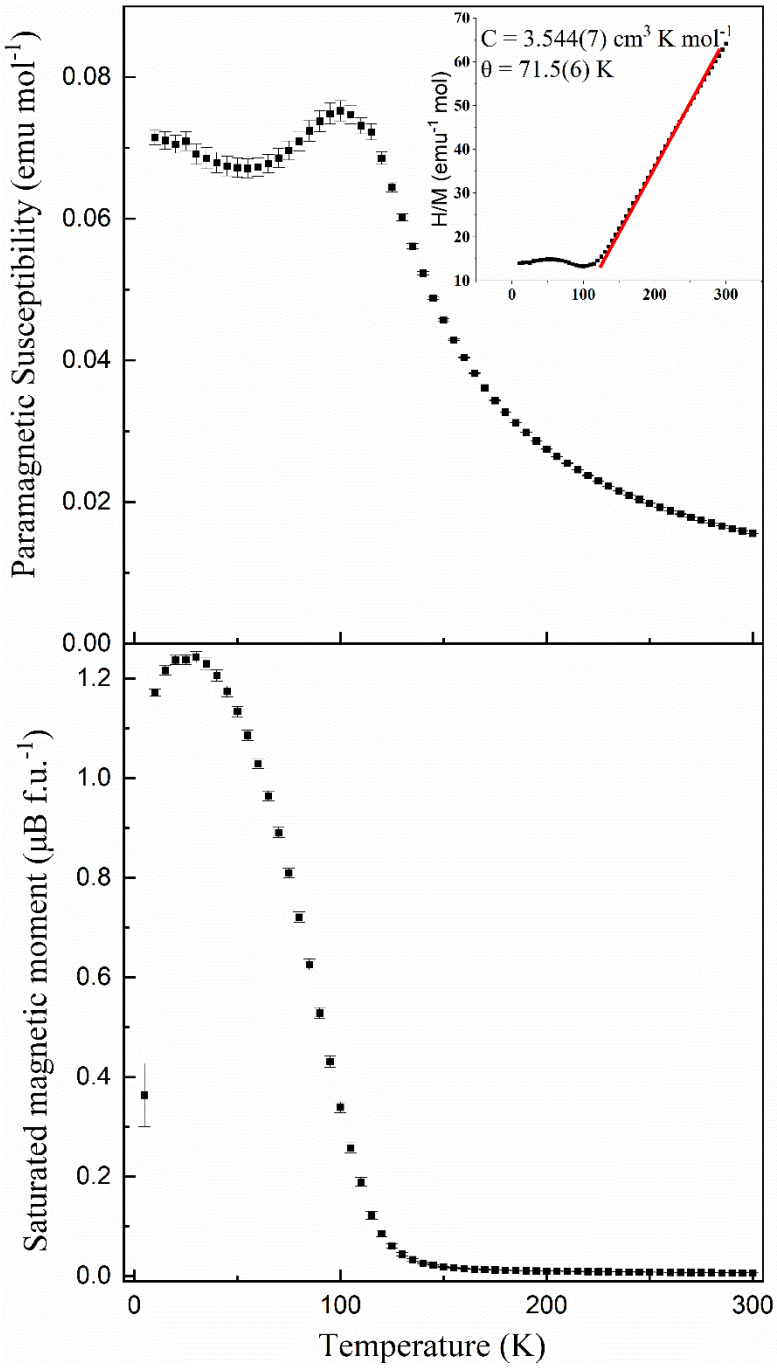


Figure A2-34. The paramagnetic susceptibility and saturated magnetic moment of $La_{1.3}Sr_{0.7}CoRuO_5$ as a function of temperature.

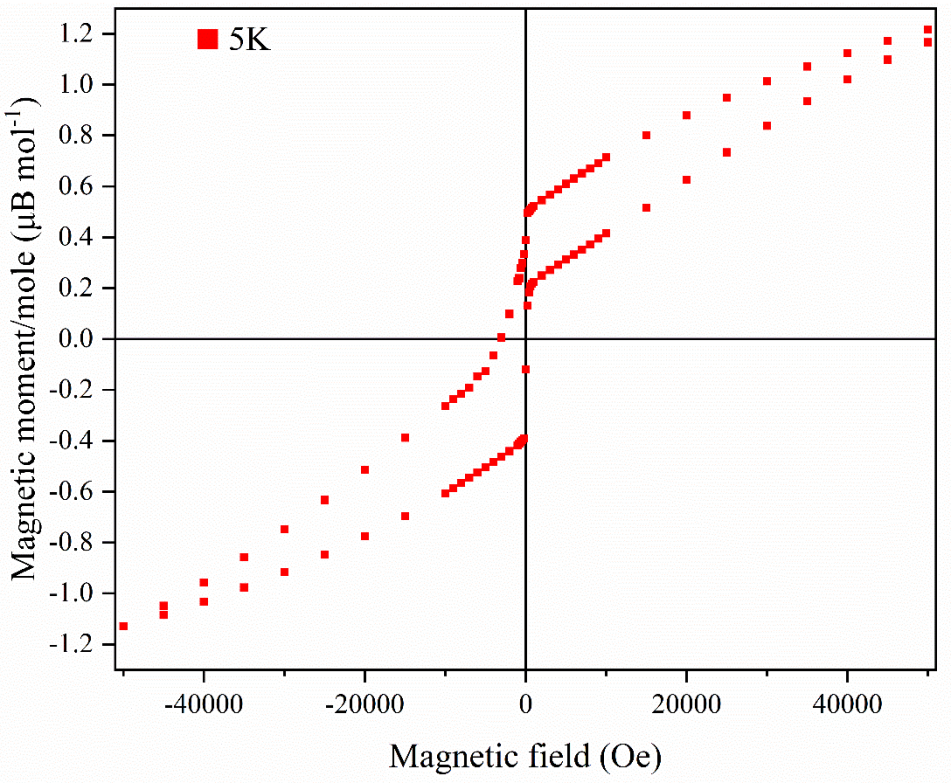


Figure A2-35. Magnetisation-field data collected from $La_{0.7}Sr_{1.3}CoRuO_5$ at 5 K.

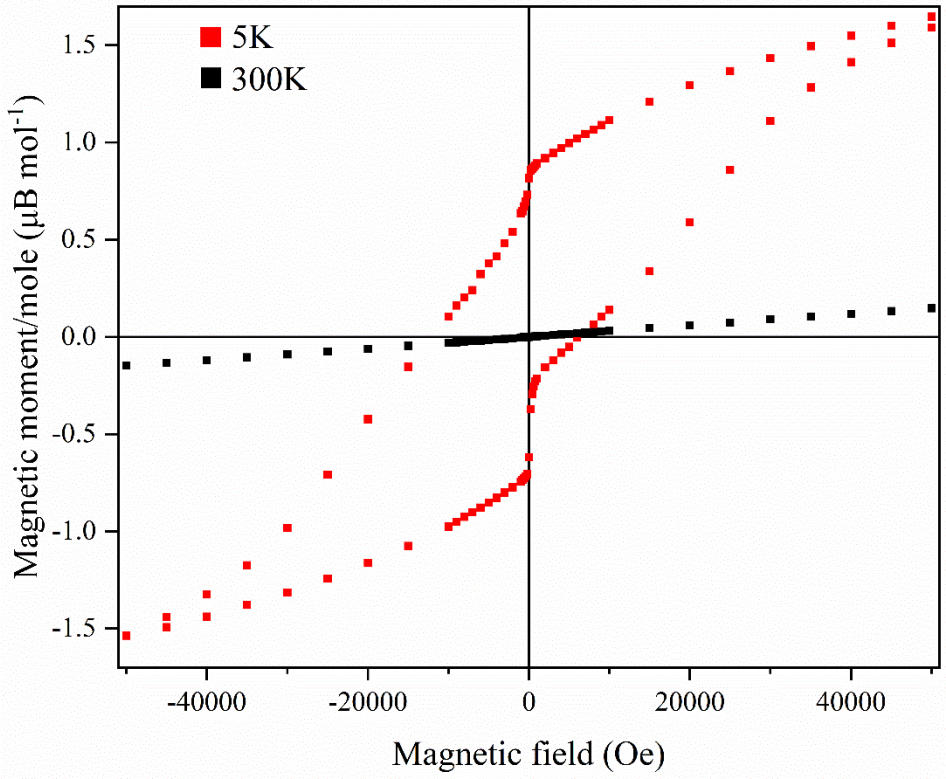


Figure A2-36. Magnetisation-field data collected from $La_{0.9}Sr_{1.1}CoRuO_5$ at 5 K and 300 K.

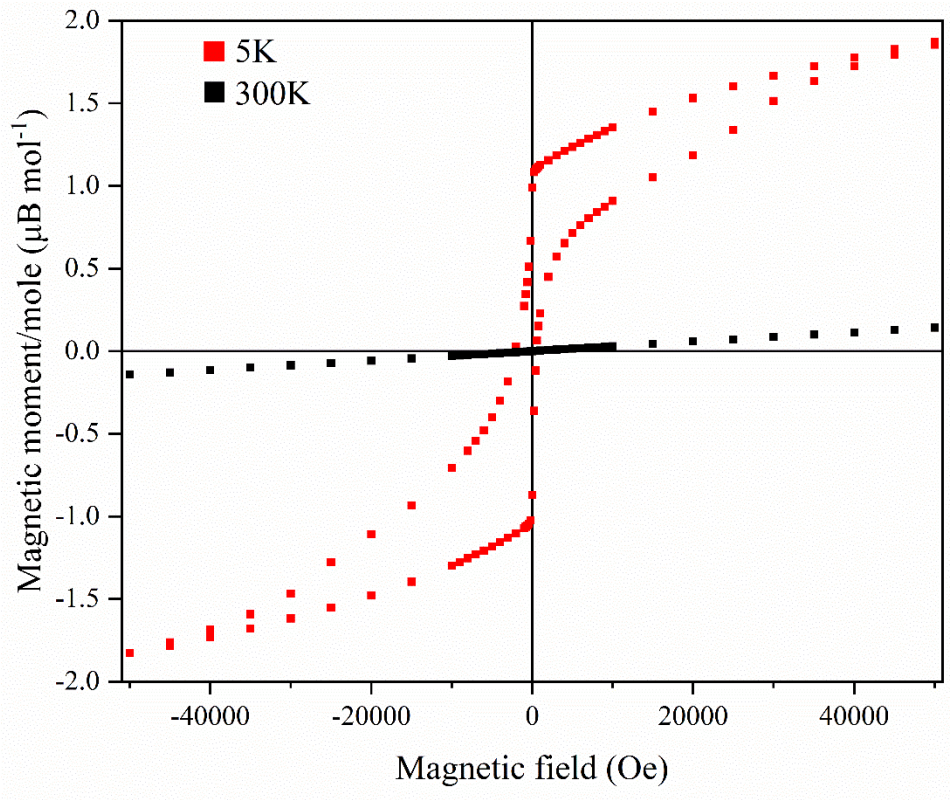


Figure A2-37. Magnetisation-field data collected from $La_{1.1}Sr_{0.9}CoRuO_5$ at 5 K and 300 K.

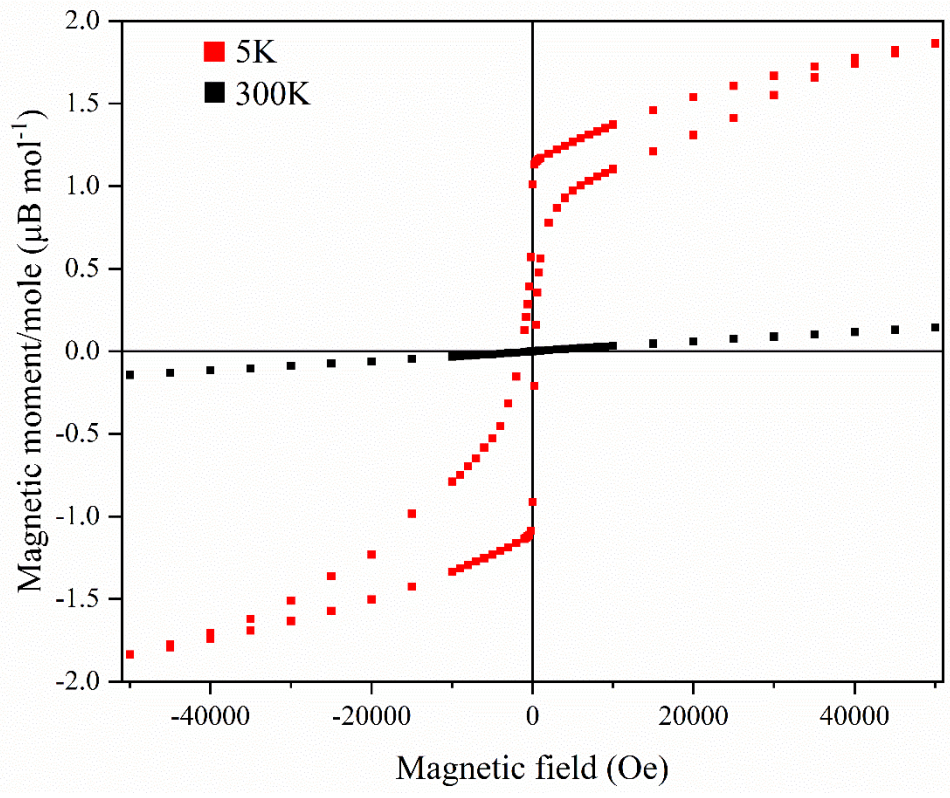


Figure A2-38. Magnetisation-field data collected from $La_{1.2}Sr_{0.8}CoRuO_5$ at 5 K and 300 K.

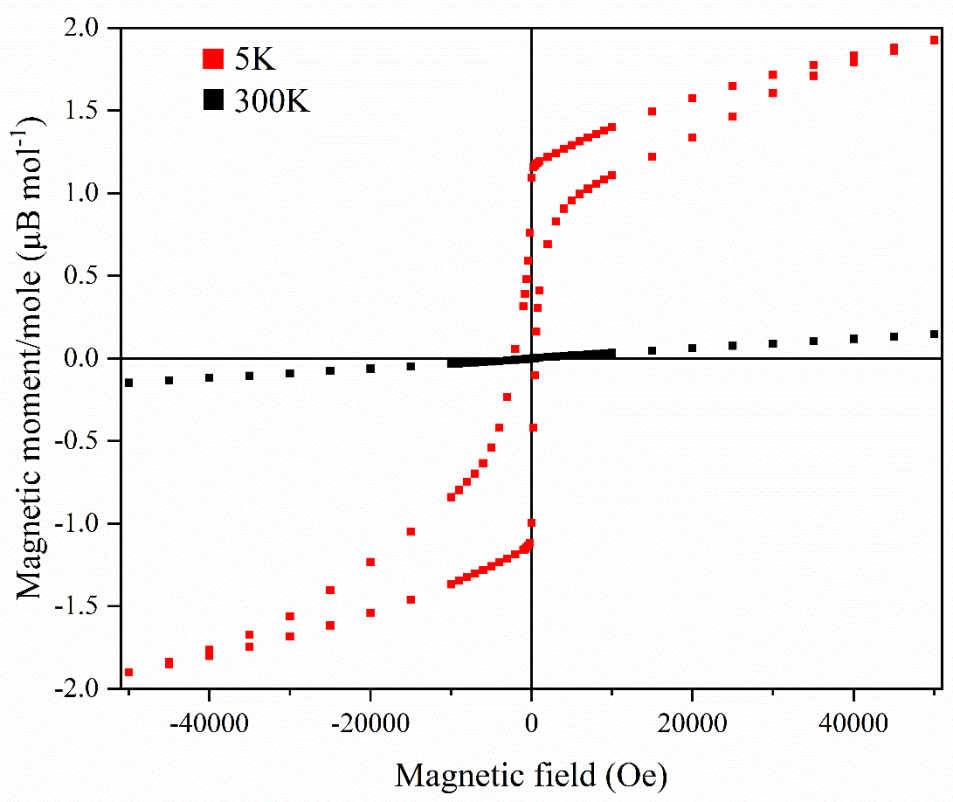


Figure A2-39. Magnetisation-field data collected from $La_{1.3}Sr_{0.7}CoRuO_5$ at 5 K and 300 K.

Appendix 2.8 TGA-MS of $LaSrCoRuO_6$

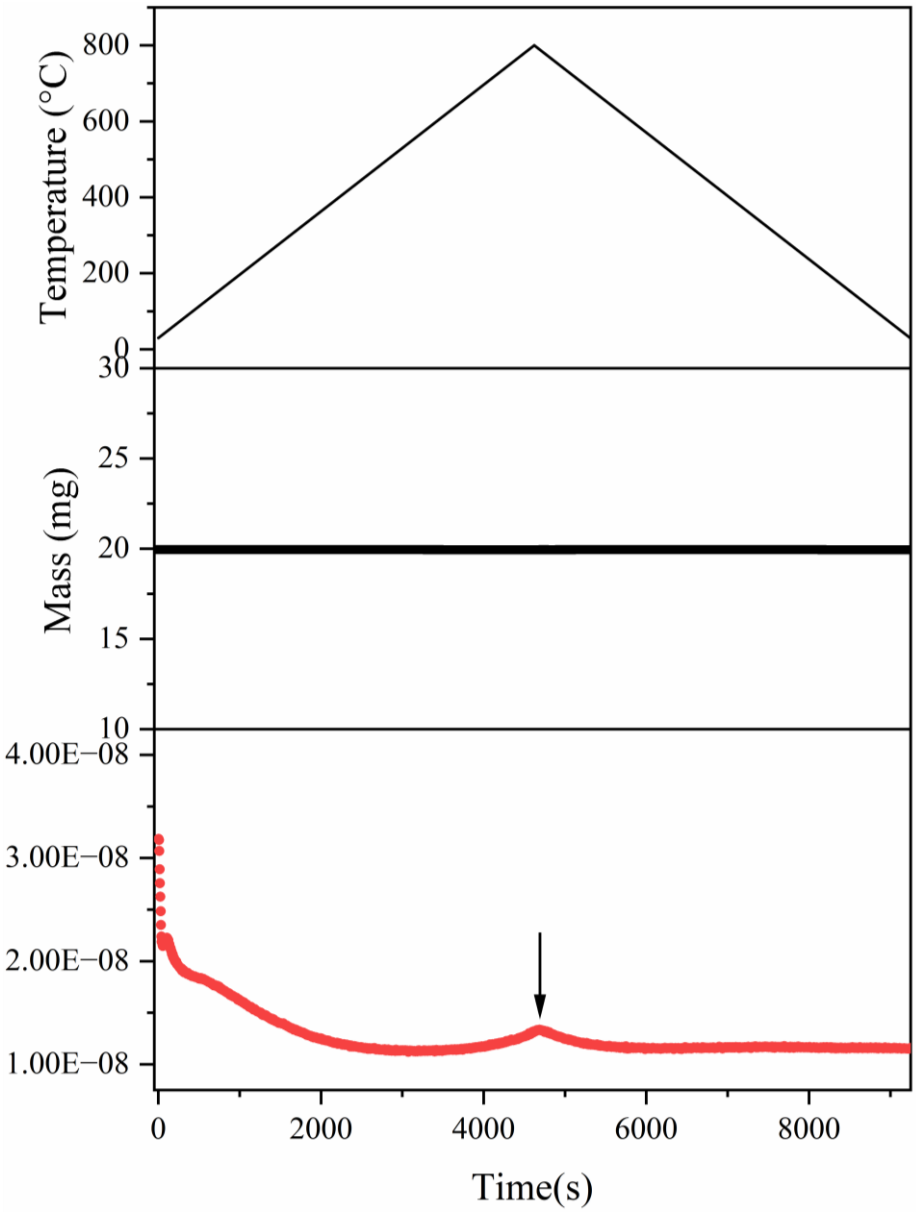


Figure A2-40. TGA-MS data collected from $LaSrCoRuO_6$ under a constant flow of oxygen. Arrow indicates the H_2O signal related to the TGA-MS machine.

Appendix 3 Bibliography

1 R. Mahendiran, S. Tiwary, A. Raychaudhuri, T. Ramakrishnan, R. Mahesh, N. Rangavittal and C. Rao, *Phys. Rev. B - Condens. Matter Mater. Phys.*, 1996, **53**, 3348–3358.

2 C. N. R. Rao, A. K. Cheetham and R. Mahesh, *Chem. Mater.*, 1996, **8**, 2421–2432.

3 P. Schiffer, A. P. Ramirez, W. Bao and S. W. Cheong, *Phys. Rev. Lett.*, 1995, **75**, 3336–3339.

4 J. G. Bednorz and K. A. Müller, *Zeitschrift für Phys. B Condens. Matter*, 1986, **64**, 189–193.

5 J. B. Goodenough, *Phys. Rev.*, 1967, **164**, 785–789.

6 M. Dawber, K. M. Rabe and J. F. Scott, *Rev. Mod. Phys.*, 2005, **77**, 1083–1130.

7 W. Eerenstein, N. D. Mathur and J. F. Scott, *Nature*, 2006, **442**, 759–765.

8 N. A. Spaldin and M. Fiebig, *Science (80-.).*, 2005, **309**, 391–392.

9 N. Spaldin, *Magnetic Materials: Fundamentals and Applications*, 2003.

10 B. D. Josephson, *Proc. IEEE*, 1974, **62**, 838–841.

11 J. B. Goodenough and J.-S. Zhou, *Chem. Mater.*, 1998, **10**, 2980–2993.

12 J. Hutton and R. J. Nelmes, *J. Phys. C Solid State Phys.*, 1981, **14**, 1713–1736.

13 V. M. Goldschmidt, *Naturwissenschaften*, 1926, **14**, 477–485.

14 S. Sasaki, C. T. Prewitt, J. D. Bass and W. A. Schulze, *Acta Crystallogr. Sect. C*, 1987, **43**, 1668–1674.

15 J. L. García-Muñoz, J. Rodríguez-Carvajal, P. Lacorre and J. B. Torrance, *Phys. Rev. B*, 1992, **46**, 4414–4425.

16 R. Morrow, M. A. McGuire, J. Yan and P. M. Woodward, *Inorg. Chem.*, 2018, **57**, 2989–3001.

17 L. T. Nguyen and R. J. Cava, *Chem. Rev.*, 2021, **121**, 2935–2965.

18 Y. Takeda, F. Kanamura, M. Shimada and M. Koizumi, *Acta Crystallogr. Sect. B Struct. Crystallogr. Cryst. Chem.*, 1976, **32**, 2464–2466.

19 G. King and P. M. Woodward, *J. Mater. Chem.*, 2010, **20**, 5785–5796.

20 P. D. Battle, T. C. Gibb, C. W. Jones and F. Studer, *J. Solid State Chem.*, 1989, **78**, 281–293.

21 M. A. Hayward, *Semicond. Sci. Technol.*, , DOI:10.1088/0268-1242/29/6/064010.

22 M. Hayward, in *Comprehensive Inorganic Chemistry II (Second Edition)*, eds. J. Reedijk and K. Poeppelmeier, Elsevier, Amsterdam, Second Edi., 2013, pp. 417–453.

23 M. A. Hayward and M. J. Rosseinsky, *Nature*, 2007, **450**, 960–961.

24 M. A. Hayward, M. A. Green, M. J. Rosseinsky and J. Sloan, *J. Am. Chem. Soc.*, 1999, **121**, 8843–8854.

25 Y. Tsujimoto, C. Tassel, N. Hayashi, T. Watanabe, H. Kageyama, K. Yoshimura, M. Takano, M. Ceretti, C. Ritter and W. Paulus, *Nature*, 2007, **450**, 1062–1065.

26 F. Denis Romero, S. J. Burr, J. E. McGrady, D. Gianolio, G. Cibin and M. A. Hayward, *J. Am. Chem. Soc.*, 2013, **135**, 1838–1844.

27 F. Denis Romero, P. A. Bingham, S. D. Forder and M. A. Hayward, *Inorg. Chem.*, 2013, **52**, 3388–3398.

28 M. A. Hayward, E. J. Cussen, J. B. Claridge, M. Bieringer, M. J. Rosseinsky, C. J. Kiely, S. J. Blundell, I. M. Marshall and F. L. Pratt, *Science (80-.).*, 2002, **295**, 1882–1884.

29 Y. Kobayashi, O. J. Hernandez, T. Sakaguchi, T. Yajima, T. Roisnel, Y. Tsujimoto, M. Morita, Y. Noda, Y. Mogami, A. Kitada, M. Ohkura, S. Hosokawa, Z. Li, K. Hayashi, Y. Kusano, J. E. Kim, N. Tsuji, A. Fujiwara, Y. Matsushita, K. Yoshimura, K.

Takegoshi, M. Inoue, M. Takano and H. Kageyama, *Nat. Mater.*, 2012, **11**, 507–511.
30 M. Cardona, *Phys. Rev.*, , DOI:10.1103/PhysRev.140.A651.
31 H. Kageyama, K. Hayashi, K. Maeda, J. P. Attfield, Z. Hiroi, J. M. Rondinelli and K. R. Poeppelmeier, *Nat. Commun.*, 2018, **9**, 772.
32 Y. Kobayashi, O. Hernandez, C. Tassel and H. Kageyama, *Sci. Technol. Adv. Mater.*, 2017, **18**, 905–918.
33 N. N. Greenwood and A. B. T. Earnshaw, in *Chemistry of the Elements (Second Edition)*, eds. N. N. Greenwood and A. Earnshaw, Butterworth-Heinemann, Oxford, Second Edi., 1997, pp. 32–67.
34 J. Seddon, E. Suard and M. A. Hayward, *J. Am. Chem. Soc.*, 2010, **132**, 2802.
35 J. A. Pratt, A. M. Shepherd and M. A. Hayward, *Inorg. Chem.*, 2015, **54**, 10993–10997.
36 J. E. Page, H. W. T. Morgan, D. Zeng, P. Manuel, J. E. McGrady and M. A. Hayward, *Inorg. Chem.*, 2018, **57**, 13577.
37 M. A. Patino, D. Zeng, R. Bower, J. E. McGrady and M. A. Hayward, *Inorg. Chem.*, 2016, **55**, 9012–9016.
38 L. Jin, M. Lane, D. Zeng, F. K. K. Kirschner, F. Lang, P. Manuel, S. J. Blundell, J. E. McGrady and M. A. Hayward, *Angew. Chemie - Int. Ed.*, 2018, **57**, 5025–5028.
39 J. J. Adkin and M. A. Hayward, *Inorg. Chem.*, 2008, **47**, 10959–10964.
40 B. C. Hansteen, Ole H. Fjellvåg, Helmer.Hauback, *J. Mater. Chem.*, 1998, **8**, 2081–2088.
41 P. M. Woodward, P. Karen, J. S. O. Evans and T. Vogt, *Solid State Materials Chemistry*, 2021.
42 M. Swart and M. Costas, *Spin States in Biochemistry and Inorganic Chemistry: Influence on Structure and Reactivity*, 2015.
43 T. M. Schuler, D. L. Ederer, S. Itza-Ortiz, G. T. Woods, T. A. Callcott and J. C. Woicik, *Phys. Rev. B - Condens. Matter Mater. Phys.*, 2005, **71**, 1–7.
44 J. Hugel and M. Kamal, *Solid State Commun.*, 1996, **100**, 457–461.
45 P. A. Cox, *The Electronic Structure and Chemistry of Solids*, Oxford University Press, 2005.
46 P. W. Anderson, *Phys. Rev.*, 1950, **79**, 350–356.
47 J. B. Goodenough, *Magnetism and the chemical bond*, Interscience publishers, 1963, vol. 1.
48 M. A. Hayward, *Inorg. Chem.*, 2019, **58**, 11961–11970.
49 M. P. Pechini, *US Pat.*, 1967, 697.
50 T. Yamamoto and H. Kageyama, *Chem. Lett.*, 2013, **42**, 946–953.
51 A. J. Blake, W. Clegg, J. M. Cole, J. S. O. Evans, P. Main, S. Parsons and D. J. Watkin, *Crystal Structure Analysis Principles and Practice Second Edition*, 2009.
52 B. D. Cullity, *Elements of X-Ray Diffraction*, 1956.
53 http://pd.chem.ucl.ac.uk/pdnn/inst2/synindex.htm.
54 S. P. Thompson, J. E. Parker, J. Potter, T. P. Hill, A. Birt, T. M. Cobb, F. Yuan and C. C. Tang, *Rev. Sci. Instrum.*, , DOI:10.1063/1.3167217.
55 R. Dinnebier, A. Leineweber and J. Evans, *Rietveld Refinement: Practical Powder Diffraction Pattern Analysis using TOPAS (De Gruyter STEM)*, 2018.
56 V. F. Sears, *Neutron News*, 1992, **3**, 26–37.
57 J. Rodríguez-Carvajal, *Phys. B Condens. Matter*, 1993, **192**, 55–69.
58 https://www.isis.stfc.ac.uk/Pages/Wish.aspx.
59 L. C. Chapon, P. Manuel, P. G. Radaelli, C. Benson, L. Perrott, S. Ansell, N. J. Rhodes, D. Raspino, D. Duxbury, E. Spill and J. Norris, *Neutron News*, 2011, **22**, 22–25.

60 http://pd.chem.ucl.ac.uk/pdnn/inst3/diff1.htm.
61 H. M. Rietveld, *J. Appl. Crystallogr.*, 1969, **2**, 65–71.
62 A. A. Coelho, *J. Appl. Crystallogr.*, 2018, **51**, 210–218.
63 B. . Toby, *Int. Tables Crystallogr. Vol. H*, 2019, **H**, 468.
64 J. Clark, 1994, **271**, 46–53.
65 P. M. Woodward, P. Karen, J. S. O. Evans and T. Vogt, *Solid State Materials Chemistry*, Cambridge University Press, 2021.
66 N. E. Brese and M. O'Keeffe, *Acta Crystallogr. Sect. B*, 1991, **47**, 192–197.
67 F. W. Fifield and D. Kealey, *Principles and Practice of Analytical Chemistry*, 2000.
68 M. Gateshki and J. M. Igartua, *Mater. Res. Bull.*, 2003, **38**, 1893–1900.
69 P. M. Woodward, *Acta Crystallogr. Sect. B*, 1997, **53**, 32–43.
70 Z. Liang, M. Amano Patino, M. Hendrickx, J. Hadermann and M. A. Hayward, *ACS Org. Inorg. Au*, 2021, **2**, 75–82.
71 M. E. A. Patiño, University of Oxford, 2016.
72 K. Kageyama, Y. Yang, T. Kageyama, K. Murayama, K. Shitara, T. Saito, H. Ubukata, C. Tassel, A. Kuwabara and H. Kageyama, *Inorganics*, 2022, **10**, 73.
73 N. Meethong, H. Y. S. Huang, S. A. Speakman, W. C. Carter and Y. M. Chiang, *Adv. Funct. Mater.*, 2007, **17**, 1115–1123.
74 F. Denis Romero, A. Leach, J. S. Möller, F. Foronda, S. J. Blundell and M. A. Hayward, *Angew. Chemie Int. Ed.*, 2014, **53**, 7556–7559.
75 R. Bower, University of Oxford, 2014.
76 S. Aasland, H. Fjellvåg and B. C. Hauback, *J. Solid State Chem.*, 1998, **135**, 103–110.
77 Y. Shimakawa, S. Inoue, M. Haruta, M. Kawai, K. Matsumoto, A. Sakaiguchi, N. Ichikawa, S. Isoda and H. Kurata, *Cryst. Growth Des.*, 2010, **10**, 4713–4715.
78 J. Akimoto, Y. Gotoh and Y. Oosawa, *J. Solid State Chem.*, 1998, **141**, 298–302.
79 Z. Xu, P. K. Thakur, T.-L. Lee, A. Regoutz, E. Suard, I. Puente-Orench and M. A. Hayward, *Inorg. Chem.*, 2022, **61**, 15686–15692.
80 Z. Xu, R. G. Palgrave and M. A. Hayward, *Inorg. Chem.*, 2020, **59**, 13767–13773.
81 W. Yi, Y. Matsushita, M. Tanaka and A. A. Belik, *Inorg. Chem.*, 2012, **51**, 7650–7656.
82 R. V. Panin, N. R. Khasanova, C. Bougerol, W. Schnelle, G. Van Tendeloo and E. V. Antipov, *Inorg. Chem.*, 2010, **49**, 1295–1297.
83 Y. Hosaka, N. Ichikawa, T. Saito, J. P. Attfield and Y. Shimakawa, *Phys. Rev. B*, 2016, **94**, 104429.
84 H. Guo, Y. Hosaka, H. Seki, T. Saito, N. Ichikawa and Y. Shimakawa, *J. Solid State Chem.*, 2017, **246**, 199–202.
85 S. J. Kim, M. J. Martinez-Lope, M. T. Fernandez-Diaz, J. A. Alonso, I. Presniakov and G. Demazeau, *Chem. Mater.*, 2002, **14**, 4926–4932.
86 J. A. Alonso, J. L. García-Muñoz, M. T. Fernández-Díaz, M. A. G. Aranda, M. J. Martínez-Lope and M. T. Casais, *Phys. Rev. Lett.*, 1999, **82**, 3871–3874.
87 J. E. Page, H. W. T. Morgan, D. Zeng, P. Manuel, J. E. McGrady and M. A. Hayward, *Inorg. Chem.*, 2018, **57**, 13577–13585.
88 H. T. Stokes, D. M. Hatch and B. J. Campbell, ISODISTORT, ISOTROPY Software Suite.
89 S. Zhu, F. Fan, K. Yang and H. Wu, *Epl*, 2017, **117**, 2–7.
90 P. Tomeš, J. Hejtmánek and K. Knížek, *Solid State Sci.*, 2008, **10**, 486–490.
91 J.-W. G. Bos and J. Paul Attfield, *Chem. Mater.*, 2004, **16**, 1822–1827.
92 R. D. Shannon and C. T. Prewitt, *Acta Crystallogr. Sect. B*, 1969, **25**, 925–946.
93 Z. Xu, L. Jin, J.-K. Backhaus, F. Green and M. A. Hayward, *Inorg. Chem.*, 2021, **60**, 14904–14912.

94 L. Jin and M. A. Hayward, *Angew. Chemie - Int. Ed.*, 2020, **59**, 2076–2079.
95 C. Tassel, J. M. Pruneda, N. Hayashi, T. Watanabe, A. Kitada, Y. Tsujimoto, H. Kageyama, K. Yoshimura, M. Takano, M. Nishi, K. Ohoyama, M. Mizumaki, N. Kawamura, J. Íñiguez and E. Canadell, *J. Am. Chem. Soc.*, 2009, **131**, 221–229.
96 L. Seinberg, T. Yamamoto, C. Tassel, Y. Kobayashi, N. Hayashi, A. Kitada, Y. Sumida, T. Watanabe, M. Nishi, K. Ohoyama, K. Yoshimura, M. Takano, W. Paulus and H. Kageyama, *Inorg. Chem.*, 2011, **50**, 3988–3995.
97 S. Zeng, C. Li, L. E. Chow, Y. Cao, Z. Zhang, C. S. Tang, X. Yin, Z. S. Lim, J. Hu, P. Yang and A. Ariando, *Sci. Adv.*, 2022, **8**, eabl9927.
98 R. Phatak, K. Krishnan, S. K. Sali, A. Das and A. K. Nigam, *J. Magn. Magn. Mater.*, 2013, **344**, 129–133.
99 J. W. G. Bos and J. P. Attfield, *J. Mater. Chem.*, 2005, **15**, 715–720.
100 L. Jin, M. Batuk, F. K. K. Kirschner, F. Lang, S. J. Blundell, J. Hadermann and M. A. Hayward, *Inorg. Chem.*, 2019, **58**, 14863–14870.
101 M. Yang, J. Oró-Solée, J. A. Rodgers, A. B. Jorge, A. Fuertes and J. P. Attfield, *Nat. Chem.*, 2011, **3**, 47–52.
102 L. Jin and M. A. Hayward, *Chem. Commun.*, 2019, **55**, 4861–4864.